Ali Koochi
Mohamadreza Abadyan

Nonlinear Differential Equations in Micro/nano Mechanics

Application in Micro/nano Structures and Electromechanical Systems

ELSEVIER

NONLINEAR DIFFERENTIAL EQUATIONS IN MICRO/NANO MECHANICS

NONLINEAR DIFFERENTIAL EQUATIONS IN MICRO/NANO MECHANICS

Application in micro/nanostructures and electromechanical systems

ALI KOOCHI
Department of Mechanical Engineering
University of Torbat Heydarieh
Torbat Heydarieh, Iran

MOHAMADREZA ABADYAN
Department of Mechanical & Aerospace Engineering
Ramsar Branch, Islamic Azad University
Ramsar, Iran

Elsevier
Radarweg 29, PO Box 211, 1000 AE Amsterdam, Netherlands
The Boulevard, Langford Lane, Kidlington, Oxford OX5 1GB, United Kingdom
50 Hampshire Street, 5th Floor, Cambridge, MA 02139, United States

Copyright © 2020 Elsevier Ltd. All rights reserved.

No part of this publication may be reproduced or transmitted in any form or by any means, electronic or mechanical, including photocopying, recording, or any information storage and retrieval system, without permission in writing from the publisher. Details on how to seek permission, further information about the Publisher's permissions policies and our arrangements with organizations such as the Copyright Clearance Center and the Copyright Licensing Agency, can be found at our website: www.elsevier.com/permissions.

This book and the individual contributions contained in it are protected under copyright by the Publisher (other than as may be noted herein).

Notices

Knowledge and best practice in this field are constantly changing. As new research and experience broaden our understanding, changes in research methods, professional practices, or medical treatment may become necessary.

Practitioners and researchers must always rely on their own experience and knowledge in evaluating and using any information, methods, compounds, or experiments described herein. In using such information or methods they should be mindful of their own safety and the safety of others, including parties for whom they have a professional responsibility.

To the fullest extent of the law, neither the Publisher nor the authors, contributors, or editors, assume any liability for any injury and/or damage to persons or property as a matter of products liability, negligence or otherwise, or from any use or operation of any methods, products, instructions, or ideas contained in the material herein.

Library of Congress Cataloging-in-Publication Data
A catalog record for this book is available from the Library of Congress

British Library Cataloguing-in-Publication Data
A catalogue record for this book is available from the British Library

ISBN: 978-0-12-819235-1

For information on all Elsevier publications
visit our website at https://www.elsevier.com/books-and-journals

Publisher: Matthew Deans
Acquisitions Editor: Simon Holt
Editorial Project Manager: Gabriela D. Capille
Production Project Manager: Nirmala Arumugam
Designer: Alan Studholme

Typeset by VTeX

To my wife Fatemeh,

my daughter Kousar,

and my son Kiarash.

Ali Koochi

To O. B.
For O. B. was an inspiring friend even though we've never met.
O. B. knew the secrets of seasons,
And lives far away, where one might miss home.

…If all these reasons are not enough, I will dedicate the book to KOOCHI from whom O. B. grew… And so I correct my dedication: To O. B. when O. B. was KOOCHI.

Mohamadreza Abadyan

Contents

Preface *ix*
Acknowledgments *xi*

1. Differential equations in miniature structures **1**
1.1. Introduction to miniature structures 1
1.2. Physics of small-scale structures 4
1.3. Modeling of small-scale structures 17
1.4. Conclusion 26
References 26

2. Semianalytical solution methods **31**
2.1. Introduction 31
2.2. Homotopy perturbation method 31
2.3. Adomian decomposition methods 43
2.4. Green's function methods 63
2.5. Differential transformation method 77
2.6. Variation iteration methods 84
2.7. Galerkin method for static problems 90
2.8. Conclusion 100
References 100

3. Numerical solution methods **107**
3.1. Introduction 107
3.2. Generalized differential quadrature method 107
3.3. Finite difference method 124
3.4. Finite element method 136
3.5. Conclusion 156
References 156

4. Dynamic and time-dependent equations **161**
4.1. Introduction 161
4.2. Reduced-order approaches 161
4.3. Runge–Kutta method 195
4.4. Homotopy perturbation method for time-dependent differential equations 217
4.5. Energy balance method 227
4.6. Method of multiple scales 237
4.7. Conclusion 248
References 248

Index *253*

Preface

Introduction

With the new advances in micro- and nanotechnology, ultrasmall structures have been increasingly considered in various engineering and science branches. In-depth knowledge of the miniature structures under various physical phenomena can significantly reduce the time and cost of designing, developing, and optimizing these structures, compared to repetitive fabrication and testing in the laboratory.

The purpose of this book is to bring together the various concepts, methods, and techniques needed to attack and solve a wide array of problems, including modeling, simulation, analysis, and design of small-scale structures such as micro- and nanoelectromechanical systems (NEMS/MEMS).

Generally, accurate models are crucial for nanostructure design and analysis due to the high costs and complexity of experimental setups and fabrication processes. On the other hand, reliable simulation of miniature systems requires a comprehensive understanding of the mechanical behaviors of devices, as well as the interaction between the system and external force fields. In this way, new physical phenomena will emerge in the case of decreasing the dimensions of a structure from microscale to nanoscale. The precise simulation of MEMS/NEMS needs a comprehensive knowledge of nanoscale phenomena and efficient methods to include these issues in the final model. The mechanical performance of nanostructures can be modeled using various techniques such as molecular dynamics/mechanics, multiscale modeling, modified mechanics models, and the like. In this regard, the use of nonclassical continuum mechanics is regarded as one of the powerful techniques for modeling miniature structures. The continuum mechanic does not require computational equipment as the molecular dynamics or ab-initio methods and provides sufficiently accurate results for simulating nanostructures. However, continuum mechanics usually leads to a highly nonlinear differential equation that cannot be solved using conventional techniques.

This book attempts to apply various efficient numerical and semianalytical methods for solving the nonlinear governing equations of micro/nanostructures that emerged from the modified continuum mechanics models. The proposed solution methods are employed to evaluate the static and dynamic behaviors of micro/nanostructures through some appropriate examples. To this aim, we simulated various structures, including beam type MEMS/NEMS, carbon nanotube actuators, nanotweezers, nanobridges, plate-type microsystems, nanoresonators, and rotational micromirrors. The book also includes the modeling process needed for simulating numerous nonlinearities in micro- and nanostructures due to physical phenomena such as dispersion forces, damping effect,

nonclassic boundary conditions, fluid–solid interactions, electromechanical instability, surface energies, nonlocal and size-dependency.

The material of the current book is organized as follows. Chapter 1 introduces the essential concepts for the modeling of ultrasmall structures and explains the physical phenomena emerging on the nano- and microscale. Chapter 2 discusses some semianalytical approaches to solve nonlinear differential equations, in addition to investigating the behavior of various micro- and nanostructures based on semianalytical methods. Chapter 3 presents a variety of numerical approaches to solve the nonlinear differential equations for evaluating the behavior of some micro- and nanostructures. Finally, Chapter 4 provides some mathematical approaches to solve the nonlinear partial differential equation describing the dynamic performance of micro/nanostructures.

It should be acknowledged that no matter how many times the material is reviewed and how many efforts are spent to guarantee the highest quality, the authors cannot ensure that the manuscript is free from minor errors and shortcomings. We are looking forward to receiving everyone's feedback and comments on the errors or subject of the book. Please send your comments to the first author's email at the Department of Mechanical Engineering, University of Torbat Heydarieh, with the address: A.koochi@gmail.com (Ali Koochi).

Audience

This book is a comprehensive text on nonlinear differential equations in micro- and nanostructures, and it has been prepared for a wide range of readers, especially academics, who need to learn how to solve nonlinear ordinary and partial differential equations, and professional researchers who investigate in the field of nanostructures and NEMS/MEMS modeling. The proposed methods are appropriate for multidisciplinary researchers in the field of micro/nano-computations. To be more precise:

- The book is suitable for students participating in the courses and researches on the nonlinear differential equation and analytical methods in micro- and nanostructures.
- The book can be useful for professionals, due to the consideration of different physical phenomena and various nano/microstructures.
- The solution methods of the differential equations are presented practically and straightforwardly. Therefore, the book will be suitable for both undergraduate and postgraduate levels, i.e., for Bachelor students and Master/PhD students and lecturers.
- This book can also be adapted for a short-term professional course on the subject matter. Engineers and applied science researchers will be able to draw upon the book in selecting and developing mathematical models for analysis and design purposes in applied conditions.

Acknowledgments

We would like to express our gratitude and appreciation to all those who have had an impact on this work. Many people working in the general areas of micro- and nanostructures, analytical methods, nonlinear phenomena, nonlinear differential equations, mathematical and physical problems, and nonlinear continuum mechanics, have influenced the format of this book.

We are particularly thankful to the Department of Mechanical Engineering at the University of Torbat Heydarieh, Iran, which provides an excellent scholarly environment, especially, **Dr. Mohammad Reza Gharib** and **Dr. Masoud Goharimanesh**. We also give our sincere acknowledgments and gratitude to many colleagues and peers, as well as our collaborators in the field of NEMS analysis, especially, **Prof. Randolph Rach**, **Dr. Hamid M. Sedighi**, **Dr. Javad Mokhtari**, **Prof. Hossein Hosseini-Toudeshky**, **Prof. Hamid Reza Ovesy**, **Dr. Amin Farrokhabadi**, **Dr. Ehsan Roohi**, **Prof. Aminreza Noghrehabadi**, **Dr. Asieh Sadat Kazemi**, **Mr. Morteza Rezaei**, **Ms. Naeime Abadian**, and **Ms. Fatemeh Abadian,** and all the professors and students who helped us develop research skill, edit the electronic text and gave useful consultations and precious guidance. Special thanks to **Mr. Alireza Gerami** for his help with schematic illustrations.

Moreover, we owe to all the authors of the articles listed in the bibliography of this book.

We would like to appreciate the publisher and the chief editor of the publication for their excellent revision of the English language, and editing the electronic text.

Most importantly, our deepest and heartfelt gratitude to our wives **Fatemeh** and **Maryam**. This book could not have been completed without the devotion, encouragement, patience, and support provided by our family.

CHAPTER 1

Differential equations in miniature structures

1.1. Introduction to miniature structures

Today, the application of miniature structures has increased dramatically in various industries because of the increasing need for precise instruments and extensive efforts to reduce the volume and weight of equipment. The diminutive size, low power consumption, high precision, and reliability of these systems make them attractive. Miniature structures might refer to microstructure or nanostructures. The *United States National Nanotechnology Initiative* defines nanotechnology as "the understanding and control of matter at the nanoscale, at dimensions between approximately 1 and 100 nanometers" [1]. Referring to this definition, a nanostructure can be defined as a structure that has at least one dimension in the range of 1 to 100 nm. Because a nanostructure must build from atoms and molecules, the lower limit is fixed by the size of the molecules and atoms. For instance, the diameter of an H_2 molecule is about 0.25 nm, and the fullerene (C_{60}) ball outer diameter is about 1 nm. The upper limit is roughly contractual. However, 100 nm is approximately the size at which nanoscale phenomena cannot be observed or are negligible. Similarly, a microstructure can be described as a structure with at least one dimension sized from 1 to 100 micrometers [2].

Microelectromechanical and nanoelectromechanical systems (MEMS/NEMS) are well-known ultrasmall structures with broad applications in science and technology. Referring to the appellation of NEMS/MEMS might be a simple way to recognize their meanings: the first part of MEMS signifies "micro," and the first part of NEMS signifies "nano." These terms specify their scales. Hence MEMS and NEMS are devices on the "micro" and "nano" scale, respectively. The subsequent parts are similar. The "electro" component specifies that NEMS and MEMS use electronics or electric power. "Mechanical" refers to mechanical action or motion. The "system" indicates that these devices are a set of integrated components, not individual parts.

NEMS and MEMS have distinguished properties and unique characteristics, such as easy fabrication, high efficiency, low power consumption, and quick response. These devices can be utilized as sensors and actuators. There are different actuation techniques, such as the piezoelectric, thermal, piezoresistive, optical, electromagnetic, and electrostatic methods. While the actuation method is dependent upon the application of the device, electrostatics is the most popular actuating and sensing method [3].

NEMS/MEMS and microstructures/nanostructures have been used widely in different branches of science and technology as sensors and actuators. The application of

Nonlinear Differential Equations in Micro/nano Mechanics
https://doi.org/10.1016/B978-0-12-819235-1.00005-9
Copyright © 2020 Elsevier Ltd.
All rights reserved.

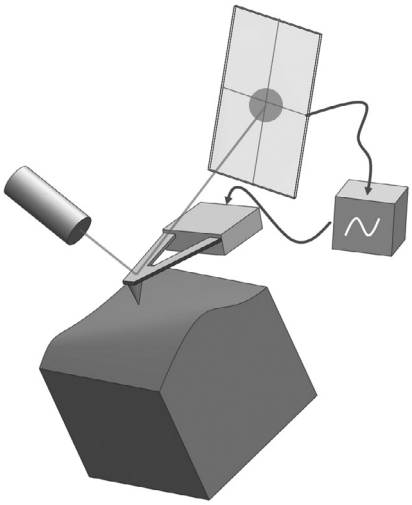

Figure 1.1 Atomic force microscopy sensor [12]: (A) schematic view, (B) SEM image.

these systems includes, but is not limited to, atomic force microscopy (AFM) [4], micro- and nanoswitches [5], micro- and nanoresonators [6], pressure sensors [7], accelerometers [8], micro- and nanotweezers [9], neuronal recordings device [10], and micro- and nano-optical switches [11]. Fig. 1.1 shows the scanning electron microscope (SEM) image and schematic view of an atomic force microscope (AFM) sensor. As can be seen, the AFM sensor can be modeled as a cantilever micro/nanobeam. The SEM image of a radio frequency (RF) microswitch and a microresonator are presented in Figs. 1.2 and 1.3, respectively. A clamped–clamped micro/nanobeam hung over a fixed substrate with a dielectric in-between can model these structures. Fig. 1.4 demonstrates the SEM image of an accelerometer microsensor. These sensors can be simulated as a cantilever beam with a concentrated mass on the tip. The SEM image of microtweezers is illustrated in Fig. 1.5. This structure can be modeled as a two parallel cantilever micro/nanobeams with a rectangular, or circular cross-section depends on the manufacturing method.

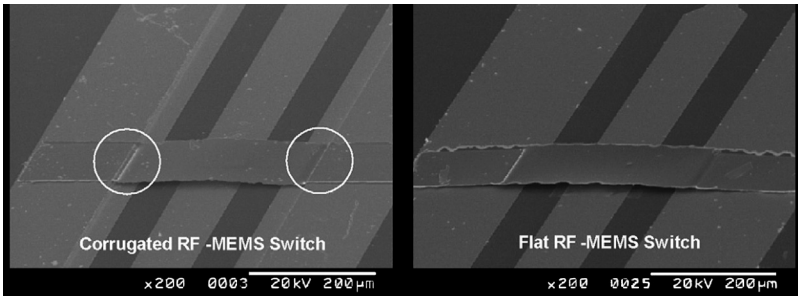

Figure 1.2 SEM image of an RF microswitch [13].

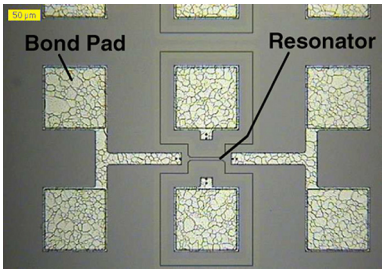

Figure 1.3 A microresonator [6].

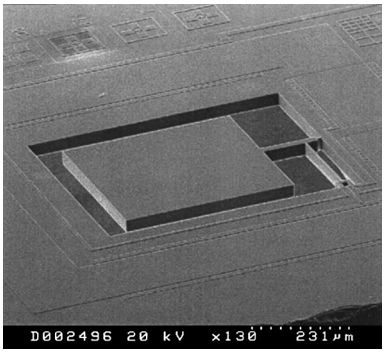

Figure 1.4 An MEMS accelerometer sensor [14].

A typical optical switch is illustrated in Fig. 1.6. This type of NEMS/MEMS can be simulated as a plate supported by torsional arms. A carbon nanotube probe used in the tip of an atomic force microscopy is shown in Fig. 1.7.

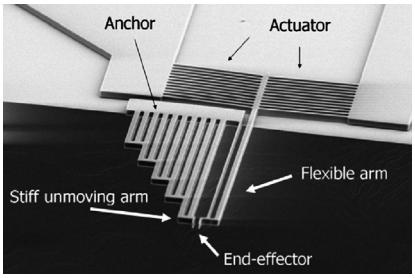

Figure 1.5 SEM image of nanotweezers [15].

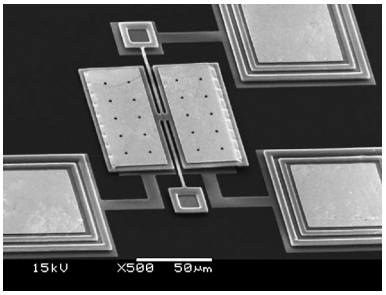

Figure 1.6 SEM image of an optical microswitch [16].

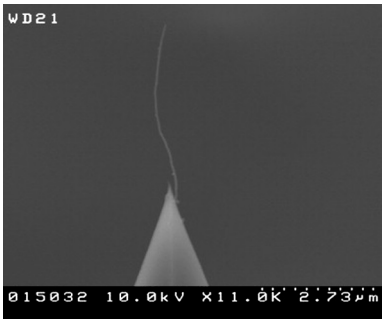

Figure 1.7 SEM image of a carbon nanotube probe [17].

1.2. Physics of small-scale structures

When dimensions of a system are reduced to submicron scale, some physical aspects appear, which may not exist at the macroscale. In this section, the essential physical phenomena of NEMS and MEMS are discussed. The impact of the proposed phenomena on the performances of micro- and nanostructures are discussed through several examples in the subsequent sections.

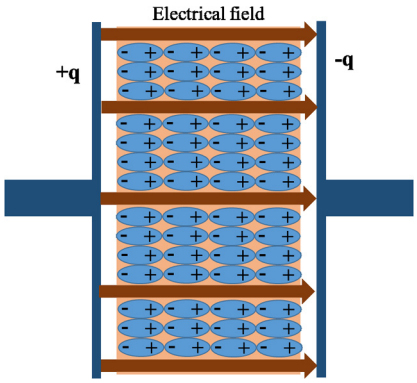

Figure 1.8 The ideal electric field between parallel plates' capacitors.

1.2.1 Electrostatic actuation

As mentioned previously, electrostatic actuation is the most popular actuation method in MEMS and NEMS. Because a widespread group of NEMS and MEMS can be considered as parallel beams or plates, the electrical field between two parallel plates is introduced. When a voltage difference is applied between two parallel plates, the plates construct a capacitor. The electrical force acting on the parts can be achieved by differentiating the stored potential energy of the capacitor. For two infinite parallel plates, the electrical field is uniform, as shown in Fig. 1.8. For this ideal case, the capacitance of two parallel plates is directly proportional to the plates' area and inversely proportional to the separation or distance between the plates. Hence, the capacitance can be formulated as [18]

$$C(g) = \frac{\varepsilon A}{g} \tag{1.1}$$

where ε is the permittivity of vacuum. The electrical energy per unit length is determined as

$$E_{elec} = \frac{1}{2} C(g) V^2 = \frac{\varepsilon A V^2}{2g}. \tag{1.2}$$

Therefore, the electrical force between two infinite parallel plates is achieved as

$$f_{elec} = -\frac{\partial E_{elec}}{\partial g} = \frac{\varepsilon A V^2}{2g^2}. \tag{1.3}$$

The electrical force explained in Eq. (1.3) is for two infinite parallel plates. In this equation, the electrical field is assumed to be ideally uniform, and the effect of the plate's

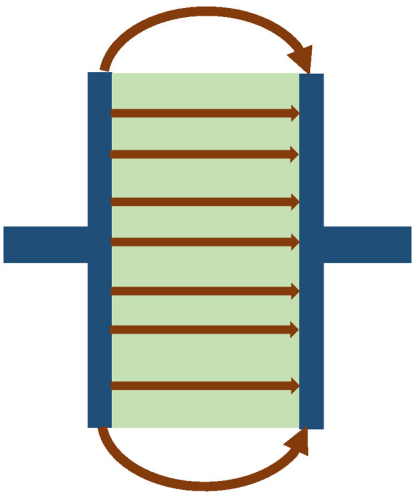

Figure 1.9 Fringing field effect in parallel plates' capacitors.

thickness is neglected. However, for a finite plate, the impact of the nonuniform electrical field in the edges (i.e., flinging field) might affect the capacitance (see Fig. 1.9). To incorporate the fringing field in the simulation of the electrical force, several modified models have been developed. For a finite plate (beam) with thickness h, width b, and length L, parallel to an infinite plate at distance g, the models for capacitance by considering fringing field effect are summarized in Table 1.1.

1.2.2 Pull-in instability

NEMS and MEMS are widely applied as sensors and actuators. While detection methods require for NEMS/MEMS sensors, the actuation techniques are essential in the application of NEMS/MEMS as actuators. A sensing or detection method is a transform in a physical quantity such as force, pressure, acceleration, or temperature into a measurable electrical signal. Conversely, an actuation method is the transformation of electrical potential to the mechanical movement, which can be used for motion, applying force, and switching. There are different sensing and actuation techniques in NEMS and MEMS, including electro-thermal [26,27], electromagnetic [28,29], electrostatic [30,31], piezoelectric [32,33], and piezoresistive [34,35] methods. While the actuation method strongly depends on the practical application of the devices, the electrostatic actuation scheme is the most commonly used in MEMS and NEMS because of its numerous inherent benefits [3]. However, this mechanism results in highly nonlinear instability behavior called "pull-in instability." The electric voltage acts on an NEMS/MEMS, leading to an electrostatic force followed by the deflection of the moveable components into a new equilibrium position. The electrical force has an upper

Table 1.1 Capacitance models by considering the fringing field effect.

Model	Capacitance per unit length
Palmer [19]	$C = \frac{\varepsilon b}{g}\left[1 + \frac{2g}{\pi b}\left(1 + \ln\left(\frac{\pi b}{g}\right)\right)\right]$
Chang [20]	$C = \frac{2\varepsilon}{\pi}\ln\left(\frac{2R_b}{R_a}\right)$ $\ln(R_a) = -1 - \frac{\pi b}{2g} - \frac{p+1}{\sqrt{p}}\tanh^{-1}(1/\sqrt{p}) - \ln\frac{p-1}{4p}$ $R_b = \eta + \frac{p+1}{2}\ln\Delta$ $\eta = \sqrt{p}\left\{\frac{\pi b}{2g} + \frac{p+1}{2\sqrt{p}}\left(1 + \ln\frac{4}{p-1}\right) - 2\tanh^{-1}\frac{1}{\sqrt{p}}\right\}$ $\Delta = \max(\eta, p)$ $p = 2B^2 - 1 + \sqrt{(2B^2-1)^2 - 1}$ $B = 1 + h/g$
Yuan and Trick [21]	$C = \frac{\varepsilon(b-h/2)}{g} + \frac{2\pi\varepsilon}{\ln\left[1+\frac{2g}{h}+\sqrt{\frac{2g}{h}\left(\frac{2g}{h}+2\right)}\right]}$
Sakurai and Tamaru [22]	$C = \varepsilon\left[1.15\left(\frac{b}{g}\right) + 2.80\left(\frac{h}{g}\right)^{0.22}\right]$
Van der Meijs and Fokkema [23]	$C = \varepsilon\left[\left(\frac{b}{g}\right) + 0.77 + 1.06\left(\frac{b}{g}\right)^{0.25} + 1.06\left(\frac{h}{g}\right)^{0.5}\right]$
Elliott [24]	$C = \frac{\varepsilon b}{g}\left[1 + \frac{g}{\pi b}\ln\left(\frac{\pi b}{g}\right)\right]$
Batra et al. [25]	$C = \varepsilon\left(\frac{b}{g} + c_0 + c_1\left(\frac{b}{g}\right)^{c_2} + c_3\left(\frac{h}{g}\right)^{c_4} + c_5\left(\frac{h}{b}\right)^{c_6} + c_7\left(\frac{h^2}{bg}\right)^{c_8}\right)$ $c_0 = -5.40$ $c_1 = 4.60$ $c_2 = 0.325$ $c_3 = 0.126$ $c_4 = -0.554$ $c_5 = -0.00388$ $c_6 = 0.891$ $c_7 = 3.47$ $c_8 = 0.118$
Batra et al. [25]	$C = \varepsilon\left(\frac{b}{g} + c_0 + c_1\left(\frac{b}{g}\right)^{c_2} + c_3\left(\frac{h}{g}\right)^{c_4}\right)$ $c_0 = -0.36$ $c_1 = 0.85$ $c_2 = 0.2$ $c_3 = 2.5$ $c_4 = 0.24$

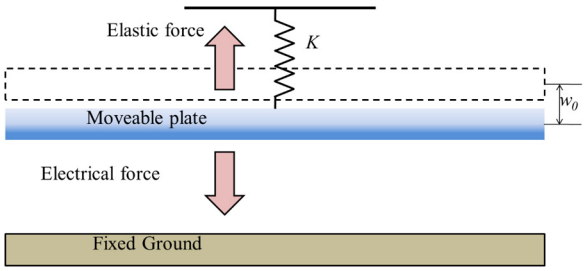

Figure 1.10 A parallel plate capacitor (the upper plate hung by a spring).

limit. If the electrical force passes this limit, it overcomes the mechanical resistance, thereby increasing the moveable component deflection. Accordingly, the electrostatic force is enhanced in a positive loop. This phenomenon is known as "pull-in," and its pertinent voltage is known as the "pull-in voltage" [36]. Sometimes the pull-in phenomenon is the essential aspect for the proper performance of NEMS. For example, the pull-in instability organizes the basis of the RF switch operation [37,38]. Conversely, the key point in the designing of micro nanoresonators and micromirrors are avoiding the pull-in phenomena [39,40].

To explain this phenomenon more clearly, consider a parallel plate microcapacitor. This structure can be considered as a movable plate hung over a fixed ground by a spring, as demonstrated in Fig. 1.10. It should be noted that this simple model, known as the "lumped parameter model," is sometimes used to model the behavior of beam-type MEMS and NEMS [41]. The lumped parameter model is discussed in detail in Section 1.3.1. The plate's area is assumed to be 0.16 mm^2, the initial gap between the plates is 4 μm, and the spring constant is 0.816 N/m. By applying the voltage difference between two plates, the moveable plate moves toward the fixed one until the electrical force is equal to the spring force. The electrical and spring forces for different values of external voltage are plotted in Fig. 1.11. The interaction point between the electrical and spring forces is the equilibrium point. When the applied voltage is lower than the pull-in value, there are two equilibrium points (Fig. 1.11A–B); by increasing the applied voltage, the spring force is tangent to the electrical force at the pull-in voltage (Fig. 1.11C). If the applied voltage rises more, there is no intersection between the electrical and spring forces. In other words, the electrical force is always higher than the spring force. Therefore, the spring force cannot overcome the electrical force, and the upper plate falls to the fixed ground, i.e., instability occurs.

It is worth noting that when the DC voltage leads to pull-in, the instability is called "static pull-in" or just "pull-in." However, in the case of AC loading or transient DC voltage, the instability is known as "dynamic pull-in" [42].

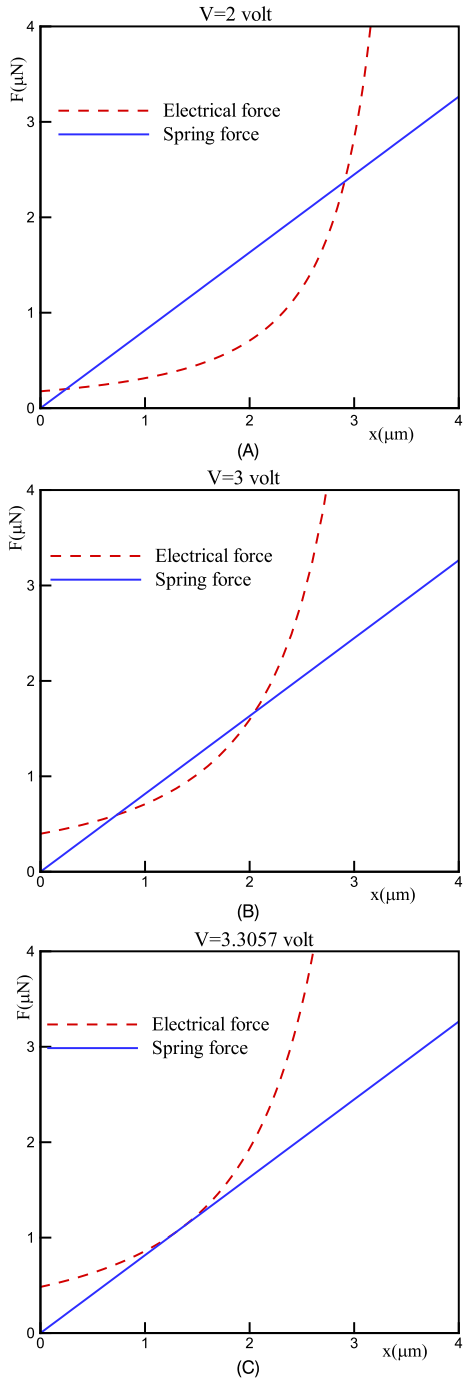

Figure 1.11 Electrical and spring forces for different applied voltages: (A) $V = 2$ volts; (B) $V = 3$ volts; (C) $V = 3.3057$ volts (pull-in); and (D) $V = 3.4$ volts.

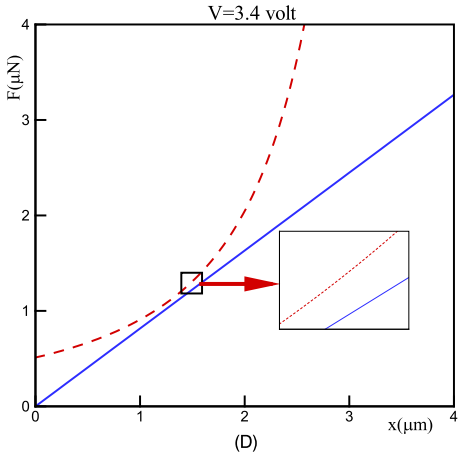

Figure 1.11 continued

1.2.3 Dispersion forces

The dispersion forces are the forces that act like gravity between all atoms and molecules, even between two uncharged bodies in a vacuum. Lifshitz developed the cohesive theory of the van der Waals and Casimir forces as subdivisions of dispersion forces [43]. Based on this theory, the dispersion interaction between two parallel plates is related to the frequency-dependent dielectric permittivities and magnetic permeabilities of plates' materials. When the distance between the bodies is smaller than the retardation length, the van der Waals force should be considered. The van der Waals attraction between two infinite parallel plates is proportional to the inverse-cube of the distance between the plates [44]. The van der Waals attraction per unit area between two ideal parallel flat plates is defined as [45]

$$f_{vdw} = \frac{\bar{A}}{6\pi g^3} \tag{1.4}$$

where g is the distance between the plates and $\bar{A}$ is the Hamaker's constant.

An appropriate method for calculating the van der Waals force between two arbitrary bodies is to employ the Lennard-Jones potential, which expresses the potential between two atoms as

$$\phi_{ij} = \frac{C_{12}}{r_{ij}^{12}} - \frac{C_6}{r_{ij}^6} \tag{1.5}$$

where C_{12} is the repulsive constant, C_6 is the attractive constant, and r_{ij} is the distance of the atoms. For distances greater than 3.4 Å, the repulsive term is negligible in comparison with the attractive term. A reliable continuum model has been established to compute the van der Waals energy using the double-volume integral of the Lennard-

Jones potential, which is [46]

$$E_{vdW} = \int_{\upsilon_1} \int_{\upsilon_2} (-\frac{C_6 \rho_1 \rho_2}{r^6(\upsilon_1, \upsilon_2)}) d\upsilon_1 d\upsilon_2 \tag{1.6}$$

where υ_1 and υ_2 represent the two domains of integration, and ρ_1 and ρ_2 are the densities of atoms in these domains. The distance between any two points on υ_1 and υ_2 is $r(\upsilon_1, \upsilon_2)$.

Another subdivision of dispersion force is the Casimir force. This force acts at larger separations than the van der Waals force. Indeed, when the separation between the two bodies is greater than the retardation length, the Casimir force is dominant. The Casimir attraction per unit area between two parallel conducting plates is not affected by the material's properties and is proportional to the inverse fourth power of distance. For two infinite conducting parallels separated by a distance, g the Casimir force is defined as [47]

$$f_{Cas} = \frac{\pi^2 \hbar c}{240 g^4} \tag{1.7}$$

where $c = 2.9979 \times 10^8$ m/s is the light speed and $\hbar = 1.0546 \times 10^{-34}$ J.s is the reduced Planck's constant.

1.2.4 Size dependency

Experimental observation demonstrated that the stiffness of metal-based ultra-small structures is scale-dependent. For example, empirical observation of the bending of nickel microbeams carried out by Stolken, and Evans [48] confirmed that when the beam thickness decreases, the microbeam plastic work hardening is enhanced considerably. Fleck et al. [49] investigated the torsional hardening of copper wires. They detected the hardening of a 12-μm diameter wire to be about three times greater than the hardening of a similar 170-μm diameter wire. This phenomenon has also been discovered in some polymers. Chong and Lam [50] demonstrated that a decrease in the thickness of epoxy beams results in the enhancement of their normalized bending stiffness. They determined that the bending rigidity of an epoxy beam with a 20-μm thickness is about 2.4 times greater than the bending stiffness of a similar beam with a 115-μm thickness. McFarland and Colton [51] evaluated the stiffness of polypropylene microcantilevers and determined it to be at least four times greater than the values expected with the classical elasticity theory. This size-dependent behavior of materials and structures cannot be simulated through classical continuum elasticity. To bridge the gap between the theoretical simulation and the experimental results, various size-dependent continuum theories were proposed.

In 1962, Mindlin developed the couple stress elasticity theory for simulating the scale-dependent behavior of miniature structures [52]. For this purpose, a higher-order

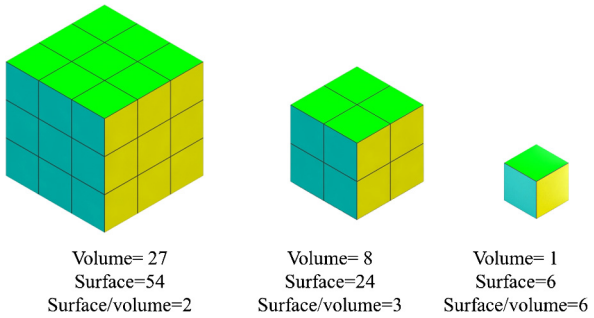

Figure 1.12 Simple illustration of increasing the surface to volume ratio by reducing the size.

stress tensor (i.e., couple stress tensor) was introduced in addition to the classical stress tensor. The couple stress tensor components were expressed in terms of the gradient of elements rotation and new material constants, which were pertinent to the conventional material constants by the material length scale. Yang et al. [53] modified the Mindlin couple stress theory. They developed the couple moments equilibrium rather than classical forces and moments equilibrium. This additional equilibrium condition dictated that the couple stress tensor must be symmetric. Thereby, two material length-scale parameters of a general couple stress tensor were reduced to one material parameter in the modified couple stress tensor.

The most comprehensive strain gradient model was expressed by Mindlin [54]. This theory includes five added material parameters, and the other strain gradient theories can extract from the Mindlin general strain gradient theory Lam et al. [55] expressed a modified strain gradient. They decomposed the second-order deformation gradient tensor into the stretch gradient tensor and the rotation gradient tensor. This decomposition reduced the material length-scale parameter from five in the general strain gradient theory to three in the modified strain gradient theory.

Eringen develops the nonlocal theory in the 1970s [56]. In the classical or local continuum mechanics, the stress at each point depends on the strains at that point. In contrast, in the nonlocal continuum mechanic, the stress at a reference point in the domain depends not only on the strains at that point but also on the strain field at every point in the body. In this regard, scale-dependent parameters (internal characteristic length) appear in the constitutive equations which can simulate the size dependency of the miniature structures.

1.2.5 Surface effects

Reducing the structure size enhances its surface area-to-volume ratio. A simple demonstration of the enhancement of the surface to volume ration is illustrated in Fig. 1.12. As seen by reducing the volume from 9 to one unit, the surface to volume ratio increases from 2 to 6. To clarify this fact, the surface-to-volume ratio as a function of the basic di-

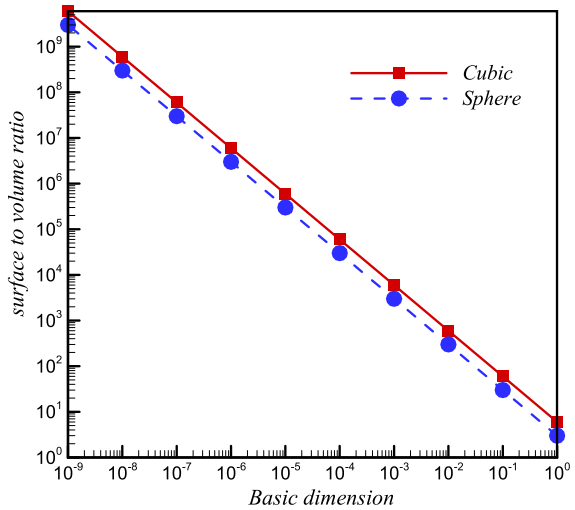

Figure 1.13 Surface-to-volume ratio as a function of basic dimension.

mension is illustrated in Fig. 1.13. This figure demonstrates that the surface-to-volume ratio of a 1 nm width cube is 10^9 times greater than the surface-to-volume ratio of a 1 m width cube. The same can be observed for a nanoscale sphere.

For mechanical elements with a high surface–volume ratio, the surface energies can significantly affect their mechanical properties. To simulate the surface energies, the molecular dynamic method can be employed. However, this method is highly time-consuming and requires high-performance computers. To overcome the inefficiency of the molecular dynamics procedure for structures, the surface elasticity theory developed by Gurtin and Murdoch [57] can be employed [58]. It is capable of simulating both the residual surface stress and the surface elasticity.

1.2.6 Damping in NEMS/MEMS

The resources for energy dissipation in NEMS/MEMS can be classified into intrinsic and environmental effects. The intrinsic energy loss resources include thermoplastic damping and surface phonon scattering. Also, the most common environmental resources of energy loss in NEMS and MEMS are anchors, acoustic, and viscous damping [36]. In the ultrasmall structures, the intrinsic energy loss is negligible in comparison with the external resources. Nevertheless, the intrinsic effect should be considered when achieving a high-quality factor is desired. To determine the effect of all energy dissipation resources, each source can be defined in terms of a corresponding quality factor (Q_i). The total quality factor is given by

$$\frac{1}{Q} = \sum \frac{1}{Q_i}. \tag{1.8}$$

Table 1.2 Parameter α in Eq. (1.10) [36].

Boundary condition	Vibrating mode				
	1	2	3	4	5
Cantilever beam	2.081	0.173	0.064	0.033	0.02
Clamped beam	0.683	0.223	0.114	0.069	0.046

The quality factor has an inverse relationship with the damping ratio (ξ) and the energy loss of the system. Therefore, a higher quality factor indicates a lower rate of energy loss relative to the stored energy. In contrast, a lower quality factor indicates a higher rate of energy loss relative to the stored energy:

$$Q = \frac{1}{2\xi}. \tag{1.9}$$

Energy loss in the supports in known as anchor loss. This loss is due to uncanceled shear forces and moments in the end supports. Among these, the shear forces have a more dominant effect on energy loss. Therefore, by neglecting the impact of the uncanceled moment, the quality factor for cantilever and clamped beams is given by [59]

$$Q = \alpha \left(\frac{L}{h}\right)^3 \tag{1.10}$$

where L is the beam length, h is the beam thickness, and α is a parameter that depends on the boundary conditions, mode of vibration, and Poisson's ratio. The parameter α for cantilever and clamped boundary condition by considering the Poisson's ratio equal to 0.28 is demonstrated in Table 1.2.

1.2.6.1 Drag force

Drag force acting is the resistance force opposite to the relative motion of a body moved through the fluid. In micro- and nanostructures, the drag force might result in energy loss. Therefore, the drag force can be considered as a damping resource. Some researchers investigated the drag force of complex systems by dividing them into simple shapes. For example, the beam has been simulated as a series of spheres, and the sphere drag force is used to find the drag force over a beam [60,61]. By neglecting the effect of adding mass, the drag force over a sphere with radius R and velocity u is given by

$$F = -\beta_1 u. \tag{1.11}$$

In the above equation, the damping coefficient of a sphere for the frequency ω is defined as

$$\beta_1 = 3\pi\mu R + \frac{3}{4}\pi R^2 (2\rho_a \mu\omega)^{1/2} \tag{1.12}$$

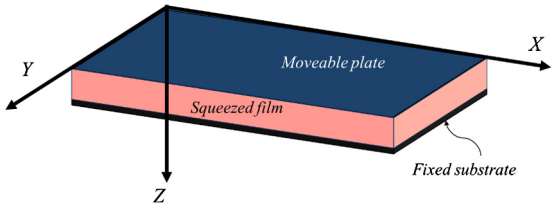

Figure 1.14 Squeezed film between two plates.

where μ is the fluid viscosity and ρ is the fluid density. Also, a beam can be simulated as a string of dishes with the diameter of the dishes equal to the width of the beam. By using this approach, Bao [62] determined the damping coefficient of a beam equal to 8μ.

1.2.6.2 Squeezed film damping

The dynamic of small parts in an ultrasmall system can be affected by the movement of the fluid trapped underneath the plate, which is known as squeezed film damping (see Fig. 1.14). For NEMS/MEMS with a moveable plate, squeeze film damping can affect the system frequency response. Squeeze film damping is the most common and dominant energy loss mechanism in NEMS/MEMS. In general, the dynamic of the squeeze film is governed by both viscous and inertial effects on fluid. However, for ultrasmall structures, the inertial effect can be negligible. In such a case, assuming ideal gas law and isothermal conditions, the behavior of a Newtonian fluid can be expressed by the Reynolds equation as

$$\frac{\partial}{\partial X}(g^3 P\frac{\partial P}{\partial X}) + \frac{\partial}{\partial Y}(g^3 P\frac{\partial P}{\partial Y}) = 12\mu\left[g\frac{\partial P}{\partial t} + P\frac{\partial g}{\partial t}\right] \tag{1.13}$$

where P is the pressure, m is the viscosity, t is the time, and g indicates the separation between the moveable and fixed plate. It should be noted that the variation of pressure across the film thickness (i.e., Z direction) is ignored in deriving the Reynolds equation.

NEMS/MEMS might operate in low-pressure conditions. In this situation, the fluid cannot consider as a continuum. Therefore, Eq. (1.13) might not predict the behavior of squeezed film correctly. However, by modifying the viscosity, more accurate results can be achieved from Eq. (1.13). Various models have been proposed for "effective viscosity," which depends directly on the Knudsen number. Some models for effective viscosity are presented in Table 1.3.

For incompressible gas, the derivative of pressure with respect to time is zero. Also, for beam type NEMS/MEMS, the length of the beam is considerably more significant than the beam widths. Therefore, the pressure in the longitudinal direction (x)

Table 1.3 Effective viscosity models (μ_{eff}).

Author	Effective viscosity
Burgdorfer [63]	$\mu_{eff} = \frac{\mu}{1+6K_n}$
Hsia and Domoto [64]	$\mu_{eff} = \frac{\mu}{1+6K_n+6K_n^2}$
Fukui and Kaneko [65]	$\mu_{eff} = \frac{\mu\sqrt{\pi}}{12K_nQ(d)}$
	Q is a coefficient related to the Poiseuille flow
Seidel et al. [66]	$\mu_{eff} = \frac{0.7\mu}{0.7+K_n}$
Mitsuya [67]	$\mu_{eff} = \frac{\mu}{1+6\frac{2-\alpha}{\alpha}K_n+\frac{3}{8}K_n^2}$
	α is the accommodation coefficient ($\alpha \approx 1$)
Andrews and Harris [68]	$\mu_{eff} = \frac{\mu}{1+6.8636K_n^{0.9906}}$
Veijola et al. [69]	$\mu_{eff} = \frac{\mu}{1+9.638K_n^{1.159}}$

approximately is constant. Hence, the Reynolds equation can be rewritten as

$$\frac{\partial^2 P}{\partial Y} = \frac{12\mu_{eff}}{g^3}\frac{\partial(gP)}{\partial t}. \tag{1.14}$$

At the edges of the beam, the pressure is equal to environmental pressure which results in the following boundary condition:

$$P(X, -b/2, t) = P(X, b/2, t) = 0. \tag{1.15}$$

By solving the differential equation (1.14) with the boundary condition of Eq. (1.15), the pressure due to squeezed film for parallel plates can be achieved as

$$P(Y, t) = -\frac{6\kappa_{eff}}{g^3}\left[(\frac{b}{2})^2 - Y^2\right]\frac{\partial g}{\partial t}. \tag{1.16}$$

Finally, the damping force due to squeezed film on a plate with length L and width b can be summarized as

$$F_{sd} = \int_{-b/2}^{b/2} P(Y, t)LdY = -\frac{\kappa_{eff}b^3L}{g^3}\frac{\partial g}{\partial t}. \tag{1.17}$$

1.2.6.3 Slide film damping

NEMS/MEMS commonly rely on the out-of-plane motion. However, some devices might rely on the in-plane motion. For the in-plane motion, the sliding of the fluid is the source of energy loss instead of drag force and the squeezed film damping. The

Couette and Stokes models can be used for the sliding motion of fluids. The main difference between them is the assumption for the fluid velocity. In the Couette model, the velocity of the fluid underneath the structure is assumed to linearly alter from zero on the substrate to the structure velocity on the lower plane of the structure.

In contrast, the Stokes model assumes a variable velocity on both sides of the structure. The results of both models are approximately similar for energy loss due to the fluid underneath the structure. However, they deviate when the impact of the fluid above the structure is dominant. Cho et al. observation demonstrated that the results of the Stokes model are closer to the experimental measurements [70].

The Stokes model damping coefficient due to the fluid underneath the structure is given by [70]:

$$\begin{aligned} c_{d,Stokes} &= \frac{\mu A}{d}\psi, \\ \psi &= \beta d \frac{\sin(2\beta d) + \sinh(2\beta d)}{\cosh(2\beta d) - \cos(2\beta d)} \end{aligned} \tag{1.18}$$

where A is the surface area of the structure and β is defined as:

$$\begin{aligned} \beta &= \frac{1}{\delta}, \\ \delta &= \sqrt{\frac{2\mu}{\rho\omega}} \end{aligned} \tag{1.19}$$

where ω is the oscillation frequency of the structures. When δ is immensely more significant than the separation distance between the structure and substrate, the damping coefficient of the Stokes model converges to that of the Couette model:

$$c_d = \frac{\mu A}{d}. \tag{1.20}$$

The Stokes model simulates the damping coefficient due to the fluid above the structure as [70]

$$c_{d,above} = \mu A \beta. \tag{1.21}$$

1.3. Modeling of small-scale structures

Accurate models for a nanostructure are crucial due to the unavoidable cost and complexity of experimental setups and fabrication proses. Reliable simulation of NEMS/MEMS requires a comprehensive understanding of the mechanical behavior of devices as well as the interaction between the device and external forces and fields. When the dimensions of a structure are reduced from microscale to nanoscale, new physics emerges. Precise simulation of NEMS needs a comprehensive knowledge of

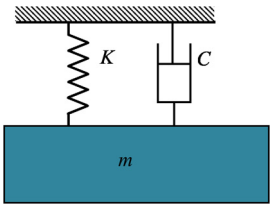

Figure 1.15 Lumped parameter model.

nanoscale phenomena as well as efficient manners for including these phenomena in the final model.

At least three approaches have been used by previous researchers to investigate the mechanical performances of micro and nanostructures, including molecular dynamics [71–75], lumped parameter model [41,76,77], and continuum approach [78–90]. Simply put, the molecular dynamics consider the body as discrete particles and simulate the interactions between them, the lumped parameter model considers a complex system as lumped elements, and in the continuum mechanics, the system modeled as a continuous mass.

The mechanical performance of nanostructures can be modeled using molecular dynamics. However, molecular mechanics involves prohibitively expensive computational resources and is not applicable to structures with a large number of atoms. To overcome the shortage of molecular dynamics for large structures, the lumped parameter model or continuum mechanics can apply to the micro- and nanostructures.

1.3.1 Lumped parameter model

A simple way to avoid the complexity of investigating the behavior of NEMS/MEMS is simulating the compliant systems as lumped elements instead of continuous structures. This simple idea has been used by many researchers to investigate the static and dynamic behavior of NEMS and MEMS [41,76,77,80,91–95]. The lumped parameter model may not provide accurate values. Nevertheless, this simple model is beneficial for first-cut designs, as well as understanding the physical aspects of the phenomena. Also, the lumped parameter model is an appropriate technique for simulating the complicated nanostructures with the coupling degree of freedom in which the modeling by considering continuous systems is very complicated.

Fig. 1.15 shows a lumped parameter model. As seen, the model includes a rigid part with three elements: a mass of m, a spring with the stiffness of K, and a damper with a damping ratio of C. Among these elements, the rigid part and spring are essential. However, in some particular cases, damping might be neglected. To establish a lumped parameter model for micro- and nanostructures, the element of the lumped parameter model should be recognized.

The spring constant in the micro- and nanostructures lumped parameter modeling is related to the stiffness of the structure. Although the micro- and nanostructures might behave nonlinearly, the linear behavior can be assumed for simplicity. It is clear that the stiffness of micro- and nanostructures depends on material properties and geometry. However, interestingly the stiffness is also dependent on external loads and boundary conditions. For example, the stiffness of the cantilever beam is different from the stiffness of a clamped beam with similar geometry and material properties. Also, the external load distribution can affect the stiffness of micro- and nanostructures. For example, the stiffness of a cantilever beam with a distributed load is different from the stiffness of the cantilever beam with the concentrated load, even though both beams have similar material properties and geometry.

The stiffness of micro- and nanostructures can be evaluated experimentally, analytically, or numerically [36]. Experimental measurements of the micro- and nanostructures stiffness are generally based on the static deflection. For example, by using atomic force microscopy, the stiffness of cantilever microactuators can be investigated. For this purpose, a force is applied at the free end of the microactuator. By measuring the tip deflection of the actuator, the stiffness can be achieved from the slope of the force–deflection curve in the linear regime. Also, the experimental results can be used for investigating the required parameters for investigating stiffness in the analytical and numerical approaches. For instance, Young's modulus, which is a crucial parameter for the analytically investigated stiffness of micro- and nanostructures, can be determined from the strain–stress curve. In addition to experimental techniques based on static deformation, dynamic measurements can also be employed for investigating the stiffness. The dynamic measurement of stiffness is generally based on the excitation of the system by frequencies very close to the natural frequencies of the system. Since it is hard to excite NEMS/MEMS by high frequencies to reach the frequencies near their natural frequencies, the dynamic measurement might be less useful for NEMS/MEMS.

In addition to experimental measurement, numerical techniques such as the finite difference method and the finite element model can be employed to determine the stiffness of micro nanostructures. To this end, the structure is simulated based on the numerical technique (i.e., finite element or finite difference method). Then, the displacement of the desired point (for example, the tip of a cantilever beam) by applying a small distributed or point load is investigated. The stiffness can be achieved by plotting the displacement–force curve.

For a simple geometry, the analytical simulation can be used to investigate the micro- and nanostructure stiffness. This method is based on the analytical solution of the differential equation that governs the displacement of the structure subjected to specific distributed or point load. Since micro- and nanobeams are the essential building blocks of many NEMS and MEMS, the linear stiffness coefficients of beams in some typical configuration are summarized in Table 1.4. In this table, L is the length, A is the

Table 1.4 Linear stiffness coefficients of beams in some typical configurations.

Boundary conditions and loads	Stiffness
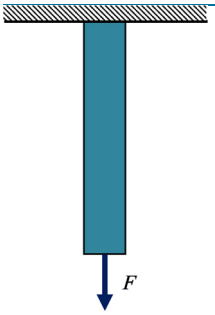	$k = \frac{EA}{L}$
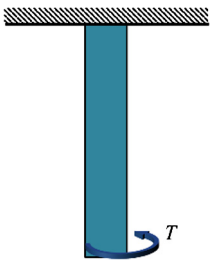	$k = \frac{GJ}{L}$
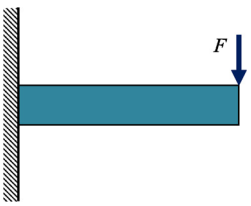	$k = \frac{3EI}{L^3}$
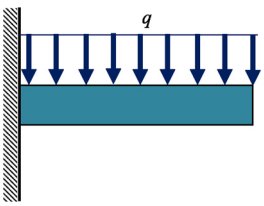	$k = \frac{8EI}{L^3}$
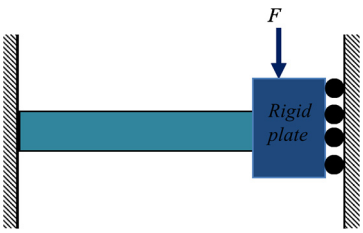	$k = \frac{12EI}{L^3}$

continued on next page

Table 1.4 (*continued*)

Boundary conditions and loads	Stiffness
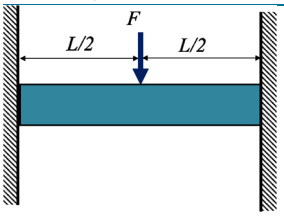	$k = \frac{192EI}{L^3}$
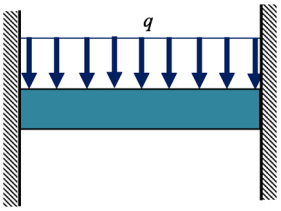	$k = \frac{384EI}{L^3} + \frac{8.32N}{L}$
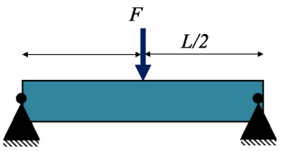	$k = \frac{48EI}{L^3}$
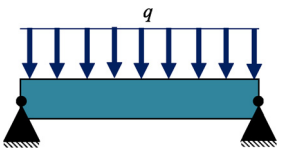	$k = \frac{384EI}{5L^3}$

cross-section area, I is the cross-section moment of inertia, J is the polar moment of inertia of the cross-section, E is the Young's modulus, G is the shear modulus, and N is the axial load. With structures constructed from more than one component, such as comb devices and accelerometers, the equivalent spring constant should be used in the lumped parameter model. If the springs have the same displacement, they act in parallel configuration. In this situation, the equivalent spring constant is given by

$$k_{eq} = k_1 + k_2 + ... \tag{1.22}$$

Instead, when the springs actuated by an equal load, the configuration is known as a series configuration. For springs in series, the equivalent spring constant is given by

$$\frac{1}{k_{eq}} = \frac{1}{k_1} + \frac{1}{k_2} + ... \tag{1.23}$$

Another essential parameter in the lumped parameter model is the mass. It should be noted that the whole mass of the system might not contribute to the motion of the

Table 1.5 Effective mass of some typical beams [96].

Configuration	Effective mass
Cantilever beam with a mass at the tip	$m_{eff} = 0.236$ m
Clamped–clamped beam with a mass at the center	$m_{eff} = 0.375$ m
Simply-supported beam with a mass at the center	$m_{eff} = 0.486$ m
Bar in axial motion with a mass at the tip	$m_{eff} = 0.333$ m

system. For example, in a cantilever beam, the mass near to the fixed end approximately has no contribution in the motion. Hence, the effective mass should be used in the lumped parameter model. To extract the effective mass, the mass–spring model might be employed. The mass–spring motion is modeled by

$$m\ddot{x} + kx = f. \tag{1.24}$$

The natural frequency of the mass–spring system is given by

$$\omega_n = \sqrt{\frac{k}{m}}. \tag{1.25}$$

Therefore, the effective mass of a limped-parameter model can be defined as

$$m_{eff} = \frac{k}{\omega_n^2} \tag{1.26}$$

where ω_n is the natural frequency of the system. For instance, the natural frequency of a cantilever beam is [36]

$$\omega_n = 3.52\sqrt{\frac{EI}{L^3 m}} \tag{1.27}$$

where m is the beam total mass. By substituting Eq. (1.27) into Eq. (1.26) and using the stiffness constant from Table 1.4, the effective mass of a cantilever beam with the point force and distributed load are determined to be 0.242 m and 0.646 m. Similarly, for other configurations, the effective mass can be obtained. The effective mass of some typical configurations as a function of total mass is summarized in Table 1.5.

The last but not the least important parameter in the lumped parameter model is the damping coefficient. The damping effect can significantly change the performance of NEMS/MEMS. Also, the application of ultrasmall structures might specify the type and magnitude of damping. For instance, in accelerometers, a high damping ratio is required to attain the most extensive operation range. In contrast, micro- and nanoresonators should be manufactured with a low damping ratio to achieve high resolution and sensitivity.

Identifying all elements of the lumped parameter model, the equation of motion of the system can be extracted by using Newton's second law. For example, the equation of motion for simple mass–spring–damper illustrated in Fig. 1.15 can be explained as

$$m\ddot{x} + c\dot{x} + kx = F_e \tag{1.28}$$

where the overdots indicate derivatives with respect to the time, and F_e is the total external force.

1.3.2 Micro/nanoscale continuum mechanics

Nanoscale continuum models are applicable approaches for predicting the behavior of nanostructures. The continuum mechanics does not require computational equipment as the molecular dynamics method, and its results are more accurate than those of the lumped method. However, nanoscale continuum mechanics usually lead to a highly nonlinear differential equation that cannot be solved using conventional techniques. The basic idea of the nanoscale continuum models is similar to the classical continuum theory. However, as some physical phenomena appear at the nanoscale, the classical continuum theory must be modified to incorporate the nanoscale phenomena in the simulation.

The nanoscale continuum mechanics is founded based on the classical continuum mechanics. So, for readers who are not familiar with the classical continuum mechanics, reviewing the concepts of the classical theory might be helpful. In the classical continuum theory, the governing equations are derived based on the following well-known principles:

1. Conservation of mass
2. Conservation of linear momentum
3. Conservation of angular momentum
4. Conservation energy

However, by using just the above principles, the obtained governing equations are incapable of simulating the total response of the continuum. Therefore, the following equation must also be considered:

1. Strain–displacement relations (kinematics)
2. Stress–strain relations (constitutive equation)

1.3.2.1 Strain–displacement relations

The strain–displacement (or kinematic) relations describe how the strains related to the displacements in a body. Consider an arbitrary undeformed body shown in Fig. 1.16. The displacement of any point in the body is a function of its location (x_i). For a rigid body motion, the displacements of all points are equal. However, unequal displacement results in the deformation or stretching of the body (see Fig. 1.17).

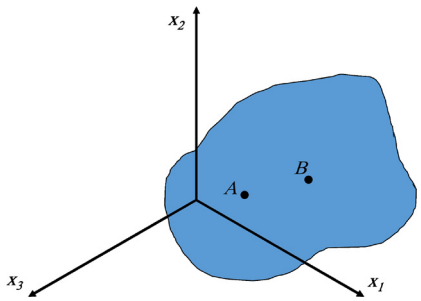

Figure 1.16 Undeformed body.

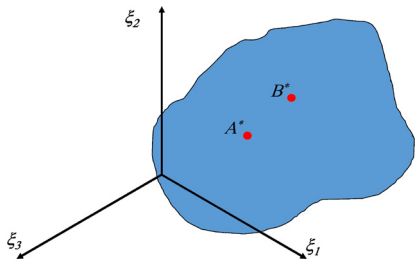

Figure 1.17 Deformed body.

Consider point A at position x_i and point B at position $x_i + dx_i$. The distance between these points is given by

$$\overline{AB}^2 = dx_1^2 + dx_2^2 + dx_3^2 = dx_i dx_i. \tag{1.29}$$

The position of points A and B in the deformed body are A^* and B^*, respectively. Point A^* is at position ξ_i and point B at position $\xi_i + d\xi_i$. The distance between A and B in the deformed body is given by

$$\overline{A^*B^*}^2 = d\xi_1^2 + d\xi_2^2 + d\xi_3^2 = d\xi_i d\xi_i = \frac{\partial \xi_i}{\partial x_k}\frac{\partial \xi_i}{\partial x_l} dx_k dx_l. \tag{1.30}$$

The change in the length of AB is required for determining the strain:

$$\overline{A^*B^*}^2 - \overline{AB}^2 = \frac{\partial \xi_i}{\partial x_k}\frac{\partial \xi_j}{\partial x_l} dx_k dx_l - dx_i dx_i = \left(\frac{\partial \xi_k}{\partial x_i}\frac{\partial \xi_k}{\partial x_j} - \delta_{ij}\right) dx_i dx_j. \tag{1.31}$$

By defining the Green's strain tensor, the above relation can be rewritten as the following form [97]:

$$\overline{A^*B^*}^2 - \overline{AB}^2 = 2\varepsilon_{ij} dx_i dx_j. \tag{1.32}$$

Replacing Eq. (1.32) in Eq. (1.33) results in

$$\varepsilon_{ij} = \frac{1}{2}\left(\frac{\partial \xi_k}{\partial x_i}\frac{\partial \xi_k}{\partial x_j} - \delta_{ij}\right). \tag{1.33}$$

The displacement field of the body is defined as

$$u_i = \xi_i - x_i. \tag{1.34}$$

Substituting Eq. (1.34) into Eq. (1.33) yields

$$\varepsilon_{ij} = \frac{1}{2}\left(\frac{\partial u_i}{\partial x_j} + \frac{\partial u_j}{\partial x_i} + \frac{\partial u_k}{\partial x_i}\frac{\partial u_k}{\partial x_j}\right). \tag{1.35}$$

In the case of a small deformation, the above relation reduces to the following equation:

$$\varepsilon_{ij} = \frac{1}{2}\left(\frac{\partial u_i}{\partial x_j} + \frac{\partial u_j}{\partial x_i}\right). \tag{1.36}$$

1.3.2.2 Constitutive equation

The linear elastic model is the most straightforward constitutive relation for the solid material. Herein, the linear elastic model for stress–strain relations is addressed. Referring to the appellation, the linear elastic model has two essential parts, which should be considered in the description of the model. The first part is "linear," which means that the strains in the material are small, and the stress and strains are linearly proportional to one another. The elastic part implies that the unloading path is the same as the loading path, which means the material returns to its original state by removing the applied load regardless of the load rating.

The stress–strain relation of a linear-elastic solid is known as Hooke's law and is given as [97]

$$\sigma_{ij} = C_{ijkl}\varepsilon_{kl} \tag{1.37}$$

where σ_{ij} indicate the components of the stress tensor, ε_{ij} are the components of the strain tensor, and C_{ijkl} is the fourth-order stiffness or Hooke's tensor. Eq. (1.37) can also be rewritten as

$$\boldsymbol{\sigma} = \mathbf{C} : \boldsymbol{\varepsilon}. \tag{1.38}$$

By using the symmetry of the stress tensor and after some mathematical elaborations, the Hooke's law for linear elastic isotropic materials is given as

$$\sigma_{ij} = \frac{E\nu}{(1+\nu)(1-2\nu)}\delta_{ij}\varepsilon_{kk} + 2G\varepsilon_{ij} \tag{1.39}$$

where δ is the Kronecker delta, E is the elastic modulus (Young's modulus), ν is the Poisson ratio, and G is the shear modulus. For linear elastic isotropic materials, the strain tensor components can be expressed in terms of the stress tensor by using the inverse Hooke's law

$$\varepsilon_{ij} = \frac{1+\nu}{E}\sigma_{ij} - \frac{\nu}{E}\sigma_{kk}\delta_{ij}. \tag{1.40}$$

1.4. Conclusion

In this chapter, the micro- and nanoelectromechanical systems were introduced. Then, the concepts of the physical phenomena which appear at the micro- and nanoscale were explained. Finally, the continuum mechanics as an advantageous method for simulating the micro- and nanostructure was explained.

In the rest of the book, NEMS and MEMS are modeled using nanoscale continuum, and the details of each model will be discussed accordingly. Various mathematical methods for solving the obtained nonlinear differential equations will be presented. Then, the proposed solution methods are employed to investigate the behavior of some micro- or nanostructure by some appropriate examples. The examples not only explain the implementation of the mathematical methods but also describe the nanostructure simulation procedure, incorporating the micro- and nanoscale phenomena techniques, and the impact of the physical phenomena on the behavior of the nanostructures. We try to use different examples to clarify the numerous nanoscale effects.

References

[1] Initiative, U.S.N.N. What is Nanotechnology? Available from: https://www.nano.gov/nanotech-101/what/definition.
[2] Microtechnology. Available from: https://www.encyclopedia.com/science/encyclopedias-almanacs-transcripts-and-maps/microtechnology-0. (Accessed 27 January 2019).
[3] R.C. Batra, M. Porfiri, D. Spinello, Review of modeling electrostatically actuated microelectromechanical systems, Smart Materials and Structures 16 (2007) R21–R31.
[4] A. Nafari, et al., MEMS sensor for in situ TEM atomic force microscopy, Journal of Microelectromechanical Systems 17 (2) (2008) 328–333.
[5] K.D. Leedy, et al., Thin-film encapsulated RF MEMS switches, Journal of Microelectromechanical Systems 16 (2) (2007) 304–309.
[6] R. Mestrom, et al., Modelling the dynamics of a MEMS resonator: simulations and experiments, Sensors and Actuators. A, Physical 142 (1) (2008) 306–315.
[7] D.J. Young, et al., High-temperature single-crystal 3C-SiC capacitive pressure sensor, IEEE Sensors Journal 4 (4) (2004) 464–470.
[8] A. Albarbar, et al., Performance evaluation of MEMS accelerometers, Measurement 42 (5) (2009) 790–795.
[9] P. Kim, C.M. Lieber, Nanotube nanotweezers, Science 286 (5447) (1999) 2148–2150.
[10] M.R. Angle, A.T. Schaefer, Neuronal recordings with solid-conductor intracellular nanoelectrodes (SCINEs), PLoS ONE 7 (8) (2012).

[11] B. Borovic, et al., Control of a MEMS optical switch, in: 2004 43rd IEEE Conference on Decision and Control (CDC) (IEEE Cat. No. 04CH37601), IEEE, 2004.
[12] S. Rao, K.D. Costa, 2-Atomic Force Microscopy (AFM) in biomedical research, in: P. Morris (Ed.), Biomedical Imaging, Woodhead Publishing, 2014, pp. 41–64.
[13] Y.-T. Song, H.-Y. Lee, M. Esashi, A corrugated bridge of low residual stress for RF-MEMS switch, Sensors and Actuators. A, Physical 135 (2) (2007) 818–826.
[14] M. Aikele, et al., Resonant accelerometer with self-test, Sensors and Actuators. A, Physical 92 (1) (2001) 161–167.
[15] K.N. Andersen, et al., Electrothermal microgrippers for pick-and-place operations, Microelectronic Engineering 85 (5) (2008) 1128–1130.
[16] J.M. Huang, et al., An approach to the coupling effect between torsion and bending for electrostatic torsional micromirrors, Sensors and Actuators. A, Physical 115 (1) (2004) 159–167.
[17] R.M. Stevens, New carbon nanotube AFM probe technology, Materials Today 12 (10) (2009) 42–45.
[18] W.H. Hayt, J.A. Buck, Engineering Electromagnetics, 6 ed., McGraw-Hill, New York, 2001.
[19] H.B. Palmer, The capacitance of a parallel-plate capacitor by the Schwartz–Christoffel transformation, Electrical Engineering 56 (3) (1937) 363–368.
[20] W. Chang, Analytical IC metal-line capacitance formulas (Short Papers), IEEE Transactions on Microwave Theory and Techniques 24 (9) (1976) 608–611.
[21] C. Yuan, T. Trick, A simple formula for the estimation of the capacitance of two-dimensional interconnects in VLSI circuits, IEEE Electron Device Letters 3 (12) (1982) 391–393.
[22] T. Sakurai, K. Tamaru, Simple formulas for two-and three-dimensional capacitances, I.E.E.E. Transactions on Electron Devices 30 (2) (1983) 183–185.
[23] N. Van Der Meijs, J. Fokkema, VLSI circuit reconstruction from mask topology, Integration 2 (2) (1984) 85–119.
[24] R.S. Elliott, Electromagnetics: History, Theory and Applications, IEEE Computer Society Press, 1993.
[25] R.C. Batra, M. Porfiri, D. Spinello, Electromechanical model of electrically actuated narrow microbeams, Journal of Microelectromechanical Systems 15 (5) (2006) 1175–1189.
[26] Z. Feng, et al., Design and modeling of RF MEMS tunable capacitors using electro-thermal actuators, in: 1999 IEEE MTT-S International Microwave Symposium Digest (Cat. No. 99CH36282), IEEE, 1999.
[27] J.J. Khazaai, H. Qu, Electro-thermal MEMS switch with latching mechanism: design and characterization, IEEE Sensors Journal 12 (9) (2012) 2830–2838.
[28] H. Miyajima, et al., A MEMS electromagnetic optical scanner for a commercial confocal laser scanning microscope, Journal of Microelectromechanical Systems 12 (3) (2003) 243–251.
[29] K.H. Kim, et al., Fabrication and test of a micro electromagnetic actuator, Sensors and Actuators. A, Physical 117 (1) (2005) 8–16.
[30] C.-H. Ke, et al., Experiments and modeling of carbon nanotube-based NEMS devices, Journal of the Mechanics and Physics of Solids 53 (6) (2005) 1314–1333.
[31] R. Poelma, et al., A numerical experimental approach for characterizing the elastic properties of thin films: application of nanocantilevers, Journal of Micromechanics and Microengineering 21 (6) (2011) 065003.
[32] R. Andosca, et al., Experimental and theoretical studies on MEMS piezoelectric vibrational energy harvesters with mass loading, Sensors and Actuators. A, Physical 178 (2012) 76–87.
[33] A.A.M. Ralib, et al., Fabrication of aluminium doped zinc oxide piezoelectric thin film on a silicon substrate for piezoelectric MEMS energy harvesters, Microsystem Technologies 18 (11) (2012) 1761–1769.
[34] A.A. Mohammed, W.A. Moussa, E. Lou, Development and experimental evaluation of a novel piezoresistive MEMS strain sensor, IEEE Sensors Journal 11 (10) (2011) 2220–2232.
[35] Y. Zhao, et al., Design, fabrication and experiment of a MEMS piezoresistive high-g accelerometer, Journal of Mechanical Science and Technology 27 (3) (2013) 831–836.

[36] M.I. Younis, MEMS linear and nonlinear statics and dynamics, in: R.T. Howe, A.J. Ricco (Eds.), Microsystems, Springer, New York, 2011.
[37] G.M. Rebeiz, RF MEMS: Theory, Design, and Technology, John Wiley & Sons, 2004.
[38] V.K. Varadan, et al., RF MEMS and Their Applications, John Wiley & Sons, England, 2003, p. 406.
[39] H.C. Nathanson, et al., The resonant gate transistor, I.E.E.E. Transactions on Electron Devices 14 (3) (1967) 117–133.
[40] T. Juneau, et al., Dual-axis optical mirror positioning using a nonlinear closed-loop controller, in: TRANSDUCERS'03. 12th International Conference on Solid-State Sensors, Actuators and Microsystems. Digest of Technical Papers (Cat. No. 03TH8664), IEEE, 2003.
[41] W.H. Lin, Y.P. Zhao, Casimir effect on the pull-in parameters of nanometer switches, Microsystem Technologies 11 (2) (2005) 80–85.
[42] H.M. Sedighi, A. Koochi, M. Abadyan, Modelling the size dependent static and dynamic pull-in instability of cantilever nanoactuator based on strain gradient theory, International Journal of Applied Mechanics 6 (5) (2014) 1450055.
[43] L.D. Landau, E.M. Lifshitz, L.P. Pitaevskii, Course of Theoretical Physics: Statistical Physics, Part 2: by E.M. Lifshitz and L.P. Pitaevskii, Pergamon Press, 1980.
[44] Y.P. Zhao, L.S. Wang, T.X. Yu, Mechanics of adhesion in MEMS — a review, Journal of Adhesion Science and Technology 18 (4) (2003) 519–546.
[45] J.N. Israelachvili, Intermolecular and Surface Forces, third edition, Academic Press, USA, 2013.
[46] C. Ke, H.D. Espinosa, Nanoelectromechanical systems and modeling, in: M. Rieth, W. Schommers (Eds.), Handbook of Theoretical and Computational Nanotechnology, American Scientific Publishers, 2006, pp. 1–38.
[47] A. Gusso, G.J. Delben, Dispersion force for materials relevant for micro- and nanodevices fabrication, Journal of Physics. D, Applied Physics 2008 (41) (2008) 175405.
[48] J.S. Stölken, A.G. Evans, A microbend test method for measuring the plasticity length scale, Acta Materialia 46 (14) (1998) 5109–5115.
[49] N.A. Fleck, et al., Strain gradient plasticity: theory and experiment, Acta Metallurgica Et Materialia 42 (2) (1994) 475–487.
[50] A.C.M. Chong, D.C.C. Lam, Strain gradient plasticity effect in indentation hardness of polymers, Journal of Materials Research 14 (10) (1999) 4103–4110.
[51] A.W. McFarland, J.S. Colton, Role of material microstructure in plate stiffness with relevance to microcantilever sensors, Journal of Micromechanics and Microengineering 15 (5) (2005) 1060–1067.
[52] R.D. Mindlin, H.F. Tiersten, Effects of couple-stresses in linear elasticity, Archive for Rational Mechanics and Analysis 11 (1) (1962) 415–448.
[53] F. Yang, et al., Couple stress based strain gradient theory for elasticity, International Journal of Solids and Structures 39 (10) (2002) 2731–2743.
[54] R.D. Mindlin, Second gradient of strain and surface-tension in linear elasticity, International Journal of Solids and Structures 1 (4) (1965) 417–438.
[55] D.C.C. Lam, et al., Experiments and theory in strain gradient elasticity, Journal of the Mechanics and Physics of Solids 51 (8) (2003) 1477–1508.
[56] A.C. Eringen, Nonlocal polar elastic continua, International Journal of Engineering Science 10 (1) (1972) 1–16.
[57] M.E. Gurtin, A. Ian Murdoch, A continuum theory of elastic material surfaces, Archive for Rational Mechanics and Analysis 57 (4) (1975) 291–323.
[58] M. Keivani, et al., A nonlinear model for incorporating the coupled effects of surface energy and microstructure on the electromechanical stability of NEMS, Arabian Journal for Science and Engineering 41 (11) (2016) 4397–4410.
[59] Z. Hao, A. Erbil, F. Ayazi, An analytical model for support loss in micromachined beam resonators with in-plane flexural vibrations, Sensors and Actuators. A, Physical 109 (1–2) (2003) 156–164.

[60] H. Hosaka, K. Itao, S. Kuroda, Damping characteristics of beam-shaped micro-oscillators, Sensors and Actuators. A, Physical 49 (1–2) (1995) 87–95.
[61] F. Blom, et al., Dependence of the quality factor of micromachined silicon beam resonators on pressure and geometry, Journal of Vacuum Science & Technology. B, Microelectronics and Nanometer Structures Processing, Measurement and Phenomena 10 (1) (1992) 19–26.
[62] M. Bao, Analysis and Design Principles of MEMS Devices, Elsevier, 2005.
[63] A. Burgdorfer, The influence of the molecular mean free path on the performance of hydrodynamic gas lubricated bearings, Journal of Basic Engineering 81 (1) (1959) 94–98.
[64] Y.-T. Hsia, G. Domoto, An Experimental Investigation of Molecular Rarefaction Effects in Gas Lubricated Bearings at Ultra-Low Clearances, 1983.
[65] S. Fukui, R. Kaneko, Analysis of ultra-thin gas film lubrication based on linearized boltzmann equation: first report—derivation of a generalized lubrication equation including thermal creep flow, 1988.
[66] H. Seidel, et al., Capacitive silicon accelerometer with highly symmetrical design, Sensors and Actuators. A, Physical 21 (1–3) (1990) 312–315.
[67] Y. Mitsuya, Modified Reynolds Equation for Ultra-Thin Film Gas Lubrication Using 1.5-Order Slip-Flow Model and Considering Surface Accommodation Coefficient, 1993.
[68] M. Andrews, I. Harris, G. Turner, A comparison of squeeze-film theory with measurements on a microstructure, Sensors and Actuators. A, Physical 36 (1) (1993) 79–87.
[69] T. Veijola, et al., Equivalent-circuit model of the squeezed gas film in a silicon accelerometer, Sensors and Actuators. A, Physical 48 (3) (1995) 239–248.
[70] Y.-H. Cho, A.P. Pisano, R.T. Howe, Viscous damping model for laterally oscillating microstructures, Journal of Microelectromechanical Systems 3 (2) (1994) 81–87.
[71] L. Wang, H. Hu, W. Guo, Thermal vibration of carbon nanotubes predicted by beam models and molecular dynamics, Proceedings of the Royal Society A. Mathematical, Physical and Engineering Sciences 466 (2120) (2010) 2325–2340.
[72] R. Ansari, S. Ajori, B. Arash, Vibrations of single-and double-walled carbon nanotubes with layerwise boundary conditions: a molecular dynamics study, Current Applied Physics 12 (3) (2012) 707–711.
[73] R. Nazemnezhad, S. Hosseini-Hashemi, Free vibration analysis of multi-layer graphene nanoribbons incorporating interlayer shear effect via molecular dynamics simulations and nonlocal elasticity, Physics Letters A 378 (44) (2014) 3225–3232.
[74] F. Mehralian, Y.T. Beni, M.K. Zeverdejani, Nonlocal strain gradient theory calibration using molecular dynamics simulation based on small scale vibration of nanotubes, Physica. B, Condensed Matter 514 (2017) 61–69.
[75] T. Lin, et al., A molecular dynamics investigation on effects of nanostructures on thermal conductance across a nanochannel, International Communications in Heat and Mass Transfer 97 (2018) 118–124.
[76] O. Bochobza-Degani, Y. Nemirovsky, Modeling the pull-in parameters of electrostatic actuators with a novel lumped two degrees of freedom pull-in model, Sensors and Actuators. A, Physical 97–98 (2002) 569–578.
[77] L. Wen-Hui, Z. Ya-Pu, Dynamic behaviour of nanoscale electrostatic actuators, Chinese Physics Letters 20 (11) (2003) 2070.
[78] H. Sadeghian, G. Rezazadeh, P.M. Osterberg, Application of the generalized differential quadrature method to the study of pull-in phenomena of MEMS switches, Journal of Microelectromechanical Systems 16 (6) (2007) 1334–1340.
[79] Q. Wang, K. Liew, Application of nonlocal continuum mechanics to static analysis of micro-and nano-structures, Physics Letters A 363 (3) (2007) 236–242.
[80] J. Abdi, et al., Modeling the effects of size dependence and dispersion forces on the pull-in instability of electrostatic cantilever NEMS using modified couple stress theory, Smart Materials and Structures 20 (5) (2011) 55011.
[81] Y. Beni, et al., Modeling the influence of surface effect and molecular force on pull-in voltage of rotational nano–micro mirror using 2-DOF model, Canadian Journal of Physics 90 (10) (2012) 963–974.

[82] N. Fazli, et al., Influence of electrostatic force and the van der Waals attraction on the pull-in instability of the CNT-based probe–actuator, Canadian Journal of Physics 92 (9) (2013) 1047–1057.
[83] A. Farrokhabadi, A. Koochi, M. Abadyan, Modeling the instability of CNT tweezers using a continuum model, Microsystem Technologies 20 (2) (2014) 291–302.
[84] A. Farrokhabadi, et al., Effects of size-dependent elasticity on stability of nanotweezers, Applied Mathematics and Mechanics 35 (12) (2014) 1573–1590.
[85] Y. Beni, A. Koochi, M. Abadyan, Using modified couple stress theory for modeling the size-dependent pull-in instability of torsional nano-mirror under Casimir force, International Journal of Optomechatronics 8 (1) (2014) 47–71.
[86] H.M. Sedighi, F. Daneshmand, M. Abadyan, Modeling the effects of material properties on the pull-in instability of nonlocal functionally graded nano-actuators, ZAMM-Journal of Applied Mathematics and Mechanics (Zeitschrift für Angewandte Mathematik und Mechanik) 96 (3) (2016) 385–400.
[87] H.M. Sedighi, A. Bozorgmehri, Dynamic instability analysis of doubly clamped cylindrical nanowires in the presence of Casimir attraction and surface effects using modified couple stress theory, Acta Mechanica 227 (6) (2016) 1575–1591.
[88] R. Soroush, et al., A bilayer model for incorporating the coupled effects of surface energy and microstructure on the electromechanical stability of NEMS, International Journal of Structural Stability and Dynamics 17 (4) (2017) 1771005.
[89] A. Yekrangi, et al., Scale-dependent dynamic behavior of nanowire-based sensor in accelerating field, Journal of Applied and Computational Mechanics 5 (2) (2019) 486–497.
[90] H.M. Ouakad, H.M. Sedighi, Static response and free vibration of MEMS arches assuming out-of-plane actuation pattern, International Journal of Non-Linear Mechanics 110 (2019) 44–57.
[91] A. Ramezani, A. Alasty, J. Akbari, Pull-in parameters of cantilever type nanomechanical switches in presence of Casimir force, Nonlinear Analysis: Hybrid Systems 1 (3) (2007) 364–382.
[92] R. Soroush, et al., Investigating the effect of Casimir and van der Waals attractions on the electrostatic pull-in instability of nano-actuators, Physica Scripta 82 (4) (2010) 045801.
[93] A. Koochi, et al., Theoretical study of the effect of Casimir attraction on the pull-in behavior of beam-type NEMS using modified Adomian method, Physica. E, Low-Dimensional Systems and Nanostructures 43 (2) (2010) 625–632.
[94] A. Koochi, A. Noghrehabadi, M. Abadyan, Approximating the effect of van der Waals force on the instability of electrostatic nano-cantilevers, International Journal of Modern Physics B 25 (29) (2011) 3965–3976.
[95] A. Koochi, et al., Modeling the influence of surface effect on instability of nano-cantilever in presence of Van der Waals force, International Journal of Structural Stability and Dynamics 13 (4) (2013) 1250072.
[96] W.J. Palm, Mechanical Vibration, John Wiley, Hoboken, NJ, 2007.
[97] C.L. Dym, I.H. Shames, Solid Mechanics: A Variational Approach, augmented edition, Springer, New York, USA, 2013.

CHAPTER 2

Semianalytical solution methods

2.1. Introduction

The governing NEMS/MEMS equations are usually highly nonlinear, and a precise solution cannot be obtained for them. Therefore, researchers are driven towards approximate solutions, based on numerical methods or a combination of analytical techniques and numerical solutions, to describe the behavior of these devices. Such combinations had already resulted in potent, adaptable techniques known as semianalytical approaches. The semianalytical approaches such as homotopy perturbation method [1–12], Adomian decomposition method [5,13–15], modified Adomian decomposition method [16–24], Green's function [25–29], monotonic iteration method [7,30,31], differential transformation method [32–37], and variation iteration method [30,31,38,39] have been applied extensively to investigate the behavior of micro- and nanostructures.

This chapter discusses the semianalytical methods for solving nonlinear differential equations. Following the introduction of the concept of each method, as an example, a constitutive nonlinear differential equation for an NEMS/MEMS is extracted, and it is solved using the proposed semianalytical method. In addition to employing the solution method, the micro- and nanoscale phenomena connected to proposed structures are discussed. The content of this chapter is arranged as follows:

- "Homotopy perturbation method,"
- "Conventional Adomian decomposition method,"
- "Modified Adomian decomposition method,"
- "General Green's function,"
- "Monotonic iteration method,"
- "Differential transformation method,"
- "Variation iteration methods," and
- "Galerkin method for static problems."

2.2. Homotopy perturbation method

The homotopy perturbation method is developed by coupling the conventional perturbation and homotopy techniques. Unlike the conventional methods, it is not affected by small perturbations in parameters of the equation [40].

To demonstrate homotopy perturbation method, consider a general differential equation on the domain Ω as

$$A(u) - f(\mathbf{r}) = 0, \quad \mathbf{r} \in \Omega \tag{2.1}$$

Nonlinear Differential Equations in Micro/nano Mechanics
https://doi.org/10.1016/B978-0-12-819235-1.00006-0
Copyright © 2020 Elsevier Ltd.
All rights reserved.

where A is a general differential operator, and $f(\mathbf{r})$ is a known function. By defining a boundary operator B, the boundary conditions for Eq. (2.1) can be defined as

$$B(u, \partial u/\partial n) = 0, \quad \mathbf{r} \in \Gamma. \tag{2.2}$$

The differential operator A can be divided into a nonlinear part ($N(u)$) and a linear component ($L(u)$). Therefore, Eq. (2.1) can be rearranged as

$$L(u) + N(u) - f(\mathbf{r}) = 0, \quad \mathbf{r} \in \Omega. \tag{2.3}$$

A homotopy $\kappa(r, p) : \Omega \times [0, 1] \to \mathbb{R}$ can be constructed as follows to satisfy the equation [40]:

$$\mathcal{H}(\kappa, p) = (1 - p)[L(\kappa) - L(u_0)] + p[A(\kappa) - f(\mathbf{r})] = 0, \quad p \in [0, 1], \quad \mathbf{r} \in \Omega \tag{2.4}$$

where p is an embedding parameter, and u_0 is an approximate solution for the differential equation that satisfies the boundary conditions. It is clear from Eq. (2.4) that

$$\mathcal{H}(\kappa, 0) = L(\kappa) - L(u_0) = 0, \tag{2.5}$$

$$\mathcal{H}(\kappa, 1) = A(\kappa) - f(\mathbf{r}) = 0. \tag{2.6}$$

In the above relations, $\kappa(r, p)$ is defined as the following power series in p:

$$\kappa = \kappa_0 + \kappa_1 p + \kappa_2 p^2 + \kappa_3 p^3 + \cdots. \tag{2.7}$$

What is evident is that changing the parameter p from zero to 1 alters $\kappa(r, p)$ from $u_0(r)$ to $u(r)$. Therefore, an approximate solution for the differential equation (2.1) can be achieved via setting $q = 1$:

$$u = \lim_{p \to 1} \kappa = \kappa_0 + \kappa_1 + \kappa_2 + \kappa_3 + \cdots. \tag{2.8}$$

2.2.1 Cantilever nanoactuator in van der Waals regime

Electrostatic cantilever microbeams and nanobeams are widely used as an essential elements in diverse micro- and nanoscale structures such as atomic force microscopy [41–43], resonators [44–46], switches [47–51], mass sensors [52–54], martial properties investigations [55], and micro- and nanopositioners [56].

The SEM images of two different cantilever MEMS resonators used for mass sensing are illustrated in Figs. 2.1 and 2.2. These ultrasmall structures can be simulated as a cantilever beam. Fig. 2.3 demonstrates a schematic illustration of a cantilever nanoactuator. The nanoactuator is constructed from a nanobeam over a fixed plate. The nanobeam is

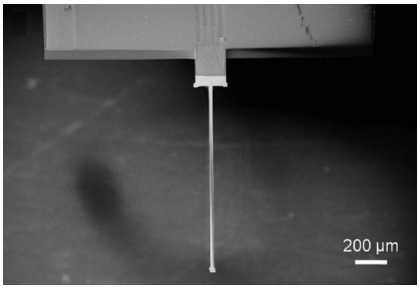

Figure 2.1 SEM image of a nanoparticle mass sensor [54].

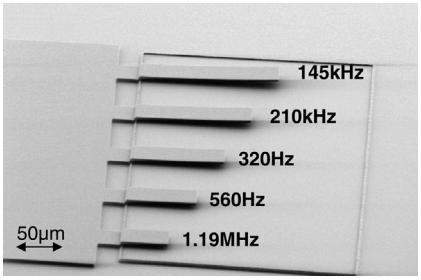

Figure 2.2 SEM image of cantilever MEMS resonator array used for mass sensing application [52].

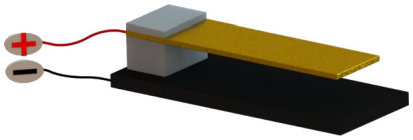

Figure 2.3 Schematic illustration of a cantilever nanoactuator.

fixed at one end and free at the other end (i.e., cantilever). When an electrical potential is applied to the nanoactuator, the beam deflects towards the fixed plane due to an attracting electrical force.

The moving part of the nanoactuator can be modeled as a cantilever Euler–Bernoulli beam with the length of L. The beam has a rectangular cross-section with thickness h and width b. The Euler–Bernoulli beam displacement is explained as [57]:

$$u_X = -Z\frac{\partial W}{\partial X}, \quad u_Y = 0, \quad u_Z = W \tag{2.9}$$

where u_x, u_y, and u_z depict the movement of the beam towards x, y, and z axes, respectively. Moreover, W is the deflection of the beam from the neutral position towards the Z-axis. The moveable actuator and fixed ground create a parallel plate capacitor. As mentioned in Section 1.2.1, for two infinite parallel plates, the electrical field is

uniform. In such a case, the capacitance is directly proportional to the plates' area and inversely proportional to the separation or distance between the plates. For the nanoactuator, the capacitor is constructed from a beam/plate parallel to a fixed ground with a nonuniform electric field near the edges. The non-uniform electrical force at the edges (i.e., fringing field effect) can affect the capacitance of parallel plate capacitors. Therefore, to enhance the accuracy of the electrical force which acts on a nanoactuator, the fringing field effect should be incorporated into the simulation. Using Palmer's formula for a finite plate over a semiinfinite ground, the capacitance per unit length is expressed as [58]

$$C(g) = \frac{\varepsilon b}{g}\left[1 + \frac{2g}{\pi b}\left(1 + \ln\left(\frac{\pi b}{g}\right)\right)\right]. \tag{2.10}$$

Using Eq. (2.10), the electrical energy per unit length is determined as

$$E_{elec} = \frac{1}{2}C(g)V^2 = \frac{\varepsilon b V^2}{2g}\left[1 + \frac{2g}{\pi b}\left(1 + \ln\left(\frac{\pi b}{g}\right)\right)\right]. \tag{2.11}$$

Finally, the electrical force per unit length for a nanoactuator (when considering the nonuniform electric field) can be investigated by differentiating the electrical energy with respect to the gap:

$$f_{elec} = -\frac{\partial E_{elec}}{\partial g} = \frac{\varepsilon b V^2}{2g^2}\left[1 + \frac{2}{\pi}\left(\frac{g}{b}\right)\right]. \tag{2.12}$$

When an electrical potential is applied, the moving part of the nanoactuator deflects towards the fixed plate. Therefore, the gap between the fixed plate and moving arm is reduced from g to $g - W$. Hence, by replacing g with $g - W$ in Eq. (2.12), the electrical force is obtained as

$$f_{elec} = \frac{\varepsilon b V^2}{2(g-W)^2}\left[1 + \frac{2}{\pi}\left(\frac{g-W}{b}\right)\right] \approx \frac{\varepsilon b V^2}{2(g-W)^2}\left[1 + 0.65\left(\frac{g-W}{b}\right)\right]. \tag{2.13}$$

Reducing the structure size from micro- to nanoscale results in the emergence of the impact of the dispersion force. For separation lengths less than 20 nm, the van der Waals attraction is dominant [59]. As mentioned in the previous chapter, the van der Waals force for two parallel plates is determined using Eq. (1.4). In a similar manner with electrical force, by replacing g with $g - W$ in Eq. (1.4), the van der Waals force per unit length of the deflected nanoactuator is obtained as

$$f_{vdw} = \frac{\bar{A}b}{6\pi(g-W)^3} \tag{2.14}$$

where $\bar{A}$ is the Hamaker constant, which is dependent on the nanobeam constructing material. The Hamaker constant is mainly in the range of $[0.4, 4] \times 10^{-19}$ J.

The virtual work principle might be applied to extract the constitutive equation of the nanoactuator. In the case of small deformations, elastic virtual work (W_{elas}), electrical virtual work (W_{elec}), and van der Waals virtual work (W_{vdW}) are defined as follows:

$$W_{elas} = \int\int\int \boldsymbol{\sigma}^{\mathbf{T}} \boldsymbol{\varepsilon} dX dY dZ, \tag{2.15}$$

$$W_{elec} = \int_0^L f_{elec} W dX, \tag{2.16}$$

$$W_{vdW} = \int_0^L f_{vdW} W dX \tag{2.17}$$

where W is virtual deflection, while $\boldsymbol{\sigma}$ is the virtual stress opposed by the virtual deflection. The components of stress tensor (ε) and strain tensor (σ) are defined in Chapter 1. By replacing Eq. (2.9) in Eqs. (1.36) and (1.39), the following relations are obtained:

$$\varepsilon_{XX} = -Z\frac{d^2W}{dX^2}, \quad \varepsilon_{XY} = \varepsilon_{YZ} = \varepsilon_{ZX} = \varepsilon_{YY} = \varepsilon_{ZZ} = 0, \tag{2.18}$$

$$\sigma_{XX} = -ZE\frac{d^2W}{dX^2}, \quad \sigma_{XY} = \sigma_{YZ} = \sigma_{ZX} = \sigma_{YY} = \sigma_{ZZ} = 0. \tag{2.19}$$

In the above equations, E is the Young's modulus for a narrow beam (i.e., $b < 5h$). However, for wide beams in which their width is at least five times greater than their thickness (i.e., $b > 5h$), the plate modulus ($E/(1-\nu^2)$) should be used instead of the Young's modulus [60].

By replacing Eqs. (2.18) and (2.19) in Eq. (2.15), the elastic virtual work is defined as

$$W_{elas} = \int\int\int Z^2 E\frac{d^2W}{dX^2}\frac{d^2W}{dX^2} dX dY dZ. \tag{2.20}$$

According to the virtual work principle, the equilibrium in the system requires

$$W_{elas} = W_{elec} + W_{vdW}. \tag{2.21}$$

By replacing Eqs. (2.12), (2.14), (2.16), and (2.20) in Eq. (2.21), and integrating by parts, from the resulting formula the governing equation for nanoactuator is obtained as

$$EI\frac{d^4W}{dX^4} = \frac{\varepsilon_0\varepsilon_r b V^2}{2(g-W)^2}\left[1 + 0.65\left(\frac{g-W}{b}\right)\right] + \frac{\bar{A}b}{6\pi(g-W)^3}. \tag{2.22}$$

The fixed end of the nanoactuator is clamped, which result in zero deflection and rotation:

$$W(0) = 0, \quad \frac{dW}{dX}(0) = 0. \tag{2.23}$$

At the free end of the nanoactuator, both shear force and moment are zero. Therefore, the boundary conditions at the free end are:

$$\frac{dW^2}{dX^2}(L) = 0, \quad \frac{d^3W}{dX^3}(L) = 0. \tag{2.24}$$

Employing dimensionless parameters offers many benefits, including compact characterization, avoiding mixed and ambiguous units, reducing variable numbers. Besides, using a dimensionless setting leads to dimensionless equations that are capable of providing insight into controlling parameters and the nature of the problem. By considering $w = W/g$, $x = X/L$, the dimensionless governing equation for the nanoactuator is defined as

$$\frac{d^4w}{dx^4} = \frac{\beta_{vdW}}{(1-w)^3} + \frac{\alpha}{(1-w)^2} + \frac{\alpha\gamma}{(1-w)}, \tag{2.25}$$

$$\begin{aligned} &w(0) = 0, \quad \frac{dw}{dx}(0) = 0, \\ &\frac{d^2w}{dx^2}(1) = 0, \quad \frac{d^3w}{dx^3}(1) = 0 \end{aligned} \tag{2.26}$$

where the dimensionless parameter of van der Waals force (β_{vdW}), the dimensionless parameter of the electrical force (α), and the gap-to-width ratio (γ), which is related to the fringing field effect, are defined as:

$$\beta_{vdW} = \frac{AbL^4}{6\pi g^4 EI}, \tag{2.27}$$

$$\alpha = \frac{\varepsilon_0 \varepsilon_r b V^2 L^4}{2g^3 EI}, \tag{2.28}$$

$$\gamma = 0.65\frac{g}{b}. \tag{2.29}$$

By considering $y(x) = 1 - w(x)$, Eqs. (2.25) and (2.26) can be rewritten as:

$$\frac{d^4y}{dx^4} + \frac{\beta_{vdW}}{y^3} + \frac{\alpha}{y^2} + \frac{\alpha\gamma}{y} = 0, \tag{2.30}$$

$$\begin{aligned} &y(0) = 1, \quad \frac{dy}{dx}(0) = 0, \\ &\frac{d^2y}{dx^2}(1) = 0, \quad \frac{d^3y}{dx^3}(1) = 0. \end{aligned} \tag{2.31}$$

The transformation $dy/dx = u(x)$, $du/dx = v(x)$, $dv/dx = z(x)$ can be used to transform Eq. (2.30) into a system of differential equations:

$$\frac{dy}{dx} = u(x), \tag{2.32}$$

$$\frac{du}{dx} = v(x), \tag{2.33}$$

$$\frac{dv}{dx} = z(x), \tag{2.34}$$

$$\frac{dz}{dx} = -\frac{\beta_{vdW}}{\gamma(x)^3} - \frac{\alpha}{\gamma(x)^2} - \frac{\gamma\alpha}{\gamma(x)}, \tag{2.35}$$

with the following initial conditions:

$$\gamma(0) = 1, \tag{2.36}$$

$$u(0) = 0, \tag{2.37}$$

$$v(0) = A = \frac{d^2\gamma}{dx^2}(0), \tag{2.38}$$

$$z(0) = B = \frac{d^3\gamma}{dx^3}(0). \tag{2.39}$$

Integrating Eqs. (2.32) to (2.35), the following system of equations is achieved:

$$\gamma(x) = 1 + \int_0^x u(t)\,dt, \tag{2.40}$$

$$u(x) = 0 + \int_0^x v(t)\,dt, \tag{2.41}$$

$$v(x) = A + \int_0^x z(t)\,dt, \tag{2.42}$$

$$z(x) = B - \int_0^x \left(\beta_{vdW}\gamma(x)^{-3} + \alpha\gamma(x)^{-2} + \alpha\gamma\gamma(x)^{-1}\right) dt. \tag{2.43}$$

Eqs. (2.40) to (2.43) can be expanded into Taylor series with respect to homotopy parameter p, which results in the following equations:

$$\sum_{k=0}^{\infty} p^k\gamma_k = 1 + p\int_0^x \left(\sum_{k=0}^{\infty} p^k u_k\right) dt, \tag{2.44}$$

$$\sum_{k=0}^{\infty} p^k u_k = 0 + p\int_0^x \left(\sum_{k=0}^{\infty} p^k v_k\right) dt, \tag{2.45}$$

$$\sum_{k=0}^{\infty} p^k v_k = A + p\int_0^x \left(\sum_{k=0}^{\infty} p^k z_k\right) dt, \tag{2.46}$$

$$\sum_{k=0}^{\infty} p^k z_k = B - p\int_0^x \left(\beta_{vdW}\sum_{k=0}^{\infty} p^k\varphi_{k,3} + \alpha\sum_{k=0}^{\infty} p^k\varphi_{k,2} + \alpha\gamma\sum_{k=0}^{\infty} p^k\varphi_{k,1}\right) dt \tag{2.47}$$

where $\varphi_{k,n}$ is defined as

$$\varphi_{k,n} = \frac{1}{k!}\frac{d^k}{dp^k}\left[\left(\sum_{i=0}^{\infty} p^i \gamma_i\right)^{-n}\right]_{p=0}. \tag{2.48}$$

Now, by expanding Eq. (2.41), we obtain:

$$\begin{aligned}
&\varphi_{0,n} = \gamma_0^{-n},\\
&\varphi_{1,n} = -n\gamma_0^{-n-1}\gamma_1,\\
&\varphi_{2,n} = \frac{1}{2}n(n+1)\gamma_0^{-n-2}\gamma_1^2 - n\gamma_0^{-n-1}\gamma_2,\\
&\varphi_{3,n} = -\frac{1}{6}n(n+1)(n+2)\gamma_0^{-n-3}\gamma_1^3 + n(n+1)\gamma_0^{-n-2}\gamma_1\gamma_2 - n\gamma_0^{-n-1}\gamma_3,\\
&\varphi_{4,n} = \frac{1}{24}(n+1)(n+2)(n+3)\gamma_0^{-n-4}\gamma_1^4 - \frac{1}{2}(n+1)(n+2)\gamma_0^{-n-3}\gamma_1^2\gamma_2\\
&\qquad + \frac{1}{6}(n+1)\gamma_0^{-n-2}\gamma_3 - n\gamma_0^{-n-1}\gamma_4,\\
&\quad \vdots = \vdots
\end{aligned} \tag{2.49}$$

While replacing Eq. (2.49) in Eqs. (2.44) to (2.47), we should note that the coefficients of the same powers of p should be equal. Therefore,

$$p^{(0)}: \begin{cases} \gamma_0 = 1,\\ u_0 = 0,\\ v_0 = A,\\ z_0 = B, \end{cases} \qquad p^{(1)}: \begin{cases} \gamma_1 = 0,\\ u_1 = Ax,\\ v_1 = Bx,\\ z_1 = -(\beta_{vdW} + \alpha + \alpha\gamma)x, \end{cases} \tag{2.50}$$

$$p^{(2)}: \begin{cases} \gamma_2 = \dfrac{Ax^2}{2},\\ u_2 = \dfrac{Bx^2}{2},\\ v_2 = -(\beta_{vdW} + \alpha + \alpha\gamma)\dfrac{x^2}{2},\\ z_2 = 0, \end{cases} \qquad p^{(3)}: \begin{cases} \gamma_3 = \dfrac{Bx^3}{6},\\ u_3 = -(\beta_{vdW} + \alpha + \alpha\gamma)\dfrac{x^3}{6},\\ v_3 = 0,\\ z_3 = A(3\beta_{vdW} + 2\alpha + \alpha\gamma)\dfrac{x^3}{6}, \end{cases}$$

$$p^{(4)}: \begin{cases} \gamma_4 = -(\beta_{vdW} + \alpha + \alpha\gamma)\dfrac{x^4}{24},\\ u_4 = 0,\\ v_4 = A(3\beta_{vdW} + 2\alpha + \alpha\gamma)\dfrac{x^4}{24},\\ z_4 = B(3\beta_{vdW} + 2\alpha + \alpha\gamma)\dfrac{x^4}{24}, \end{cases}$$

$$p^{(5)}:\begin{cases} y_5 = 0, \\ u_5 = A(3\beta_{vdW} + 2\alpha + \alpha\gamma)\dfrac{x^5}{120}, \\ v_5 = B((3\beta_{vdW} + 2\alpha + \alpha\gamma)\dfrac{x^5}{120}, \\ z_5 = -\left[A^2(6\beta_{vdW} + 3\alpha + \alpha\gamma) + \dfrac{(3\beta_{vdW} + 2\alpha + \alpha\gamma)(\beta_{vdW} + \alpha + \alpha\gamma)}{6}\right]\dfrac{x^5}{20}, \end{cases}$$

$$p^{(6)}:\begin{cases} y_6 = A(3\beta_{vdW} + 2\alpha + \alpha\gamma)\dfrac{x^6}{720}, \\ u_6 = B(3\beta_{vdW} + 2\alpha + \alpha\gamma)\dfrac{x^6}{720}, \\ v_6 = -\left[A^2(6\beta_{vdW} + 3\alpha + \alpha\gamma) + \dfrac{(3\beta_{vdW} + 2\alpha + \alpha\gamma)(\beta_{vdW} + \alpha + \alpha\gamma)}{6}\right]\dfrac{x^6}{120}, \\ z_6 = -A(6\beta_{vdW} + 3\alpha + \alpha\gamma)\dfrac{x^6}{36}, \end{cases}$$

$$p^{(7)}:\begin{cases} y_7 = B(3\beta_{vdW} + 2\alpha + \alpha\gamma)\dfrac{x^7}{5040}, \\ u_7 = -\left[A^2(6\beta_{vdW} + 3\alpha + \alpha\gamma) + \dfrac{(3\beta_{vdW} + 2\alpha + \alpha\gamma)(\beta_{vdW} + \alpha + \alpha\gamma)}{6}\right]\dfrac{x^7}{840}, \\ v_7 = -A(6\beta_{vdW} + 3\alpha + \alpha\gamma)\dfrac{x^7}{252}, \\ z_7 = \big[90A^3(10\beta_{vdW} + 4\alpha + \alpha\gamma) - 20B^3(6\beta_{vdW} + 3\alpha + \alpha\gamma) + \\ \quad A\left(189\beta_{vdW}^2 + 94\alpha^2 + 282\alpha\beta_{vdW} + 216\beta_{vdW}\alpha\gamma + 124\alpha^2\gamma + 31\alpha^2\gamma^2\right)\big]\dfrac{x^7}{5040}, \end{cases}$$

$$p^{(8)}:\begin{cases} y_8 = -\left[A^2(6\beta_{vdW} + 3\alpha + \alpha\gamma) + \dfrac{(3\beta_{vdW} + 2\alpha + \alpha\gamma)(\beta_{vdW} + \alpha + \alpha\gamma)}{6}\right]\dfrac{x^8}{6720}, \\ u_8 = -AB(6\beta_{vdW} + 3\alpha + \alpha\gamma)\dfrac{x^8}{2016}, \\ v_8 = \left[\begin{array}{l} 90A^3(10\beta_{vdW} + 4\alpha + \alpha\gamma) - 20B^3(6\beta_{vdW} + 3\alpha + \alpha\gamma) \\ +A\left(189\beta_{vdW}^2 + 94\alpha^2 + 282\alpha\beta_{vdW} + 216\alpha\gamma\beta_{vdW}\right. \\ \left.+124\alpha^2\gamma + 31\alpha^2\gamma^2\right) \end{array}\right]\dfrac{x^8}{40320}, \\ z_8 = \left[\begin{array}{l} 630A^2B(10\beta_{vdW} + 4\alpha + \alpha\gamma) \\ +A\left(429\beta_{vdW}^2 + 214\alpha^2 + 642\alpha\beta_{vdW} + 469\alpha\gamma\beta_{vdW}\right. \\ \left.+284\alpha^2\gamma + 71\alpha^2\gamma^2\right) \end{array}\right]\dfrac{x^8}{40320}, \end{cases}$$

$$
p^{(9)}:\begin{cases}
y_9=-AB(6\beta_{vdW}+3\alpha+\alpha\gamma)\dfrac{x^9}{18144},\\
w_9=\left[\begin{array}{l}90A^3(10\beta_{vdW}+4\alpha+\alpha\gamma)-20B^3(6\beta_{vdW}+3\alpha+\alpha\gamma)\\+A\big(189\beta_{vdW}^2+94\alpha^2+282\alpha\beta_{vdW}+216\alpha\gamma\beta_{vdW}\\+124\alpha^2\gamma+31\alpha^2\gamma^2\big)\end{array}\right]\dfrac{x^9}{362880},\\
v_9=\left[\begin{array}{l}630A^2B(10\beta_{vdW}+4\alpha+\alpha\gamma)\\+A\big(429\beta_{vdW}^2+214\alpha^2+642\alpha\beta_{vdW}+469\alpha\gamma\beta_{vdW}\\+284\alpha^2\gamma+71\alpha^2\gamma^2\big)\end{array}\right]\dfrac{x^9}{362880},\\
z_9=-\left[\begin{array}{l}2520A^4(15\beta_{vdW}+5\alpha+\alpha\gamma)-1680AB^2(10\beta_{vdW}+4\alpha+\alpha\gamma)\\+2A^2(6858\beta_{vdW}^2+2706\alpha^2+661\alpha^2\gamma^2+9471\alpha\beta_{vdW}\\+7194\alpha\gamma\beta_{vdW}+3305\alpha^2\gamma)+567\beta_{vdW}\alpha^2\gamma^2+1422\beta_{vdW}\alpha^2\gamma\\+1071\alpha\beta_{vdW}^2+925\alpha\gamma\beta_{vdW}^2+429\beta_{vdW}^3+864\beta_{vdW}\alpha^2\\+355\alpha^3\gamma^2+71\alpha^3\gamma^3+214\alpha^3+498\alpha^3\gamma\end{array}\right]\dfrac{x^9}{362880},
\end{cases}
$$

$$
p^{(10)}:\begin{cases}
y_{10}=\big[90A^3(10\beta_{vdW}+4\alpha+\alpha\gamma)-20B^3(6\beta_{vdW}+3\alpha+\alpha\gamma)+\\
A\left(189\beta_{vdW}^2+94\alpha^2+282\alpha\beta_{vdW}+216\alpha\gamma\beta_{vdW}+124\alpha^2\gamma+31\alpha^2\gamma^2\right)\big]\dfrac{x^{10}}{3628800},\\
w_{10}=\left[\begin{array}{l}630A^2B(10\beta_{vdW}+4\alpha+\alpha\gamma)\\+A\big(429\beta_{vdW}^2+214\alpha^2+642\alpha\beta_{vdW}+469\alpha\gamma\beta_{vdW}\\+284\alpha^2\gamma+71\alpha^2\gamma^2\big)\end{array}\right]\dfrac{x^{10}}{3628800},\\
v_{10}=-\big[2520A^4(15\beta_{vdW}+5\alpha+\alpha\gamma)-1680AB^2(10\beta_{vdW}+4\alpha+\alpha\gamma)\\
+2A^2\big(6858\beta_{vdW}^2+2706\alpha^2+661\alpha^2\gamma^2+9471\alpha\beta_{vdW}+7194\alpha\gamma\beta_{vdW}\\
+3305\alpha^2\gamma\big)+567\beta_{vdW}\alpha^2\gamma^2+1422\alpha^2\gamma\beta_{vdW}+1071\alpha\beta_{vdW}^2+925\alpha\gamma\beta_{vdW}^2\\
+429\beta_{vdW}^3+864\alpha^2\beta_{vdW}+355\alpha^3\gamma^2+71\alpha^3\gamma^3+214\alpha^3+498\alpha^3\gamma\big]\dfrac{x^{10}}{3628800},\\
z_{10}=-\big[1512A^3B(15\beta_{vdW}+5\alpha+\alpha\gamma)-84B^3(10\beta_{vdW}+4\alpha+\alpha\gamma)\\
+AB\big(4014\beta_{vdW}^2+1590\alpha^2+391\alpha^2\gamma^2+4275\alpha\gamma\beta_{vdW}+5565\alpha\beta_{vdW}\\
+1955\alpha^2\gamma\big)\big]\dfrac{x^{10}}{181440}.
\end{cases}
$$

Finally, the solution for Eq. (2.25) is explained as:

$$
\begin{aligned}
w(x)=&-\frac{Ax^2}{2}-\frac{Bx^3}{6}+(\beta_{vdW}+\alpha+\alpha\gamma)\frac{x^4}{24}-(3\beta_{vdW}+2\alpha+\alpha\gamma)\frac{Ax^6}{720}\\
&+\left[A^2(6\beta_{vdW}+3\alpha+\alpha\gamma)+\frac{(3\beta_{vdW}+2\alpha+\alpha\gamma)(\beta_{vdW}+\alpha+\alpha\gamma)}{6}\right]\frac{x^8}{6720}
\end{aligned}
$$

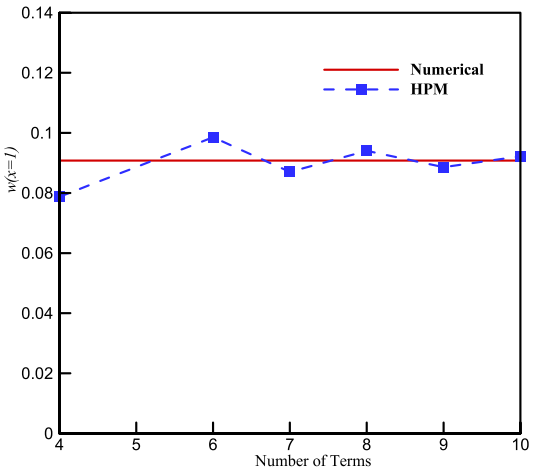

Figure 2.4 Convergence check for the homotopy perturbation solution.

$$
\begin{aligned}
&-(3\beta_{vdW}+2\alpha+\alpha\gamma)\frac{Bx^7}{5040}+AB(10\beta_{vdW}+3\alpha+\alpha\gamma)\frac{x^9}{18144}\\
&+\left[90A^3(10\beta_{vdW}+4\alpha+\alpha\gamma)-20B^3(6\alpha+3\alpha+\alpha\gamma)\right.\\
&+A\left(189\beta_{vdW}^2+94\alpha^2+282\alpha\beta_{vdW}+216\alpha\gamma\beta_{vdW}+124\alpha^2\gamma\right.\\
&\left.\left.+31\alpha^2\gamma^2\right)\right]\frac{x^{10}}{3628800}+\ldots. \qquad (2.51)
\end{aligned}
$$

The boundary condition at the free end of the beam ($x=1$) can be employed to determine the unknown parameters A and B.

To evaluate the convergence of the homotopy perturbation solution, the tip deflection of a typical nanoactuator is demonstrated in Fig. 2.4. In the studied typical actuator, the dimensionless parameter for the van der Waals force is presumed to be 0.3 ($\beta_{vdW}=0.3$), the dimensionless parameter for the voltage is 0.2 ($\alpha=0.2$), and the beam width is considered equal to the initial gap. The results demonstrated in Fig. 2.4 indicate that increasing the number of homotopy perturbation terms results in higher solution accuracy. By considering ten terms in the homotopy perturbation solution, the relative error between the numerical solution and semianalytical data is approximately 1.5%, which is in an acceptable range.

The centerline bending of the nanoactuator for various applied voltages is presented in Fig. 2.5. In this figure, the dimensionless parameter for the van der Waals force is presumed to be 0.4 ($\beta_{vdW}=0.4$), and the beam width is considered equal to the initial gap. Fig. 2.5 demonstrates that beam deflection increases by enhancing the applied voltage until the pull-in value. As can be seen in Fig. 2.5, even without external voltage (i.e., $\alpha=0$), the van der Waals force creates an initial bending in the nanoactuator.

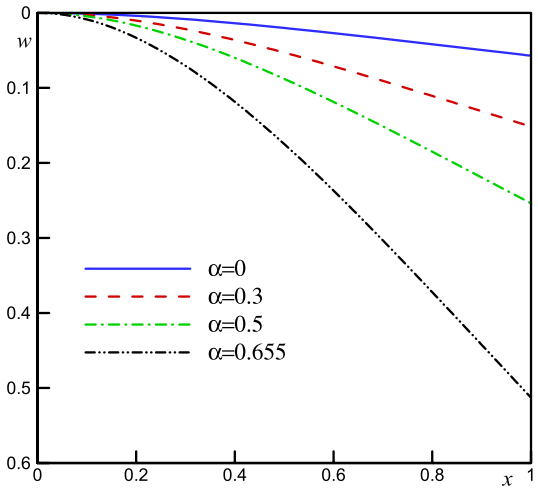

Figure 2.5 Nanoactuator deflection (i.e., *w* vs. *x*) for different applied voltages.

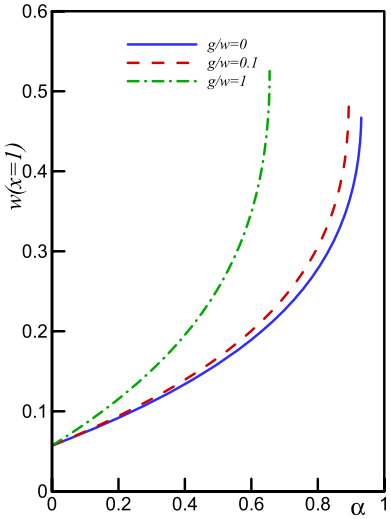

Figure 2.6 The impact of fringing field effect on the nanoactuator tip deflection.

To investigate the influence of the finite dimension correction (fringing field effect) on the static deflection of the nanoactuator, the dimensionless tip deflection (i.e., $w(x=1)$ of the nanoactuator for different values of the gap-to-width ratio is demonstrated in Fig. 2.6. In this figure, $g/w=0$ is neglecting the fringing field effect. In other words, when the nanobeam width is considerably more significant than the initial gap, the electrical field is approximately uniform, and the fringing field effect is negligible.

As can be seen, considering the fringing field effect increases the tip deflection of the nanoactuator, because of an enhancement in the electrical force due to the finite dimension correction. The results of Fig. 2.6 clarify that for a beam type nanoactuator, the fringing field effect can significantly change the behavior of the actuator and should be incorporated in the simulation.

2.3. Adomian decomposition methods

George Adomian introduced and developed a semianalytical technique (i.e., Adomian decomposition method) for solving nonlinear differential equations. In this method, Adomian polynomials are utilized to deduce a recursive relation. In the following subsections, conventional and modified Adomian decomposition methods are discussed.

2.3.1 Conventional Adomian decomposition method

In Adomian decomposition techniques, a general differential equation is considered as follows:

$$D(w(t)) = g(t) \tag{2.52}$$

where D is a general differential operator, which can be decomposed into linear (L) and nonlinear (N) parts. Therefore, the differential equation can be represented as

$$L(w) + N(w) = g. \tag{2.53}$$

By ignoring the boundary conditions and settings, the general solution for Eq. (2.53) can be determined as

$$w = f + L^{-1}(g) - L^{-1}(N(w)) \tag{2.54}$$

where L^{-1} is the inverse integral of L, and function f represents the general solution for the linear equation $L(w) = 0$.

In Adomian decomposition, the solution $w(x)$ is defined as

$$w = \sum_{n=0}^{\infty} w_n \tag{2.55}$$

where

$$\begin{aligned} &w_0 = f, \\ &w_{k+1} = -L^{-1}(Rw_k) - L^{-1}(Nw_k), \quad k \geq 0. \end{aligned} \tag{2.56}$$

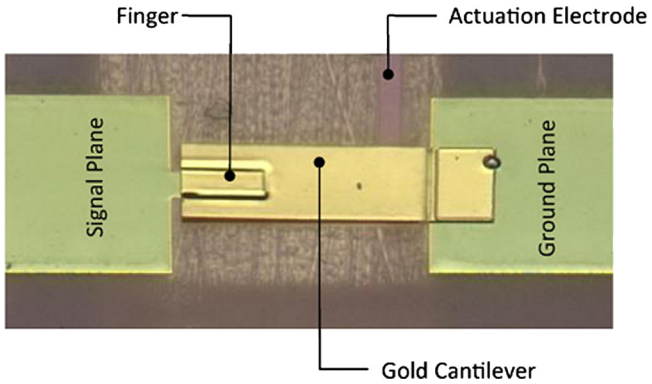

Figure 2.7 Cantilever MEMS switch [47].

The nonlinear term $N(w)$ can be expressed as the sum of Adomian polynomials (A_n) [61]:

$$N(w) = \sum_{n=0}^{\infty} A_n(w). \tag{2.57}$$

The Adomian polynomials are obtained from the nonlinear part using the following relation:

$$A_n = \frac{1}{n!}\frac{\partial^n}{\partial \lambda^n}\left[f\left(\sum_{k=0}^{\infty} w_k \lambda^k\right)\right]_{\lambda=0}, \quad n = 0, 1, 2, \cdots. \tag{2.58}$$

2.3.1.1 Nanoswitch in Casimir regime

As mentioned in Section 2.2.1, cantilever micro- and nanobeams have been used widely in several NEMS and MESM. The static behavior of a cantilever nanoactuator operated in the van der Waals regime is investigated in Section 2.2.1. In this section, the static behavior of a cantilever nanoswitch is discussed by considering the impacts of the Casimir force. It worth noting that while avoiding the pull-in phenomenon is crucial for the appropriate operation of a micro- and nanoactuator, the pull-in instability organizes the application of nanoswitches. An image of a cantilever nanoswitch is illustrated in Fig. 2.7. A two-dimensional view of a cantilever nanoswitch is illustrated in Fig. 2.8. As can be seen, the nanoswitch is constructed from a nanobeam placed over a fixed plate with a gap. As a DC potential is applied to the nanobeam and the substrate, the attracting electrical force deflects the nanobeam. When the applied voltage is increased, the nanobeam deflection is enhanced. Then, at a critical voltage (i.e., the pull-in voltage), the elastic rigidity of the nanobeam fails to resist the electrical attracting force. Hence,

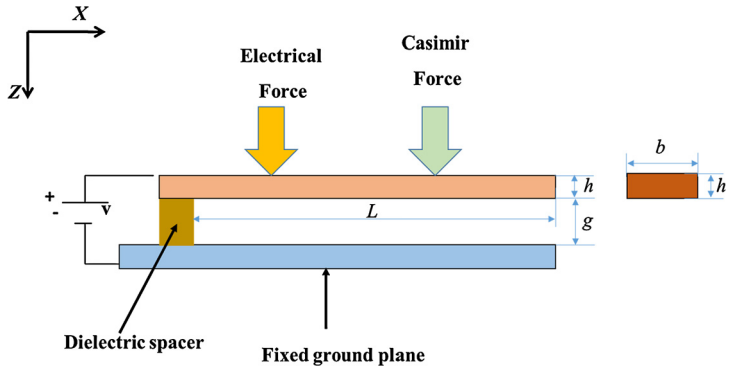

Figure 2.8 Two-dimensional view of a nanoswitch.

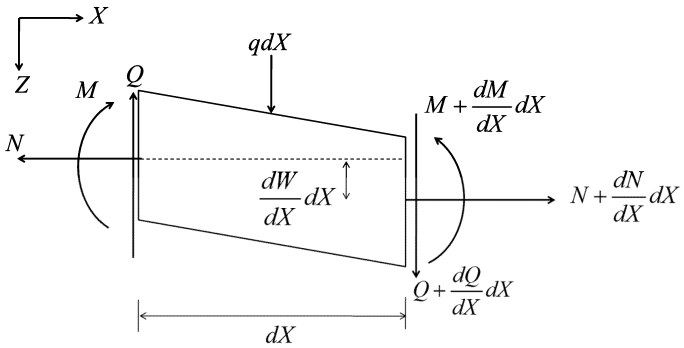

Figure 2.9 Forces and moments acting on an incrementing element of the beam.

the beam deflection increases with positive feedback, and the tip of the nanobeam will stick to the substrate. This phenomenon can be employed for current switching.

Similar to the nanoactuator, the moving part in a nanoswitch is modeled as an Euler–Bernoulli beam. The width, length, and thickness of the beam are b, L, and h, respectively. To extract the equation of a nanoswitch, the equilibrium for an incremental element is discussed. The forces and moments acting on an incrementing element with the length dx are illustrated in Fig. 2.9. The equilibriums of force and moment result in:

$$\frac{dQ}{dX} + q(X) = 0, \tag{2.59}$$

$$\frac{dM}{dX} - N\frac{dw}{dX} + Q = 0 \tag{2.60}$$

where N is the axial force, Q is the shear force, M is the bending moment, and $q(X)$ is the transverse force. Now, by differentiation Eq. (2.60) and using $\frac{dQ}{dX}$ from Eq. (2.59),

one obtains

$$\frac{d^2M}{dX^2} - \frac{d}{dX}\left(N\frac{dW}{dX}\right) - q(X) = 0. \tag{2.61}$$

The equation for the moment equilibrium yields

$$M = -\int_{-h/2}^{h/2} \sigma_{xx} z b dz. \tag{2.62}$$

By replacing the values for Eq. (2.19) in Eq. (2.62), the moment–displacement relation is obtained as

$$M = -EI\frac{d^2w}{dx^2}. \tag{2.63}$$

As no axial force is applied to the cantilever nanoswitch, the governing equation for the nanoswitch is obtained via assuming $N = 0$ and substituting Eq. (2.63) into Eq. (2.61) as follows:

$$\frac{d^2}{dX^2}\left(EI\frac{d^2W}{dX^2}\right) = q(X). \tag{2.64}$$

For the problem under study, the lateral force ($q(X)$) affects by the electrical field and Casimir force.

As mentioned in Section 2.2.1, the van der Waals force should be considered for separations less than 20 nm. However, for larger separations, the Casimir force is dominant [62]. The Casimir interaction between two conductive parallel plates is introduced in Chapter 1 (Eq. (1.7)). For a deflected nanoswitch, the separation gap should be replaced by $g - W$. Therefore, the Casimir force per unit length of a nanoswitch is obtained as

$$f_{Cas} = \frac{\pi^2 \hbar c b}{240(g - W)^4} \tag{2.65}$$

where $c = 2.998 \times 10^8$ ms^{-1} is the speed of light, and $\hbar = 1.055 \times 10^{-34}$ Js is the reduced Planck constant.

Since the nanoswitch has the same geometry as the studied nanoactuator (i.e., a rectangular cross-section beam parallel to a fixed plate), the electrical force is the same as that of the nanoactuator. Therefore, the electrical force acting on the nanoswitch can be obtained from Eq. (2.12). By replacing the values in Eqs. (2.12) and (2.65) into Eq. (2.64), the governing equation for a nanoswitch with a uniform cross-section constructed from an isotropic material is obtained as

$$EI\frac{d^4W}{dX^4} = \frac{\varepsilon_0 \varepsilon_r b V^2}{2(g - W)^2}\left[1 + 0.65\left(\frac{g - W}{b}\right)\right] + \frac{\pi^2 \hbar c b}{240(g - W)^4}. \tag{2.66}$$

We associate the following boundary conditions for a cantilever nanoswitch:

$$\begin{aligned} &W(0)=0, \quad \frac{dW}{dX}(0)=0, \\ &EI\frac{d^2W}{dX^2}(L)=0, \quad EI\frac{d^3W}{dX^3}(L)=0. \end{aligned} \tag{2.67}$$

By considering $w=W/g$, $x=X/L$, the dimensionless equation for the nanoactuator is defined as:

$$\frac{d^4w}{dx^4}=\frac{\beta_{Cas}}{(1-w)^4}+\frac{\alpha}{(1-w)^2}+\frac{\alpha\gamma}{(1-w)}, \tag{2.68}$$

$$\begin{aligned} &w(0)=0, \quad \frac{dw}{dx}(0)=0, \\ &\frac{d^2w}{dx^2}(1)=0, \quad \frac{d^3w}{dx^3}(1)=0 \end{aligned} \tag{2.69}$$

where

$$\beta_{Cas}=\frac{\pi^2\hbar cbL^4}{240g^5EI}, \tag{2.70}$$

$$\alpha=\frac{\varepsilon_0\varepsilon_r bV^2L^4}{2g^3EI}, \tag{2.71}$$

$$\gamma=0.65\frac{g}{b}. \tag{2.72}$$

In the above equation β_{Cas} is the dimensionless parameter of the Casimir force, α indicates the dimensionless parameter of the electrical force, and γ is related to the gap-to-width ratio which is associated with the fringing field effect.

Eq. (2.68) can be transformed to a system of integral equations by defining $y(x)=1-w(x)$:

$$\begin{aligned} y(x)&=y(0)+\int_0^x p_1(t)dt, \\ p_1(x)&=p_1(0)+\int_0^x p_2(t)dt, \\ p_2(x)&=p_2(0)+\int_0^x p_3(t)dt, \\ p_3(x)&=\int_0^x\left(\frac{\beta_{Cas}}{y(t)^4}+\frac{\alpha}{y(t)^2}+\frac{\alpha\gamma}{y(t)}\right)dt. \end{aligned} \tag{2.73}$$

The nonlinear term $\frac{\beta_{Cas}}{y^4}+\frac{\alpha}{y^2}+\frac{\alpha\gamma}{y}$ is deconstructed into a sum of Adomian polynomials, defined as:

$$
\begin{aligned}
A_0 &= \frac{\beta_{Cas}}{\gamma_0^4} + \frac{\alpha}{\gamma_0^2} + \frac{\alpha\gamma}{\gamma_0}, \\
A_1 &= -\frac{4\beta_{Cas}\gamma_1}{\gamma_0^5} - \frac{2\alpha\gamma_1}{\gamma_0^3} - \frac{\alpha\gamma\gamma_1}{\gamma_0^2}, \\
A_2 &= \frac{20\beta_{Cas}\gamma_1^2}{\gamma_0^6} - \frac{8\beta_{Cas}\gamma_2}{\gamma_0^5} + \frac{6\alpha\gamma_1^2}{\gamma_0^4} - \frac{4\alpha\gamma_2}{\gamma_0^3} + \frac{2\alpha\gamma\gamma_1^2}{\gamma_0^3} - \frac{2\alpha\gamma\gamma_2}{\gamma_0^2}, \\
&\ldots
\end{aligned}
\tag{2.74}
$$

By substituting Eq. (2.74) into Eq. (2.73), we have:

$$\gamma_0 = 1, \quad p_{1,0} = 0, \quad p_{2,0} = A, \quad p_{3,0} = B, \tag{2.75}$$

$$\gamma_1 = 0, \quad p_{1,1} = Ax, \quad p_{2,1} = Bx, \quad p_{3,1} = -(\beta_{Cas} + \alpha + \alpha\gamma)x, \tag{2.76}$$

$$\gamma_2 = \frac{Ax^2}{2}, \quad p_{1,2} = \frac{Bx^2}{2}, \quad p_{2,2} = -(\beta_{Cas} + \alpha + \alpha\gamma)\frac{x^2}{2}, \quad p_{3,2} = 0, \tag{2.77}$$

$$
\begin{aligned}
&\gamma_3 = \frac{Bx^3}{6}, \quad p_{1,3} = -(\beta_{Cas} + \alpha + \alpha\gamma)\frac{x^3}{6}, \quad p_{2,3} = 0, \\
&p_{3,3} = A(4\beta_{Cas} + 2\alpha + \alpha\gamma)\frac{x^3}{6},
\end{aligned}
\tag{2.78}
$$

$$
\begin{aligned}
&\gamma_4 = -(\beta_{Cas} + \alpha + \alpha\gamma)\frac{x^4}{24}, \quad p_{1,4} = 0, \quad p_{2,4} = A(4\beta_{Cas} + 2\alpha + \alpha\gamma)\frac{x^4}{24}, \\
&p_{3,4} = B(4\beta_{Cas} + 2\alpha + \alpha\gamma)\frac{x^4}{24},
\end{aligned}
\tag{2.79}
$$

$$
\begin{aligned}
&\gamma_5 = 0, \quad p_{1,5} = A(4\beta_{Cas} + 2\beta + \alpha\gamma)\frac{x^5}{120}, \\
&p_{2,5} = B(4\beta_{Cas} + 2\alpha + \alpha\gamma)\frac{x^5}{120}, \quad p_{3,5} = -C\frac{x^5}{20},
\end{aligned}
\tag{2.80}
$$

$$
\begin{aligned}
&\gamma_6 = A(4\beta_{Cas} + 2\alpha + \alpha\gamma)\frac{x^6}{720}, \quad p_{1,6} = B(4\beta_{Cas} + 2\alpha + \alpha\gamma)\frac{x^7}{5040}, \\
&p_{3,6} = -C\frac{x^6}{120}, \ldots
\end{aligned}
\tag{2.81}
$$

$$\gamma_7 = B(4\beta_{Cas} + 2\alpha + \alpha\gamma)\frac{x^7}{5040}, \quad p_{1,7} = -C\frac{x^6}{840}, \ldots, \tag{2.82}$$

$$\gamma_8 = -C\frac{x^8}{6720}, \ldots, \tag{2.83}$$

$$C = \left[A^2(10\beta_{Cas} + 3\alpha + \alpha\gamma) + \frac{(4\beta_{Cas} + 2\alpha + \alpha\gamma)(\beta_{Cas} + \alpha + \alpha\gamma)}{6}\right]. \tag{2.84}$$

Finally, the solution for Eq. (2.68) is obtained as:

$$w(x) = -\frac{Ax^2}{2!} - \frac{Bx^3}{3!} + (\beta_{Cas} + \alpha + \alpha\gamma)\frac{x^4}{4!} - (4\beta_{Cas} + 2\alpha + \alpha\gamma)\left[\frac{Ax^6}{6!} + \frac{Bx^7}{7!}\right]$$

Table 2.1 The nanoswitch tip displacement for different number of terms in the ADM series ($\beta_{Cas} = 0.3, \alpha = 0.2$, and $\gamma = 1$).

	w_{tip}	Error (%)
Four terms Adomian	0.0788	16.6
Six terms Adomian	0.1039	9.95
Seven terms Adomian	0.0890	5.82
Eight terms Adomian	0.0999	5.71
Nine terms Adomian	0.0909	3.80
Ten terms Adomian	0.0972	2.86
Numerical	0.0945	–

$$+\frac{\left[6A^2\left(10\beta_{Cas}+3\alpha+\alpha\gamma\right)+\left(4\beta_{Cas}+2\alpha+\alpha\gamma\right)\left(\beta_{Cas}+\alpha+\alpha\gamma\right)\right]x^8}{8!}+\ldots. \tag{2.85}$$

The unknown parameters A and B can be obtained by solving Eq. (2.85) with the boundary condition (i.e., Eq. (2.69)), which leads to:

$$\begin{cases} -A-B+\dfrac{\beta_{Cas}+\alpha+\alpha\gamma}{2}-\left(4\beta_{Cas}+2\alpha+\alpha\gamma\right)\left[\dfrac{A}{24}+\dfrac{B}{120}\right]+\dfrac{Cx^8}{120}+\ldots=0, \\ -B+\left(\beta_{Cas}+\alpha+\alpha\gamma\right)-\left(4\beta_{Cas}+2\alpha+\alpha\gamma\right)\left[\dfrac{Ax^6}{6}+\dfrac{Bx^7}{24}\right]+\dfrac{Cx^8}{20}+\ldots=0. \end{cases} \tag{2.86}$$

To validate the convergence of the Adomian decomposition, the tip deflection of the nanoswitch (w_{tip}) is calculated using Adomian decomposition and compared with the numerical solution stated in Table 2.1. As is revealed in Table 2.1, increasing the number of terms in the Adomian decomposition solution reduces the error in the obtained solution. By employing ten Adomian terms, the difference between the Adomian decomposition and the numerical data (i.e., error) is less than 3%, which is acceptable for many engineering applications.

The pull-in behavior occurs when the electrical and Casimir forces become more significant than the elastic resistance of the nanoswitch. When the force exceeds the pull-in threshold, the moving component of the nanoswitch sticks to the substrate. The pull-in voltage for a nanoswitch can be investigated via setting $dw(1)/d\alpha \to \infty$. The instability voltage of the nanoswitch for different Casimir parameters (β_{Cas}) is demonstrated in Fig. 2.10. As can be seen, increasing the Casimir force reduces the pull-in voltage of the nanoswitch. Also, this figure considers the impact of fringing as well. The line $\gamma = 0$ is related to neglecting the fringing field, while $\gamma = 1$ is relevant to considering the fringing effect. As seen by considering the fringing field effect, the pull-in voltage of the nanoswitch is reduced, which is due to increasing the electrical force as a result of the fringing field effect.

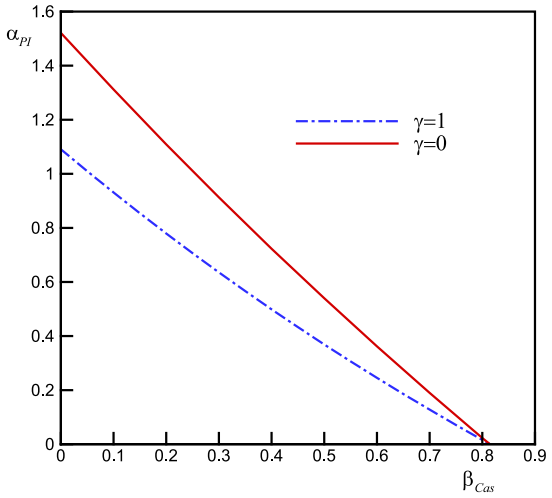

Figure 2.10 Impact of the Casimir force on the pull-in voltage of the nanoswitch.

2.3.2 Modified Adomian decomposition method

The Adomian decomposition method was modified by Wazwaz [63]. In this modification, the general solution for the linear equation (i.e., function f in Eq. (2.54)) is divided into two parts. The first part includes the zero component w_0, while the second part is associated with other terms, as stated in Eq. (2.87):

$$f = f_1 + f_2. \tag{2.87}$$

According to this modification, the improved recursive algorithm can be defined as:

$$\begin{aligned} u_0 &= f_1, \\ u_1 &= f_2 - L^{-1}(Rw_0) - L^{-1}(Nw_0), \\ u_{k+2} &= -L^{-1}(Rw_{k+1}) - L^{-1}(Nw_{k+1}), \quad k \geq 0. \end{aligned} \tag{2.88}$$

This modification is known as the modified Adomian decomposition method. Wazwaz showed that the convergence of the modified Adomian decomposition method is faster compared to the conventional Adomian decomposition method [63].

2.3.2.1 Size-dependent behavior of the NEMS with elastic boundary condition

Doubly supported MEMS/NEMS have been used widely in various ultrasmall structures such as resonators [64–66], switches [67,68], micromirrors [69–71], and mass sensors [72,73]. The SEM image and modeling two-dimensional view of a typical doubly-supported NEMS are illustrated in Figs. 2.11 and 2.12, respectively. The NEMS

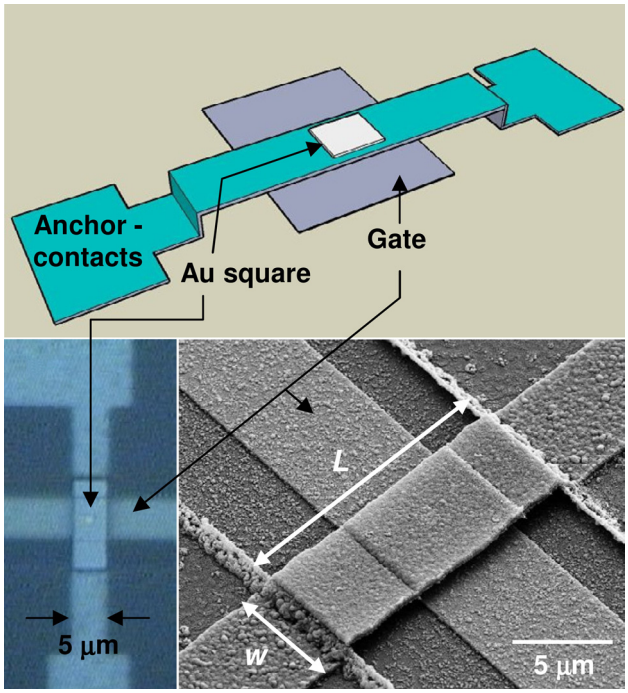

Figure 2.11 SEM image and cross-section view of doubly supported MEMS [72].

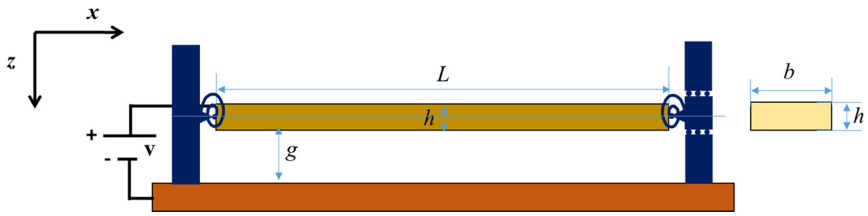

Figure 2.12 Schematic representation of the doubly-supported beam-type NEMS.

is modeled using a beam suspended over a fixed plate. While the beam geometry is similar to the illustrations in Section 2.3.1, its boundary conditions are different. The boundary condition can play a significant role in the mechanical performance of beam type NEMS/MEMS [20,74]. Although usually the classical boundary conditions, such as clamped and simply supported, are used for NEMS/MEMS simulation, the manufacturing technique at the micro- and nanoscale may not be capable of providing the ideal boundary condition. Therefore, modeling NEMS using classical boundary conditions, such as the clamped or simply-supported conditions, may yield undesirable simulation results. To avoid this inaccuracy in simulation, the theoretical measurement should be

incorporated with the experimental validation to modify the boundary conditions of beam type NEMS/MEMS [75]. The torsional springs can be used to simulate the rotation in the nonideal clamped supports. Therefore, two rotational springs are considered to simulate the nonclassical elastic supports of the nanobeam.

Instead of the nonclassical boundary conditions, we investigate the impact of the scale dependency on the static behavior of doubly-supported beam-type NEMS. Based on some experimental results, when the dimensions of the metal-manufactured structures are on the order of the internal material length scale, the material size dependency can substantially affect the material properties [76–78]. This phenomenon cannot be simulated using conventional continuum theory. To overcome this deficiency in conventional elasticity for simulation of the scale dependency, higher-order continuum theories were developed to consider the size-dependency in miniature structures. Modified couple stress theory is one of the most popular and practical size-dependent approaches. This size-dependent theory introduces only one additional material property to investigate the scale-dependent behavior of materials.

To derive the constitutive equation of the system, Hamilton's principle can be employed. To this end, firstly, the strain energy of the system should be computed. The stored energy of the doubly-supported NEMS is the sum of size-dependent strain energy and the potential energy of rotational springs. The size-dependent strain energy is dependent on both conventional stress tensor (σ_{ij}) and couple stress tensor (m_{ij}) in the context of the modified couple stress theory. Therefore, we have

$$U=\frac{1}{2}\int_0^L\int_A(\sigma_{ij}\varepsilon_{ij}+m_{ij}\chi_{ij})dAdX+\frac{1}{2}K_1\left(\frac{dW(0)}{dX}\right)^2+\frac{1}{2}K_2\left(\frac{dW(L)}{dX}\right)^2 \tag{2.89}$$

where ε_{ij} and χ_{ij} are the strain and curvature tensors, respectively. The parameters appearing in Eq. (2.89) can be determined using the following relations [79]:

$$m_{ij}=2l^2\mu\chi_{ij}, \tag{2.90}$$

$$\chi_{ij}=\frac{1}{2}\left((\nabla\theta)_{ij}+(\nabla\theta)_{ij}^T\right), \tag{2.91}$$

$$\theta_i=\frac{1}{2}(\nabla\times\vec{r})_i\,. \tag{2.92}$$

In these equations, l is an additional material length scale parameter introduced to model the size dependency. Moreover, r and θ are displacement and rotation vectors, respectively.

For an Euler–Bernoulli beam, the stress and strain are explained in Eqs. (2.18) and (2.19), respectively. By replacing the displacement field (Eq. (2.9)) in Eqs. (2.90)–(2.92)

the couple stress and curvature tensors are obtained as:

$$\chi_{XY} = \chi_{YX} = -\frac{1}{2}\frac{d^2W}{dX^2}, \tag{2.93}$$
$$\chi_{XX} = \chi_{YY} = \chi_{ZZ} = \chi_{YZ} = \chi_{ZY} = \chi_{XZ} = \chi_{ZX} = 0,$$

$$m_{XY} = m_{YX} = -\mu l^2\frac{d^2W}{dX^2}, \tag{2.94}$$
$$m_{XX} = m_{YY} = m_{ZZ} = m_{YZ} = m_{ZY} = m_{XZ} = m_{ZX} = 0.$$

Now, by substituting Eqs. (2.18), (2.19), (2.93), and (2.94) into Eq. (2.89), the strain energy (U) is summarized as:

$$\begin{aligned} U &= \frac{1}{2}\int_0^L \int_A \left\{-Z\frac{d^2W}{dX^2}\left(-ZE\frac{d^2W}{dX^2}\right) + \mu l^2\left(\frac{d^2W}{dX^2}\right)^2\right\} dA dX \\ &\quad + \frac{1}{2}K_1\left(\frac{dW(0)}{dX}\right)^2 + \frac{1}{2}K_2\left(\frac{dW(L)}{dX}\right)^2 \\ &= \frac{1}{2}\int_0^L \left\{EI\left(\frac{d^2W}{dX^2}\right)^2 + \mu l^2\left(\frac{d^2W}{dX^2}\right)^2\right\} dX + \frac{1}{2}K_1\left(\frac{dW(0)}{dX}\right)^2 + \frac{1}{2}K_2\left(\frac{dW(L)}{dX}\right)^2. \end{aligned} \tag{2.95}$$

Integrating the strain energy through the cross-section area results in

$$U = \frac{1}{2}\int_0^L \left\{EI\left(\frac{d^2W}{dX^2}\right)^2 + \mu l^2\left(\frac{d^2W}{dX^2}\right)^2\right\} dX + \frac{1}{2}K_1\left(\frac{dW(0)}{dX}\right)^2 + \frac{1}{2}K_2\left(\frac{dW(L)}{dX}\right)^2. \tag{2.96}$$

The work of the external force can be defined as

$$W_{ext} = \int_0^L q(X)w(X)dX. \tag{2.97}$$

The distributed external force ($q(X)$) per unit length can be obtained using Eqs. (2.12) and (2.65) as follows:

$$q(X) = f_{elec} + f_{Cas} = \frac{\varepsilon_0 b V^2}{2(g-W)^2}\left[1 + 0.65\left(\frac{g-W}{b}\right)\right] + \frac{\pi^2\hbar c b}{240(g-W)^4}. \tag{2.98}$$

To extract the system equation, one can employ Hamilton's principle:

$$\delta U - \delta W_{ext} = 0 \tag{2.99}$$

where δ denotes the variation symbol. Now, employing Eq. (2.99) in conjunction with Eqs. (2.95) and (2.97) results in

$$\int_0^L \left[(EI+\mu Al^2)\frac{d^4W}{dX^4} - q(X) \right] \delta W dX - (EI+\mu Al^2)\frac{d^3W}{dX^3}\delta W \Big|_0^L + (EI+\mu Al^2)\frac{d^2W}{dX^2}\delta\left(\frac{dW}{dX}\right)\Big|_0^L + K_1\frac{dW(0)}{dX}\delta\left(\frac{dW}{dX}\right) + K_2\frac{dW(L)}{dX}\delta\left(\frac{dW}{dX}\right) = 0. \tag{2.100}$$

Finally, the size-dependent governing equation and boundary condition for the doubly-supported beam-type NEMS is obtained as:

$$\left(EI+\mu Al^2\right)\frac{d^4w}{dX^4} = \frac{\varepsilon_0\varepsilon_r b V^2}{2(g-W)^2}\left[1+0.65\left(\frac{g-W}{b}\right)\right] + \frac{\pi^2\hbar c b}{240(g-W)^4}, \tag{2.101}$$

$$\begin{aligned} &W(0)=0,\\ &\left(EI+\mu Al^2\right)\frac{d^2W(0)}{dX^2} = K_1\frac{dW(0)}{dX},\\ &W(L)=0,\\ &\left(EI+\mu Al^2\right)\frac{d^2W(L)}{dX^2} = K_2\frac{dW(L)}{dX}. \end{aligned} \tag{2.102}$$

Using the dimensionless parameter $w = W/g$ and $x = X/L$, the dimensionless equation is determined as:

$$(1+\delta)\frac{d^4w}{dx^4} = \frac{\beta_{Cas}}{(1-w(x))^4} + \frac{\alpha}{(1-w(x))^2} + \frac{\alpha\gamma}{(1-w(x))}, \tag{2.103}$$

$$\begin{aligned} &w(0)=w(1)=0,\\ &w''(0)=\kappa_1 w'(0), \quad w''(1)=-\kappa_2 w'(1), \end{aligned} \tag{2.104}$$

where

$$\beta_{Cas} = \frac{\pi^2\hbar c b L^4}{240 g^5 EI}, \tag{2.105}$$

$$\alpha = \frac{\varepsilon_0\varepsilon_r b V^2 L^4}{2g^3 EI}, \tag{2.106}$$

$$\gamma = 0.65\frac{g}{b}, \tag{2.107}$$

$$\kappa_1 = \frac{K_1 L}{EI+\mu Al^2}, \tag{2.108}$$

$$\kappa_2 = \frac{K_2 L}{EI+\mu Al^2}, \tag{2.109}$$

$$\delta = \frac{\mu Al^2}{EI}. \tag{2.110}$$

In the above relations, κ_1 and κ_2 are dimensionless parameters associated with the spring constant at the nonclassical supports. Also, δ is the dimensionless parameter for incorpo-

rating the size effect. To simplify Eq. (2.103), the transformation $\gamma = 1 - w$ is employed. Therefore, the relation is changed to the following differential equation:

$$\frac{d^4\gamma}{dx^4} = -\frac{\beta_{Cas}}{(1+\delta)\gamma^4(x)} - \frac{\alpha}{(1+\delta)\gamma^2(x)} - \frac{\alpha\gamma}{(1+\delta)\gamma(x)}, \tag{2.111}$$

$$\begin{aligned} &\gamma(0) = \gamma(1) = 1, \\ &\gamma''(0) = K_1\gamma'(0), \\ &\gamma''(1) = -K_2\gamma'(1). \end{aligned} \tag{2.112}$$

To apply the modified Adomian decomposition method, a general, fourth-order boundary value problem is considered as follows:

$$\begin{aligned} &L^{(4)}[\gamma(x)] = N(x,\gamma), \quad 0 \le x \le L_b, \\ &\gamma(0) = C_1, \quad \gamma'(0) = C_2 \end{aligned} \tag{2.113}$$

where $L^{(4)}$ is the fourth-order differential operator and $L^{(-4)}$ is the fourth-order integrator operator:

$$L^{(4)} = \frac{d^4}{dx^4}(), \tag{2.114}$$

$$L^{(-4)} = \int_0^x \int_0^x \int_0^x \int_0^x () dx dx dx dx. \tag{2.115}$$

Based on the modified Adomian decomposition method, the solution for Eq. (2.111) can be rewritten as the following series:

$$\begin{aligned} \gamma(x) &= \sum_{n=0}^{\infty} \gamma_n(x) \\ &= C_1 + C_2 x + \frac{1}{2!}C_3 x^2 + \frac{1}{3!}C_4 x^3 \\ &\quad - \frac{1}{(1+\delta)} L^{(-4)} \left[\beta_{Cas} \sum_{n=0}^{\infty} N_{n,4}(x) + \alpha \sum_{n=0}^{\infty} N_{n,2}(x) + \alpha\gamma \sum_{n=0}^{\infty} N_{n,1}(x) \right]. \end{aligned} \tag{2.116}$$

The nonlinear function $N_k(x,\gamma)$, which approximates the γ^{-k} term, is represented as a series of Adomian polynomials:

$$N_k(x,\gamma) = \sum_{n=0}^{\infty} N_{n,k}(x). \tag{2.117}$$

Now, according to [80,81], this series of Adomian polynomial can further be presented as

$$N_{n,k} = \sum_{\nu=1}^{n} C(\nu, n) h_\nu(g_0) \tag{2.118}$$

where

$$C(v,n)=\sum_{p_i}\prod_{i=1}^{v}\frac{1}{k!}g_{p_i}^{k_i},$$
$$\sum_{i=1}^{v}k_ip_i=n,\quad n>0,\ 0\le i\le n,\quad 1\le p_i\le n-v+1, \tag{2.119}$$
$$h_v(g_0)=\frac{d^v}{dg^v}[f(g(\lambda))]_{\lambda=0}.$$

Finally, the Adomian polynomials are obtained as:

$$\begin{aligned}
&N_{0,k}=\gamma_0^{-k},\\
&N_{1,k}=-k\gamma_1\gamma_0^{-k-1},\\
&N_{2,k}=-k\gamma_2\gamma_0^{-k-1}+\frac{k(k+1)}{2!}\gamma_1^2\gamma_0^{-k-2},\\
&N_{3,k}=-k\gamma_3\gamma_0^{-k-1}+k(k+1)\gamma_1\gamma_2\gamma_0^{-k-2}+\frac{k(k+1)(k+2)}{3!}\gamma_1^3\gamma_0^{-k-3},\\
&\cdots
\end{aligned} \tag{2.120}$$

By substituting relations in (2.120) into Eq. (2.116), we obtain:

$$\gamma_0=1, \tag{2.121}$$
$$\gamma_1=C_1+C_2x+\frac{1}{2!}C_3x^2+\frac{1}{3!}C_4x^3-\frac{1}{(1+\delta)4!}(\beta_{Cas}+\alpha+\alpha\gamma)x^4, \tag{2.122}$$
$$\gamma_2=\frac{4\beta_{Cas}+2\alpha+\alpha\gamma}{(1+\delta)}\left(\frac{1}{4!}C_1x^4+\frac{1}{5!}C_2x^5+\frac{1}{6!}C_3x^6+\frac{1}{7!}C_4x^7-\frac{\beta_{Cas}+\alpha+\alpha\gamma}{(1+\delta)8!}x^8\right), \tag{2.123}$$
$$\begin{aligned}
\gamma_3=&-\frac{C_1^2}{(1+\delta)4!}(10\beta_{Cas}+3\alpha+\alpha\gamma)x^4-\frac{2C_1C_2}{(1+\delta)5!}(10\beta_{Cas}+3\alpha+\alpha\gamma)x^5\\
&-\frac{2C_1C_3+2C_2^2}{(1+\delta)6!}(10\beta_{Cas}+3\alpha+\alpha\gamma)x^6-\frac{2C_1C_4+6C_2C_3}{(1+\delta)7!}(10\beta_{Cas}+3\alpha+\alpha\gamma)x^7\\
&+\frac{1}{(1+\delta)8!}\left[\begin{array}{l}\dfrac{C_1(4\beta_{Cas}+2\alpha+\alpha\gamma)^2}{1+\delta}\\ +\left(\dfrac{2C_1(\beta_{Cas}+2\alpha+\alpha\gamma)}{1+\delta}-8C_2C_4-6C_3^2\right)(10\beta_{Cas}+3\alpha+\alpha\gamma)\end{array}\right]x^8\\
&+\frac{1}{(1+\delta)9!}\left[\begin{array}{l}\dfrac{C_2(4\beta_{Cas}+2\alpha+\alpha\gamma)^2}{1+\delta}\\ +\left(\dfrac{10C_2(\beta_{Cas}+2\alpha+\alpha\gamma)}{1+\delta}-20C_3C_4\right)(10\beta_{Cas}+3\alpha+\alpha\gamma)\end{array}\right]x^9
\end{aligned}$$

$$+\frac{1}{(1+\delta)10!}\left[\begin{array}{l}\dfrac{C_3(4\beta_{Cas}+2\alpha+\alpha\gamma)^2}{1+\delta}\\ +\left(\dfrac{30C_3(\beta_{Cas}+2\alpha+\alpha\gamma)}{1+\delta}-20C_4^2\right)(10\beta_{Cas}+3\alpha+\alpha\gamma)\end{array}\right]x^{10}$$
$$+\frac{1}{(1+\delta)^2 11!}\left[C_4(4\beta_{Cas}+2\alpha+\alpha\gamma)^2-35C_4(\beta_{Cas}+\alpha+\alpha\gamma)(20\beta_{Cas}+3\alpha+\alpha\gamma)\right]x^{11}$$
$$+\frac{1}{(1+\delta)^3 12!}\left[\begin{array}{l}(\beta_{Cas}+2\alpha+\alpha\gamma)(4\beta_{Cas}+2\alpha+\alpha\gamma)^2\\ -70(\beta_{Cas}+\alpha+\alpha\gamma)^2(10\beta_{Cas}+3\alpha+\alpha\gamma)\end{array}\right]x^{12}. \tag{2.124}$$

Using the above relations, the solution for Eq. (2.103) is summarized as:

$$w(x)=-C_1-C_2x-\frac{1}{2!}C_3x^2-\frac{1}{3!}C_4x^3$$
$$+\frac{1}{(1+\delta)4!}[(\beta_{Cas}+\alpha+\alpha\gamma)-(4\beta_{Cas}+2\alpha+\alpha\gamma)C_1+(10\beta_{Cas}+3\alpha+\alpha\gamma)C_1^2]x^4$$
$$+\frac{1}{(1+\delta)5!}[2C_1C_2(10\beta_{Cas}+3\alpha+\alpha\gamma)-(4\beta_{Cas}+2\alpha+\alpha\gamma)]x^5$$
$$+\frac{1}{(1+\delta)6!}[(2C_1C_3+2C_2^2)(10\beta_{Cas}+3\alpha+\alpha\gamma)-C_3(4\beta_{Cas}+2\alpha+\alpha\gamma)]x^6$$
$$+\frac{1}{(1+\delta)7!}[(2C_1C_4+6C_2C_3)(10\beta_{Cas}+3\alpha+\alpha\gamma-C_4(4\beta_{Cas}+2\alpha+\alpha\gamma))]x^7$$
$$-\frac{1}{(1+\delta)8!}\left[\begin{array}{l}\dfrac{C_1(4\beta_{Cas}+2\alpha+\alpha\gamma)^2}{1+\delta}\\ +\left(\dfrac{2C_1(\beta_{Cas}+2\alpha+\alpha\gamma)}{1+\delta}-8C_2C_4-6C_3^2\right)(10\beta_{Cas}+3\alpha+\alpha\gamma)\end{array}\right]x^8$$
$$-\frac{1}{(1+\delta)9!}\left[\begin{array}{l}\dfrac{C_2(4\beta_{Cas}+2\alpha+\alpha\gamma)^2}{1+\delta}\\ +\left(\dfrac{10C_2(\beta_{Cas}+2\alpha+\alpha\gamma)}{1+\delta}-20C_3C_4\right)(10\beta_{Cas}+3\alpha+\alpha\gamma)\end{array}\right]x^9$$
$$-\frac{1}{(1+\delta)10!}\left[\begin{array}{l}\dfrac{C_3(4\beta_{Cas}+2\alpha+\alpha\gamma)^2}{1+\delta}\\ +\left(\dfrac{30C_3(\beta_{Cas}+2\alpha+\alpha\gamma)}{1+\delta}-20C_4^2\right)(10\beta_{Cas}+3\alpha+\alpha\gamma)\end{array}\right]x^{10}$$
$$-\frac{1}{(1+\delta)^2 11!}[C_4(4\beta_{Cas}+2\alpha+\alpha\gamma)^2-35C_4(\beta_{Cas}+\alpha+\alpha\gamma)(20\beta_{Cas}+3\alpha+\alpha\gamma)]x^{11}$$
$$-\frac{1}{(1+\delta)^3 12!}\left[\begin{array}{l}(\beta_{Cas}+2\alpha+\alpha\gamma)(4\beta_{Cas}+2\alpha+\alpha\gamma)^2\\ -70(\beta_{Cas}+\alpha+\alpha\gamma)^2(10\beta_{Cas}+3\alpha+\alpha\gamma)\end{array}\right]x^{12}$$
$$+\ldots \tag{2.125}$$

where C_i $(i = 1, 2, 3, 4)$ constants can be determined through boundary conditions (i.e., Eq. (2.112)).

To examine the pull-in performance of NEMS, three cases with classical boundary conditions, including doubly-clamped ($\kappa_1 = \infty$, $\kappa_2 = \infty$), clamped–hinged ($\kappa_1 = \infty$, $\kappa_2 = 0$), and hinged–hinged ($\kappa_1 = 0$, $\kappa_2 = 0$) were investigated. Fig. 2.13 demonstrates the deflection of these cases for different size dependency parameters at the pull-in point. As can be vividly seen, the pull-in voltage of the nanostructure is affected by the scale-dependency. For instance, when the size-dependency dimensionless parameter δ is 0.5, the pull-in voltage dimensionless parameter is twice the parameters obtained via classical elasticity (i.e., neglecting the size-dependency). Nevertheless, the pull-in deflection does not change significantly by considering the size-dependency.

Fig. 2.14 depicts the influence of the boundary conditions on the instability voltage. As can be seen, restricting the boundary conditions increases the NEMS pull-in voltage.

2.3.3 Comparison between the conventional and modified Adomian decomposition methods

The concepts of conventional and modified Adomian decomposition method are presented in Sections 2.3.1 and 2.3.2, respectively. Although both methods are based on the Adomian polynomials, their convergence rates are different [63,82–84]. In this section, the pull-in parameters of the nanoactuator operated in van der Waals regime with two different boundary conditions are investigated by using both conventional and modified Adomian decomposition methods, and their solutions are compared.

The dimensionless governing equation of a nanoactuator in van der Waals force is extracted in Eq. (2.25). In this section, the pull-in performances of clamped-free and clamped–clamped nanoactuators are investigated. The boundary condition for clamped-free is expressed in Eq. (2.26). For the clamped–clamped nanoactuator, the deflection and rotation at both ends are restricted. Therefore, the dimensionless boundary conditions for a clamped–clamped nanoactuator are given as:

$$\begin{aligned} w(0) &= 0, \quad \frac{dw}{dx}(0) = 0, \\ w(1) &= 0, \quad \frac{dw}{dx}(1) = 0. \end{aligned} \tag{2.126}$$

By considering $\gamma(x) = 1 - w(x)$, the dimensionless governing equation of nanoactuator can be rewritten as:

$$\frac{d^4\gamma}{dx^4} + \frac{\beta_{vdW}}{\gamma^3} + \frac{\alpha}{\gamma^2} + \frac{\alpha\gamma}{\gamma} = 0. \tag{2.127}$$

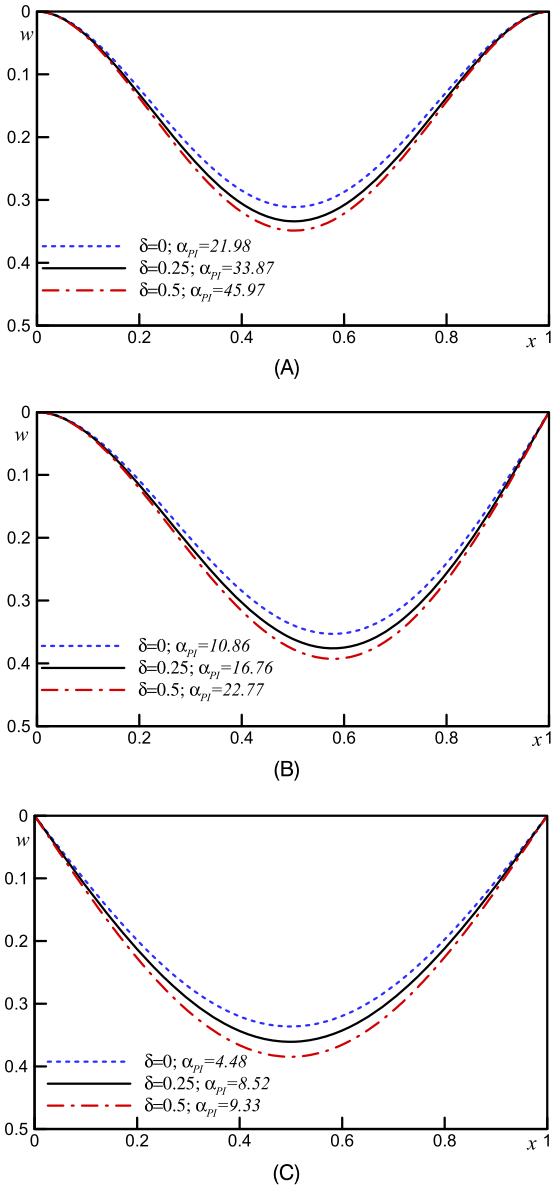

Figure 2.13 Size-dependent deflection on NEMS at pull-in point: (A) doubly-clamped, (B) clamped–hinged, and (C) hinged–hinged.

Furthermore, the boundary condition for a clamped-free nanoactuator is defined as:

$$y(0) = 1, \quad \frac{dy}{dx}(0) = 0,$$

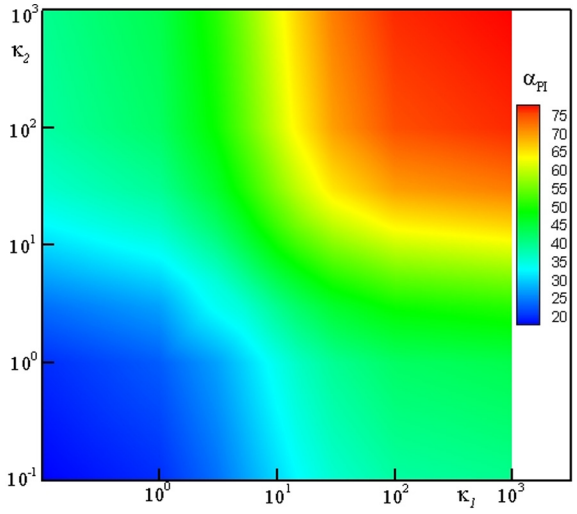

Figure 2.14 Impact of boundary condition on the pull-in voltage.

$$\frac{d^2\gamma}{dx^2}(1) = 0, \quad \frac{d^3\gamma}{dx^3}(1) = 0. \tag{2.128}$$

Similarly, the new boundary condition for a clamped–clamped nanoactuator is given as:

$$\begin{aligned} \gamma(0) &= 1, \quad \frac{d\gamma}{dx}(0) = 0, \\ \gamma(1) &= 1, \quad \frac{d\gamma}{dx}(1) = 0. \end{aligned} \tag{2.129}$$

Following the procedure mentioned in Section 2.3.1, the deflection of a nanoactuator by using the conventional Adomian decomposition method is obtained as:

$$\begin{aligned} w(x) = &-\frac{C_1x^2}{2!} - \frac{C_2x^3}{3!} + (\beta_{vdW} + \alpha + \alpha\gamma)\frac{x^4}{4!} - (3\beta_{vdW} + 2\alpha + \alpha\gamma)\frac{C_1x^6}{6!} \\ &- (3\beta_{vdW} + 2\alpha + \alpha\gamma)\frac{C_2x^7}{7!} \\ &+ \left[C_1^2(6\beta_{vdW} + 3\alpha + \alpha\gamma) + \frac{(3\beta_{vdW} + 2\alpha + \alpha\gamma)(\beta_{vdW} + \alpha + \alpha\gamma)}{6}\right]\frac{x^8}{8!} + \ldots. \end{aligned} \tag{2.130}$$

Similarly, the deflection of a nanoactuator by using the modified Adomian decomposition method can be obtained by using the procedure mentioned in Section 2.3.2 as follows:

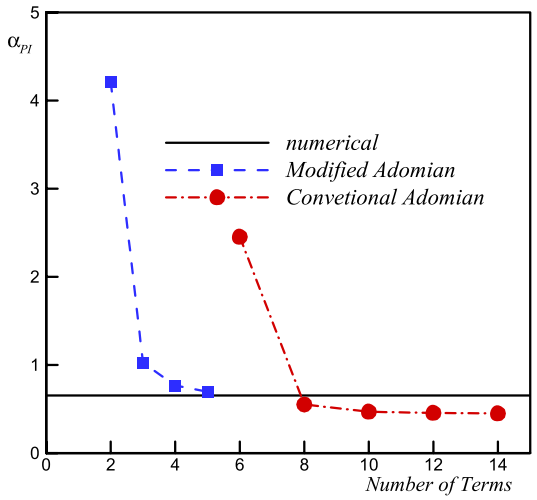

Figure 2.15 Pull-in voltage of a clamped-free nanoswitch for the different number of terms in conventional and modified Adomian decomposition methods.

$$
\begin{aligned}
w(x) = &-\frac{1}{2!}C_1x^2 - \frac{1}{3!}C_2x^3 + \frac{1}{4!}(\beta_{vdW}+\alpha+\alpha\gamma)x^4 - \frac{C_1}{6!}(3\beta_{vdW}+2\beta\alpha+\alpha\gamma)x^6 \\
&- \frac{C_2}{7!}(3\beta_{vdW}+2\alpha+\alpha\gamma)x^7 + \frac{20C_1C_2}{9!}(6\beta_{vdW}+3\alpha+\alpha\gamma)x^9 \\
&+ \frac{1}{8!}\left[6C_1^2(6\beta_{vdW}+3\alpha+\alpha\gamma) + (\beta_{vdW}+\alpha+\alpha\gamma)(3\beta_{vdW}+2\alpha+\alpha\gamma)\right]x^8 \\
&- \frac{1}{10!}\left[(3\beta_{vdW}+2\alpha+\alpha\gamma)^2C_1 + (\beta_{vdW}+\alpha+\alpha\gamma)(6\beta_{vdW}+3\alpha+\alpha\gamma)(30C_1-20C_2^2)\right]x^{10} \\
&- \frac{1}{11!}\left[(3\beta_{vdW}+2\alpha+\alpha\gamma)^2C_2 + 70C_2(\beta_{vdW}+\alpha+\alpha\gamma)(6\beta_{vdW}+3\alpha+\alpha\gamma)\right]x^{11} + \ldots .
\end{aligned}
\tag{2.131}
$$

The pull-in voltage of a nanoactuator for the different number of series terms in the conventional and modified Adomian decomposition solutions is presented in Fig. 2.15. This figure demonstrates that the modified Adomian solution converges to the numerical solution quickly. In addition, the conventional Adomian decomposition method converges to a pull-in value, which is lower than the pull-in voltage obtained numerically. Fig. 2.16 demonstrates the tip deflection of nanoactuator at the pull-in voltage (i.e., the pull-in deflection) from the different number of terms in the conventional and modified Adomian decomposition methods. This figure reveals that the modified Adomian decomposition method not only predicts the pull-in deflation more accurately than the conventional Adomian decomposition method but also converges faster to the numerical pull-in deflection.

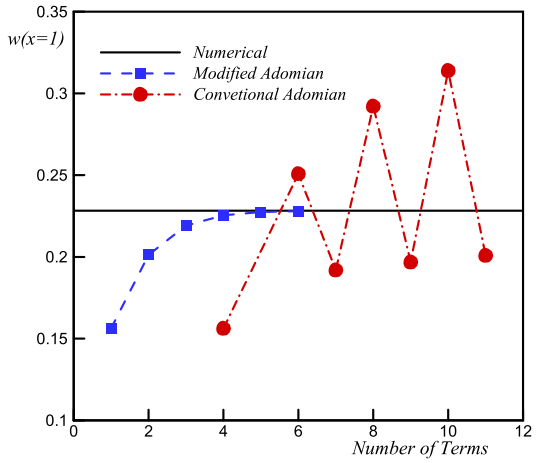

Figure 2.16 Pull-in deflection of clamped-free nanoswitch for the different number of terms in conventional and modified Adomian decomposition methods.

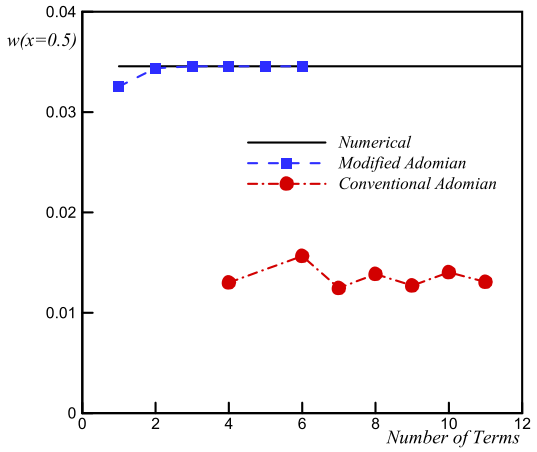

Figure 2.17 The maximum deflection of a clamped–clamped nanoswitch for the different number of terms in conventional and modified Adomian decomposition methods.

In the case of the clamped-clamped nanoactuator, while both conventional and modified Adomian decomposition methods can investigate the actuator deflection below the pull-in voltage, the conventional Adomian decomposition method is not able to capture the pull-in voltage of the clamped–clamped nanoactuator.

Fig. 2.17 shows the variation of maximum deflection of a clamped–clamped nanoactuator (i.e., $w(x = 0.5)$). In this figure, the dimensionless parameters of the electrical and van der Waals forces are assumed to be 5 ($\alpha = \beta_{vdW} = 5$), and the gap is 1.3 times of

Table 2.2 Pull-in voltage of a typical clamped–clamped nanoactuator for different numbers of modified Adomian decomposition terms.

	Pull-in voltage (α_{PI})				
	2 Terms	**3 Terms**	**4 Terms**	**5 Terms**	**6 Terms**
Modified Adomian decomposition method	Cannot determine pull-in	61.701	Cannot determine pull-in	45.298	Cannot determine pull-in
The difference with numerical (%)	Cannot determine pull-in	41.6	Cannot determine pull-in	3.95	Cannot determine pull-in

the actuator width (i.e., $\gamma = 0.5$). This figure demonstrates that while the modified Adomian series converges rapidly to the numerical solution, the conventional series converges to an unacceptable value.

Table 2.2 shows the pull-in voltage of a typical clamped–clamped NEMS obtained by the modified Adomian decomposition method using various number of series terms. As seen, the modified Adomian decomposition solution converges to the numerical value, i.e., $\alpha_{PI} = 43.575$. Since the conventional Adomian decomposition method is not reliable for simulating a clamped–clamped nanoactuator, only the pull-in voltages obtained by the modified method are presented in Table 2.2. This table also reveals that the modified Adomian decomposition with two, four, and six terms cannot predict the pull-in behavior. Thus, selecting the appropriate number of series terms is crucial in the modified Adomian decomposition solution.

2.4. Green's function methods

2.4.1 General Green's function

Using Green's function is a useful method to investigate the beam deflection under an arbitrary load condition. Therefore, this method can be employed to simulate beam-type NEMS and MEMS behavior. According to this method, the concentrated load response is employed for investigating the system performance under an arbitrary load [25].

Considering Eq. (2.64), the dimensionless equation for a beam-type NEMS constructed from isotropic materials with uniform cross-section can be explained as

$$\frac{d^4w}{dx^4} = q(x) \tag{2.132}$$

where $q(x)$ is the dimensionless external force. Now, by replacing $q(x)$ with $\delta(x-\xi)$, the differential equation of a beam with a unit concentrated load at $x=\xi$ is obtained as

$$\frac{d^4G}{dx^4} = \delta(x-\xi). \tag{2.133}$$

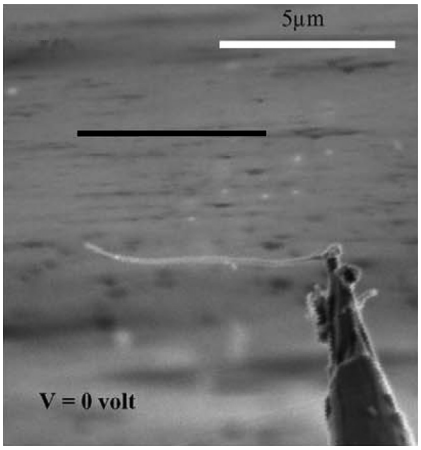

Figure 2.18 Freestanding carbon nanotube [90].

The following Green's function is a solution for the above differential equation:

$$G(x) = \begin{cases} a_0x^3 + a_1x^2 + a_2x + a_3, & 0 \le x < \xi, \\ b_0x^3 + b_1x^2 + b_2x + b_3, & \xi \le x < 1. \end{cases} \tag{2.134}$$

Therefore, the solution for the Eq. (2.132) is

$$w(x) = \int_0^1 G(x, \xi) \cdot q(\xi) d\xi. \tag{2.135}$$

The above procedure can be used for investigating the deflection of beam type MEMS/NEMS.

2.4.1.1 Carbon-nanotube actuator close to graphite sheets

Owing to their extraordinary mechanical properties, carbon nanotubes have potential to be used in many different application of NEMS, such as atomic force microscope probes [85,86], nanosensors [87–89], nanomanipulators [90], nanotweezers [86,91,92], nanoactuators [93], and nanoswitches [94,95].

Fig. 2.18 shows a SEM image of a freestanding carbon-nanotube. The simulation model of a carbon nanotube over graphene sheets is illustrated in Fig. 2.19. The actuator is an N_W walled MWCNT with length L. The mean radius of the CNTs is R_W, and the initial distance between the MWCNT and the graphite plate is D.

Lennard-Jones potential is an efficient method to investigate the van der Waals force between two bodies. Based on this technique, Dequesnes et al. [96] developed a continuum approach to examine the van der Waals force between MWCNT and a plate.

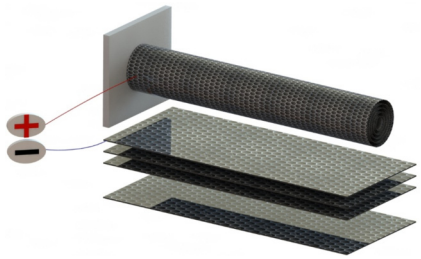

Figure 2.19 Carbon nanotube actuator over a graphene sheet.

Using this continuum method, the van der Waals force per unit length for the nanotube (f_{vdW}) is determined as [96]

$$f_{vdW}(r) = 4C_6\sigma^2\pi^2 N_W R_W \sum_{r=D}^{D+(N-1)d} \frac{1}{r^5} \tag{2.136}$$

where $C_6 = 15.2$ eVÅ^6 is the carbon–carbon interaction attracting constant and $\sigma \approx 38$ nm^{-2} is the graphene surface density [25].

When the graphite sheet has multiple graphene layers, the sum in Eq. (2.136) can be approximated using an integral as follows:

$$\sum_{r=D}^{D+(N-1)d} \frac{1}{r^5} \approx \frac{1}{d}\int_{D}^{D+(N-1)d} \frac{1}{r^5}dr = \frac{1}{4d}\left[\frac{1}{D^4} - \frac{1}{(D+(N-1)d)^4}\right] \approx \frac{1}{4dD^4}. \tag{2.137}$$

By substituting the above approximation in Eq. (2.136), the van der Waals force between carbon nanotube and graphene substrate is determined as

$$f_{vdW}(D) \approx C_6\sigma^2\pi^2 N_W R_W d^{-1} D^{-4}. \tag{2.138}$$

Moreover, if the number of layers is low, r can be replaced with $D + Nd/2 + id$. Therefore, by considering $D + Nd/2 \pm id \approx D + Nd/2$,

$$\sum_{r=D}^{D+(N-1)d} \frac{1}{r^5} = \sum_{i=-N/2}^{N/2} \frac{1}{(D+Nd/2+id)^5} \approx \frac{N}{(D+Nd/2)^5}. \tag{2.139}$$

The van der Waals attraction deflects the nanotube towards the graphene plate, reducing their displacement to $D - w$. Therefore, if the nanotube diameter is negligible in comparison with the initial gap between the nanotube and graphite plate, the van der

Waals force is defined as

$$f_{vdW} = \begin{cases} \dfrac{C_6\sigma^2\pi^2 N_W R_W}{d(D-W)^4} & \text{for large number of graphene layers,} \\ \dfrac{4C_6\sigma^2\pi^2 N N_W R_W}{(D-W+Nd/2)^5} & \text{for small number of graphene layers.} \end{cases} \tag{2.140}$$

By using Eq. (2.140) in Eq. (2.132), the equation on the cantilever MWCNT actuator is obtained as:

$$EI\frac{d^4\hat{W}}{dX^4} = \begin{cases} \dfrac{C_6\sigma^2\pi^2 N_W R_W}{d(D-W)^4} & \text{for large number of layers } (n=4), \\ \dfrac{4C_6\sigma^2\pi^2 N N_W R_W}{(D-W+Nd/2)^5} & \text{for small number of layers } (n=5), \end{cases} \tag{2.141}$$

$$W(0) = \frac{dW}{dX}(0) = 0, \tag{2.142}$$

$$\frac{d^2W}{dX^2}(L) = \frac{d^3W}{dX^3}(L) = 0. \tag{2.143}$$

The following replacements can be employed to extract the dimensionless form of Eqs. (2.141) to (2.143):

$$x = \frac{X}{L}, \tag{2.144}$$

$$w = \begin{cases} \dfrac{W}{D} & \text{for large number of layers } (n=4), \\ \dfrac{W}{D+Nd/2} & \text{for small number of layers } (n=5), \end{cases} \tag{2.145}$$

$$\beta_n = \begin{cases} \dfrac{C_6\sigma^2\pi^2 N_W L^4}{dEID^4} & \text{for large number of layers } (n=4), \\ \dfrac{4C_6\sigma^2\pi^2 N N_W R_W L^4}{EI(D+Nd/2)^6} & \text{for small number of layers } (n=5) \end{cases} \tag{2.146}$$

where β_n indicates the dimensionless parameter of van der Waals force. These transformations yield:

$$\frac{d^4w}{dx^4} = \frac{\beta_n}{(1-w(x))^n}, \tag{2.147}$$

$$w(0) = \frac{dw}{dx}(0) = 0, \tag{2.148}$$

$$\frac{d^2w}{dx^2}(1) = \frac{d^3w}{dx^3}(1) = 0. \tag{2.149}$$

To solve the nonlinear differential equation of MWCNT, the Green's function of Eq. (2.134) is considered. By applying the boundary conditions (i.e., Eqs. (2.148) and

(2.149)), the number of unknown parameters in Green's function (Eq. (2.134)) is reduced from 8 to 4 as follows:

$$G(x) = \begin{cases} a_0 x^3 + a_1 x^2, & 0 \le x < \xi, \\ b_2 x + b_3, & \xi \le x < 1. \end{cases} \tag{2.150}$$

The unknown parameters a_0, a_1, b_2, and b_3 are determined by considering the compatibility condition. In other words, the solution and its first and second derivatives should be continuous at $x = \xi$:

$$\begin{aligned} &G(\xi^-) = G(\xi^+) \\ &\frac{dG}{dx}(\xi^-) = \frac{dG}{dx}(\xi^+), \\ &\frac{d^2G}{dx^2}(\xi^-) = \frac{d^2G}{dx^2}(\xi^+). \end{aligned} \tag{2.151}$$

Besides, integrating Eq. (2.133) results in

$$\frac{d^3G}{dx^3}(\xi^+) - \frac{d^3G}{dx^3}(\xi^-) = 1. \tag{2.152}$$

Using Eqs. (2.151) and (2.152), the remaining unknown parameters in the Green's function are defined as:

$$\begin{aligned} &a_0 = -\frac{1}{6}, \quad a_1 = \frac{\xi}{2}, \\ &b_2 = \frac{\xi^2}{2}, \quad b_3 = -\frac{\xi^3}{6}. \end{aligned} \tag{2.153}$$

Replacing Eq. (2.153) in Eqs. (2.156) yields

$$G(x,\xi) = \begin{cases} \frac{x^2}{6}(3\xi - x), & 0 \le x < \xi, \\ \frac{\xi^2}{6}(3x - \xi), & \xi \le x < 1. \end{cases} \tag{2.154}$$

Using Eq. (2.154), dimensionless deflection of the carbon nanotube actuator can be determined as

$$w(\xi) = \int_0^1 G(x,\xi) \cdot \frac{\beta_n}{(1 - w(x))^n} dx. \tag{2.155}$$

In this equation, $G(x,\xi)$ is a symmetric function of ζ and x. Therefore, Eq. (2.155) can be rewritten as

$$w(x) = \int_0^1 G(x,\xi) \cdot \frac{\beta_n}{(1 - w(\xi))^n} dx. \tag{2.156}$$

The actuator deflection can be estimated using the following function that satisfies the boundary conditions:

$$w(x) = w_0 x^2 \tag{2.157}$$

where w_0 is the maximum actuator bending at its free end (i.e., $w(x=1)$). To investigate the behavior of the nanoactuator, the unknown parameter w_0 in Eq. (2.157) should be determined. By considering $x=1$ in Eq. (2.156), we have

$$w_0 = w(x=1) = \int_0^1 G(x=1,\xi)\cdot\frac{\beta_n}{(1-w(\xi))^n}d\xi = \int_0^1 \frac{\xi^2(3-\xi)}{6}\cdot\frac{\beta_n}{(1-w_0\xi^2)^n}d\xi. \tag{2.158}$$

The deflection for the nanoactuator can be achieved through evaluating the integral in Eq. (2.158) and solving the obtained equation for w_0. By solving Eq. (2.158) for α_n, the following equations are obtained:

$$\beta_4 = \frac{288w_0^2}{\frac{-5w_0^2+12w_0+9}{(1-w_0)^3} - 9\frac{\tanh^{-1}(\sqrt{w_0})}{\sqrt{w_0}}} \quad \text{(for large number of layers)}, \tag{2.159}$$

$$\beta_5 = \frac{768w_0^2}{\frac{29w_0^3-101w_0^2+123w_0+45}{(1-w_0)^4} - 15\frac{\tanh^{-1}(\sqrt{w_0})}{\sqrt{w_0}}} \quad \text{(for small number of layers)}. \tag{2.160}$$

The critical van der Waals force can be obtained from Eqs. (2.159) and (2.160) by choosing $d\beta_n/dw_0 = 0$, which results in $\beta_4 = 1.025$ and $\beta_5 = 0.84$. It should be noted that these critical values are related to the maximum allowable length of the nanobeam, and the lowest allowable initial gap between the actuator and graphite sheet. For the nanotube length larger than the detachment length, for the initial gap smaller than the permissible value or both, the probe collapses into the substrate due to van der Waals attraction, even without external force. The lowest permissible gap and the maximum length can be obtained using the following relations:

$$D_{min} = \begin{cases} \sqrt[5]{\dfrac{0.976C_6\sigma^2\pi N_W L^4}{dEtR_w^2}}, & n=4, \\ \sqrt[6]{\dfrac{4.756C_6\sigma^2\pi NN_W L^4}{EtR_w^2}} - \dfrac{Nd}{2}, & n=5, \end{cases} \tag{2.161}$$

$$L_{\max} = \begin{cases} \sqrt[4]{\dfrac{1.025dEtR_w^2D^5}{C_6\sigma^2\pi N_W}}, & n=4, \\ \sqrt[4]{\dfrac{0.210EtR_w^2(D+Nd/2)^6}{C_6\sigma^2\pi NN_W}}, & n=5. \end{cases} \tag{2.162}$$

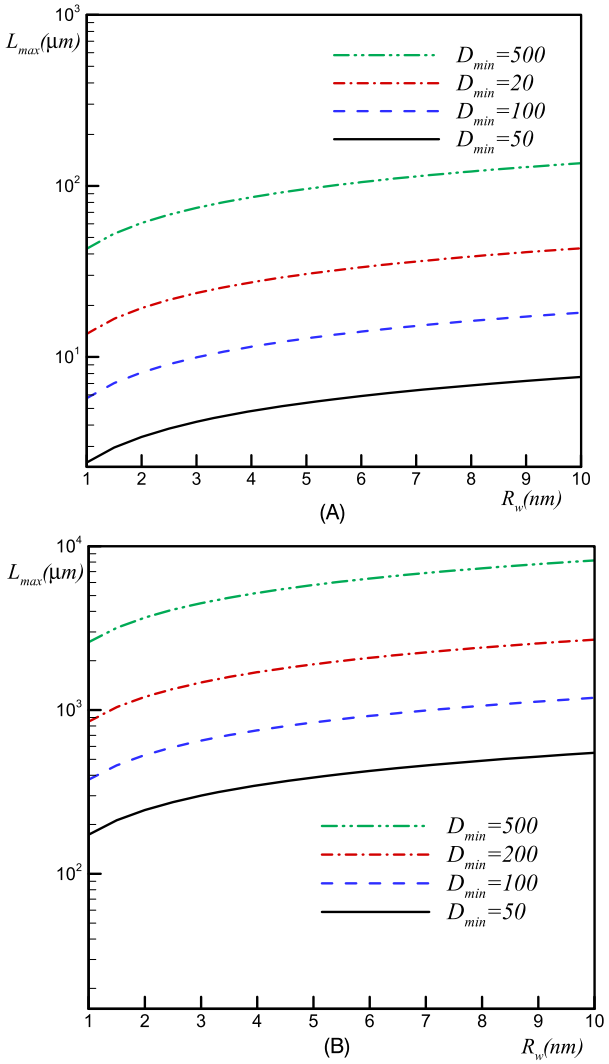

Figure 2.20 The maximum length and lowest permissible gaps as a function of MWCNT radii: (A) a large number of graphene layers, (B) small number of graphene layers ($N = 50$).

The detachment length and the lowest permissible gap of the nanoactuator for different MWCNT radii with Young's modulus of 1 TPa are presented in Fig. 2.20. As can be seen, van der Waals force is dominant in MWCNT over thick graphite sheet in comparison with thin plates.

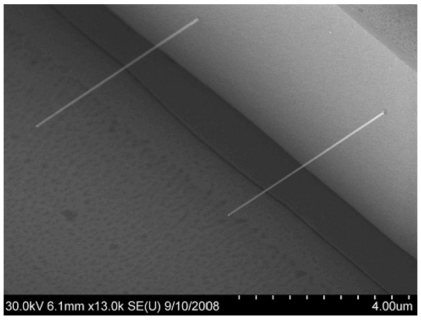

Figure 2.21 A silicon nanowire [104].

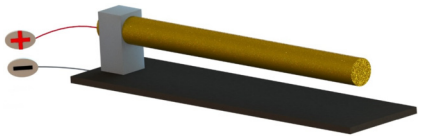

Figure 2.22 A typical nanowire fabricated switch.

2.4.2 Monotonic iteration method

Since the external loads in NEMS are nonlinear, the integration of Eq. (2.158) is not a straightforward task. To overcome difficulties in integration, a numerical procedure can be employed. Alves et al. [97] proved that the solution to Eq. (2.132) can be expressed as

$$w^{i+1}(x) = \int_0^1 G(x, \xi) \cdot q(\xi, w^i) d\xi. \tag{2.163}$$

2.4.2.1 Size-dependent behavior of the nanowire manufactured nanoswitch

As mentioned in Section 2.3.2.1, the scale-dependent response of constitutive material is an inherent property of ultrasmall structures when their dimensions are on the scale of the material length scale. In this section, the size-dependent behavior of nanowire manufactured nanoswitch is investigated by using the monotonic iteration method. A nanowire is a circular cross-section cylinder with its diameter being on the order of nanometers. However, there is almost no constraint for the length of the nanowire. Nanowires have been used as a building blocks of various nanostructures such as nanoresonators [98,99], logic switching devices [100], nanosensors [101,102], and energy harvesting devices [103].

Figs. 2.21 and 2.22 demonstrate a silicon nanowire and the modeling simulation of a typical nanowire fabricated switch, respectively. The nanoswitch is fabricated using a

movable nanowire with length L and radius r, suspended at a distance g over a fixed plate.

To simulate the size dependency, the modified couple stress theory can be employed. According to this theory, strain energy density ($\hat{U}$) is defined as [79]

$$\hat{U} = \frac{1}{2}\boldsymbol{\sigma} : \boldsymbol{\varepsilon} + \frac{1}{2}\mathbf{m} : \boldsymbol{\chi} \tag{2.164}$$

where $\boldsymbol{\sigma}$ and $\boldsymbol{\varepsilon}$ are the Cauchy stress and strain tensor variables, respectively. Moreover, $\mathbf{m}$ is the deviatoric part of the couple stress tensor, and $\boldsymbol{\chi}$ is the curvature tensor defined as:

$$\boldsymbol{\sigma} = \lambda \operatorname{tr}(\boldsymbol{\varepsilon})\mathbf{I} + 2\mu\boldsymbol{\varepsilon}, \tag{2.165}$$

$$\boldsymbol{\varepsilon} = \frac{1}{2}\left((\nabla\vec{v}) + (\nabla\vec{v})^T + (\nabla\vec{v})^T : (\nabla\vec{v})\right), \tag{2.166}$$

$$\mathbf{m} = 2l^2\mu\boldsymbol{\chi}, \tag{2.167}$$

$$\boldsymbol{\chi} = \frac{1}{2}\left((\nabla\vec{\theta}) + (\nabla\vec{\theta})^T\right), \tag{2.168}$$

$$\vec{\theta} = \frac{1}{2}\operatorname{curl}(\vec{v}) \tag{2.169}$$

where $\vec{\theta}$ is the rotation vector, and $\overrightarrow{v}$ is the displacement vector defined as:

$$\vec{v} = \left(U(X) - z\frac{dU(X)}{dX}\right)\hat{\mathbf{i}} + U(X)\hat{\mathbf{k}}. \tag{2.170}$$

Replacing Eq. (2.170) in Eqs. (2.165) to (2.169) yields:

$$\chi_{XY} = \chi_{YX} = -\frac{1}{2}\frac{d^2W(X)}{dX^2}, \tag{2.171}$$
$$\chi_{XX} = \chi_{YY} = \chi_{ZZ} = \chi_{YZ} = \chi_{ZY} = \chi_{ZX} = \chi_{XZ} = 0,$$

$$m_{XY} = m_{YX} = -\mu l^2\frac{d^2W(X)}{dX^2}, \tag{2.172}$$
$$m_{XX} = m_{YY} = m_{ZZ} = m_{YZ} = m_{ZY} = m_{ZX} = m_{XZ} = 0,$$

$$\varepsilon_{XX} = \frac{\partial u}{\partial X} + \frac{1}{2}\left(\frac{dW(X)}{dX}\right)^2 - Z\frac{d^2W(X)}{dX^2}, \tag{2.173}$$
$$\varepsilon_{YY} = \varepsilon_{ZZ} = \varepsilon_{XY} = \varepsilon_{YZ} = \varepsilon_{ZX} = 0,$$

$$\sigma_{XX} = E\left(\frac{dU}{dX} + \frac{1}{2}\left(\frac{dW(X)}{dX}\right)^2 - Z\frac{d^2W(X)}{dX^2}\right), \tag{2.174}$$
$$\sigma_{YY} = \sigma_{ZZ} = \sigma_{YZ} = \sigma_{ZX} = \sigma_{XY} = 0.$$

Moreover, by substituting Eqs. (2.171) to (2.174) into Eq. (2.164), the strain energy can be defined as

$$\begin{aligned} U_{elas} &= \frac{1}{2}\int_0^L \int_A (\boldsymbol{\sigma} : \boldsymbol{\varepsilon} + \mathbf{m} : \boldsymbol{\chi}) dA dX \\ &= \frac{1}{2}\int_0^L \int_A \left\{ (EZ^2 + \mu l^2)\left(\frac{d^2W}{dX^2}\right) + E\left(\frac{dU}{dX} + \frac{1}{2}\left(\frac{dW}{dX}\right)^2\right)^2 \right\} dA dX \\ &= \frac{1}{2}(EI + \mu A l^2)\int_0^L \left(\frac{d^2W}{dX^2}\right)^2 dX + EA\int_0^L \left(\frac{dU}{dX} + \frac{1}{2}\left(\frac{dW}{dX}\right)^2\right)^2 dX. \end{aligned} \tag{2.175}$$

Also, the work done by van der Waals attraction (W_{vdW}) and electric force (W_{elec}) is determined as:

$$W_{vdW} = \int_0^L \int_0^w f_{vdW}\, dw dX, \tag{2.176}$$

$$W_{elec} = \int_0^L \int_0^w f_{elec}\, dw dX. \tag{2.177}$$

By applying a voltage difference, a capacitor is established between the nanowire and the substrate. The electrical force acting on the nanowire can be determined by investigating the capacitance. The capacitance per unit length of a very long cylinder over a fixed plate is [105]

$$C(D) = \frac{2\pi\varepsilon_0}{\operatorname{arccosh}\left(1 + \frac{g}{r}\right)}. \tag{2.178}$$

Hence, the stored electrostatic energy can be obtained as

$$E_{elec} = \frac{1}{2}C(g)V^2 = \frac{\pi\varepsilon_0 V^2}{\operatorname{arccosh}\left(1 + \frac{g}{r}\right)}. \tag{2.179}$$

Therefore, the electric force per unit length, f_{elec}, is obtained as

$$f_{elec} = \frac{d(E_{elec})}{dg} = \frac{\pi\varepsilon_0 V^2}{\sqrt{g(g+2r)}\operatorname{arccosh}^2\left(1 + \frac{g}{r}\right)}. \tag{2.180}$$

For a deflected nanoswitch, the gap is reduced from g to $g - W$. In addition, the nanowire diameter is usually negligible in comparison to the wire–plate gap. Therefore, the electric force acting on the deflected nanowire can be simplified as

$$f_{elec} \approx \frac{\pi\varepsilon_0 V^2}{(g-W)\operatorname{arccosh}^2\left(\frac{g-W}{r}\right)} \approx \frac{\pi\varepsilon_0 V^2}{(g-W)\ln^2\left(2\frac{g-W}{r}\right)}. \tag{2.181}$$

Using the Lennard-Jones potential, the van der Waals energy can be investigated as [96]

$$E_{vdW} = \oint_{v_1} \oint_{v_2} \left(-\frac{C_{1,2}\rho_1\rho_2}{r^6(v_1, v_2)} \right) dv_1 dv_2 \tag{2.182}$$

where $C_{1,2}$ is the attracting coefficient, ρ_i $(i = 1, 2)$ is the number of atoms per unit volume i, and $(\cdot_1, \cdot_2)$ is the distance between two points of volume 1 and 2. By integrating Eq. (2.182) in the nanowire and the plate, the Lennard-Jones potential is determined as

$$E_{vdw} = -\frac{\pi^2 C_{1,2}\rho_1\rho_2 rL}{3g^3} = -\frac{\bar{A}r^2 L}{3g^3}. \tag{2.183}$$

The van der Waals force is determined via differentiating the Lennard-Jones potential with respect to the gap:

$$f_{vdW} = \frac{d(E_{vdW}/L)}{dg} = \frac{\bar{A}r^2}{g^4}. \tag{2.184}$$

Similar to the electrical effect, replacing g with the $g - w$ (i.e., when the van der Waals force acts on a deflected nanowire) results in

$$f_{vdW} = \frac{\bar{A}r^2}{(g - W)^4}. \tag{2.185}$$

The minimum energy principle can be employed to find the equilibrium equation for a system. As indicated by this principle, the equilibrium occurs when the system energy reaches its lowest value. To find the states of the minimum energy, the energy variation can be equalized to zero (i.e., $\delta(U_{elas} - W_{elec} - W_{vdw}) = 0$). Therefore, the equations for the nanowire fabricated switch are obtained as:

$$\left(EI + \mu Al^2\right) \frac{d^4 W}{dX^4} - EA \frac{d}{dX} \left[\left(\frac{dU}{dX} + \frac{1}{2} \left(\frac{dW}{dX} \right)^2 \right) \frac{dW}{dX} \right] = f_{vdW} + f_{elec}. \tag{2.186}$$

$$\frac{d}{dX} \left(\frac{dU}{dX} + \frac{1}{2} \left(\frac{dW}{dX} \right)^2 \right) = 0. \tag{2.187}$$

These equations are associated with the following boundary conditions:

$$U(0) = \frac{dU}{dX} + \frac{1}{2} \left(\frac{dW}{dX} \right)^2 \Bigg|_{X=L} = 0, \tag{2.188}$$

$$W(0) = \frac{dW(0)}{dX} = 0, \tag{2.189}$$

$$\frac{d^2 W(L)}{dX^2} = \frac{d^3 W(L)}{dX^3} = 0. \tag{2.190}$$

Since no axial force is active on the nanowire, the normal stress along the wire should be zero:

$$\int_A \sigma_{11} dA = E \int_A \left[\frac{dU}{dX} - Z\frac{d^2W}{dX^2} + \frac{1}{2}\left(\frac{dW}{dX}\right)^2 \right] dA = 0, \tag{2.191}$$

which yields

$$\frac{dU}{dX} + \frac{1}{2}\left(\frac{dW}{dX}\right)^2 = 0. \tag{2.192}$$

By replacing Eq. (2.192) in Eqs. (2.186) and (2.187), the equation for the nanowire is defined as:

$$\left(EI + \mu A l^2\right)\frac{d^4W}{dX^4} = \frac{\pi \varepsilon_0 V^2}{(g-W)\ln^2\left(2\frac{g-W}{r}\right)} + \frac{\bar{A}r^2}{(g-W)^4}, \tag{2.193}$$

$$W(0) = \frac{dW}{dX}(0) = 0, \tag{2.194}$$

$$\frac{d^2W}{dX^2}(L) = \frac{d^3W}{dX^3}(L) = 0. \tag{2.195}$$

The following dimensionless parameters can be employed to obtain the dimensionless equation:

$$x = \frac{X}{L}, \tag{2.196}$$

$$w = \frac{W}{g}, \tag{2.197}$$

$$\alpha = \frac{\varepsilon_0 \pi V^2 L^4}{\left(EI + \mu A l^2\right) g^2}, \tag{2.198}$$

$$\beta_{vdW} = \frac{\bar{A}rL^4}{g^4\left(EI + \mu A l^2\right)}, \tag{2.199}$$

$$k = \frac{g}{r}, \tag{2.200}$$

$$\delta = \frac{\mu A l^2}{E}. \tag{2.201}$$

In the above relation, k indicates the gap to nanowire radius ratio, α is the dimensionless parameter associated with the external voltage, β is the van der Waals force dimensionless parameter, and δ is the size-dependent dimensionless parameter. Using these

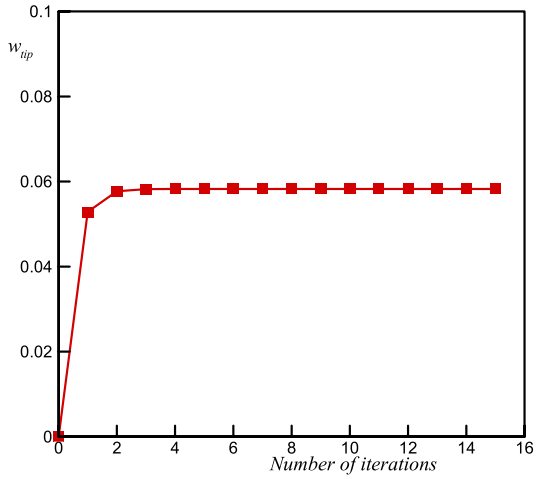

Figure 2.23 Tip deflection of the nanoswitch for different iterations ($\beta_{vdW} = 2; k = 10; \alpha = 2; \delta = 0.1$).

dimensionless parameters, the governing equation is determined as:

$$\frac{d^4w}{dx^4} = \frac{\beta_{vdW}}{k(1+\delta)(1-w)^4} + \frac{\alpha}{(1-w)(1+\delta)\ln^2[2k(1-w)]}, \tag{2.202}$$

$$w(0) = \frac{dw}{dx}(0) = 0, \tag{2.203}$$

$$\frac{d^2w}{dx^2}(1) = \frac{d^3w}{dx^3}(1) = 0. \tag{2.204}$$

The wire bending can roughly be estimated using a parabolic function (i.e., $w(x) = w_{tip}x^2$). Now, by using this shape function and replacing the right-hand side of Eq. (2.202) in Eq. (2.163), we have

$$w_{tip}^{i+1} = \int_0^1 G(x,\xi)\cdot\left[\frac{\beta_{vdW}}{k(1+\delta)(1-w_{tip}^i)^4} + \frac{\alpha}{(1-w_{tip}^i)(1+\delta)\ln^2[2k(1-w_{tip}^i)]}\right]d\xi \tag{2.205}$$

where $G(x,\xi)$ is defined in Eq. (2.154).

The obtained results for different iterations (starting with $w_{tip} = 0$) are illustrated in Fig. 2.23. As can be seen, the convergence rate is exceptionally fast.

In Fig. 2.24, the impacts of size parameter on the tip deflection of the nanowire at pull-in point for microswitch (i.e., without van der Waals force) and nanoswitch (i.e., including van der Waals effect) are illustrated. As can be seen, even though the size parameter in the microswitch does not affect the instability deflection, the deflection of the nanoswitch at the pull-in point is slightly increased by increasing the size parameter.

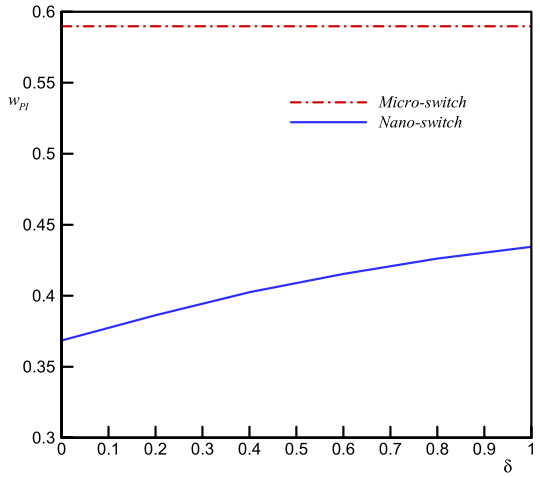

Figure 2.24 Impacts of the scale-dependent parameter on the pull-in tip deflection.

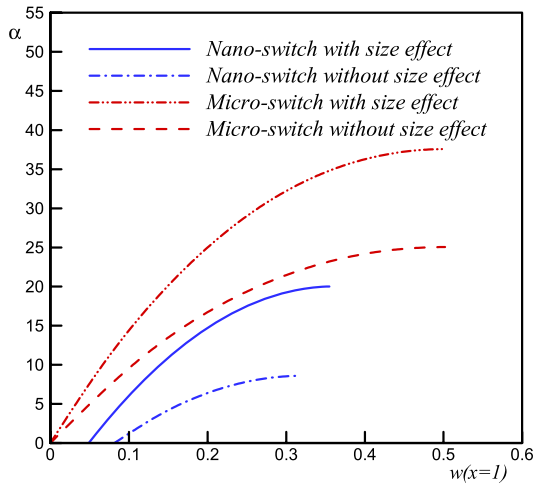

Figure 2.25 Nanowire tip deflection for various applied voltage.

The nanowire tip deflection for various values of applied voltage (the dimensionless parameter) is illustrated in Fig. 2.25. In this figure, both nanoswitch and microswitch are considered with and without size effect. As can be seen for the nanoswitch, an initial deflection exists, which is due to the presence of van der Waals force. By considering the size effect, the size dependency reduces the deflection of both microswitch and nanoswitch regardless of the applied voltage. However, at the pull-in point, while the pull-in voltage of the microswitch with size effect is higher than that of the microswitch

Table 2.3 DTM transformation.

Equation	Transformation	Boundary conditions	Transformation	Boundary conditions	Transformation
$f(x)=g(x)\pm h(x)$	$F(k)=G(k)\pm H(k)$	$f(0)=0$	$F(0)=0$	$f(1)=0$	$\sum_{k=0}^{\infty} F(k)=0$
$f(x)=g(x)\,h(x)$	$F(k)=\sum_{l=0}^{k} G(l)H(k-l)$	$\frac{df}{dx}(0)=0$	$F(1)=0$	$\frac{df}{dx}(1)=0$	$\sum_{k=0}^{\infty} kF(k)=0$
$f(x)=\frac{d^n g(x)}{dx^n}$	$F(k)=\frac{(k+n)!}{k!}G(k+n)$	$\frac{d^2f}{dx^2}(0)=0$	$F(2)=0$	$\frac{d^2f}{dx^2}(1)=0$	$\sum_{k=0}^{\infty} k(k-1)F(k)=0$
$f(x)=x^n$	$F(k)=\delta(k-n)=\begin{cases}0 & k\neq n\\ 1 & k=n\end{cases}$	$\frac{d^3f}{dx^3}(0)=0$	$F(3)=0$	$\frac{d^3f}{dx^3}(1)=0$	$\sum_{k=0}^{\infty} k(k-1)(k-2)F(k)=0$

without size effect, their deflections are similar. In other words, the size dependency does not affect the pull-in voltage of the microswitch. On the other hand, in the case of nanoswitch, both pull-in voltage and pull-in deflection are increased when the size effect is considered.

2.5. Differential transformation method

The differential transformation technique is a semianalytical method developed based on the Taylor series. In this technique, the kth derivative of an arbitrary function ($f(X)$) is considered as a transfer function $F(k)$ [106,107],

$$F(k)=\frac{1}{k!}\left[\frac{d^k}{dx^k}f(x)\right]_{x=x_0}. \tag{2.206}$$

Using the definition for Taylor series, the inverse transformation can be defined as [106, 107]

$$f(x)=\sum_{k=0}^{\infty} F(k)\,(x-x_0)^k. \tag{2.207}$$

The conversions that can be construed according to the above equation are listed in Table 2.3.

2.5.1 Size-dependent instability of a double-sided nanobridge

In a double-sided MEMS/NEMS, the movable part is hanged between two fixed plates. This nanostructure has been used in several NEMS and MEMS such as angular speed measurement devices [108], resonators [109,110], microphones [111], and accelerometers [112]. An SEM image of a double-sided microcantilever is illustrated in Fig. 2.26. The double-sided nanobridge has a similar structure with clamped–clamped boundary conditions instead of the clamped-free boundary conditions.

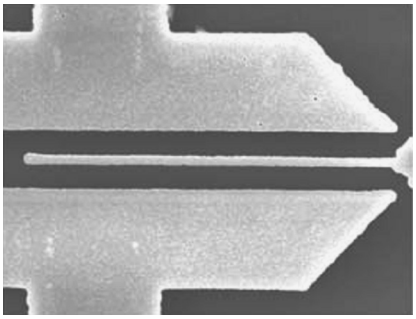

Figure 2.26 SEM image of a double-sided NEMS [113].

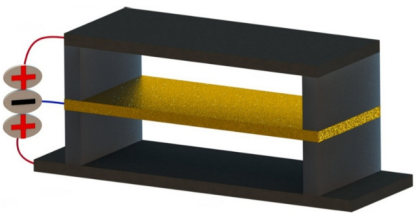

Figure 2.27 Double-sided nanobridge.

Fig. 2.27 shows a schematic view of a typical double-sided nanobridge. This nanostructure is constructed from a moving electrode hanged between two fixed electrodes. The geometrical properties of the moving nanobeam are similar to the those provided in Section 2.2.1. The initial gaps between the nanobeam and the lower and upper fixed electrodes are g and Ωg, respectively ($\Omega > 1$).

As mentioned in Section 2.3.2.1, the size-dependent behavior of the material affects the performance of ultrasmall structures. The couple stress theory is capable of simulating material scale dependency. Based on this approach, the strain energy is determined as [32,114]

$$\tilde{u} = \frac{1}{2}\lambda\varepsilon_{ij}\varepsilon_{ij} + \mu\varepsilon_{ij}\varepsilon_{ij} + 2\eta\kappa_{ij}\kappa_{ij} + 2\eta'\kappa_{ij}\kappa_{ij}, \tag{2.208}$$

where

$$\varepsilon_{ij} = \frac{1}{2}(u_{i,j} + u_{j,i} + u_{m,i}u_{m,j}), \tag{2.209}$$

$$\sigma_{ij} = \frac{\partial\tilde{u}}{\partial\varepsilon_{ij}} = \lambda\varepsilon_{mm}\delta_{ij} + 2\mu\varepsilon_{ij}, \tag{2.210}$$

$$\kappa_{ij} = \frac{1}{2}e_{jkl}u_{l,ki}, \tag{2.211}$$

$$m_{ij} = \frac{\partial \tilde{u}}{\partial \kappa_{ij}} = 4\eta\kappa_{ij} + 4\eta'\kappa_{ji}. \tag{2.212}$$

In these equations, η and η' are additional material constants introduced to simulate the size dependency. Moreover, e_{ijk} is the permutation symbol, and δ_{ij} is Kronecker delta.

The Euler–Bernoulli beam model can be employed to investigate the behavior of the moveable electrode. The displacement field of the Euler–Bernoulli beam is presented in Eq. (2.170). According to this equation, the components of the displacement vector are defined as:

$$u_X = U - Z\frac{\partial W}{\partial X}, \quad u_Y = 0, \quad u_Z = W(X). \tag{2.213}$$

By replacing Eq. (2.213) in Eq. (2.209), components of the von Karman strain tensor are stated as:

$$\begin{aligned} &\varepsilon_{XX} = \frac{\partial u_x}{\partial X} + \frac{1}{2}\left(\frac{\partial W}{\partial X}\right)^2 = \frac{\partial U}{\partial X} - Z\frac{\partial^2 W}{\partial X^2} + \frac{1}{2}\left(\frac{\partial W}{\partial X}\right)^2, \\ &\varepsilon_{XY} = \varepsilon_{YZ} = \varepsilon_{ZX} = \varepsilon_{YY} = \varepsilon_{ZZ} = 0. \end{aligned} \tag{2.214}$$

Similarly, by replacing Eq. (2.213) in Eq. (2.211), the nonzero components are determined as

$$\kappa_{YX} = -\frac{1}{2}\frac{\partial^2 W}{\partial X^2}. \tag{2.215}$$

Now, by integrating Eqs. (2.214) and (2.215) into Eqs. (2.210) and (2.212), respectively, the nonzero components of stress and couple stress tensors are determined as:

$$\sigma_{XX} = E\left(\frac{\partial U}{\partial X} - Z\frac{\partial^2 W}{\partial X^2} + \frac{1}{2}\left(\frac{\partial W}{\partial X}\right)^2\right), \tag{2.216}$$

$$m_{XY} = -4\eta\frac{\partial^2 W}{\partial X^2}, \quad m_{YX} = -4\eta'\frac{\partial^2 W}{\partial X^2}. \tag{2.217}$$

By using Eqs. (2.214) to (2.217) in Eq. (2.208), the total strain energy is obtained as:

$$\begin{aligned} U_S &= \oint_{\vartheta} \tilde{u} d\vartheta = \frac{1}{2}\int_0^L \int_A \left[\varepsilon_{XX}\sigma_{XX} + \kappa_{XY}m_{XY} + \kappa_{YX}m_{YX}\right] dA dX \\ &= \frac{1}{2}\int_0^L \left[(EI + 4A\eta)\left(\frac{\partial^2 W}{\partial X^2}\right)^2 + EA\left(\frac{\partial U}{\partial X} + \frac{1}{2}\left(\frac{\partial W}{\partial X}\right)^2\right)^2\right] dX. \end{aligned} \tag{2.218}$$

This equation implies that the strain energy of an Euler–Bernoulli beam in the context of the couple stress theory is solely dependent on one size-dependent material constant,

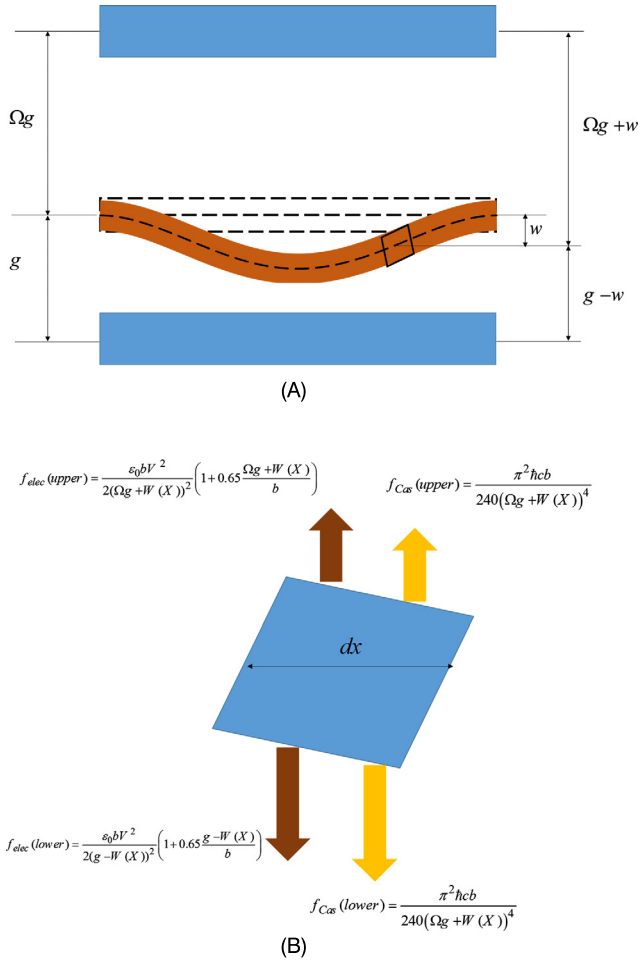

Figure 2.28 (A) Deflected double side nanobridge; (B) The forces acting on double side nanobridge.

which has the following relation with the material length scale parameter (l) and shear modulus (μ):

$$\eta = \mu l^2. \tag{2.219}$$

The forces' distribution of a nanobridge element is illustrated in Fig. 2.28. The effect of external forces (i.e., electrical force (f_{elec}) and Casimir force (f_{Cas})) on the beam is defined as

$$W_{ext} = \int_0^L \left[f_{elec} + f_{Cas}\right] W(X)\, dX. \tag{2.220}$$

The electrical force is constructed from the upper and lower attractions. Now, according to Eq. (2.12), the total electrical force per unit length that is effective on the moving electrode is obtained as

$$f_{elec} = \frac{\varepsilon_0 b V^2}{2(g - W(X))^2}\left(1 + 0.65\frac{g - W(X)}{b}\right) - \frac{\varepsilon_0 b V^2}{2(\Omega g + W(X))^2}\left(1 + 0.65\frac{\Omega g + W(X)}{b}\right). \tag{2.221}$$

Similarly, using Eq. (2.65), the Casimir force per unit length is obtained as

$$f_{Cas} = \frac{\pi^2 \hbar c b}{240\left(g - W(X)\right)^4} - \frac{\pi^2 \hbar c b}{240\left(\Omega g + W(X)\right)^4}. \tag{2.222}$$

By employing the Hamilton principle (i.e., $\delta(U_S - W_{ext}) = 0$), after some mathematical ellaboration, the nanobridge constitutive equations are derived as:

$$EA\frac{\partial}{\partial X}\left(\frac{\partial U}{\partial X} + \frac{1}{2}\left(\frac{\partial W}{\partial X}\right)^2\right) = 0, \tag{2.223}$$

$$-EA\frac{\partial}{\partial X}\left[\left(\frac{\partial U}{\partial X} + \frac{1}{2}\left(\frac{\partial W}{\partial X}\right)^2\right)\frac{\partial W}{\partial X}\right] + \left(EI + 4\mu A l^2\right)\frac{\partial^4 W}{\partial X^4} = f_{elec} + f_{Cas}. \tag{2.224}$$

These equations are associated with the following boundary conditions:

$$U(0) = U(L) = 0, \tag{2.225}$$

$$W(0) = \frac{\partial W(0)}{\partial X} = W(L) = \frac{\partial W(L)}{\partial X} = 0. \tag{2.226}$$

The first term of the left-hand side of Eq. (2.224) can be simplified as

$$\frac{\partial}{\partial X}\left[\left(\frac{\partial U}{\partial X} + \frac{1}{2}\left(\frac{\partial W}{\partial X}\right)^2\right)\frac{\partial W}{\partial X}\right] = \frac{\partial}{\partial X}\left(\frac{\partial U}{\partial X} + \frac{1}{2}\left(\frac{\partial W}{\partial X}\right)^2\right)\frac{\partial W}{\partial X} + \left(\frac{\partial U}{\partial X} + \frac{1}{2}\left(\frac{\partial W}{\partial X}\right)^2\right)\frac{\partial^2 W}{\partial X^2}. \tag{2.227}$$

Eq. (2.223) (see also Eq. (2.114)) states that the first term of the right-hand side of the above relation is equal to zero. By integrating Eq. (2.223), we have

$$\frac{\partial U}{\partial X} + \frac{1}{2}\left(\frac{\partial W}{\partial X}\right)^2 = C \tag{2.228}$$

where C is a constant value. By integrating Eq. (2.228) over the beam length, we have

$$U(L) - U(0) + \frac{1}{2}\int_0^L \left(\frac{\partial W}{\partial X}\right)^2 dX = CL. \tag{2.229}$$

By applying the boundary condition $U(0) = U(L) = 0$, the constant value C is determined as

$$C = \frac{1}{2L}\int_0^L \left(\frac{\partial W}{\partial X}\right)^2 dX. \tag{2.230}$$

By replacing Eqs. (2.230) and (2.228) in Eq. (2.223), one obtains

$$\frac{\partial}{\partial X}\left[\left(\frac{\partial U}{\partial X} + \frac{1}{2}\left(\frac{\partial W}{\partial X}\right)^2\right)\frac{\partial W}{\partial X}\right] = \left[\frac{1}{2L}\int_0^L \left(\frac{\partial W}{\partial X}\right)^2 dX\right]\frac{\partial^2 W}{\partial X^2}. \tag{2.231}$$

Using the above relation, the governing equation of a nanobridge reduces from a system of two ordinary differential equations to an ordinary differential equation as follows:

$$\left(EI + 4\mu A l^2\right)\frac{\partial^4 W}{\partial X^4} - \left[\frac{EA}{2L}\int_0^L \left(\frac{\partial W}{\partial X}\right)^2 dX\right]\frac{\partial^2 W}{\partial X^2} = f_{elec} + f_{Cas}. \tag{2.232}$$

Finally, by considering $w = W/x$ and $x = X/L$, the dimensionless governing equation and the boundary conditions of the double-sided nanobridge are determined as:

$$\begin{aligned}
&(1+\delta)\frac{d^4 w}{dx^4} - \eta\left(\int_0^1 \left(\frac{dw}{dx}\right)^2 dx\right)\frac{d^2 w}{dx^2} \\
&= \frac{\beta_{Cas}}{(1-w(x))^4} - \frac{\beta_{Cas}}{(\Omega + w(x))^4} \\
&+ \frac{\alpha}{(1-w(x))^2} - \frac{\alpha}{(\Omega + w(x))^2} + \frac{\alpha\gamma}{1-w(x)} - \frac{\alpha\gamma}{\Omega + w(x)},
\end{aligned} \tag{2.233}$$

$$w(0) = w(1) = w'(0) = w'(1) = 0 \tag{2.234}$$

where

$$\beta_{Cas} = \frac{\pi^2 hcbL^4}{240EIg^5}, \tag{2.235}$$

$$\alpha = \frac{\varepsilon_0 bV^2 L^4}{2g^3 EI}, \tag{2.236}$$

$$\gamma = 0.65\frac{g}{b}, \tag{2.237}$$

$$\delta = \frac{48\mu l^2}{Eh^2}, \tag{2.238}$$

$$\eta = 6\frac{g^2}{h^2}. \tag{2.239}$$

In the above equation, β_{Cas} is the dimensionless parameter of the Casimir force, α is the dimensionless parameter of the electrical force, δ indicates the size-dependent dimensionless parameter, and η is pertinent to the gap-to-thickness ratio, which indicates the geometrical nonlinearity of the nanobridge due to the stretching of the neutral axis. The differential transformations for zero displacements and rotation at $x = 0$ are

$$\bar{W}(0) = \bar{W}(1) = 0. \tag{2.240}$$

Multiplying the differential equation (2.233) by $(1 - w(x))^4 (\Omega + w(x))^4$ and using the relations presented in Table 2.3 yields:

$$\bar{W}(2) = a, \tag{2.241}$$

$$\bar{W}(3) = b, \tag{2.242}$$

$$\bar{W}(4) = \frac{\Omega^4(8a^3\eta + 18a^2b\eta + 3\alpha\gamma + 3\beta_{Cas} + 3\alpha) - 3\alpha\gamma\Omega^3 - 3\alpha\Omega^2 - 3\beta_{Cas}}{72(1+\delta)\Omega^4}, \tag{2.243}$$

$$\bar{W}(5) = \frac{\eta[24\eta a^3 b(4a+9b)+36ab(\beta_{Cas}+\alpha+\alpha\gamma)+9(54b^2+90ab+40a^2)(1+\delta)b]\Omega^4-36ab\eta(\Omega^3\alpha\gamma+\Omega^2\alpha+\beta_{Cas})}{5400(1+\delta)^2\Omega^4}. \tag{2.244}$$

The deflection of nanobridge can be considered as a series of transformation functions $(\bar{W})$:

$$w(x) = \sum_{k-0}^{\infty} \bar{W}(k)x^k = \bar{W}(0) + \bar{W}(1)x + \bar{W}(2)x^2 + \bar{W}(3)x^3 + \ldots. \tag{2.245}$$

By substituting Eqs. (2.240) to (2.244) into Eq. (2.245), the deflection is obtained as

$$w(x) = ax^2 + bx^3 + \frac{(8a^3\eta + 18a^2b\eta + 3\alpha\gamma + 3\beta_{Cas} + 3\alpha)\Omega^4 - 3\alpha\gamma\Omega^3 - 3\alpha\Omega^2 - 3\beta_{Cas}}{72(1+\delta)\Omega^4}x^4$$
$$+ \frac{\eta[24\eta a^3 b(4a+9b)+36ab(\alpha\gamma+\beta_{Cas}+\alpha)+9(54b^2+90ab+40a^2)(1+\delta)b]\Omega^4-36ab\eta(\Omega^3\alpha\gamma+\Omega^2\alpha+\beta_{Cas})}{5400(1+\delta)^2\Omega^4}x^5 + \ldots \tag{2.246}$$

where a and b are the unknown parameters evaluated using the boundary conditions at $x = 1$. The pull-in occurs when $dw(x = 0.5)/d\beta \to 0$.

Fig. 2.29 illustrates the impacts of scale dependency and Casimir force on the instability voltage of the nanobridge. As can be seen, an increase in the size parameter results in an increase in the pull-in voltage.

The effect of the upper gap on the instability voltage of the nanobridge is demonstrated in Fig. 2.30. This figure demonstrates that, when the upper-to-lower gap ratio increases, the nanobridge pull-in voltage reduces, which is due to a decrease in the returning forces.

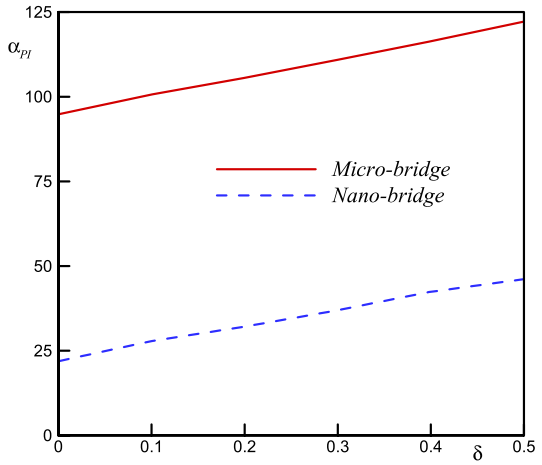

Figure 2.29 Impacts of the scale dependency and Casimir force on the pull-in voltage.

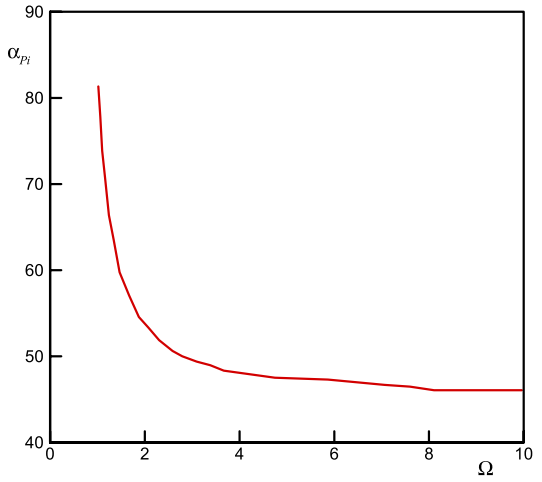

Figure 2.30 Impact of the upper gap on the instability voltage.

2.6. Variation iteration methods

In the variation iteration method, a correction functional is intruded by using the Lagrange multipliers to correct the initial approximated solution. The Lagrange multipliers are optimally obtained according to the variational theory. The selection method of the initial solution is almost arbitrary.

To provide an example of the basic concepts of variation iteration, the following general nonlinear system is considered:

$$\begin{aligned} L_1[w(\zeta)] + N_1[w(\zeta), u(\zeta)] &= 0, \\ L_2[w(\zeta)] + N_2[w(\zeta), u(\zeta)] &= 0 \end{aligned} \tag{2.247}$$

where $L_1[w(\zeta)]$ and $L_2[w(\zeta)]$ are linear differential operators. Also, $N_1[w(\zeta), u(\zeta)]$ and $N_2[w(\zeta), u(\zeta)]$ are nonlinear analytic operators. The fundamental feature of this method is constructing a correction functional for the system as follows [115]:

$$w_{n+1}(\zeta) = w_n(\zeta) + \int_0^{\zeta} \lambda_1(\tau)\{L_1[w_n(\zeta)] + N_1[\tilde{w}_n(\zeta), \tilde{u}_n(\zeta)]\}d\tau, \tag{2.248}$$

$$u_{n+1}(\zeta) = u_n(\zeta) + \int_0^{\zeta} \lambda_2(\tau)\{L_2[u_n(\zeta)] + N_2[\tilde{w}_n(\zeta), \tilde{u}_n(\zeta)]\}d\tau. \tag{2.249}$$

In this equation, $\lambda_1(\tau)$ and $\lambda_2(\tau)$ are general Lagrange multipliers identified optimally via the variational theory. Moreover, w_n and u_n are the nth approximate solutions, while $\tilde{w}_n$ and $\tilde{u}_n$ represent restricted variations (i.e., $\delta\tilde{w}_n = 0$ and $\delta\tilde{u}_n = 0$). Through determining the variations in Eqs. (2.248) and (2.249) and considering $\delta\tilde{w}(\tau) = 0$ and $\delta\tilde{u}(\tau) = 0$, the Lagrange multipliers can be obtained.

2.6.1 Nanowire manufactured nanotweezers

Manipulating nanoscale matter has received excessive attention in nanobiotechnology, nanoelectronics, ultramicroscopy, and nanofabrication. Nanotweezers are simple manipulators usually constructed from two parallel arms. The nanotweezers' arms are capable of deflecting towards each other by applying a DC voltage. Pull-in phenomena limit the operating ranges of electrostatic nanotweezers (and accordingly, the size of the smallest objects tweezers can operate on). At the pull-in voltage, the electrodes become unstable and collide with each other. This critical voltage limits the tweezing range. SEM images of a typical nanotweezers for different applied voltage until the pull-in voltage are provided in Fig. 2.31.

Fig. 2.32 demonstrates typical nanowire manufactured nanotweezers. While Fig. 2.32A illustrates a two-dimensional view of freestanding nanotweezers, the operated nanotweezers are presented in Fig. 2.32B. Each arm of these nanotweezers can be modeled as a cylindrical Euler–Bernoulli beam. As mentioned in Section 2.3.2.1, the strain energy from an Euler–Bernoulli beam in the framework of the modified couple stress theory (U) and the work by the axial force (W_{ext}) can be determined as:

$$\begin{aligned} U &= \frac{1}{2}\int_0^L \int_A \left\{ -Z\frac{d^2W}{dX^2}\left(-ZE\frac{d^2W}{dX^2}\right) + \mu l^2\left(\frac{d^2W}{dX^2}\right)^2 \right\} dA dX \\ &= \frac{1}{2}\int_0^L \left\{ EI\left(\frac{d^2W}{dX^2}\right)^2 + \mu l^2\left(\frac{d^2W}{dX^2}\right)^2 \right\} dX, \end{aligned} \tag{2.250}$$

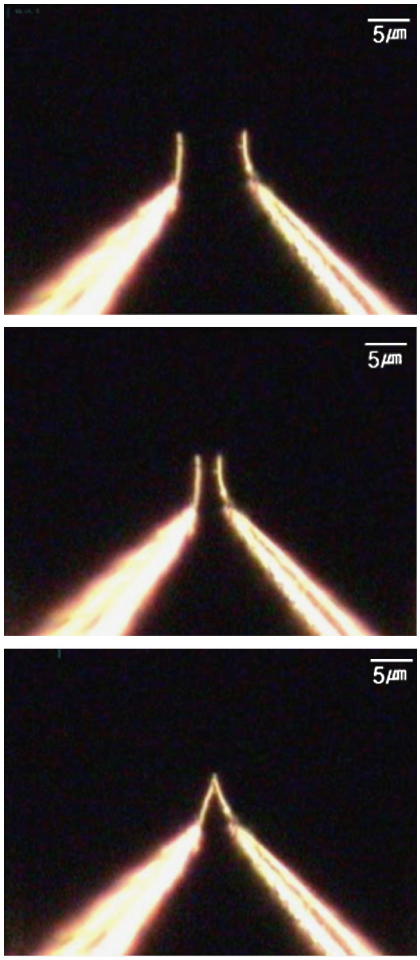

Figure 2.31 SEM image of nanotweezers electrostatic response [92].

$$W_{ext} = \int_0^L q(X)w(X)dX \tag{2.251}$$

where $q(X)$ is the sum of the electrical force and van der Waals attraction.

To determine the electrostatic attraction, a capacitance model is employed. The capacitance of a capacitor constructed from two parallel cylinders is given by [105]

$$C(g) = \frac{2\pi\varepsilon_0}{\ln\left[1 + \frac{g}{r} + \sqrt{(\frac{g}{r}+1)^2 - 1}\right]} \tag{2.252}$$

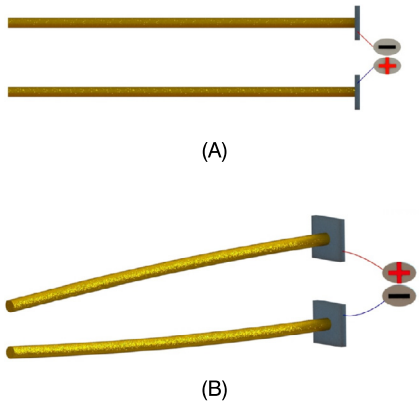

Figure 2.32 Typical nanowire manufactured nanotweezers: (A) freestanding nanotweezers; (B) deflected nanotweezers.

where ε_0 is the vacuum permittivity, r is the arms radius, and g is the arms' distance. Therefore, electrostatic energy per unit length is obtained as

$$E_{elec} = \frac{1}{2} C(g) V^2 = \frac{\pi \varepsilon_0 V^2}{\ln\left[1 + \frac{g}{r} + \sqrt{(\frac{g}{r} + 1)^2 - 1}\right]}. \tag{2.253}$$

The electric force is obtained by differentiating the electrostatic energy with respect to the gap:

$$f_{elec} = \frac{dE_{elec}}{dg} = \frac{\varepsilon_0 \pi V^2}{\sqrt{g^2 + 2gr} \times [\ln(1 + \frac{g}{r} + \frac{g}{r}\sqrt{1 + \frac{2r}{g}})]^2}. \tag{2.254}$$

When a voltage is applied, the tweezers' arms bend towards each other to reduce the gap to $g - W_1 - W_2$. If the tweezers have identical arms, electrode deflections are equal ($W_1 = W_2 = W$). Thus, the electric force of the deflected tweezers is

$$f_{elec} = \frac{\varepsilon_0 \pi V^2}{\sqrt{(g - 2W)^2 + 2r(g - 2W)} \times [\ln(1 + \frac{g-2W}{r} + \frac{g-2W}{r}\sqrt{1 + \frac{2r}{g-2W}})]^2}. \tag{2.255}$$

In standard applications, the gap separation is considerably more significant than the wire diameter. Hence, the electrostatic force can be simplified as

$$f_{elec} = \frac{\varepsilon_0 \pi V^2}{g(1 - \frac{2W}{g}) \times [\ln(\frac{2g}{r}(1 - \frac{2W}{g}))]^2}. \tag{2.256}$$

As mentioned in Section 2.4.1.1, the Lennard-Jones potential is an appropriate method to investigate the van der Waals force between two arbitrary bodies. If this potential is

applied to both arms, the van der Waals energy is defined as

$$E_{vdW} = \int_{\upsilon_1}\int_{\upsilon_2} n_1 n_2 \left(-\frac{C_6}{r^6(\upsilon_1,\upsilon_2)}\right) d\upsilon_1 d\upsilon_2 = \frac{\bar{A}L\sqrt{r}}{24g^{3/2}}. \tag{2.257}$$

By differentiating the van der Waals energy with respect to the gap, the van der Waals force is determined as

$$f_{vdW} = \frac{dE_{vdW}}{dg} = \frac{\bar{A}\sqrt{r}}{16g^{\frac{5}{2}}}. \tag{2.258}$$

Similar to electrical force, for nanotweezers with identical arms, the van der Waals is defined as

$$f_{vdW} = \frac{\bar{A}\sqrt{r}}{16(g-2W)^{\frac{5}{2}}}. \tag{2.259}$$

By exploiting the minimum energy principle and using Eqs. (2.250), (2.251), (2.256), and (2.259), the arms' equation for the manufactured nanowire is defined as

$$(EI+\mu Al^2)\frac{d^4W}{dX^4} = \frac{\bar{A}\sqrt{r}}{16(g-2W)^{\frac{5}{2}}} + \frac{\varepsilon_0 \pi V^2}{g(1-\frac{2W}{g})\times[\ln(\frac{2g}{r}(1-\frac{2W}{g}))]^2}, \tag{2.260}$$

$$W(0) = \frac{dW}{dX}(0) = 0, \tag{2.261}$$

$$\frac{d^2W}{dX^2}(L) = \frac{d^3W}{dX^3}(L) = 0. \tag{2.262}$$

To extract the dimensionless governing equation, the following dimensionless parameters can be used:

$$x = \frac{X}{L}, \tag{2.263}$$

$$w = \frac{W}{g}, \tag{2.264}$$

$$\alpha = \frac{2\varepsilon_0 \pi V^2 L^4}{EIg^2}, \tag{2.265}$$

$$\beta_{vdW} = \frac{6\bar{A}t^2L^4}{128\sqrt{2}r^{3/2}EIg^{7/2}}, \tag{2.266}$$

$$k = \frac{2g}{r}, \tag{2.267}$$

$$\delta = \frac{\mu Al^2}{EI} \tag{2.268}$$

where β_{vdW} indicates the van der Waals force dimensionless parameter, the dimensionless parameter α is pertinent to the electrical force, δ is the dimensionless parameter of the size dependency, and k is the geometrical parameter related to the gap-to-nanowire-diameter ratio. Finally, the dimensionless equation is obtained as

$$\frac{d^4w}{dx^4} = \frac{\alpha}{2(1+\delta)(1-2w)[\ln(k(1-2w))]^2} + \frac{\beta_{vdW}}{2(1+\delta)(1-2w)^{5/2}}, \tag{2.269}$$

$$w(0) = \frac{dw}{dx}(0) = 0, \tag{2.270}$$

$$\frac{d^2w}{dx^2}(1) = \frac{d^3w}{dx^3}(1) = 0. \tag{2.271}$$

To imply the variation iteration method, the right-hand side of the differential equation (2.269) is transformed using Taylor expansion as

$$\frac{d^4w}{dx^4} = a_0 + a_1[w(x)] + a_2[w(x)]^2 + a_3[w(x)]^3 + a_4[w(x)]^4 + a_5[w(x)]^5 + \ldots. \tag{2.272}$$

Now, the equation described in (2.248) is reduced to a set of integral-differential equations via assuming $w''''(x) = f(w, x)$ and $w'''(x) = u(x)$ as follows:

$$\begin{aligned} w''(x) &= w''(0) + \int_0^x u(\tau)d\tau, \\ w'(x) &= w'(0) + w''(0)x + \int_0^{x_1}\int_0^x u(\tau)d\tau\, dx_1. \end{aligned} \tag{2.273}$$

Then, an expansion of the integral-differential equations system is considered as

$$\begin{aligned} u'(x) &= f(w, x), \\ w'(x) &= w'(0) + w''(0)x + F(u(x)) \end{aligned} \tag{2.274}$$

where $F(u(x)) = \int_0^{x_1}\int_0^x u(\tau)d\tau\, dx_1$. Now, if we consider Eq. (2.272), correctional functions are constructed as:

$$\begin{aligned} w_{n+1}(x) &= w_n(x) + \int_0^x \lambda_1(s)\{w_n'(x) - \tilde{F}[u_n(s))]ds, \\ u_{n+1}(x) &= u_n(x) + \int_0^x \lambda_2(\tau)\{u_n(s) - f(w_n(s))\}ds. \end{aligned} \tag{2.275}$$

The functions $\tilde{F}(u_n(s))$ and $w_n(s)$ are deemed to be restricted variations (i.e., $\delta\tilde{F}(u_n(s)) = 0$ and $\delta w_n(s) = 0$). The Lagrange multipliers can be determined as $\lambda_1 = \lambda_2 = 1$. Finally,

the iterations can be written in the following form:

$$\begin{aligned} w_{n+1}(x) &= w_n(x) + \int_0^x \lambda_1(s)\{w_n'(x) - \tilde{F}[u_n(s))]ds, \\ u_{n+1}(x) &= u_n(x) + \int_0^x \lambda_2(\tau)\{u_n(s) - f(w_n(s))\}ds. \end{aligned} \tag{2.276}$$

As an initial value, we consider $w_0(x) = 0$ and $u_0(x) = 0$. If we assume $w_0''(0) = c_1$ and acknowledge the physical boundary conditions provided in Eq. (2.271), it is concluded that

$$\begin{aligned} w_{n+1}(x) &= \frac{c_1}{2}x^2 + \frac{1}{2}\int_0^x (x-\tau)^2 u_n(\tau)d\tau, \\ u_{n+1}(x) &= c_2 + a_0 x + \int_0^x \left\{\sum_{j=1}^{\infty} a_j [w(s)]^j\right\} ds. \end{aligned} \tag{2.277}$$

Finally, the solution for Eq. (2.269) can be summarized as

$$w(x) = \frac{c_1}{2}x^2 + \frac{c_2}{6}x^3 + \frac{a_0}{24}x^4 + \frac{a_1 c_1}{720}x^6 + \frac{a_1 c_2}{5040}x^7 + \frac{a_2 c_1^2}{6720}x^8 + \ldots \tag{2.278}$$

where c_1 and c_2 are unknown parameters that can be determined according to Eq. (2.271).

The arms' deflections of microtweezers and nanotweezers for different voltage ranges from zero to pull-in are illustrated in Fig. 2.33. While the van der Waals force is crucial for the nanotweezers, this intermolecular force can be neglected in the microtweezers. An increase in the applied voltage results in a rise in the deflection of the arms. However, no solution was obtained for voltages higher than the pull-in voltage. Also, Fig. 2.33 demonstrates that while the microtweezers have no initial deflection when no external voltage is applied, the freestanding nanotweezers have an initial deflection even without any external voltage applied, which is due to the van der Waals force.

Fig. 2.34 illustrates the tip deflection of the nanotweezers' arms as a function of the applied voltage. As can be seen, increasing the gap to arms' radius ratio parameter (i.e., k) increases the pull-in voltage and the pull-in bending of the nanotweezers.

2.7. Galerkin method for static problems

The weighted residual method is a powerful technique to approximate the solution of a boundary value problem. In this procedure, some trial functions are considered, and the weighted error across the domain is minimized [116]. A general one-dimensional differential equation is assumed to explain the concepts of the weighted residual method. It should be noted that similar to the derived one-dimensional differential equation, the

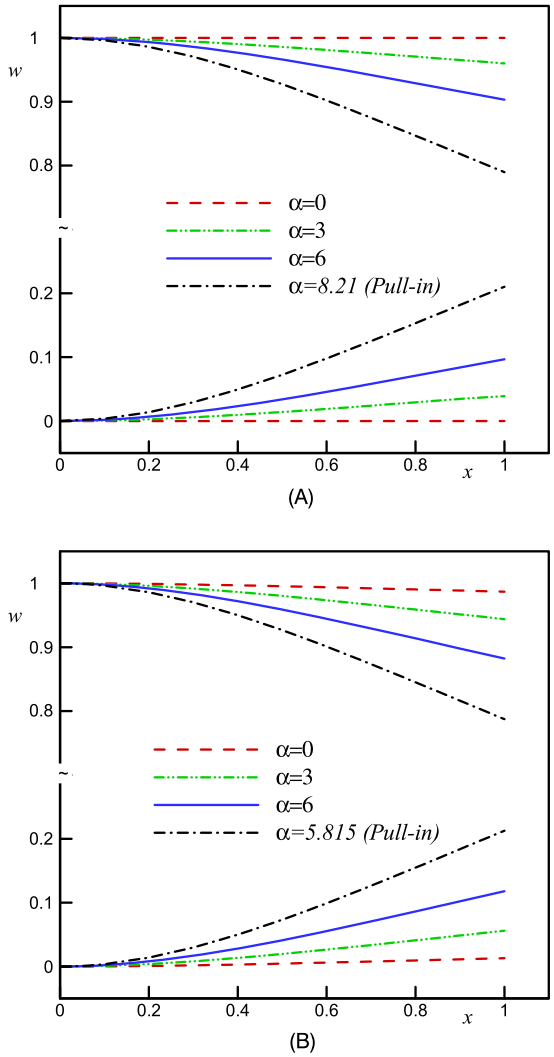

Figure 2.33 Deflection of the arms of the tweezers ($k = 10$) for different values of α ranging from zero to pull in (A) microtweezers and (B) nanotweezers.

procedure for higher-order differential equations is straightforward. We consider the following general differential equation:

$$D[y(x), x] = 0, \quad c_1 < x < c_2, \tag{2.279}$$

under the following homogeneous boundary conditions:

$$y(c_1) = 0, \quad y(c_2) = 0. \tag{2.280}$$

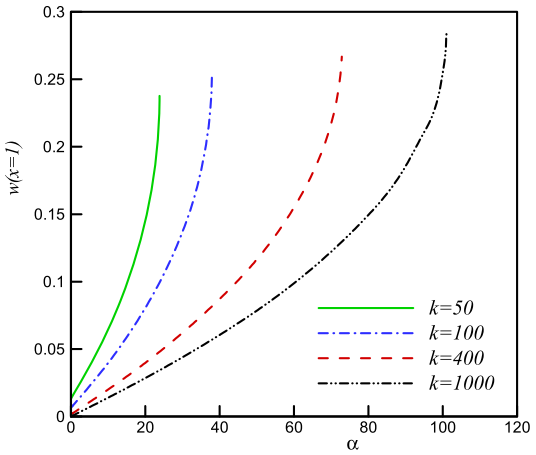

Figure 2.34 Tip deflection versus the applied voltage for various geometrical parameters (*k*).

The weighted residual method explores an approximated solution as follows:

$$\tilde{y}(x) = \sum_{i=1}^{n} q_i N_i(x) \tag{2.281}$$

where is an approximated solution for $y(x)$, q_i represents unknown constants which can be determined by minimizing the error, and $N_i(x)$ stands for trial functions. Also, the trial functions must be admissible, i.e., the trial solution needs to be a continuous function across the entire domain, satisfying the boundary conditions. By replacing the approximated solution ($\tilde{y}$) in Eq. (2.279), the residual error (or *residual* ($R(x)$)) is achieved as:

$$R(x) = D\left[\tilde{y}(x), x\right] \neq 0. \tag{2.282}$$

It is worth noting that the residual is correspondingly a function of the unknown parameters q_i. These parameters obey the following relation:

$$\int_{c_1}^{c_2} w_i(x) R(x) dx = 0, \quad i = 1, ..., n \tag{2.283}$$

where $w_i(x)$ is the ith weighting function. A system of n algebraic equations is obtained by integrating Eq. (2.283) whereby n unknown q_i parameters can be determined. Eq. (2.283) implies that the summation of the weighted residual errors is zero within the problem domain. Owing to the requirements imposed on the trial functions, the solution is exact on the boundaries since the trial solution must satisfy the boundary conditions. However, at any internal point, the residual error might be nonzero.

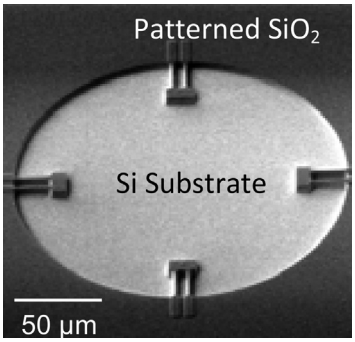

Figure 2.35 SEM image of a pressure sensor [121].

The weighting factors can be assessed through different methods such as least squares, subdomain collocation, point collocation, and Galerkin's method. In the Galerkin's method, the weighting functions are selected based on the trial solution as

$$w_i(x) = N_i(x), \quad i = 1, n. \tag{2.284}$$

Hence, the unknown parameters are investigated as follows:

$$\int_a^b w_i(x)R(x)dx = \int_a^b N_i(x)R(x) = 0, \quad i = 1, n. \tag{2.285}$$

This leads to n algebraic equations which can be solved to define the final solution of the differential equation.

2.7.1 Circular micromembrane subjected to hydrostatic pressure and electrostatic force

Suspended micro- and nanoplates can be used as an essential part of various electrostatically actuated MEMS/NEMS, such as ultrasonic transducers [117], pressure sensors [118], miniature pumps [119], and gas detectors [120].

Fig. 2.35 shows an SEM image of a microscale pressure sensor. In this pressure sensor, the deflection of a circular silicon diaphragm is measured by using piezoresistive silicon nanowires. The model of an electrostatic circular micromembrane is presented in Fig. 2.36. The micromembrane is constructed from a clamped circular plated hanged over a fixed plate. The plate radius, plate thickness, and initial gap between the flexible and fixed plates are R, h, and g, respectively. By applying a voltage difference between the micromembrane and fixed ground, the membrane deflects toward the fixed plate. In addition to external voltage, the microplate might be subjected to external hydrostatic pressure. The micromembrane is modeled as a clamped circular plate.

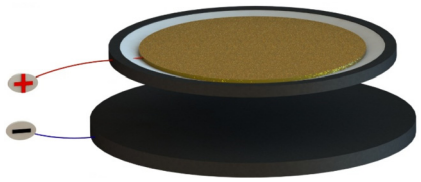

Figure 2.36 A typical electrostatically actuated circular micromembrane.

To extract the governing equation of a circular microplate, the cylindrical coordinate system (r, θ, z) is considered. According to the symmetry, the displacement field of a circular plate is defined as [122]

$$u_r = -Z\frac{\partial W(r)}{\partial r}, \quad u_\theta = 0, \quad u_z = W(r) \tag{2.286}$$

where u_r, u_θ, u_z denote the deflection in r, θ, and z directions, respectively. Also, in Eq. (2.286) the centerline deflection ($z = 0$) is in the z direction. By using Eq. (2.286), the radial and tangential strain components of an axisymmetric circular membrane are obtained as:

$$\varepsilon_r = -Z\frac{\partial^2 W(r)}{\partial r^2}, \quad \varepsilon_\theta = -\frac{z}{r}\frac{\partial W(r)}{\partial r}, \quad \varepsilon_{r\theta} = 0. \tag{2.287}$$

Therefore, the stress component can be explained in the term of midplane deflection as:

$$\sigma_r = \frac{E}{1-\upsilon^2}(\varepsilon_r + \upsilon\varepsilon_\theta) = -\frac{EZ}{1-\upsilon^2}\left(\frac{\partial^2 W}{\partial r^2} + \frac{\upsilon}{r}\frac{\partial W}{\partial r}\right), \tag{2.288}$$

$$\sigma_\theta = \frac{E}{1-\upsilon^2}(\varepsilon_\theta + \upsilon\varepsilon_r) = -\frac{EZ}{1-\upsilon^2}\left(\frac{1}{r}\frac{\partial W}{\partial r} + \upsilon\frac{\partial^2 W}{\partial r^2}\right). \tag{2.289}$$

Using the above equation, the bending moments can be determined as:

$$M_r = \int_{-\frac{h}{2}}^{\frac{h}{2}} \sigma_r z dz = -\frac{Et^3}{12(1-\upsilon^2)}\left(\frac{\partial^2 W}{\partial r^2} + \frac{\upsilon}{r}\frac{\partial W}{\partial r}\right), \tag{2.290}$$

$$M_\theta = \int_{-\frac{h}{2}}^{\frac{h}{2}} \sigma_\theta z dz = -\frac{Et^3}{12(1-\upsilon^2)}\left(\frac{1}{r}\frac{\partial W}{\partial r} + \upsilon\frac{\partial^2 W}{\partial r^2}\right). \tag{2.291}$$

The distributed pressure (q) acting on the microplates results in a shear force. This shear force can be calculated by the following equation:

$$Q_r = -\frac{1}{2\pi r}\int_0^{2\pi}\int_0^R qrdrd\theta = -\frac{1}{r}\int_0^R qrdr. \tag{2.292}$$

In the problem understudy, q is the sum of the electrical force and electrostatic pressure.

To extract the governing equation of a micromembrane, the equilibrium condition is considered [123]:

$$\frac{\partial M_r}{\partial r} + \frac{M_r - M_\theta}{r} = Q_r. \tag{2.293}$$

By substituting Eqs. (2.290)–(2.292) in Eq. (2.293), the constitutive equation for axisymmetric bending of a circular plate is obtained as

$$D\left(\frac{\partial^4 W}{\partial r^4} + \frac{2}{r}\frac{\partial^3 W}{\partial r^3} - \frac{1}{r^2}\frac{\partial^2 W}{\partial r^2} + \frac{1}{r^3}\frac{\partial W}{\partial r}\right) = q \tag{2.294}$$

where D is the bending rigidity of the microplate which defined as

$$D = \frac{Et^3}{12(1-\upsilon^2)}. \tag{2.295}$$

The boundary conditions at the clamped edges are defined as follows:

$$W(R,\theta) = 0, \tag{2.296}$$

$$\frac{\partial W}{\partial R}(R,\theta) = 0. \tag{2.297}$$

For microplates with the simply-supported conditions, the boundary conditions at simply supported edges are explained as:

$$W(R,\theta) = 0, \tag{2.298}$$

$$M_r(R,\theta) = 0. \tag{2.299}$$

The microplate is subjected to both external electrostatic potential and hydrostatic pressure. The electrical force can be achieved through the capacitance model. The capacitance of two parallel plates capacitor is

$$C(g) = \frac{\varepsilon A}{2g}. \tag{2.300}$$

By using the above relation, the electrical energy per unit area for parallel plates capacitor is determined as

$$E_{elec} = \frac{1}{2}C(g)V^2 = \frac{\varepsilon A V^2}{2g}. \tag{2.301}$$

Therefore, the electrical force per unit area of a micromembrane is identified as

$$f_{elec} = -\frac{\partial E_{elec}}{\partial g} = \frac{\varepsilon V^2}{2g^2}. \tag{2.302}$$

For a deflected membrane, the gap reduces from g to $g - W$. Therefore, the electrical force should be modified as

$$f_{elec} = \frac{\varepsilon V^2}{2(g-W)^2}. \tag{2.303}$$

By substituting Eq. (2.303) into Eq. (2.294) and considering a uniform electrostatic pressure (P), the governing equation of a micromembrane is obtained as

$$D\left(\frac{\partial^4 W}{\partial r^4} + \frac{2}{r}\frac{\partial^3 W}{\partial r^3} - \frac{1}{r^2}\frac{\partial^2 W}{\partial r^2} + \frac{1}{r^3}\frac{\partial W}{\partial r}\right) = p + \frac{\varepsilon V^2}{2(g-W)^2}. \tag{2.304}$$

The above equation can also be expressed as

$$D\nabla^4 W = p + \frac{\varepsilon V^2}{2(g-W)^2}. \tag{2.305}$$

In the Galerkin method, the displacement is assumed to be a sum of admissible trial functions as follows:

$$W(r) = \sum_{i=1}^{n} c_i \phi_i(r) \tag{2.306}$$

where C_i's are unknown parameters, and n is the number of selected trial functions. To execute the Galerkin's procedure, firstly, the admissible trial functions for the axisymmetric circular plate should be selected. For axisymmetric bending of a clamped circular plate, the following trial solution which satisfies all boundary conditions can be chosen:

$$\phi_n = (R^2 - r^2)^{n+1}, \quad n = 1, 2, \ldots. \tag{2.307}$$

There are two methods to generate a Galerkin's solution for nonlinear differential equations. In the first method, the nonlinear terms (i.e., electrical force) are expanded around the freestanding condition (i.e., $W = 0$) by using the Taylor expansion series as follows:

$$f_{elec} = \frac{\varepsilon V^2}{2g^2}\left\{1 + 2\frac{W}{g} + 3\frac{W^2}{g^2} + 4\frac{W^3}{g^3} + 5\frac{W^4}{g^4} + \ldots\right\}. \tag{2.308}$$

By using Eq. (2.307), substituting Eq. (2.306) into Eq. (2.304), multiplying the obtained equation and integrating the results from 0 to R, a system of n algebraic equations is

Table 2.4 Geometrical and mechanical properties of studied circular electrostatic microplate.

Parameter	Value
Radius (R)	40 μm
Thickness	1 μm
Separation distance (g)	1 μm
Poisson's ratio (ν)	0.3
Young's modulus	1.65 Gpa

obtained as:

$$\int_0^R D\nabla^4\left(\sum_{i=1}^{n} c_i\phi_i\right)\phi_j dr = \int_0^R p\phi_j dr + \int_0^R \frac{\varepsilon V^2}{2g^2}\left\{1+\frac{2\sum_{i=1}^{n} c_i\phi_i}{g}+\frac{3\left(\sum_{i=1}^{n} c_i\phi_i\right)^2}{g^2}+\frac{4\left(\sum_{i=1}^{n} c_i\phi_i\right)^3}{g^3}+\frac{5\left(\sum_{i=1}^{n} c_i\phi_i\right)^4}{g^4}+\ldots\right\}\phi_j dr. \tag{2.309}$$

In the second method, both sides of Eq. (2.304) are multiplied by $(g-W)^2$. Then similar to the first method, the obtained equation is multiplied by and integrated from 0 to R. Again, this leads to a system of n algebraic equations:

$$\int_0^R D\left(g-\sum_{i=1}^{n} c_i\phi_i\right)^2\nabla^4\left(\sum_{i=1}^{n} c_i\phi_i\right)\phi_j dr = \int_0^R p\left(g-\sum_{i=1}^{n} c_i\phi_i\right)^2\phi_j dr + \int_0^R \frac{\varepsilon V^2}{2g^2}\phi_j dr. \tag{2.310}$$

We use the second method with four trial functions. It is worth noting that by increasing the number of trial functions in the Galerkin procedure, the solution error reduces.

To examine the accuracy of the proposed model and Galerkin solution, an electrostatic circular microplate is considered. The geometrical and mechanical properties of the microplate are presented in Table 2.4. The bending of a similar microplate has been investigated by Zhao et al. [124] using the finite element method in NASYS commercial software.

Fig. 2.37 demonstrates the deflection profile of a microplate when the applied voltage is 90 V. The maximum deflection of the microplate in this situation is approximately 0.107 μm, which is less than 30% of the plate thickness. This deflection can be considered as small deformation. As seen, for a small deformation, not only Galerkin solution is in good agreement with the FEM solution but also the considered trial functions

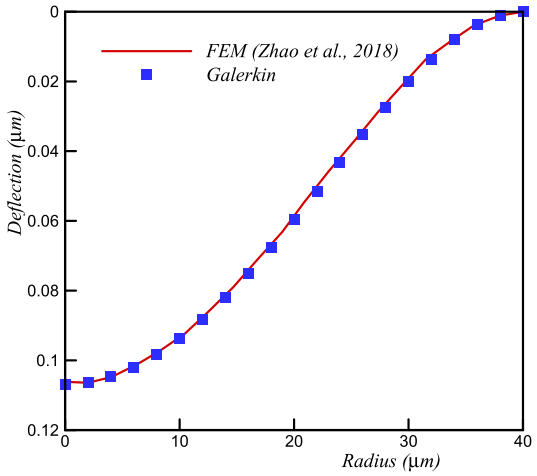

Figure 2.37 Deflection of microplate subjected to only 90 V electrical potential (comparison between finite element solution [124] and Galerkin method).

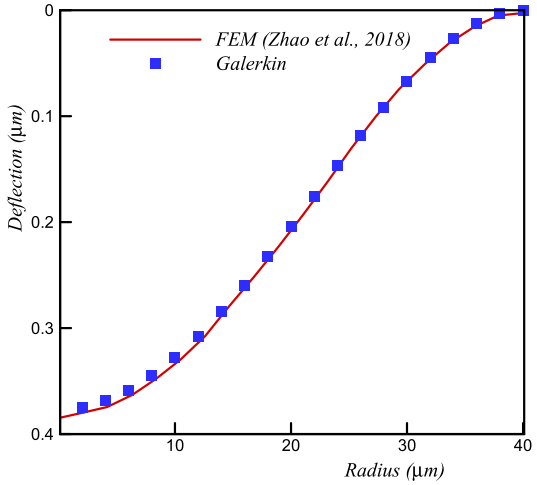

Figure 2.38 Deflection of microplate subjected to only 136 V electrical potential (comparison between finite element solution [124] and Galerkin method).

(Eq. (2.307)) can predict the axisymmetric microplate deflection. The deflection profile of the circular microplate subjected to 136 V DC potential is illustrated in Fig. 2.38. In this figure, the maximum deflection of the microplate is approximately 0.38 μm, which is 38% of plate thickness, this can be considered as a relatively large deformation. Figs. 2.37 and 2.38 demonstrate that the Galerkin method results are in perfect agreement with the FEM solution for both small and large deformation.

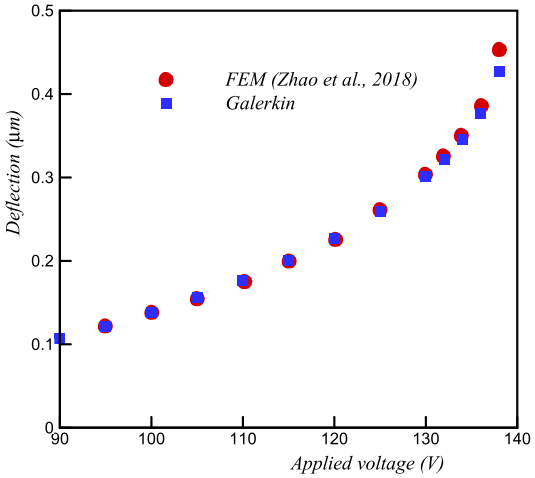

Figure 2.39 Maximum deflection of microplate subjected to only electrical potential for different applied voltage (comparison between finite element solution [124] and Galerkin method).

Previously, the pull-in phenomenon has been introduced. The behavior of a microplate near the pull-in point is crucial for designing, manufacturing, and analyzing of MEMS and NEMS. To investigate the capability of the Galerkin method for predicting the pull-in behavior of the circular microplate, the maximum deflection of the microplate for various applied voltage from 90 V to pull-in value is plotted in Fig. 2.39. In addition to Galerkin method results, the maximum deflection of the microplate computed by Zhao et al. [124] using ANSYS software is presented in this figure. Fig. 2.39 demonstrates that while the applied voltage near the pull-in point for the Galerkin solution data is not as close as the lower voltage for the FEM simulation, the Galerkin method results are in good agreement with the FEM solution even at the pull-in point. The pull-in voltage predicted by the Galerkin method is 138.6 V which has only 0.4 V difference from the values obtained by the FEM (i.e., 139 V).

The mode shapes used for the Galerkin procedure are obtained for a circular plate subjected to uniform pressure [125]. To test the ability of the Galerkin method for investigating the behavior of the axisymmetric microplate with both electrical force and hydrostatic pressure, the maximum deflection of the microplate for different applied hydrostatic pressure is shown in Fig. 2.40. In this figure, the external DC voltage is 100 V. Fig. 2.40 illustrates that the Galerkin solution for the microplate subjected to both hydrostatic pressure and electrical force is also in excellent agreement with the FEM simulation.

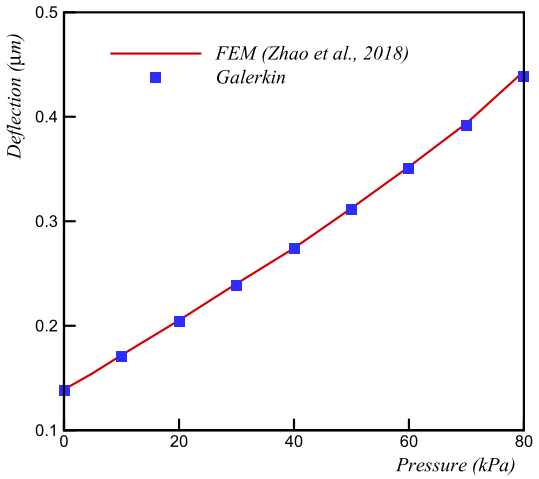

Figure 2.40 Maximum deflection of microplate subjected to 100 V electrical potential and hydrostatic pressure (comparison between finite element solution [124] and Galerkin method).

2.8. Conclusion

In this chapter, eight semianalytical methods for solving the nonlinear governing equation of the NEMS/MEMS were introduced. After introducing the mathematical concepts of each method, the constitutive equation of a micro- and nanostructure was extracted based on the continuum mechanics. Subsequently, the static behavior of nanostructures was investigated by semianalytical solutions.

In the next section, some numerical solutions for simulating the static behavior of NEMS/MEMS are addressed.

References

[1] M.M.S. Fakhrabadi, Application of modified couple stress theory and homotopy perturbation method in investigation of electromechanical behaviors of carbon nanotubes, Advances in Applied Mathematics and Mechanics 9 (1) (2017) 23–42.
[2] M. Keivani, et al., Effect of surface layer on electromechanical stability of tweezers and cantilevers fabricated from conductive cylindrical nanowires, Surface Review and Letters 23 (2) (2016) 1550101.
[3] A. Farrokhabadi, A. Koochi, M. Abadyan, Modeling the instability of CNT tweezers using a continuum model, Microsystem Technologies 20 (2) (2014) 291–302.
[4] J. Zare, Pull-in behavior analysis of vibrating functionally graded micro-cantilevers under suddenly DC voltage, Journal of Applied Mathematics and Computational Mechanics 1 (1) (2014) 17–25.
[5] N. Fazli, et al., Influence of electrostatic force and the van der Waals attraction on the pull-in instability of the CNT-based probe–actuator, Canadian Journal of Physics 92 (9) (2013) 1047–1057.
[6] A. Koochi, A. Noghrehabadi, M. Abadyan, Approximating the effect of van der Waals force on the instability of electrostatic nano-cantilevers, International Journal of Modern Physics B 25 (29) (2011) 3965–3976.

[7] J. Abdi, et al., Modeling the effects of size dependence and dispersion forces on the pull-in instability of electrostatic cantilever NEMS using modified couple stress theory, Smart Materials and Structures 20 (5) (2011) 55011.

[8] A. Koochi, A. Kazemi, M. Abadyan, Simulating deflection and determining stable length of free-standing carbon nanotube probe/sensor in the vicinity of graphene layers using a nanoscale continuum model, NANO 6 (5) (2011) 419–429.

[9] J.B. Ma, L. Jiang, S.F. Asokanthan, Influence of surface effects on the pull-in instability of NEMS electrostatic switches, Nanotechnology 21 (50) (2010) 505708.

[10] F. Tajaddodianfar, et al., Nonlinear dynamics of electrostatically actuated micro-resonator: analytical solution by homotopy perturbation method, in: 2014 IEEE/ASME International Conference on Advanced Intelligent Mechatronics, 2014.

[11] F. Tajaddodianfar, M.R.H. Yazdi, H.N. Pishkenari, Nonlinear dynamics of MEMS/NEMS resonators: analytical solution by the homotopy analysis method, Microsystem Technologies 23 (6) (2017) 1913–1926.

[12] M. Mojahedi, et al., Analytic solutions to the oscillatory behavior and primary resonance of electrostatically actuated microbridges, International Journal of Structural Stability and Dynamics 11 (06) (2011) 1119–1137.

[13] R. Soroush, et al., Investigating the effect of Casimir and van der Waals attractions on the electrostatic pull-in instability of nano-actuators, Physica Scripta 82 (4) (2010) 045801.

[14] J.-S. Duan, R. Rach, A.-M. Wazwaz, Solution of the model of beam-type micro-and nano-scale electrostatic actuators by a new modified Adomian decomposition method for nonlinear boundary value problems, International Journal of Non-Linear Mechanics 49 (2013) 159–169.

[15] A. Noghrehabadi, M. Ghalambaz, A. Ghanbarzadeh, A new approach to the electrostatic pull-in instability of nanocantilever actuators using the ADM–Padé technique, Computers & Mathematics with Applications 64 (9) (2012) 2806–2815.

[16] A. Koochi, N. Fazli, R. Rach, Modeling the pull-in instability of the CNT-based probe/actuator under the Coulomb force and the van der Waals attraction, Latin American Journal of Solids and Structures 11 (8) (2014) 1315–1328.

[17] A. Koochi, et al., Modeling the influence of surface effect on instability of nano-cantilever in presence of Van der Waals force, International Journal of Structural Stability and Dynamics 13 (4) (2013) 1250072.

[18] R. Soroush, et al., Modeling the effect of Van Der Waals attraction on the instability of electrostatic cantilever and doubly-supported nano-beams using modified Adomian method, International Journal of Structural Stability and Dynamics 12 (5) (2012) 1250036.

[19] A. Koochi, et al., Influence of surface effects on size-dependent instability of nano-actuators in the presence of quantum vacuum fluctuations, Physica Scripta 85 (3) (2012) 35804.

[20] Y. Beni, A. Koochi, M. Abadyan, Theoretical study of the effect of Casimir force, elastic boundary conditions and size dependency on the pull-in instability of beam-type NEMS, Physica. E, Low-Dimensional Systems and Nanostructures 43 (4) (2011) 979–988.

[21] A. Koochi, et al., Theoretical study of the effect of Casimir attraction on the pull-in behavior of beam-type NEMS using modified Adomian method, Physica. E, Low-Dimensional Systems and Nanostructures 43 (2) (2010) 625–632.

[22] M. Ghalambaz, M. Ghalambaz, M. Edalatifar, Buckling analysis of cantilever nanoactuators immersed in an electrolyte: a close form solution using Duan-Rach modified Adomian decomposition method, Journal of Applied and Computational Mechanics 1 (4) (2015) 207–219.

[23] A. Farrokhabadi, et al., An improved model for the cantilever NEMS actuator including the surface energy, fringing field and Casimir effects, Physica. E, Low-Dimensional Systems and Nanostructures 75 (2016) 202–209.

[24] A. Noghrehabadi, M. Eslami, M. Ghalambaz, Influence of size effect and elastic boundary condition on the pull-in instability of nano-scale cantilever beams immersed in liquid electrolytes, International Journal of Non-Linear Mechanics 52 (2013) 73–84.
[25] A. Koochi, et al., New approach to model the buckling and stable length of multi walled carbon nanotube probes near graphite sheets, Materials & Design 32 (5) (2011) 2949–2955.
[26] A. Ramezani, A. Alasty, J. Akbari, Closed-form solutions of the pull-in instability in nano-cantilevers under electrostatic and intermolecular surface forces, International Journal of Solids and Structures 44 (14–15) (2007) 4925–4941.
[27] A. Ramezani, A. Alasty, J. Akbari, Analytical investigation and numerical verification of Casimir effect on electrostatic nano-cantilevers, Microsystem Technologies 14 (2) (2008) 145–157.
[28] A. Ramezani, A. Alasty, J. Akbari, Influence of van der Waals force on the pull-in parameters of cantilever type nanoscale electrostatic actuators, Microsystem Technologies 12 (12) (2006) 1153–1161.
[29] A. Ramezani, A. Alasty, J. Akbari, Pull-in parameters of cantilever type nanomechanical switches in presence of Casimir force, Nonlinear Analysis: Hybrid Systems 1 (3) (2007) 364–382.
[30] A. Farrokhabadi, et al., Effects of size-dependent elasticity on stability of nanotweezers, Applied Mathematics and Mechanics 35 (12) (2014) 1573–1590.
[31] A. Koochi, A. Farrokhabadi, M. Abadyan, Modeling the size dependent instability of NEMS sensor/actuator made of nano-wire with circular cross-section, Microsystem Technologies 21 (2) (2015) 355–364.
[32] I. Karimipour, et al., Using couple stress theory for modeling the size-dependent instability of double-sided beam-type nanoactuators in the presence of Casimir force, Journal of the Brazilian Society of Mechanical Sciences and Engineering 38 (2016) 1779–1795.
[33] I. Karimipour, et al., Modeling the electromechanical behavior and instability threshold of NEMS bridge in electrolyte considering the size dependency and dispersion forces, Physica. E, Low-Dimensional Systems and Nanostructures 74 (2015) 140–150.
[34] F. Ebrahimi, et al., Application of the differential transformation method for nonlocal vibration analysis of functionally graded nanobeams, Journal of Mechanical Science and Technology 29 (3) (2015) 1207–1215.
[35] F. Ebrahimi, E. Salari, Size-dependent free flexural vibrational behavior of functionally graded nanobeams using semi-analytical differential transform method, Composites. Part B, Engineering 79 (2015) 156–169.
[36] Y.T. Beni, I. Karimipöur, M. Abadyan, Modeling the effect of intermolecular force on the size-dependent pull-in behavior of beam-type NEMS using modified couple stress theory, Journal of Mechanical Science and Technology 28 (9) (2014) 3749–3757.
[37] O. Rahmani, et al., In-plane vibration of FG micro/nano-mass sensor based on nonlocal theory under various thermal loading via differential transformation method, Superlattices and Microstructures 101 (2017) 23–39.
[38] A. Farrokhabadi, et al., A theoretical model for investigating the effect of vacuum fluctuations on the electromechanical stability of nanotweezers, Indian Journal of Physics 89 (6) (2015) 599–609.
[39] M. Mohammadian, Application of the variational iteration method to nonlinear vibrations of nanobeams induced by the van der Waals force under different boundary conditions, The European Physical Journal Plus 132 (4) (2017) 169.
[40] J.H. He, Homotopy perturbation technique, Computer Methods in Applied Mechanics and Engineering 178 (1999) 257–262.
[41] A. Nafari, et al., MEMS sensor for in situ TEM atomic force microscopy, Journal of Microelectromechanical Systems 17 (2) (2008) 328–333.
[42] S. Rao, K.D. Costa, 2-Atomic Force Microscopy (AFM) in biomedical research, in: P. Morris (Ed.), Biomedical Imaging, Woodhead Publishing, 2014, pp. 41–64.

[43] T.-S. Wu, W.-J. Chang, J.-C. Hsu, Effect of tip length and normal and lateral contact stiffness on the flexural vibration responses of atomic force microscope cantilevers, Microelectronic Engineering 71 (1) (2004) 15–20.
[44] B. Sviličić, et al., Tunable MEMS cantilever resonators electrothermally actuated and piezoelectrically sensed, Microelectronic Engineering 145 (2015) 38–42.
[45] D.I. Caruntu, I. Martinez, Reduced order model of parametric resonance of electrostatically actuated MEMS cantilever resonators, International Journal of Non-Linear Mechanics 66 (2014) 28–32.
[46] A.K. Pandey, R. Pratap, Effect of flexural modes on squeeze film damping in MEMS cantilever resonators, Journal of Micromechanics and Microengineering 17 (12) (2007) 2475–2484.
[47] N. Dumas, et al., Design of smart drivers for electrostatic MEMS switches, Sensors and Actuators. A, Physical 167 (2) (2011) 422–432.
[48] B. Peng, et al., Modeling microwave behaviors of series cantilever MEMS switch, Sensors and Actuators. A, Physical 125 (2) (2006) 471–476.
[49] L. Liu, High performance RF MEMS series contact switch - design and simulations, in: 2007 Proceedings 57th Electronic Components and Technology Conference, 2007.
[50] B. Schauwecker, et al., Toggle-switch - a new type of RF MEMS switch for power applications, in: 2002 IEEE MTT-S International Microwave Symposium Digest (Cat. No. 02CH37278), 2002.
[51] H.-C. Lee, J.-H. Park, Y.-H. Park, Development of shunt type ohmic RF MEMS switches actuated by piezoelectric cantilever, Sensors and Actuators. A, Physical 136 (1) (2007) 282–290.
[52] Z.J. Davis, W. Svendsen, A. Boisen, Design, fabrication and testing of a novel MEMS resonator for mass sensing applications, Microelectronic Engineering 84 (5) (2007) 1601–1605.
[53] M. Villarroya, et al., System on chip mass sensor based on polysilicon cantilevers arrays for multiple detection, Sensors and Actuators. A, Physical 132 (1) (2006) 154–164.
[54] H.S. Wasisto, et al., Airborne engineered nanoparticle mass sensor based on a silicon resonant cantilever, Sensors and Actuators. B 180 (2013) 77–89.
[55] H. Sadeghian, et al., Characterizing size-dependent effective elastic modulus of silicon nanocantilevers using electrostatic pull-in instability, Applied Physics Letters 94 (22) (2009) 221903.
[56] M. Maroufi, S.O.R. Moheimani, Design, fabrication and characterization of a high-bandwidth 2DOF MEMS nanopositioner, in: 2013 IEEE/ASME International Conference on Advanced Intelligent Mechatronics, 2013.
[57] C.L. Dym, I.H. Shames, Solid Mechanics: A Variational Approach, augmented edition, Springer, New York, USA, 2013.
[58] H.B. Palmer, The capacitance of a parallel-plate capacitor by the Schwartz–Christoffel transformation, Electrical Engineering 56 (3) (1937) 363–368.
[59] F.M. Serry, D. Walliser, G.J. Maclay, The anharmonic Casimir oscillator (ACO) – the Casimir effect in a model microelectromechanical system, Journal of Microelectromechanical Systems 4 (4) (1995) 193–205.
[60] S.P. Timoshenko, S. Woinowsky-Krieger, Theory of Plates and Shells, McGraw-Hill, 1959.
[61] J.S. Duan, et al., A review of the Adomian decomposition method and its applications to fractional differential equations, Communications in Fractional Calculus 3 (2) (2012) 73–99.
[62] J.N. Israelachvili, Intermolecular and Surface Forces, third edition, Academic Press, USA, 2013.
[63] A.M. Wazwaz, A reliable modification of Adomian decomposition method, Applied Mathematics and Computation 102 (1999) 77–86.
[64] R. Mestrom, et al., Modelling the dynamics of a MEMS resonator: simulations and experiments, Sensors and Actuators. A, Physical 142 (1) (2008) 306–315.
[65] A.M. Bataineh, M.I. Younis, Dynamics of a clamped–clamped microbeam resonator considering fabrication imperfections, Microsystem Technologies 21 (11) (2015) 2425–2434.
[66] A. Bouchaala, A.H. Nayfeh, M.I. Younis, Analytical study of the frequency shifts of micro and nano clamped–clamped beam resonators due to an added mass, Meccanica 52 (1–2) (2017) 333–348.

[67] D. Balaraman, et al., Low-cost low actuation voltage copper RF MEMS switches, in: 2002 IEEE MTT-S International Microwave Symposium Digest (Cat. No. 02CH37278), 2002.
[68] R. Mahameed, G.M. Rebeiz, RF MEMS capacitive switches for wide temperature range applications using a standard thin-film process, IEEE Transactions on Microwave Theory and Techniques 59 (7) (2011) 1746–1752.
[69] F. Hu, et al., A MEMS micromirror driven by electrostatic force, Journal of Electrostatics 68 (3) (2010) 237–242.
[70] C. Winter, et al., Micro-beamer based on MEMS micro-mirrors and laser light source, Procedia Chemistry 1 (1) (2009) 1311–1314.
[71] Y.-C. Cheng, et al., A MEMS micromirror fabricated using CMOS post-process, Sensors and Actuators. A, Physical 120 (2) (2005) 573–581.
[72] S. Patil, V. Chu, J. Conde, Mass sensing using an amorphous silicon MEMS resonator, Procedia Chemistry 1 (1) (2009) 1063–1066.
[73] A. Bouchaala, et al., Mass and position determination in MEMS mass sensors: a theoretical and an experimental investigation, Journal of Micromechanics and Microengineering 26 (10) (2016) 105009.
[74] Y. Li, M. Packirisamy, R.B. Bhat, Shape optimizations and static/dynamic characterizations of deformable microplate structures with multiple electrostatic actuators, Microsystem Technologies 14 (2) (2008) 255–266.
[75] G. Rinaldi, M. Packirisamy, I. Stiharu, Quantitative boundary support characterization for cantilever MEMS, Sensors 7 (10) (2007) 2062–2079.
[76] N.A. Fleck, et al., Strain gradient plasticity: theory and experiment, Acta Metallurgica Et Materialia 42 (2) (1994) 475–487.
[77] D.C.C. Lam, et al., Experiments and theory in strain gradient elasticity, Journal of the Mechanics and Physics of Solids 51 (8) (2003) 1477–1508.
[78] A.W. McFarland, J.S. Colton, Role of material microstructure in plate stiffness with relevance to microcantilever sensors, Journal of Micromechanics and Microengineering 15 (5) (2005) 1060–1067.
[79] F. Yang, et al., Couple stress based strain gradient theory for elasticity, International Journal of Solids and Structures 39 (10) (2002) 2731–2743.
[80] R. Rach, A convenient computational form for the Adomian polynomials, Journal of Mathematical Analysis and Applications 102 (1984) 415–419.
[81] G. Adomian, Stochastic Systems, Academic Press, London, 1983.
[82] M.M. Hosseini, H. Nasabzadeh, On the convergence of Adomian decomposition method, Applied Mathematics and Computation 182 (1) (2006) 536–543.
[83] A. Koochi, M. Abadyan, Evaluating the ability of modified Adomian decomposition method to simulate the instability of freestanding carbon nanotube: comparison with conventional decomposition method, Journal of Applied Sciences 11 (2011) 3421–3428.
[84] A. Kooch, M. Abadyan, Efficiency of modified Adomian decomposition for simulating the instability of nano-electromechanical switches: comparison with the conventional decomposition method, Trends in Applied Sciences Research 7 (1) (2012) 57.
[85] R.M. Stevens, New carbon nanotube AFM probe technology, Materials Today 12 (10) (2009) 42–45.
[86] S. Akita, et al., Nanotweezers consisting of carbon nanotubes operating in an atomic force microscope, Applied Physics Letters 79 (11) (2001) 1691–1693.
[87] J. Chung, et al., Multi-walled carbon nanotubes experiencing electrical breakdown as gas sensors, Nanotechnology 15 (11) (2004) 1596.
[88] C. Wei, et al., Multifunctional chemical vapor sensors of aligned carbon nanotube and polymer composites, Journal of the American Chemical Society 128 (5) (2006) 1412–1413.
[89] P. Dharap, et al., Nanotube film based on single-wall carbon nanotubes for strain sensing, Nanotechnology 15 (3) (2004) 379.
[90] C.-H. Ke, et al., Experiments and modeling of carbon nanotube-based NEMS devices, Journal of the Mechanics and Physics of Solids 53 (6) (2005) 1314–1333.

[91] P. Kim, C.M. Lieber, Nanotube nanotweezers, Science 286 (5447) (1999) 2148–2150.
[92] J. Lee, S. Kim, Manufacture of a nanotweezer using a length controlled CNT arm, Sensors and Actuators. A, Physical 120 (1) (2005) 193–198.
[93] R.H. Baughman, et al., Carbon nanotube actuators, Science 284 (5418) (1999) 1340–1344.
[94] S. Cha, et al., Fabrication of a nanoelectromechanical switch using a suspended carbon nanotube, Applied Physics Letters 86 (8) (2005) 083105.
[95] J. Jang, et al., Nanoelectromechanical switches with vertically aligned carbon nanotubes, Applied Physics Letters 87 (16) (2005) 163114.
[96] M. Dequesnes, S.V. Rotkin, N.R. Aluru, Calculation of pull-in voltages for carbon-nanotube-based nanoelectromechanical switches, Nanotechnology 13 (2002) 120–131.
[97] E. Alves, T.F. Ma, M.L. Pelicer, Monotone positive solutions for a fourth order equation with nonlinear boundary conditions, Nonlinear Analysis 17 (9) (2009) 3834–3841.
[98] R. He, et al., Self-transducing silicon nanowire electromechanical systems at room temperature, Nano Letters 8 (6) (2008) 1756–1761.
[99] J. Zhao, et al., Nonlinear microbeam model based on strain gradient theory, Applied Mathematical Modelling 36 (6) (2012) 2674–2686.
[100] Q. Li, et al., Silicon Nanowire Electromechanical Switch for Logic Device Application, MRS Online Proceedings Library Archive, vol. 1018, 2007.
[101] I. Ouerghi, et al., High performance polysilicon nanowire NEMS for CMOS embedded nanosensors, in: 2014 IEEE International Electron Devices Meeting, IEEE, 2014.
[102] L. Lou, et al., Optimization of NEMS pressure sensors with a multilayered diaphragm using silicon nanowires as piezoresistive sensing elements, Journal of Micromechanics and Microengineering 22 (5) (2012) 055012.
[103] A. Koka, Z. Zhou, H.A. Sodano, Vertically aligned BaTiO 3 nanowire arrays for energy harvesting, Energy & Environmental Science 7 (1) (2014) 288–296.
[104] C. Guthy, et al., Large-scale arrays of nanomechanical sensors for biomolecular fingerprinting, Sensors and Actuators. B, Chemical 187 (2013) 111–117.
[105] W.H. Hayt, J.A. Buck, Engineering Electromagnetics, 6 ed., McGraw-Hill, New York, 2001.
[106] A. Arikoglu, I. Ozkol, Solution of difference equations by using differential transform method, Applied Mathematics and Computation 174 (2) (2006) 1216–1228.
[107] A. Arikoglu, I. Ozkol, Solution of boundary value problems for integro-differential equations by using differential transform method, Applied Mathematics and Computation 168 (2) (2005) 1145–1158.
[108] A. Shah-Mohammadi-Azar, et al., On the modeling of a capacitive angular speed measurement sensor, Measurement 46 (10) (2013) 3976–3981.
[109] Y. Fu, J. Zhang, L. Wan, Application of the energy balance method to a nonlinear oscillator arising in the microelectromechanical system (MEMS), Current Applied Physics 11 (3) (2011) 482–485.
[110] Y. Khan, M. Akbarzade, Dynamic analysis of nonlinear oscillator equation arising in double-sided driven clamped microbeam-based electromechanical resonator, Zeitschrift für Naturforschung. A 67 (8–9) (2012) 435–440.
[111] J. Liu, et al., Nonlinear model and system identification of a capacitive dual-backplate MEMS microphone, Journal of Sound and Vibration 309 (1) (2008) 276–292.
[112] J. Han, et al., A triaxial accelerometer based on differential resonant beams and force-balanced capacitive plates, IEEE Sensors Journal 19 (16) (2019) 6602–6609.
[113] J. Teva, et al., On the electromechanical modelling of a resonating nano-cantilever-based transducer, Ultramicroscopy 100 (3–4) (2004) 225–232.
[114] A. Anthoine, Effect of couple-stresses on the elastic bending of beams, International Journal of Solids and Structures 37 (7) (2000) 1003–1018.
[115] J.-H. He, Variational iteration method for autonomous ordinary differential systems, Applied Mathematics and Computation 114 (2) (2000) 115–123.

[116] D.V. Hutton, Fundamentals of Finite Element Analysis, McGraw-Hill, 2017.
[117] B. Ahmad, R. Pratap, Elasto-electrostatic analysis of circular microplates used in capacitive micromachined ultrasonic transducers, IEEE Sensors Journal 10 (11) (2010) 1767–1773.
[118] W.P. Eaton, et al., A new analytical solution for diaphragm deflection and its application to a surface-micromachined pressure sensor, in: International Conference on Modeling and Simulation, MSM, 1999.
[119] M.T.A. Saif, B.E. Alaca, H. Sehitoglu, Analytical modeling of electrostatic membrane actuator for micro pumps, Journal of Microelectromechanical Systems 8 (3) (1999) 335–345.
[120] F. Schedin, et al., Detection of individual gas molecules adsorbed on graphene, Nature Materials 6 (9) (2007) 652–655.
[121] B.W. Soon, et al., Ultrasensitive nanowire pressure sensor makes its debut, Procedia Engineering 5 (2010) 1127–1130.
[122] W. Yang, W. Kang, X. Wang, Thermal and surface effects on the pull-in characteristics of circular nanoplate NEMS actuator based on nonlocal elasticity theory, Applied Mathematical Modelling 43 (2017) 321–336.
[123] J.N. Reddy, Theory and Analysis of Elastic Plates and Shells, CRC Press, 2006.
[124] L. Zhao, et al., Modeling of electrostatically actuated microplates, in: Q.-A. Huang (Ed.), Micro Electro Mechanical Systems, Springer Singapore, Singapore, 2018, pp. 99–153.
[125] E. Ventsel, T. Krauthammer, E. Carrera, Thin plates and shells: theory, analysis, and applications, Applied Mechanics Reviews 55 (4) (2002) B72–B73.

CHAPTER 3

Numerical solution methods

3.1. Introduction

Nowadays, numerical solutions have become a common approach to solving ordinary and partial differentials equations in different branches of science and technology. The development of modern computers has also simplified applications of numerical methods with heavy calculations. Numerical solutions are specifically appropriate for solving the NEMS/MEMS equations. These equations are usually highly nonlinear, and a precise solution cannot be found for them. Previously researchers have extensively employed numerical methods such as the generalized differential quadrature method [1–9], finite difference method [10–16], and finite element method [17–19] to investigate the behavior of micro- and nanostructures.

In this chapter, some numerical methods for solving nonlinear differential equations are described. Following an introduction to the concept of each method, NEMS/MEMS nonlinear differential equations are considered as an example. Then, these equations are solved using the proposed numerical method. The contents of this chapter are arranged as follows:

- "Generalized differential quadrature method,"
- "Finite difference method," and
- "Finite element method."

3.2. Generalized differential quadrature method

The differential quadrature method is a numerical approach to solve a nonlinear differential equation. In this method, the derivative of a function (with respect to a coordinate) is approximated using the weighted sum of the function values at the designated points along that direction. To clarify the idea of differential quadrature, we can consider a one-dimensional function $f(x)$. The first derivative of $f(x)$ with respect to x can be approximated using the weighted sum of the function values in the defined domain:

$$\left.\frac{df}{dx}\right|_{x_i} = \sum_{j=1}^{N} a_{ij}^{(1)} f(x_j). \tag{3.1}$$

In this equation, N is the number of mesh points in the domain, and $a_{ij}^{(1)}$s are the weighting coefficients for the first derivative. Similarly, the rth order derivative with

https://doi.org/10.1016/B978-0-12-819235-1.00007-2
Copyright © 2020 Elsevier Ltd.
All rights reserved.

respect to x can be approximated by using the following relation:

$$\left.\frac{d^r f}{dx}\right|_{x_i} = \sum_{j=1}^{N} a_{ij}^{(r)} . f(x_j) \tag{3.2}$$

where $a_{ij}^{(r)}$s indicate the weighting coefficients for the rth order derivative. The efficiency of the differential quadrature method is profoundly affected by the selection of grid points, as well as the accuracy of the weighting coefficients.

The accuracy of the weighting coefficients can be determined via considering a test function (e.g., $g_k(x) = x^k$ $(k = 1, 2, ..., N-1)$). The first derivative of the test function is evaluated using Eq. (3.1), which yields a set of linear algebraic equations. The weighting coefficients can be investigated through this system of algebraic equations called the Vandermonde system of equations. However, by increasing the number of grid points, the acquisition of the weighting coefficients gets more difficult using the Vandermonde system of equations. Another assumption for the test function comes from the Nth order Legendre polynomial. While this assumption results in a simple definition for the weighting coefficients, the Legendre polynomial forces the grid points to be roots of the shifted Legendre polynomial, regardless of the problem.

Shu and Richards proposed the Generalized Differential Quadrature (GDQ) method to find the weighting coefficients without restricting the grid point selection [20]. To do so, they assumed the Lagrange interpolation polynomials as test functions:

$$g_k(x) = \frac{G(x)}{(x - x_k) G^{(1)}(x_k)} \quad (k = 1, 2, ..., N) \tag{3.3}$$

where:

$$\begin{aligned} G(x) &= \prod_{j=1;}^{N} (x - x_j), \\ G^{(1)}(x_i) &= \left.\frac{\partial G(x)}{\partial x}\right|_{x=x_i} = \prod_{j=1; j\neq i}^{N} (x_i - x_j) \quad (j = 1, 2, ..., N). \end{aligned} \tag{3.4}$$

Now, by using Eq. (3.4) in Eq. (3.1), the weighting coefficients for the first derivative are obtained as:

$$\begin{aligned} a_{ij}^1 &= \frac{\prod_{j=1; j\neq i}^{N} (x_i - x_j)}{(x_i - x_j) \prod_{i=1; i\neq j}^{N} (x_j - x_i)} \quad (i, j = 1, 2, ..., N; i \neq j), \\ a_{ii}^1 &= -\sum_{j=1}^{N} a_{ij}^1. \end{aligned} \tag{3.5}$$

Correspondingly, the weighting factors for higher derivatives can be computed as

$$a_{ij}^{(r)} = \begin{cases} r\left[a_{ij}^{(r-1)} a_{ij}^{(r)} - \dfrac{a_{ij}^{(r-1)}}{x_i - x_j}\right] & \text{for } i \neq j, \\ -\sum\limits_{j=1}^{N} a_{ij}^{(r)} & \text{for } i = j \quad (i, j = 1, 2, ..., N; 2 \leq r \leq N-1). \end{cases} \tag{3.6}$$

In GDQ, the grid point selection is somewhat arbitrary. However, Shu and Richards showed that the Chebyshev–Gauss–Lobatto mesh provides a more accurate solution for GDQ:

$$x_i = \frac{L}{2}\left(1 - \cos\frac{i-1}{N_x - 1}\pi\right), \quad i = 1, 2, 3, ..., N. \tag{3.7}$$

3.2.1 Impact of size and surface energies on the performance of nanotweezers

As mentioned in Section 2.5.1, nanotweezers are fundamental structures for manipulating nanoparticles. In Section 2.5.1, nanotweezers manufactured from a nanowire were studied. Herein, the equation for nanotweezers with rectangular cross-sections (by considering the simultaneous effect of size-dependency and surface energies) is extracted and solved using GDQ.

An SEM image of microtweezers with rectangular cross-section is illustrated in Fig. 3.1. These microtweezers were constructed from an initially curved microbeam. Fig. 3.2 demonstrates a typical rectangular cross-section of the nanotweezers. As can be seen, the nanotweezers are constructed using two identical parallel straight nanobeams with length L. The arms' cross-section is a rectangle with thickness h and width b.

The simultaneous size and surface energy effect can alter the performance of nanostructures [22–26]. To simulate the simultaneous effect of size-dependency and surface energies, each arm is considered as bulk with the zero-thickness surface. The size-dependent behavior of the bulk materials can be investigated by employing the size-dependent theories. Consistent couple stress elasticity is a scale-dependent elasticity theory developed by Hadjesfandiari and Dargush [27]. It should be noted that in the modified couple stress theory, the couple stress tensor is symmetric as a result of equilibrium in the moments of couples. However, in the consistent couple stress theory, the stress tensor is generally asymmetric.

To explain the consistent couple stress theory, equilibrium equations for the isotropic linear elastic material are considered as follows:

$$\sigma_{ij,j} + F_i = 0, \tag{3.8}$$

$$\mu_{ji,i} + e_{ijk}\sigma_{jk} + C_i = 0 \tag{3.9}$$

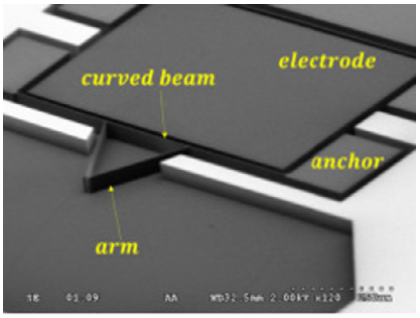

(A)

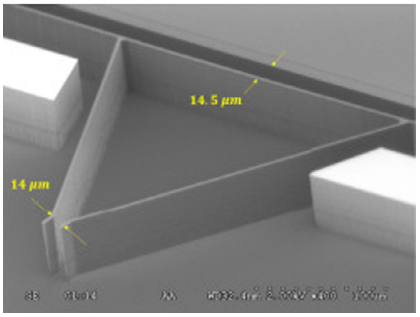

(B)

Figure 3.1 (A) SEM image of microtweezers [21]; (B) closed image of the tip of the microtweezers [21].

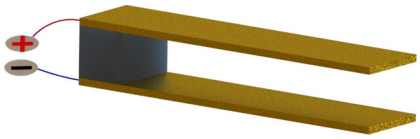

Figure 3.2 Schematic representation of nanotweezers.

where σ_{ij} is the stress tensor, μ_{ij} is the couple-stress tensor, F_i is the body force per unit volume, C_i is body couple per unit volume, and e_{ijk} is the permutation tensor.

The stress tensor can be decomposed into a symmetric ($\sigma_{(ij)}$) part (which is equal to the classical stress tensor) and a skew-symmetric ($\sigma_{[ij]}$) component, as follows:

$$\sigma_{(ij)} = \lambda \varepsilon_{mm} \delta_{ij} + 2\mu \varepsilon_{ij}. \tag{3.10}$$

In this equation, μ and λ are Lame's constants, δ_{ij} is the Kronecker delta, and ε_{ij} is the strain tensor component. Similarly, the displacement gradient can be decomposed into a symmetric component (which is the strain tensor) and a skew-symmetric part (which

is the rotation tensor (ω_{ij})), defined as follows:

$$\varepsilon_{ij} = \frac{1}{2}(u_{i,j} + u_{j,i}) = \varepsilon_{ji}, \tag{3.11}$$

$$\omega_{ij} = \frac{1}{2}(u_{i,j} - u_{j,i}) = -\omega_{ji}. \tag{3.12}$$

The rotation tensor dual-vector can be expressed as

$$\theta_i = \frac{1}{2}e_{ijk}\omega_{kj}. \tag{3.13}$$

By decomposing the rotation tensor gradient into symmetrical (χ_{ij}) and skew-symmetrical (κ_{ij}) parts, one obtains:

$$\chi_{ij} = \theta_{(i,j)} = \frac{1}{2}(\theta_{i,j} + \theta_{j,i}), \tag{3.14}$$

$$\kappa_{ij} = \theta_{[i,j]} = \frac{1}{2}(\theta_{i,j} - \theta_{j,i}). \tag{3.15}$$

The dual-vector corresponding with the skew-symmetrical couple stress tensor can be expressed as:

$$m_i = \frac{1}{2}e_{ijk}\mu_{kj}. \tag{3.16}$$

The dual-vector of the couple stress linear elastic isotropic material is [27]

$$m_i = -8\mu l^2 k_i. \tag{3.17}$$

In the above equation, l is the material's length scale parameter that represents their size-dependency and μ is the shear modulus. Also, the skew-symmetric part of the stress tensor can be explained as

$$\sigma_{[ij]} = -m_{[i,j]}. \tag{3.18}$$

Hence, the strain energy density is obtained as [2]

$$U_B = \frac{1}{2}\oint_{\vartheta}(\sigma_{(ij)}\varepsilon_{ij} + \mu_{ij}\kappa_{ij})d\vartheta. \tag{3.19}$$

By reducing the dimension of a body, its surface-to-volume ratio increases. Hence, the surface layer can affect the performance of the nanostructures remarkably. To incorporate the surface energies into the nanotweezers' constitutive equation, the Gurtin–Murdoch surface elasticity can be employed. In this theory, the impact of the surface residual stress and surface elasticity are both taken into account [28]. Based on the

Gurtin–Murdoch theory, the strain energy in the zero-thickness surface layer with (U_S) is defined as [29]

$$U_S = \frac{1}{2}\int_0^L \oint_{\partial A} \tau_{ij}\varepsilon_{ij} ds dX. \tag{3.20}$$

The surface stress can be considered as in-plane shear stress and out-of-plane shear stress. The in-plane components are formulated as

$$\tau_{\alpha\beta} = \mu_0(u_{\alpha,\beta} + u_{\beta,\alpha}) + (\lambda_0 + \tau_0)u_{p,p}\delta_{\alpha\beta} + \tau_0(\delta_{\alpha\beta} - u_{\beta,\alpha}) \tag{3.21}$$

where μ_0 and λ_0 are surface elastic parameters, and τ_0 is the residual surface stress. Moreover, the out-of-plane components are defined as

$$\tau_{n\alpha} = \tau_0(u_{n,\alpha}). \tag{3.22}$$

Each arm of the nanotweezers is modeled as an Euler–Bernoulli beam. Using the Euler–Bernoulli beam displacement vector (i.e., Eq. (2.9)), the nonzero components are obtained as:

$$\kappa_{XY} = \kappa_{YX} = -\frac{1}{2}\frac{d^2W}{dX^2}, \tag{3.23}$$

$$\mu_{XY} = -\mu_{YX} = 4\mu l^2 \frac{d^2W}{dX^2}, \tag{3.24}$$

$$\varepsilon_{XX} = -Z\frac{d^2W}{dX^2}, \tag{3.25}$$

$$\sigma_{XX} = -EZ\frac{d^2W}{dX^2}, \tag{3.26}$$

$$\tau_{XX} = \tau_0 - ZE_0\frac{d^2W}{dX^2}, \quad \tau_{YY} = -(\tau_0 + \lambda_0)Z\frac{d^2W}{dX^2}, \tag{3.27}$$

$$\tau_{nX} = \tau_0\frac{du_n}{dX}. \tag{3.28}$$

By substituting Eqs. (3.23) to (3.26) into Eq. (3.19), as well as Eqs. (3.27) and (3.28) into Eq. (3.20), and integrating the results over the beam volume, the bulk and surface strain energies are obtained as:

$$\begin{aligned} U_B &= \frac{1}{2}\int_0^L \int_A \left\{ \begin{array}{l} 4\mu l^2 \dfrac{d^2W}{dX^2}\left(\dfrac{1}{2}\dfrac{d^2W}{dX^2}\right) \\ -4\mu l^2 \dfrac{d^2W}{dX^2}\left(-\dfrac{1}{2}\dfrac{d^2W}{dX^2}\right) - Z\dfrac{d^2W}{dX^2}\left(-ZE\dfrac{d^2W}{dX^2}\right) \end{array} \right\} dA dX \\ &= \frac{1}{2}\int_0^L \left[(EI + 4\mu A l^2)\left(\frac{d^2W}{dX^2}\right)^2 \right] dX, \end{aligned} \tag{3.29}$$

$$\begin{aligned} U_S &= \frac{1}{2}\int_0^L \oint_{\partial A} \left\{ \tau_0 n_Z^2 (\frac{dW}{dX})^2 - \tau_0 Z \frac{d^2W}{dX^2} + E_0(-Z\frac{d^2W}{dX^2})^2 \right\} ds dX \\ &= \frac{1}{2}\int_0^L \{E_0 I_0 (\frac{d^2W}{dX^2})^2 + \tau_0 S_0 (\frac{dW}{dX})^2\} dX \end{aligned} \tag{3.30}$$

where A is the cross-section area, and I is the cross-section second moment of area. Besides, for the rectangular cross-section we have:

$$\begin{aligned} I_0 &= \int_S z^2 ds = \frac{1}{2}bh^2 + \frac{1}{6}h^3, \\ S_0 &= \int_S n_z^2 ds = 2b. \end{aligned} \tag{3.31}$$

The work done by the electrical and Casimir forces is determined as

$$W_{ext} = \int_0^L \int_0^W f_{elec} dW dX + \int_0^L \int_0^W f_{Cas} dW dX. \tag{3.32}$$

The electrical force can be obtained using the first derivative of the capacitor capacitance with respect to the gap. The capacitance per unit length of two finite parallel plates using Palmer's formula of fringing field is [30]

$$C(g) = \frac{\varepsilon b}{g}\left[1 + \frac{g}{\pi b} + \frac{g}{\pi b}\ln\left(\frac{2\pi b}{g}\right)\right]. \tag{3.33}$$

Using the above equation, the electrical energy per unit length is determined as

$$E_{elec} = \frac{1}{2}C(g)V^2 = \frac{\varepsilon b V^2}{2g}\left[1 + \frac{g}{\pi b} + \frac{g}{\pi b}\ln\left(\frac{2\pi b}{g}\right)\right]. \tag{3.34}$$

Finally, the electrical force per unit length of a nanotweezers' arm can be achieved by considering the nonuniform electric field as

$$f_{elec} = -\frac{\partial E_{elec}}{\partial g} = \frac{\varepsilon b V^2}{2g^2}\left[1 + \frac{1}{\pi}\left(\frac{g}{b}\right)\right]. \tag{3.35}$$

For nanotweezers with identical arms, deflections are the same ($W_1 = W_2 = W$). Therefore, by replacing the initial gap (g) with the new gap after deflection of the arms ($g - 2W$), the electrical force is obtained as

$$f_{elec} = \frac{\varepsilon b V^2}{2(g-2W)^2}\left[1 + \frac{1}{\pi}\left(\frac{g-2W}{b}\right)\right] \approx \frac{\varepsilon b V^2}{2(g-2W)^2}\left[1 + 0.32\frac{g-2W}{b}\right]. \tag{3.36}$$

As mentioned in the previous chapter, two distinct regimes (i.e., the Casimir regime for significant gaps and van der Waals force for small separations) can be considered

for submicron separation. The Casimir force between the nanotweezers arms can be achieved from the Casimir force relation of two parallel plates (i.e., Eq. (1.7)). For nanotweezers with identical arms, by replacing g with $g-2W$ in Eq. (1.7), the Casimir force per unit length of each arm after deflection is obtained as

$$f_{Cas}=\frac{\pi^2\hbar cb}{240(g-2W)^4}. \tag{3.37}$$

To derive the system equation, Hamilton's principle is applied as follows:

$$\delta(U_B+U_S-W_{ext})=0. \tag{3.38}$$

By using Eqs. (3.29), (3.30), and (3.32) in Eq. (3.38), we obtain

$$\begin{aligned}&\int_0^L\left[\begin{array}{l}(EI+4\mu Al^2+E_0I_0)\dfrac{d^4W}{dX^4}-\tau_0S_0\dfrac{d^2W}{dX^2}\\ \rho A\dfrac{d^2W}{dt^2}-F_{ext}(X)\end{array}\right]\delta W dX\\&+\left[\tau_0S\frac{dW}{dX}\delta W-(EI+4\mu Al^2+E_0I_0)\frac{d^3W}{dX^3}\delta W\right]_0^L\\&+\left[(EI+4\mu Al^2+E_0I_0)\frac{d^2W}{dX^2}\delta\left(\frac{dW}{dX}\right)\right]_0^L=0.\end{aligned} \tag{3.39}$$

The governing equation of the nanotweezers is extracted from the above variational equation as

$$(EI+\mu Al^2+E_0I_0)\frac{d^4W}{dX^4}-\tau_0S_0\frac{d^2W}{dX^2}=F_{ext}(X) \tag{3.40}$$

with the following boundary condition:

$$\begin{aligned}&\tau_0S_0\frac{dW}{dX}-(EI+\mu Al^2+E_0I_0)\frac{d^3W}{dX^3}\bigg|_{X=0,L}=0\quad\text{or}\quad\delta W|_{X=0,L}=0,\\&(EI+\mu Al^2+E_0I_0)\frac{d^2W}{dX^2}\bigg|_{X=0,L}=0\quad\text{or}\quad\delta\left(\frac{dW}{dX}\right)\bigg|_{X=0,L}=0.\end{aligned} \tag{3.41}$$

To derive the dimensionless governing equation of nanotweezers, the dimensionless parameters of length and deflection are considered as $x=X/L$ and $w=W/g$, respectively. This leads to the following dimensionless governing equation for each arm of nanotweezers:

$$\left(1+\frac{24}{1+\upsilon}\left(\frac{l}{h}\right)^2+e_0\right)\frac{d^4w}{dx^4}-t_0\frac{d^2w}{dx^2}=\frac{\alpha^2\left[1+0.32\gamma\,(1-2w)\right]}{(1-2w)^2}+\frac{\beta_{Cas}}{(1-2w)^4}, \tag{3.42}$$

$$w(0) = \frac{dw}{dx}(0) = 0, \tag{3.43}$$

$$\left(1 + \frac{24}{1+\upsilon}\left(\frac{l}{h}\right)^2 + e_0\right)\frac{d^2w}{dx^2}(1) = 0,$$
$$t_0\frac{dw}{dx}(1) - \left(1 + \frac{24}{1+\upsilon}\left(\frac{l}{h}\right)^2 + e_0\right)\frac{d^3w}{dx^3}(1) = 0 \tag{3.44}$$

with the following dimensionless parameters:

$$\alpha^2 = \frac{\varepsilon b V^2 L^4}{2g^3 EI}, \tag{3.45}$$

$$\beta_{Cas} = \frac{\pi^2 \hbar c b L^4}{240 g^5 EI}, \tag{3.46}$$

$$e_0 = \frac{E_0 I_0 h - \tau_0 \upsilon I}{EIh}, \tag{3.47}$$

$$t_0 = \frac{2b\tau_0 L^2}{EI}, \tag{3.48}$$

$$\gamma = \frac{g}{b}. \tag{3.49}$$

In the above equation, α is the dimensionless parameter related to the external force, β_{Cas} is the dimensionless parameter of Casimir force, E_0 is the dimensionless parameter pertinent to the surface elasticity, t_0 is the dimensionless parameter related to the residual surface stress, and γ is the gap-to-width ratio. To extract the discretized equation of the system, the second and the fourth derivatives of w (with respect to x) are determined according to GDQ and are replaced in Eq. (3.44):

$$\left(1 + \frac{24}{1+\upsilon}\left(\frac{l}{h}\right)^2 + e_0\right)\sum_{i=1}^{N} a_{pi}^{(4)} w_p - t_0 \sum_{i=1}^{N} a_{pi}^{(2)} w_p$$
$$= \frac{\alpha^2\left[1 + 0.32\gamma\left(1 - 2w_p\right)\right]}{(1-2w_p)^2} + \frac{\beta_{Cas}}{(1-2w_p)^4} \quad \text{for } p = 1, 2, ...N, \tag{3.50}$$

with the following boundary conditions:

$$w_1 = 0,$$
$$\sum_{i=1}^{N} a_{1i}^{(1)} w_i = 0,$$
$$\left(1 + e_0 + \frac{24}{(1+\upsilon)}\left(\frac{l}{h}\right)^2\right)\sum_{i=1}^{N} a_{Ni}^{(2)} w_i = 0,$$

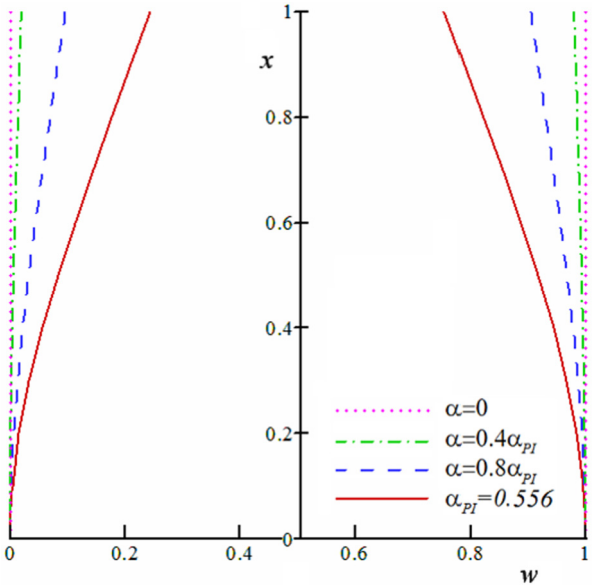

Figure 3.3 Nanotweezers' arms deflection

$$t_0 \sum_{i=1}^{N} a_{Ni}^{(1)} w_i - \left(1 + e_0 + \frac{24}{(1+\upsilon)}\left(\frac{l}{h}\right)^2\right) \sum_{i=1}^{N} a_{Ni}^{(3)} w_i = 0. \tag{3.51}$$

It should be noted that w_p determines the deflection at $x = x_p$ ($w(x = x_p)$). Moreover, $a_{pq}^{(r)}$ signifies the weighting coefficients associated with the rth-order derivatives with respect to x. The arms' deflection is achieved via solving the system of algebraic equations (3.50) and (3.51).

The deflection of nanotweezers' arms by neglecting both surface and size effect is presented in Fig. 3.3. By increasing the applied voltage (up to the pull-in voltage), the nanotweezers' arms move towards each other, reducing the gap. When the applied voltage is equivalent to the pull-in voltage, nanotweezers' arms will instantly reach each other. It should be mentioned that the pull-in voltage restricts the smallest particle size that can be manipulated using the nanotweezers.

Since dispersion forces appear at the nanoscale, investigating the behavior of free-standing nanotweezers is a crucial issue in the design and manufacture of such devices. In this case, exceeding the dispersion forces from the critical value leads to instability of the nanotweezers, even with no external voltage. It can vividly be seen in Eq. (3.46) that the dimensionless Casimir force is dependent on the arm's length, arm's thickness, and initial gap. By investigating the critical values for the Casimir force, the maximum permissible length, minimum gap, and minimum arms' thickness can be obtained. To investigate the critical values for Casimir forces (i.e., β_{Cas}^{*}), the dimensionless parameter

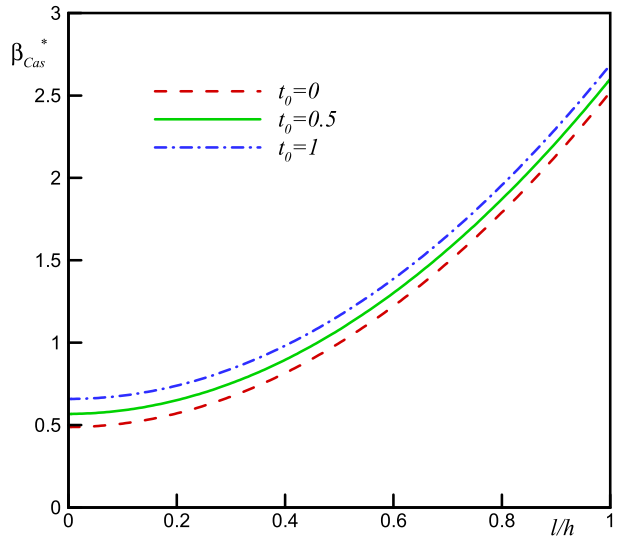

Figure 3.4 Impact of scale-dependency and surface residual stress on critical Casimir forces.

for voltage is set to zero in the equation, while the tip deflection is plotted versus β_{Cas}. For β_{Cas}s greater than the Casimir force critical value ($\beta_{Cas} > \beta^*_{Cas}$), stiction occurs. By replacing β^*_{Cas} in the definition of β_{Cas} in Eq. (3.46), the values for $L_{\max}$, $h_{\min}$, and $g_{\min}$ can be determined:

$$L_{\max} = \sqrt[4]{\frac{20g^5Eh^3\beta^*_{Cas}}{\pi^2\hbar c}}, \tag{3.52}$$

$$g_{\min} = \sqrt[5]{\frac{\pi^2\hbar cL^4}{20Eh^3\beta^*_{Cas}}}, \tag{3.53}$$

$$h_{\min} = \sqrt[3]{\frac{\pi^2\hbar cL^4}{20Eg^5\beta^*_{Cas}}}. \tag{3.54}$$

Fig. 3.4 demonstrates the impact of scale-dependency and residual surface stress on the Casimir force's critical values (β^*_{Cas}). This figure reveals that the size parameter (l/h) increases the critical values of the Casimir force, thus increasing the detachment length and reducing the minimum gap and minimum thickness (see Eqs. (3.52), (3.53), and (3.54)). Furthermore, this figure illustrates that residual surface stress increases the dispersion force's critical values (β^*_{Cas}).

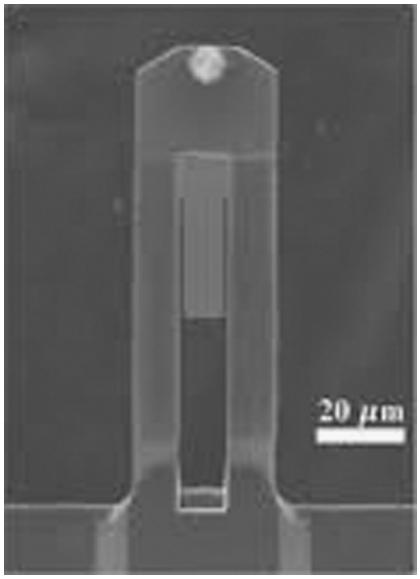

Figure 3.5 SEM image of U-shaped microcantilever with inner paddle [37].

3.2.2 U-shaped nanosensor

U-shaped NEMS/MEMS have high potential for manufacturing novel ultrasmall switches [31,32], sensors [33], and actuators [34]. A U-shaped NEMS is constructed form two parallel cantilever beams. At the free end of the beams, a rigid plate is attached. The beams can have either rectangular or circular cross-section. U-shaped NEMS/MEMS have outstanding advantages such as low actuation voltage, high flexibility, enhanced electrical performance, high ON/OFF current ratio, and repeatable switching behavior [31,34–36].

In this section, the behavior of a U-shaped nanosensor operated in the van der Waals regime is investigated. Fig. 3.5 demonstrates a U-shaped microcantilever with an inner paddle. A similar U-shaped structure with an outer paddle is modeled in Fig. 3.6. The proposed U-shaped nanosensor is manufactured from two cantilever nanowires attached to a rigid rectangular plate. The nanowires' length and radius are L and r, respectively. The attached plate at the free end of nanowires is a rectangular plate with length a, width b, and thickness t. Also, the initial gap between the U-shaped element and the plane is g.

Hamilton's principle can be employed to extract the governing equation of a U-shaped nanosensor. To this end, the strain energy and the work done by the external force should be investigated. The strain energy of each nanowire is

$$U = \frac{1}{2}\iiint \sigma_{ij}\varepsilon_{ij}dV \tag{3.55}$$

Figure 3.6 A typical U-shaped nanosensor.

where σ_{ij} is the stress tensor, and ε_{ij} is the strain tensor. Each nanowire can be modeled as a cantilever Euler–Bernoulli beam. For an Euler–Bernoulli beam, the stress and strain tensor components were computed previously. By considering the same geometry for nanowires and substituting Eqs. (2.20) and (2.21) into Eq. (3.120), furthermore, the total strain energy of two cantilever nanowires is obtained as

$$U = \int_0^L EI \left(\frac{\partial^2 W}{\partial X^2} \right)^2 dX. \tag{3.56}$$

The work by the external loads is the sum of the work done by distributed force along the beam (i.e., van der Waals and electrical force) and the concentrated force and moment at the nanobeams free end. The concentrated force and moment at the free end are the results of the van der Waals and electrical force acting on the rigid plate attached to the end of the beam. The following formula governs the work done by the distributed load:

$$V_{ext} = 2 \int_0^L \int_0^w f_{ext} dW dX. \tag{3.57}$$

In the above equation, f_{ext} is the sum of electrical and van der Waals forces. Eqs. (2.180) and (2.184) can be employed to investigate the electrical and van der Waals forces acting on a cylindrical nanowire parallel to a flat plate.

The distributed electrical and van der Waals forces acting on the rigid plate result in the stress on the nanowires. The work done by the moment traction of electrical force and van der Waals attraction acting on the rigid plate, V_M, is gained as

$$V_M = M \frac{\partial W(L)}{\partial X}. \tag{3.58}$$

The work done by the force traction of the electrical force and the van der Waals attraction acting on the rigid plate, V_F, is attained as

$$V_F = FW(L). \tag{3.59}$$

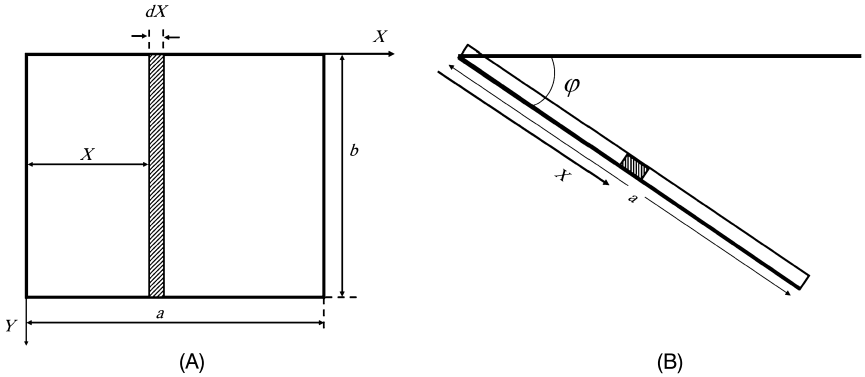

Figure 3.7 The attached rigid plate: (A) top view of integration element; (B) side view of the deflected plate.

The force and moment acting of the rigid plate can be investigated by integrating the electrical and van der Waals forces over the rigid plate area. An infinitesimal element of the rigid plate is demonstrated in Fig. 3.7.

The electrical forces acting on an infinitesimal element can be computed by using the parallel plate capacitor model:

$$dF_{elec} = \frac{\varepsilon_0 V^2 b}{2\left(g - W(L) - X\sin(\varphi)\right)^2} dX. \tag{3.60}$$

By using the above relation, the electrical moment acting on an infinitesimal element is attained as

$$dM_{elec} = \frac{\varepsilon V^2 b}{2\left(g - W(L) - X\sin(\varphi)\right)^2} X\cos(\varphi)\, dX. \tag{3.61}$$

Similarly, by considering the parallel plate formulation of van der Waals force, the van der Waals forces acting on an infinitesimal element can be determined as

$$dF_{vdW} = \frac{\bar{A} b}{6\pi\left(g - W(L) - X\sin(\varphi)\right)^3} dX. \tag{3.62}$$

By using the above relation, the van der Waals moment acting on an infinitesimal element is attained as

$$dM_{vdW} = \frac{\bar{A} b}{6\pi\left(g - W(L) - X\sin(\varphi)\right)^3} X\cos(\varphi)\, dX. \tag{3.63}$$

By integrating over the rigid plate area, the electrical force and moment acting on the rigid plate is obtained as:

$$\begin{aligned} F_{elec} &= \int_0^a \frac{\varepsilon V^2 b}{2\left(g - W(L) - X\sin(\varphi)\right)^2} dX \\ &= \frac{\varepsilon ab V^2}{2(g - W(L) - a\sqrt{\frac{W'^2(L)}{1+W'^2(L)}})(g - W(L))}, \end{aligned} \tag{3.64}$$

$$\begin{aligned} M_{elec} &= \int_0^a \frac{\varepsilon V^2 bX\cos(\varphi)\, dX}{2\left(g - W(L) - X\sin(\varphi)\right)^2} \\ &= \frac{\varepsilon ab V^2}{2} \frac{\sqrt{\frac{1}{1+W'^2(L)}}(\frac{g-W(L)}{a} - \Psi)\,\mathrm{Ln}(\frac{g-W(L)-a\Psi}{g-W(L)}) + \Psi^2}{\Psi^2(g - W(L) - a\Psi)}, \end{aligned} \tag{3.65}$$

$$\Psi = \sqrt{\frac{W'^2(L)}{1 + W'^2(L)}}.$$

In a similar manner, the van der Waals force and moment are determined as:

$$\begin{aligned} F_{vdW} &= \int_0^a \frac{\bar{A}b}{6\pi\left(g - W(L) - X\sin(\varphi)\right)^3} dX \\ &= \frac{\bar{A}ab\left[2g - 2W(L) - a\Psi\right]}{12\pi(g - W(L) - a\Psi)^2(g - W(L))^2}, \end{aligned} \tag{3.66}$$

$$\begin{aligned} M_{vdW} &= \int_0^a \frac{\bar{A}b}{6\pi\left(g - W(L) - X\sin(\varphi)\right)^3} X\cos(\varphi)\, dX \\ &= \frac{\bar{A}a^2 b\sqrt{\frac{1}{1+W'^2(L)}}}{12\pi(g - W(L) - a\Psi)^2(D - W(L))}. \end{aligned} \tag{3.67}$$

Using the above exact values of force and moment results in extremely complex boundary conditions of the constitutive differential equation. To overcome this complexity, the distributed force on the attached plated can be replaced with a concentrated force and moment at the force center of the attached plate. The force center of the attached plate is a point where the distributed force along the plate can be replaced with a concentrated force at that point. Therefore, the distance of the pressure center ($\bar{X}$) has the following relationship with the total force (F) and moment (M):

$$\bar{X} = \frac{M}{F}. \tag{3.68}$$

Based on the above-mentioned approach, the force and moment acting on the tip on nanowires are simplified as:

$$M = \frac{\varepsilon a b V^2 \bar{X}}{2(g - W(L) - \bar{X}W'(L))^2} + \frac{\bar{A} a b \bar{X}}{12\pi(D - W(L) - \bar{X}W'(L))^3}, \tag{3.69}$$

$$F = \frac{\varepsilon a b V^2}{2(g - W(L) - \bar{X}W'(L))^2} + \frac{\bar{A} a b}{12\pi(D - W(L) - \bar{X}W'(L))^3}. \tag{3.70}$$

The total energy of the system can be summarized as

$$\Pi = U - V_{ext} - V_M - V_F. \tag{3.71}$$

By substituting Eqs. (3.121)–(3.59) into Eq. (3.71) and using Eqs. (3.64)–(3.67), the total energy of the system is obtained as:

$$\begin{aligned}\Pi = &\int_0^L EI\left(\frac{d^2W}{dX^2}\right)^2 dX - 2\int_0^L \int_0^W f_{ext} dW dX \\ &- \frac{\varepsilon a b V^2 W(L)}{2(g - W(L) - \bar{X}W'(L))^2} - \frac{\bar{A} a b w(L)}{12\pi(D - W(L) - \bar{X}W'(L))^3} \\ &- \frac{\varepsilon a b V^2 \bar{X}}{2(g - W(L) - \bar{X}W'(L))^2}\frac{\partial W(L)}{\partial X} - \frac{\bar{A} a b \bar{X}}{12\pi(D - W(L) - \bar{X}W'(L))^3}\frac{dW(L)}{dX}.\end{aligned} \tag{3.72}$$

Hamilton's principle implies that in the equilibrium condition, the variation of total energy is zero (i.e., $\delta\Pi = 0$). Finally, the constitutive equation of a U-shaped nanosensor is obtained as:

$$EI\frac{d^4W}{dX^4} = \frac{\pi\varepsilon V^2}{(g - Ww)\ln^2\left(2\frac{g-W}{r}\right)} + \frac{\bar{A} r^2}{(g - W)^4}, \tag{3.73}$$

$$W(0) = 0, \tag{3.74}$$

$$\frac{dW}{dX}(0) = 0, \tag{3.75}$$

$$EI\frac{d^2W}{dX^2}(L) = \frac{\varepsilon a b V^2 \bar{X}}{2(g - W(L) - \bar{X}W'(L))^2} + \frac{\bar{A} a b \bar{X}}{12\pi(g - W(L) - \bar{X}W'(L))^3}, \tag{3.76}$$

$$EI\frac{d^3W}{dX^3}(L) = -\frac{\varepsilon a b V^2}{2(g - W(L) - \bar{X}W'(L))^2} - \frac{\bar{A} a b}{12\pi(g - W(L) - \bar{X}W'(L))^3}. \tag{3.77}$$

By defining $x = X/L$ and $w = W/g$, the dimensionless governing equation and boundary conditions of the paddle-type NEMS are obtained as:

$$\frac{d^4w}{dx^4} = \frac{\beta_{vdW}}{k(1 - w)^4} + \frac{\alpha^2}{(1 - w)\ln^2[2k(1 - w)]}, \tag{3.78}$$

$$w(0) = 0, \tag{3.79}$$

$$\frac{dw}{dX}(0) = 0, \tag{3.80}$$

$$\frac{d^2w}{dx^2}(1) = \vartheta\xi\left[\frac{\alpha^2}{k(1-w(1)-\xi w'(1))^2} + \frac{\beta_{vdW}}{6(1-w(1)-\xi w'(1))^4}\right], \tag{3.81}$$

$$\frac{d^3w}{dx^3}(1) = -\vartheta\left[\frac{\alpha^2}{k(1-w(1)-\xi w'(1))^2} + \frac{\beta_{vdW}}{6(1-w(1)-\xi w'(1))^4}\right]. \tag{3.82}$$

In the above equation, the dimensionless parameters are:

$$\xi = \frac{\bar{x}}{L}, \tag{3.83}$$

$$\vartheta = \frac{ab}{2\pi rL}, \tag{3.84}$$

$$k = \frac{g}{r}, \tag{3.85}$$

$$\beta_{vdW} = \frac{\bar{A}rL^4}{EIg^4}, \tag{3.86}$$

$$\alpha^2 = \frac{\pi\varepsilon V^2L^4}{EIg^2}. \tag{3.87}$$

It is worth mentioning that in the above relations, ξ indicates the force center distance-to-the beam length ratio, ϑ is the plate area-to-wire surface area ratio, k indicates the gap-to-radius ratio. Also, α and β_{vdW} are the dimensionless parameters of the electrical and the van der Waals forces, respectively.

To establish a GDQ solution for the nonlinear differential equation (3.78), each nanowire is divided into N elements by using the Chebyshev–Gauss–Lobatto mesh generator (i.e., Eq. (3.7)). The fourth derivative of w (with respect to x) is determined according to GDQ by using Eq. (3.2). Therefore, the discretized constitutive equation of a U-shaped nanosensor is achieved as

$$\sum_{i=1}^{N} a_{pi}^{(4)} w_p = \frac{\alpha}{k(1-w_p)^4} + \frac{\beta^2}{(1-w_p \ln^2[2k(1-w_p)]} \quad \text{for } p = 1, 2, ...N. \tag{3.88}$$

Also, since the boundary conditions depend on w and its directives with respect to x, by using Eq. (3.2), the discretized boundary conditions are obtained as:

$$\begin{aligned}
&w_1 = 0,\\
&\sum_{i=1}^{N} a_{1i}^{(1)} w_i = 0,\\
&\sum_{i=1}^{N} a_{Ni}^{(2)} w_i = \vartheta\xi\left[\frac{\beta^2}{k(1-w_N-\xi\sum_{i=1}^{N} a_{Ni}^{(1)} w_i))^2} + \frac{\alpha}{6(1-w_N-\xi\sum_{i=1}^{N} a_{Ni}^{(1)} w_i)^4}\right],\\
&\sum_{i=1}^{N} a_{Ni}^{(3)} w_i = -\vartheta\left[\frac{\beta^2}{k(1-w_N-\xi\sum_{i=1}^{N} a_{Ni}^{(1)} w_i))^2} + \frac{\alpha}{6(1-w_N-\xi\sum_{i=1}^{N} a_{Ni}^{(1)} w_i)^4}\right].
\end{aligned} \tag{3.89}$$

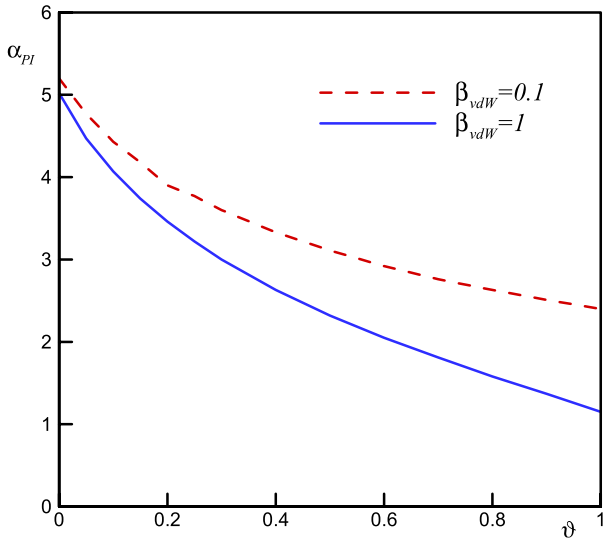

Figure 3.8 Effect of attached plate geometry and van der Waals force on the pull-in voltage of a U-shaped nanosensor ($k = 20, \xi = 0.01$).

The effects of the attached plate geometry on the instability voltage of the U-shaped nanosensor are illustrated in Fig. 3.8. In this figure, the influence of the van der Waals force is also considered. Fig. 3.8 vividly demonstrates that the pull-in voltage reduces with increasing ϑ. This reduction in the pull-in voltage implies that an increase in the attached plate surface increases the external forces and reduces the stability threshold of the sensor. Also, this figure reveals that the impact of the van der Waals force on the instability is more dominant for larger values of ϑ, which is also connected to enhancing the van der Waals force by increasing the paddle area.

Fig. 3.9 shows the impact of the gap-to-wire radius ratio (k) and the force center distance on the pull-in voltage of a U-shaped nanosensor. As seen, by increasing the force center distance, the pull-in voltage reduces. This is due to an increase in the moment of electrical force and van der Waals attraction acting on the attached rigid plate because of an increase in the distance between force center and the free end of nanowires. Besides, Fig. 3.9 demonstrates that the pull-in voltage of the U-shaped nanosensor reduces by enlarging the gap-to-the wire radius ratio. The values of k get larger by increasing the gap, which results in a growth in the pull-in voltage.

3.3. Finite difference method

The finite difference method is one of the oldest and simplest numerical methods employed for solving ordinary and partial differential equations. According to the

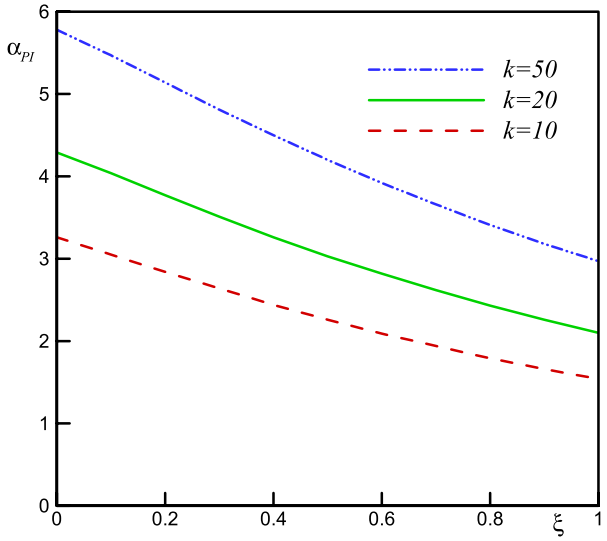

Figure 3.9 Effect of force center distance and gap-to-wire radius ratio (k) on the pull-in voltage of a U-shaped nanosensor ($\beta_{vdW} = 0.5$, $\vartheta = 0.1$).

definition, the finite difference method is a discretization method that approximates derivatives using difference equations. This approximation converts ordinary or partial differential equations into a system of algebraic equations that are solved using matrix algebra techniques. The computation capabilities provided by powerful modern computers have intensified the development of the finite difference method with considerably simple utilization. Nowadays, many commercial mathematical software packages employ finite difference methods as a basic technique to numerically solve ordinary differential equations. To illustrate the concept of the finite difference method, a one-dimensional case is considered. The first derivative of a smooth function such as $f(x)$ at an arbitrary point x can be defined as

$$f'(x) = \lim_{\Delta x \to 0} \frac{f(x + \Delta x) - f(x)}{\Delta x}. \tag{3.90}$$

When Δx converges to 0, Eq. (3.90) provides a good approximation for the first derivative of $f(x)$. In other words, to achieve a reasonable estimate for the derivatives, Δx needs to be sufficiently small. To be specific, the approximation is acceptable when the error tends to zero by converging Δx to zero.

3.3.1 Nanoactuator in ionic liquid media

Nowadays, the application of MEMS and NEMS in liquid media has increased remarkably in various branches of biotechnology and chemistry. The biological systems

such as cellular manipulators, biosensors, DNA manipulators, drug delivery systems, and biocomponents have the potential to be employed in liquid media [38–40]. The application of nanostructures in liquid media includes nanoactuators, nanoswitches, nanoprobes, nanotweezers, microvalves, microgears, supercapacitors, filters, batteries, atomic force microscopy, fuel cells, microdensitometers, micro- and nanopumps, and active microfluidic devices [41–44]. In this regard, the behavior of a nanoactuator immersed in the ionic liquid is derived in this section, and the differential equations are solved using the finite difference method.

The nanoactuator is modeled as a cantilever Euler–Bernoulli nanobeam. As mentioned in Section 2.2.1, an Euler–Bernoulli equation can be described as

$$EI\frac{d^4W}{dX^4} = q(X) \tag{3.91}$$

where $q(X)$ is the total external force acting on the beam. In our case, the external force is the sum of electrical (F_e), chemical (F_c), and Casimir (F_{Cas}) forces. For small potentials, chemical (or osmotic) and electrical forces can be determined using the following equations [41]:

$$F_c = \frac{n_\infty e^2 z_0^2 A}{K_B T}\psi^2, \tag{3.92}$$

$$F_e = -\frac{n_\infty e^2 z_0^2 A}{K_B T}\left(\frac{d\psi}{dZ}\right)^2. \tag{3.93}$$

In these equations, e is the electric charge, K_B is the Boltzmann constant, z_0 is the valence absolute value, T is the absolute temperature, n_∞ is the bulk concentration, A is the electrode area, and ψ is the electric potential of the liquid-immersed electrodes. The former equation can be further investigated using the Poisson–Boltzmann equation [45]:

$$\nabla^2\psi = \frac{2z_0 e n_\infty}{\varepsilon\varepsilon_0}\sinh\left(\frac{z_0 e\psi}{K_B T}\right). \tag{3.94}$$

For small potentials, Eq. (3.94) can be replaced with the linear Poisson–Boltzmann equation:

$$\begin{aligned} &\frac{d^2\psi}{dZ^2} = \kappa^2\psi, \\ &\psi(Z=0) = \psi_1, \\ &\psi(Z=g) = \psi_2, \end{aligned} \tag{3.95}$$

$$\kappa^2 = 2e^2 z_0^2 n_\infty/\varepsilon\varepsilon_0 K_B T \tag{3.96}$$

where $1/\kappa$ is the Debye length. By solving Eq. (3.95) and replacing the obtained solution in Eqs. (3.92) and (3.93), the electrochemical force (f_E) is obtained as

$$F_E = \frac{b\varepsilon\varepsilon_0\kappa^2\psi_1^2}{2\sinh^2(\kappa(g - W(X)))}\left(2\frac{\psi_2}{\psi_1}\cosh(\kappa(g - W(X))) - \left[1 + \left(\frac{\psi_2}{\psi_1}\right)^2\right]\right). \tag{3.97}$$

It should be noted that the electrochemical force can be either attracting or repulsing, depending on the dominant parameters.

For gap separations significantly smaller than the beam thickness, the Casimir force per unit length can be approximated as [45]

$$f_{Cas} = \frac{\pi^2\hbar b}{240\sqrt{\tau\upsilon}\left(g - W(X)\right)^4} \tag{3.98}$$

where τ and υ are permittivity and permeability of the fluid, respectively.

By replacing Eqs. (3.97) and (3.98) in Eq. (3.91), the constitutive equation of the system is obtained as

$$\begin{aligned} EI\frac{d^4W}{dX^4} = {} & \frac{b\varepsilon\varepsilon_0\kappa^2\psi_1^2}{2\sinh^2(\kappa(g - W))}\left(2\frac{\psi_2}{\psi_1}\cosh(\kappa(g - W)) - \left[1 + \left(\frac{\psi_2}{\psi_1}\right)^2\right]\right) \\ & + \frac{\pi^2\hbar b}{240\sqrt{\tau\upsilon}\left(g - W\right)^4}. \end{aligned} \tag{3.99}$$

The dimensionless equation can be explained as:

$$\frac{d^4w}{dx^4} = \frac{\alpha_{Cas}}{(1-w)^4} - \frac{\beta^2}{\sinh^2(\xi_0(1-w))}\left\{\lambda\cosh(\xi_0(1-w)) - \frac{1}{2}(1+\lambda^2)\right\}, \tag{3.100}$$

$$w(0) = \frac{dw}{dx} = 0, \tag{3.101}$$

$$\frac{d^2w}{dx^2}(1) = \frac{d^3w}{dx^3}(1) = 0 \tag{3.102}$$

where dimensionless parameters are identified as:

$$x = X/L, \tag{3.103}$$

$$w = W/g, \tag{3.104}$$

$$\beta_{Cas} = \frac{\pi^2\hbar bL^4}{240\sqrt{\tau\upsilon}g^5EI}, \tag{3.105}$$

$$\alpha = \psi_1\sqrt{\frac{b\varepsilon\varepsilon_0\kappa^2L^4}{g}}, \tag{3.106}$$

$$\gamma = \frac{g}{b}, \tag{3.107}$$

$$\lambda = \frac{\psi_2}{\psi_1}, \tag{3.108}$$

$$\xi_0 = \kappa g. \tag{3.109}$$

In the above equations, α is the dimensionless parameter of electrical force, β_{Cas} is the dimensionless parameter of the Casimir force, γ is the gap to width ratio, λ is the moveable lower surface electric potential-to-substrate electrical potential ratio, and ξ_0 indicates the bulk ion concentration parameter. To derive the finite difference solution, the beam is discretized into N equal elements, separated by $N+1$ nodes. A central derivative with second-order accuracy is considered in the FDM procedure:

$$\left.\frac{dw}{dx}\right|_{x=x_i} = \frac{-w_{i-1} + w_{i+1}}{2\Delta x}, \tag{3.110}$$

$$\left.\frac{d^2w}{dx^2}\right|_{x=x_i} = \frac{w_{i-1} - 2w_i + w_{i+1}}{\Delta x^2}, \tag{3.111}$$

$$\left.\frac{d^3w}{dx^3}\right|_{x=x_i} = \frac{-w_{i-2} + 2w_{i-1} - 2w_{i+1} + w_{i+2}}{2\Delta x^3}, \tag{3.112}$$

$$\left.\frac{d^4w}{dx^4}\right|_{x=x_i} = \frac{w_{i-2} - 4w_{i-1} + 6w_i - 4w_{i+1} + w_{i+2}}{\Delta x^4}. \tag{3.113}$$

If we replace Eq. (3.113) in Eq. (3.100), the system's discretized equation will be obtained as:

$$\begin{aligned}&\frac{w_{i-2} - 4w_{i-1} + 6w_i - 4w_{i+1} + w_{i+2}}{\Delta x^4} \\ &= \frac{\alpha_{Cas}}{(1-w_i)^4} - \frac{\beta^2}{\sinh^2(\xi_0(1-w_i))}\left\{\lambda\cosh(\xi_0(1-w_i)) - \frac{1}{2}(1+\lambda^2)\right\}.\end{aligned} \tag{3.114}$$

By applying Eq. (3.114) to all elements and by employing Eqs. (3.110) to (3.112) with the boundary conditions, a matrix form of algebraic equations of the system is obtained as

$$[\mathbf{A}]\{w\} = \{F\} \tag{3.115}$$

where

$$\{w\} = \begin{bmatrix} w_2 \\ w_3 \\ \vdots \\ w_{N+1} \end{bmatrix}, \tag{3.116}$$

$$\{F\} = \begin{bmatrix} F_2 \\ F_3 \\ \vdots \\ F_{N+1} \end{bmatrix}, \tag{3.117}$$

$$F_i = \frac{\beta_{Cas}}{(1-w_i)^4} - \frac{\alpha^2}{\sinh^2(\xi_0(1-w_i))}\left\{\lambda\cosh(\xi_0(1-w_i)) - \frac{1}{2}(1+\lambda^2)\right\}; \quad i = 2, 3, .., N+1, \tag{3.118}$$

$$[\mathbf{A}]_{N\times N} = \begin{bmatrix} 7 & -4 & 1 & 0 & 0 & \dots & 0 & 0 & 0 & 0 \\ -4 & 6 & -4 & 1 & 0 & \dots & 0 & 0 & 0 & 0 \\ 1 & -4 & 6 & -4 & 1 & \dots & 0 & 0 & 0 & 0 \\ 0 & 1 & -4 & 6 & -4 & \dots & 0 & 0 & 0 & 0 \\ 0 & 0 & 1 & -4 & 6 & \dots & 0 & 0 & 0 & 0 \\ 0 & 0 & 0 & 1 & -4 & \dots & 0 & 0 & 0 & 0 \\ \vdots & \vdots & \vdots & \vdots & \vdots & \ddots & \vdots & \vdots & \vdots & \vdots \\ 0 & 0 & 0 & 0 & 0 & \cdots & -4 & 6 & -4 & 1 \\ 0 & 0 & 0 & 0 & 0 & \cdots & 1 & -4 & 5 & -2 \\ 0 & 0 & 0 & 0 & 0 & \cdots & 0 & 2 & -4 & 2 \end{bmatrix}. \tag{3.119}$$

By employing a numerical solution to Eq. (3.115), the nodal deflection (w_i, $i = 2, 3, \dots, N+1$) is attained, while the $w_1 = 0$ is obtained from the boundary conditions provided in Eq. (3.101).

The convergence check for the finite difference solution is illustrated in Fig. 3.10. As can be seen, increasing the number of elements results in the convergence of the solution.

Fig. 3.11 illustrates the impact of the ion concentration parameter (ξ_0) on the pull-in voltage parameter (α). This figure demonstrates that an increase in the ions (in the vicinity of the surface of the electrodes) increases the pull-in voltage. In other words, an augmentation in the electrolyte Debye length increases the pull-in voltage.

3.3.2 Paddle-type nanosensor

By attaching a solid plate of the free end of a cantilever NEMS/MEMS, a new configuration is obtained which has numerous application as sensor and actuator. This structure is usually known as "paddle-type" NEMS/MEMS. Recently, some researchers have investigated the capacities of paddle-type structures as filters [46], actuators [34], sensors [47–49], and resonators [50].

Fig. 3.12 shows an SEM image of a paddle-type sensor. The schematic view for the modeling of a similar paddle-type nanosensor is illustrated in Fig. 3.13. The paddle type is modeled as a cantilever nanobeam hanged over a fixed plate. A rigid plate is attached

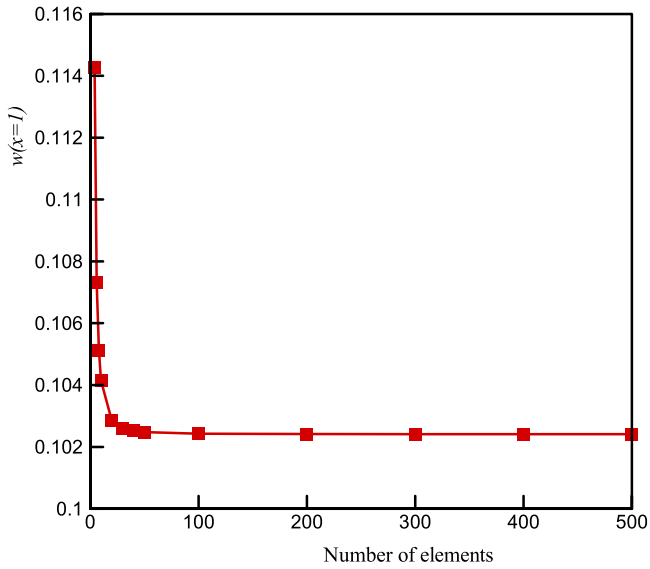

Figure 3.10 Convergence check for the finite difference solution for $\beta_{Cas} = 0.5$; $\alpha = 0.5$; $\xi_0 = 1$; $\lambda = 0.1$.

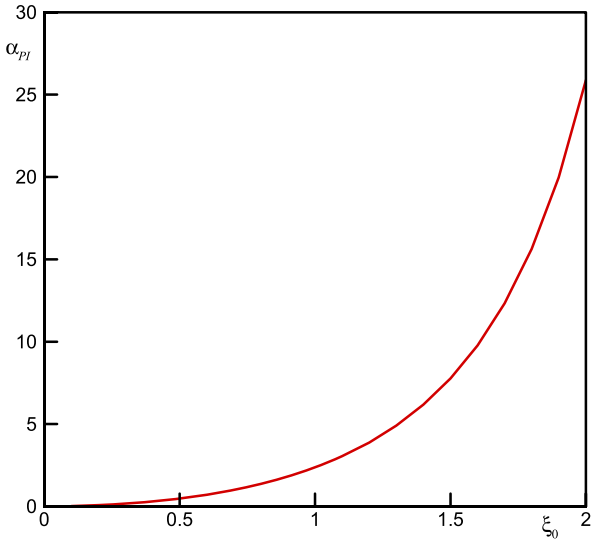

Figure 3.11 Effect of ion concentration on the pull-in voltage.

at the free end of the beam. The rigid plate is a rectangle with width b, length a, and thickness t. The nanobeam has a rectangular cross-section with length L, width h, and thickness t.

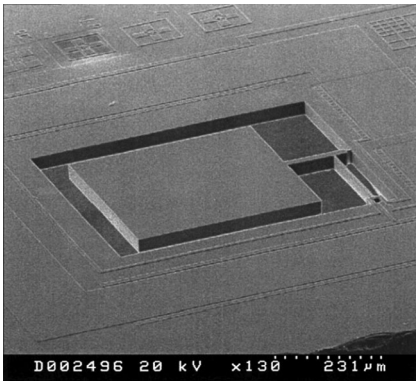

Figure 3.12 SEM image of a paddle-type sensor [51].

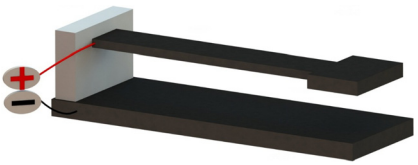

Figure 3.13 Paddle-type nanosensor.

To extract the governing equation of paddle-type nanosensor, Hamilton's principle can be employed. To this end, the strain energy and the work done by the external force should be investigated. The strain energy of a beam is

$$U = \frac{1}{2}\iiint \sigma_{ij}\varepsilon_{ij}dV \tag{3.120}$$

where σ_{ij} is the stress tensor, and ε_{ij} is the strain tensor. For an Euler–Bernoulli beam, the stress and strain tensor components were computed in Section 3.2. By substituting Eqs. (2.20) and (2.21) into Eq. (3.120), the strain energy is obtained as

$$U = \frac{1}{2}\int_0^L EI\left(\frac{\partial^2 w}{\partial X^2}\right)^2 dX. \tag{3.121}$$

The work by the external loads is the sum of the work done by distributed force along the beam and the concentrated force and moment at the nanowire free end. The concentrated force and moment at the free end are the results of the van der Waals attraction and electrical force acting on the rigid plate attached to the end of the nanobeam. The following formula gives the work done by the distributed load:

$$V_{f_{ext}} = \int_0^L \int_0^W f_{ext} dW dX. \tag{3.122}$$

The work done by the internal moment, V_M, is obtained as

$$V_M = \int_0^{\frac{\partial W(L)}{\partial X}} M\left(W(L), \frac{\partial W(L)}{\partial X}\right) \times d\frac{\partial W(L)}{\partial X}. \tag{3.123}$$

The work done by the internal force, V_F, is determined as

$$V_F = \int_0^{W(L)} F\left(W(L), \frac{\partial W(L)}{\partial X}\right) \times dW(L). \tag{3.124}$$

The total work done by the concentrated force and moment on the paddle and distributed force on the nanobeam is defined as

$$\begin{aligned} V &= V_{f_{ext}} + V_M + V_F \\ &= \int_0^L \int_0^W f_{ext} dW dX + \int_0^{\frac{\partial W(L)}{\partial X}} M\left(W(L), \frac{\partial W(L)}{\partial X}\right) \times d\frac{\partial W(L)}{\partial X} \\ &+ \int_0^{W(L)} F\left(W(L), \frac{\partial W(L)}{\partial X}\right) \times dW(L). \end{aligned} \tag{3.125}$$

Hamilton's principle can be employed to extract the governing equation:

$$\delta(V - U) = 0. \tag{3.126}$$

By substituting Eqs. (3.121) and (3.125) into Eq. (3.126), the following equation is obtained:

$$\begin{aligned} &\int_0^L \left[EI\frac{\partial^4 W}{\partial X^4} - f_{ext}\right] \delta W dX - EI\frac{\partial^3 W}{\partial X^3}\delta W\Big|_0^L + EI\frac{\partial^2 W}{\partial X^2}\delta\left(\frac{\partial W}{\partial X}\right)\Big|_0^L \\ &- M\delta\left(\frac{\partial W}{\partial X}\right)\Big|_L - F\delta W|_L = 0. \end{aligned} \tag{3.127}$$

Hence the governing equation and boundary condition of paddle-type NEMS is obtained as:

$$EI\frac{d^4 W}{dX^4} = f_{ext}, \tag{3.128}$$

$$W(0) = 0, \tag{3.129}$$

$$\frac{dW}{dX}(0) = 0, \tag{3.130}$$

$$EI\frac{d^2 W}{dX^2}(L) = M, \tag{3.131}$$

$$EI\frac{d^3 W}{dX^3}(L) = -F. \tag{3.132}$$

Figure 3.14 Concentrated force and moment on the tip of nanobeam, due to forces acting on the paddle.

The above relation can be specialized by substituting appropriate f_{ext}, M, and L. Interestingly, by setting F and M equal to zero, the governing equation of a cantilever NEMS/MEMS (without a paddle) can be achieved. In the earlier studies of the paddle-type, the external force was the sum of the accelerating, electrical, and Casimir forces. The electrical and Casimir forces were determined previously in Eqs. (2.13) and (2.68), respectively. According to the D'Alembert principle, one can transform an accelerating system into an equivalent static system by incorporating the so-called inertial force. Hence, the influence of acceleration can be modeled by considering the accelerating force per unit length (f_z) along the z-axis (a_z):

$$f_Z = ma_Z = \rho bta_Z \tag{3.133}$$

where m and ρ are mass and density of the constitutive material of the sensor, respectively.

For the paddle-type sensor, the stresses resultants F and M are induced by the electrostatic, Casimir, and accelerating forces acting on the tip plate. This for and moment can be considered as concentrated force and moment at the tip of the beam (see Fig. 3.14). To obtain appropriate boundary conditions, the distributed forces acting on the plate are replaced with an equivalent concentrated force which acts at the distance of $\bar{X}$ from the nanobeam tip (the force center). The value of $\bar{X}$ is determined from the $\bar{X} = M/F$ relation. Based on this approach, the force and moment acting on the tip on nanobeam are achieved as:

$$M = \frac{\varepsilon abV^2\bar{X}}{2(g - W(L) - \bar{X}W'(L))^2} + \frac{\pi^2\hbar cab\bar{X}}{240(g - W(L) - \bar{X}W'(L))^4} + \frac{\rho a^2 bta_Z}{2}, \tag{3.134}$$

$$F = \frac{\varepsilon abV^2}{2(g - W(L) - \bar{X}W'(L))^2} + \frac{\pi^2\hbar cab}{240(g - W(L) - \bar{X}W'(L))^4} - \rho abta_Z. \tag{3.135}$$

Finally, the governing equation of the paddle-type sensor can be rewritten as

$$EI\frac{d^4W}{dX^4} = f_{ext}. \tag{3.136}$$

It is associated with the following boundary conditions:

$$W(0) = 0, \tag{3.137}$$

$$\frac{dW}{dX}(0) = 0, \tag{3.138}$$

$$EI\frac{d^2W}{dX^2}(L) = \frac{\varepsilon ab V^2 \bar{X}}{2(g - W(L) - \bar{X}W'(L))^2} + \frac{\pi^2 \hbar cab\bar{X}}{240(g - W(L) - \bar{X}W'(L))^4} + \frac{\rho a^2 bta_Z}{2} \tag{3.139}$$

$$EI\frac{d^3W}{dX^3}(L) = -\frac{\varepsilon ab V^2}{2(g - W(L) - \bar{X}W'(L))^2} - \frac{\pi^2 \hbar cab}{240(g - W(L) - \bar{X}W'(L))^4} - \rho abta_Z. \tag{3.140}$$

By defining $x = X/L$ and $w = W/g$, the dimensionless governing equation and boundary conditions of the paddle-type nanosensor are obtained as:

$$\frac{d^4w}{dx^4} = \alpha^2\left[\frac{1}{(1-w)^2} + 0.65\frac{\gamma}{(1-w)}\right] + \frac{\beta_{Cas}}{(1-w)^4} + \bar{a}_z, \tag{3.141}$$

$$w(0) = 0, \tag{3.142}$$

$$\frac{dw}{dx}(0) = 0, \tag{3.143}$$

$$\frac{d^2w}{dx^2}(1) = \vartheta\xi\left[\frac{\alpha^2}{(1 - w(1) - \xi w'(1))^2} + \frac{\beta_{Cas}}{(1 - w(1) - \xi w'(1))^4} + \frac{\bar{a}_z}{2\Omega}\right], \tag{3.144}$$

$$\frac{d^3w}{dx^3}(1) = -\vartheta\left[\frac{\alpha^2}{(1 - w(1) - \xi w'(1))^2} + \frac{\beta_{Cas}}{(1 - w(1) - \xi w'(1))^4} + \bar{a}_z\right]. \tag{3.145}$$

In the above equation, the dimensionless parameters are:

$$\xi = \frac{\bar{x}}{L}, \tag{3.146}$$

$$\Omega = \frac{\bar{x}}{a}, \tag{3.147}$$

$$\vartheta = \frac{ab}{hL}, \tag{3.148}$$

$$\gamma = \frac{g}{h}, \tag{3.149}$$

$$\beta_{Cas} = \frac{\bar{h}c\pi^2 hL^4}{240EID^5}, \tag{3.150}$$

$$\alpha^2 = \frac{\varepsilon_0\varepsilon_r V^2 hL^4}{2EID^3}, \tag{3.151}$$

$$\bar{a}_z = \frac{\rho hta_Z L^4}{EID}. \tag{3.152}$$

It is worth mentioning that in the above relations, ξ indicates the force center distance-to-the beam length ratio, Ω is the force center distance-to-the paddle length ratio, ϑ is the plate-to-beam area ratio, and γ indicates the gap-to-width ratio. Also, α, β_{Cas}, and $\bar{a}_z$ are the dimensionless parameters of the electrical, Casimir, and accelerating forces, respectively.

The nonlinear differential equation (3.128) is associated with nonclassical boundary conditions. This fourth-order differential equation can be solved numerically by using the finite difference method. To derive the finite difference solution, the beam is discretized into N equal elements, separated by $N+1$ nodes. Subsequently, the numerical fourth-order derivatives are employed using Eq. (3.113). By substituting this numerical derivative into Eq. (3.128), the discretized system of algebraic equations is obtained as

$$\frac{w_{i-2}-4w_{i-1}+6w_i-4w_{i+1}+w_{i+2}}{\Delta x^4}=\alpha^2\left[\frac{1}{(1-w_i)^2}+0.65\frac{\gamma}{(1-w_i)}\right]+\frac{\beta_{Cas}}{(1-w_i)^4}+\bar{a}_z. \tag{3.153}$$

By applying Eq. (3.153) to all elements and by considering the boundary conditions, a matrix form of algebraic equations of the system is obtained as

$$\left[\mathbf{A}\right]\{w\}=\{F\} \tag{3.154}$$

where

$$\{w\}=\begin{bmatrix} w_2 \\ w_3 \\ \vdots \\ w_{N+1} \end{bmatrix}, \tag{3.155}$$

$$\{F\}=\begin{bmatrix} F_2 \\ F_3 \\ \vdots \\ F_{N+1} \end{bmatrix}, \tag{3.156}$$

$$F_i=\frac{\alpha^2}{(1-w_i)^2}+0.65\frac{\gamma\alpha^2}{(1-w_i)}+\frac{\beta_{Cas}}{(1-w_i)^4}+\bar{a}_z;\quad i=2,...,N-2,$$

$$F_N=\frac{\alpha^2}{(1-w_N)^2}+0.65\frac{\gamma\alpha^2}{(1-w_N)}+\frac{\beta_{Cas}}{(1-w_N)^4}+\bar{a}_z$$
$$+\frac{-\frac{\vartheta\xi}{\Delta x^2}\alpha^2}{(1-w_{N+1}-\xi\frac{w_{N+1}-w_N}{\Delta x})^2}+\frac{-\frac{\vartheta\xi}{\Delta x^2}\beta_{Cas}}{(1-w_{N+1}-\xi\frac{w_{N+1}-w_N}{\Delta x})^4}-\frac{\vartheta\xi\bar{a}_z}{2\Omega\Delta x^2},$$

$$F_{N+1}=\frac{\alpha^2}{(1-w_{N+1})^2}+0.65\frac{\gamma\alpha^2}{(1-w_{N+1})}+\frac{\beta_{Cas}}{(1-w_{N+1})^4}+\bar{a}_z \\ +\frac{\left[\frac{\vartheta\xi}{\Delta x^2}+\frac{\vartheta}{\Delta x}\right]\alpha^2}{(1-w_{N+1}-\xi\frac{w_{N+1}-w_N}{\Delta x})^2}+\frac{\left[\frac{\vartheta\xi}{\Delta x^2}+\frac{\vartheta}{\Delta x}\right]\beta_{Cas}}{(1-w_{N+1}-\xi\frac{w_{N+1}-w_N}{\Delta x})^4}+\left[\frac{\vartheta\xi}{2\Omega\Delta x^2}+\frac{\vartheta}{\Delta x}\right]\bar{a}_z, \tag{3.157}$$

$$[A]_{N\times N}=\begin{bmatrix} 7 & -4 & 1 & 0 & 0 & \dots & 0 & 0 & 0 & 0 \\ -4 & 6 & -4 & 1 & 0 & \dots & 0 & 0 & 0 & 0 \\ 1 & -4 & 6 & -4 & 1 & \dots & 0 & 0 & 0 & 0 \\ 0 & 1 & -4 & 6 & -4 & \dots & 0 & 0 & 0 & 0 \\ 0 & 0 & 1 & -4 & 6 & \dots & 0 & 0 & 0 & 0 \\ 0 & 0 & 0 & 1 & -4 & \dots & 0 & 0 & 0 & 0 \\ \vdots & \vdots & \vdots & \vdots & \vdots & \ddots & \vdots & \vdots & \vdots & \vdots \\ 0 & 0 & 0 & 0 & 0 & \cdots & -4 & 6 & -4 & 1 \\ 0 & 0 & 0 & 0 & 0 & \cdots & 1 & -4 & 5 & -2 \\ 0 & 0 & 0 & 0 & 0 & \cdots & 0 & 1 & -2 & 1 \end{bmatrix}. \tag{3.158}$$

The impact of both positive and negative acceleration force on the pull-in voltage of the paddle-type sensor is examined in Fig. 3.15. It should be noted that the paddle-type sensor used in the aeronautical or automotive industries might be affected by both positive and negative acceleration. In Fig. 3.15 three different sensors by different paddle-to-beam area ratio (i.e., $\vartheta = 0.1, 0.2, 0.3$) are investigated. This figure demonstrates that by increasing the acceleration from negative to positive, the pull-in voltage reduces. Also, it is clear from Fig. 3.15 that for larger values of ϑ, the influence of the accelerating force on the instability threshold is more dominant. It is connected to the impact of the paddle area on the accelerating force. By increasing ϑ, the paddle-to-beam area and, subsequently, its mass are enlarged. Therefore, a higher accelerating force is applied by the paddle on the beam.

The effect of paddle geometry on the instability voltage of the paddle-type NEMS is illustrated in Fig. 3.16. In this figure, the effect of the Casimir force is also investigated. The line $a = 0$ is related to neglecting the Casimir force, which can be used for analyzing the paddle-type MEMS. Fig. 3.16 vividly demonstrates that the pull-in voltage shrinks with increasing ϑ. Enlarging the value of ϑ forces a growth in the paddle surface, which results in an increase in the external forces. Also, this figure reveals that the impact of the Casimir force on the instability is more dominant for larger values of ϑ, which is also connected to increasing the Casimir force by enlarging the paddle area.

3.4. Finite element method

The finite element method (FEM) is a numerical solution method that can be employed in various branches of engineering, including stress analysis, heat transfer, buckling,

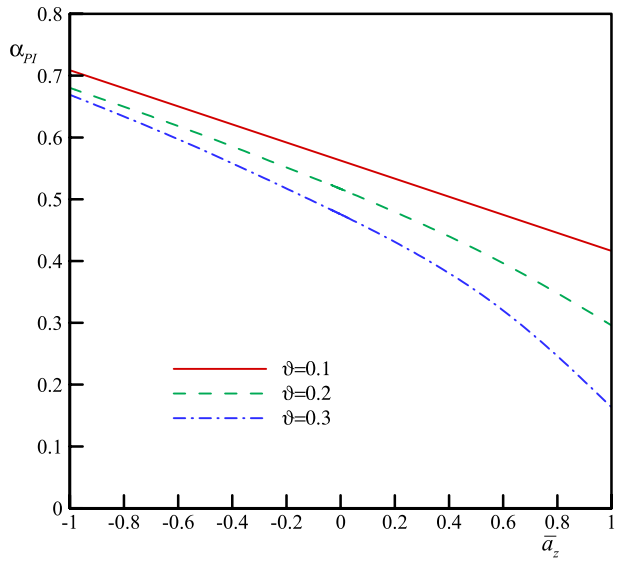

Figure 3.15 Impacts of the paddle-to-beam area ratio and accelerating field on the instability voltage ($\gamma = 6, \Omega = 0.5, \xi = 0.02$).

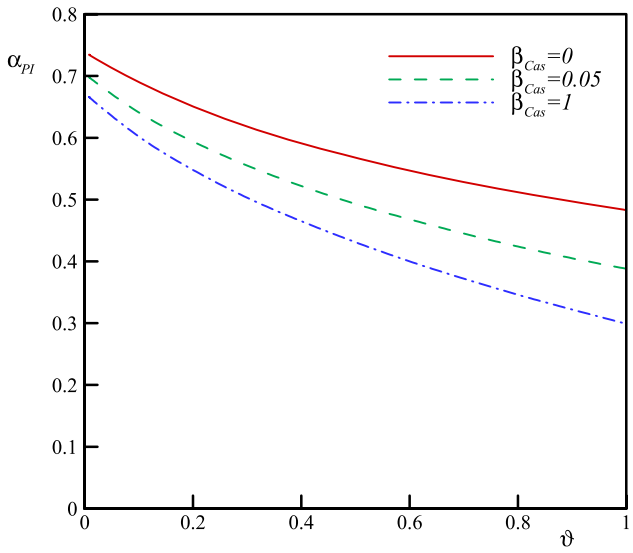

Figure 3.16 Effect of paddle geometry and Casimir force on the pull-in voltage ($\gamma = 5, \Omega = 0.5, \xi = 0.0125$).

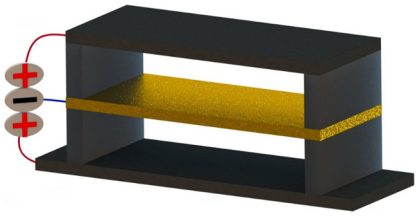

Figure 3.17 Schematic representation of a double-sided nanobridge.

fluid flow, and electromagnetism. In FEM, a complicated object is discretized into an equivalent system of smaller blocks known as elements. These blocks are interconnected at points common to two or more elements (nodes). For structural analysis, the finite element procedure can be divided into the following steps:

1. Dividing the object into small elements with nodes (discretization)
2. Finding a shape function to describe the physical quantities of the element
3. Expanding the equations for each element to calculate the desired quantities at the elements
4. Assembling the elements to form an equivalent system for the overall structure and evaluating the global stiffness matrix
5. Applying boundary conditions, initial conditions, and external loads
6. Solving a system of linear or nonlinear equations
7. Post-processing (sorting and displaying the desired results)

3.4.1 Double-sided nanobridge in Casimir regime

Double-sided nanobridges are among the essential building blocks for new accelerometers and speed sensors since they offer excellent stability for the proof masses against mechanical shocks [52,53]. Moreover, these systems provide improved controllability [54]. Therefore, they can be used for positioning the tip of the nanoindentation transducers. Fig. 3.17 illustrates a typical double-sided actuated nanobridge created from a clamped–clamped nanobeam suspended between two fixed electrodes. The lower and upper initial gaps are g_l and g_u, respectively.

The nanobridge can be simulated as a clamped–clamped Euler–Bernoulli beam. The beam element is illustrated in Fig. 3.18. This element has two nodes, each with two degrees of freedom, including transverse displacement (W_i) and small rotation (θ_i).

As mentioned in the previous section, the differential equation of an Euler–Bernoulli beam can be described as in Eq. (3.91). In the FEM, the loads are applied to the nodes. Therefore, the differential equation of the Euler–Bernoulli beam element with a uniform cross-section made from isotropic materials (i.e., EI is constant) which has only

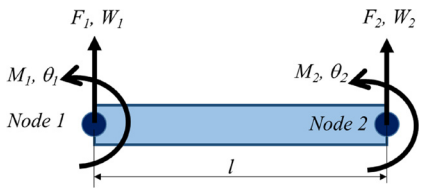

Figure 3.18 Euler–Bernoulli beam element.

nodal forces and moments can be explained as

$$EI\frac{d^4W}{dX^4} = 0. \tag{3.159}$$

The next step in the FEM solution is finding the mode shape of the element. To this end, the solution of Eq. (3.159) is obtained as

$$W(X) = a_0 + a_1X + a_2X^2 + a_3X^3. \tag{3.160}$$

By investigating the nodal deflection and rotation, unknown parameters a_0, a_1, a_2, and a_3 are recovered as:

$$\begin{aligned} &W(0) = W_1 = a_0, \\ &\frac{dW(0)}{dX} = \theta_1 = a_1, \\ &W(l) = W_2 = a_0 + a_1l + a_2l^2 + a_3l^3, \\ &\frac{dW(l)}{dX} = \theta_2 = a_1 + 2a_2l + 3a_3l^2. \end{aligned} \tag{3.161}$$

For small rotations, we have

$$\frac{dW}{dX} = \theta. \tag{3.162}$$

By replacing the solution for Eq. (3.161) in Eq. (3.160), the beam element deflection can be obtained as

$$\begin{aligned} W = &\left[\frac{2}{l^3}(W_1 - W_2) + \frac{1}{l^2}(\theta_1 + \theta_2)\right]X^3 \\ &+ \left[-\frac{3}{l^2}(W_1 - W_2) - \frac{1}{l}(2\theta_1 + \theta_2)\right]X^2 + \theta_1X + W_1. \end{aligned} \tag{3.163}$$

The above equation can be rewritten in matrix form as follows:

$$W = [N]\{d\} \tag{3.164}$$

where the shape function matrix $[N]$ and the degree of freedom vector are described as:

$$\begin{aligned}
&[N] = \begin{bmatrix} N_1 & N_2 & N_3 & N_4 \end{bmatrix}, \\
&N_1 = \frac{1}{l^3}\left(2X^3 - 3X^2 l + l^3\right), \quad N_2 = \frac{1}{l^3}\left(X^3 l - 2X^2 l^2 + X l^3\right), \\
&N_3 = \frac{1}{l^3}\left(-2X^3 + 3X^2 l\right), \quad N_4 = \frac{1}{l^3}\left(X^3 l - X^2 l^2\right),
\end{aligned} \tag{3.165}$$

$$\{d\} = \begin{Bmatrix} W_1 \\ \theta_1 \\ W_2 \\ \theta_2 \end{Bmatrix}. \tag{3.166}$$

It is worth mentioning that the cubic shape functions of Euler beam elements are known as Hermite cubic interpolation functions.

Energy methods or direct equilibrium approaches can be employed to investigate the stiffness matrix and element equations. For the elementary beam theory, the shear force (Q) and the bending moment (M) are related to transverse deflection as:

$$Q = EI\frac{d^3 W}{dX^3}, \tag{3.167}$$

$$M = EI\frac{d^2 W}{dX^2}. \tag{3.168}$$

Using Eqs. (3.167) and (3.168), the force and moment at the nodes can be obtained as:

$$\begin{aligned}
F_{1y} &= Q(X=0) = EI\frac{d^3 W(0)}{dX^3} = \frac{EI}{l^3}\left(12W_1 + 6l\theta_1 - 12W_2 + 6l\theta_2\right), \\
M_1 &= -M(X=0) = -EI\frac{d^2 W(0)}{dX^2} = \frac{EI}{l^3}\left(6lW_1 + 4l^2\theta_1 - 6lW_2 + 2l^2\theta_2\right), \\
F_{2y} &= -Q(X=l) = -EI\frac{d^3 W(l)}{dX^3} = \frac{EI}{l^3}\left(-12W_1 - 6l\theta_1 + 12W_2 - 6l\theta_2\right), \\
M_2 &= M(X=l) = EI\frac{d^2 W(l)}{dX^2} = \frac{EI}{l^3}\left(6lW_1 + 2l^2\theta_1 - 6lW_2 + 4l^2\theta_2\right).
\end{aligned} \tag{3.169}$$

Eq. (3.169) can be rewritten in matrix form as

$$\{\mathbf{F}\} = [\mathbf{K}]\{\mathbf{d}\} \tag{3.170}$$

where

$$[\mathbf{K}] = \frac{EI}{l^3}\begin{bmatrix} 12 & 6l & -12 & 6l \\ 6l & 4l^2 & -6l & 2l^2 \\ -12 & -6l & 12 & -6l \\ 6l & 2l^2 & -6l & 4l^2 \end{bmatrix},$$
$$\{\mathbf{F}\} = \begin{Bmatrix} F_{1y} \\ M_1 \\ F_{2y} \\ M_2 \end{Bmatrix}, \tag{3.171}$$
$$\{\mathbf{d}\} = \begin{Bmatrix} W_1 \\ \theta_1 \\ W_2 \\ \theta_2 \end{Bmatrix}.$$

As mentioned in previous sections, the electrical attraction (f_{elec}) and the Casimir (f_{Cas}) force between two parallel plates can be explained as in Eqs. (3.172) and (3.173), respectively:

$$f_{elec} = \frac{\varepsilon_0 \varepsilon_r b V^2}{2g^2}\left[1 + 0.65\left(\frac{g}{b}\right)\right], \tag{3.172}$$
$$f_{Cas} = \frac{\pi^2 \hbar c b}{240 g^4}. \tag{3.173}$$

By applying a voltage difference between the nanobridge and substrates, the nanobridge deflects towards the closest substrate. Therefore, the distributed electrical force per unit length for a nanobridge due to upper and lower plates is defined as:

$$f_{elec,upper} = -\frac{\varepsilon_0 \varepsilon_r b V^2}{2(g_u + W)^2}\left[1 + 0.65\left(\frac{g_u + W}{b}\right)\right], \tag{3.174}$$
$$f_{elec,lower} = \frac{\varepsilon_0 \varepsilon_r b V^2}{2(g_l - W)^2}\left[1 + 0.65\left(\frac{g_l - W}{b}\right)\right] \tag{3.175}$$

where g_u and g_l are the upper and lower initial gaps, respectively. Similarly, the distributed Casimir force per unit length for a nanobridge is achieved as:

$$f_{Cas,upper} = -\frac{\pi^2 \hbar c b}{240(g_u + W)^4}, \tag{3.176}$$
$$f_{Cas,lower} = \frac{\pi^2 \hbar c b}{240(g_l - W)^4}. \tag{3.177}$$

By using Eqs. (3.174) to (3.177) in Eq. (3.159), the differential equation for the double-sided nanobridge is obtained as

$$EI\frac{d^4W}{dX^4} = \frac{\varepsilon_0\varepsilon_r b V^2}{2(g_l - W)^2}\left[1 + 0.65\left(\frac{g_l - W}{b}\right)\right] - \frac{\varepsilon_0\varepsilon_r b V^2}{2(g_u + W)^2}\left[1 + 0.65\left(\frac{g_u + W}{b}\right)\right] + \frac{\pi^2\hbar c b}{240(g_l - W)^4} - \frac{\pi^2\hbar c b}{240(g_u + W)^4} \tag{3.178}$$

with the following boundary conditions:

$$\begin{aligned} &W(0) = W(L) = 0, \\ &\frac{dW}{dX}(0) = \frac{dW}{dX}(L) = 0. \end{aligned} \tag{3.179}$$

Moreover, the dimensionless equation for the double-sided nanobridge can be obtained as

$$\frac{d^4w}{dw^4} = \frac{\alpha^2\left[1 + 0.65\gamma\,(1 - w)\right]}{(1 - w)^2} - \frac{\alpha^2\left[1 + 0.65\gamma\,(\Omega + w)\right]}{(\Omega + w)^2} + \frac{\beta_{Cas}}{(1 - w)^4} - \frac{\beta_{Cas}}{(\Omega + w)^4} \tag{3.180}$$

where

$$\beta_{Cas} = \frac{\pi^2\hbar c b L^4}{240 g_l^5 EI}, \tag{3.181}$$

$$\alpha^2 = \frac{\varepsilon_0\varepsilon_r b V^2 L^4}{2 g_l^3 EI}, \tag{3.182}$$

$$\gamma = \frac{g_l}{b}, \tag{3.183}$$

$$\Omega = \frac{g_u}{g_l}. \tag{3.184}$$

In the above equation, α is the dimensionless parameter of the electrical force, β_{Cas} is the Casimir force dimensionless parameter, γ is the lower gap-to-width ratio, and Ω is the upper gap-to-the lower gap ratio. To obtain the FEM solution, the nanobeam is divided into N elements of equal length. A linear distribution for the external force over the element can be considered as in Fig. 3.19. In this figure, f_i and f_j indicate the dimensionless external force related to dimensionless deflection at node i and j, respectively. The external force associated with node i is determined as

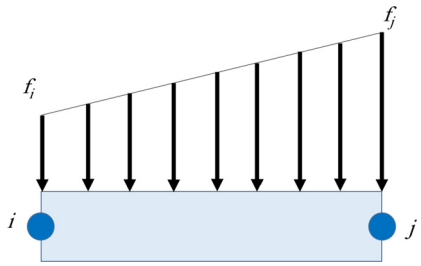

Figure 3.19 Load distribution over the beam element.

$$f_i = \frac{\alpha^2\left[1+0.65\gamma\,(1-w_i)\right]}{(1-w_i)^2} - \frac{\alpha^2\left[1+0.65\gamma\,(\Omega+w_i)\right]}{(\Omega+w_i)^2} + \frac{\beta_{Cas}}{(1-w_i)^4} - \frac{\beta_{Cas}}{(\Omega+w_i)^4}. \tag{3.185}$$

By replacing w_i with w_j in the above equation, a similar relation for the external force associated with node j can be achieved.

In FEM, the distributed loads should replace work-equivalent nodal forces and moments. In other words, the work done by the distributed force should be equal to the work done by the distributed loads:

$$\begin{aligned} &W_{distributed} = W_{discrete} \\ &\Rightarrow \int_0^l F(x)w(x)dx = F_i w_i + F_j w_j + M_i\theta_i + M_j\theta_j \end{aligned} \tag{3.186}$$

where

$$F(x) = f_i + \left(\frac{f_j - f_i}{l}\right)x. \tag{3.187}$$

By substituting Eqs. (3.163) and (3.187) into Eq. (3.186), the nodal loads are obtained as:

$$F_i = \frac{7f_i + 3f_j}{20}l, \tag{3.188}$$

$$M_i = \frac{3f_i + 2f_j}{60}l^2, \tag{3.189}$$

$$F_j = \frac{3f_i + 7f_j}{20}l, \tag{3.190}$$

$$M_j = -\frac{2f_i + 3f_j}{60}l^2. \tag{3.191}$$

Since the electrostatic force and Casimir attraction are nonlinear, conventional methods cannot be employed to obtain an FEM solution for microcapacitors. Hence, an iterative method is used. The nodal load at the nth step is determined from the nanobridge deflection at the previous step as follows:

$$F_i^n = \frac{7f_i^n + 3f_j^n}{20} l, \tag{3.192}$$

$$M_i^n = \frac{3f_i^n + 2f_j^n}{60} l^2, \tag{3.193}$$

$$F_j^n = \frac{3f_i^n + 7f_j^n}{20} l, \tag{3.194}$$

$$M_j^n = -\frac{2f_i^n{}_i + 3f_j^n}{60} l^2 \tag{3.195}$$

where

$$f_i = \frac{\alpha^2\left[1 + 0.65\gamma\left(1 - w_i^{n-1}\right)\right]}{(1 - w_i^{n-1})^2} - \frac{\alpha^2\left[1 + 0.65\gamma\left(\Omega + w_i^{n-1}\right)\right]}{(\Omega + w_i^{n-1})^2} + \frac{\beta_{Cas}}{(1 - w_i^{n-1})^4} - \frac{\beta_{Cas}}{(\Omega + w_i^{n-1})^4} \tag{3.196}$$

and where w_i^{n-1} is the dimensionless deflection of node i at step $n-1$. The initial guess considered here is $w^0(x) = 0$, and the iterations continue until the relative error in the maximum dimensionless deflection (i.e., $w(x = 0.5)$) is less than 10^{-6}, that is,

$$Error = \left|\frac{w^n(0.5) - w^{n-1}(0.5)}{w^n(0.5)}\right| \leq 10^{-6}. \tag{3.197}$$

The nanobridge deflection for different applied voltages is illustrated in Fig. 3.20. In this figure, the dimensionless parameter of the Casimir force is considered as 2.5 ($\beta_{Cas} = 2.5$), and geometrical parameters γ and Ω are assumed to be 1 and 1.1, respectively. As can be seen, increasing the applied voltage increases the beam deflection. According to this figure, it is evident that even without any external voltages, the nanobridge has an initial deflection due to the Casimir force.

The maximum deflection for the nanobridge (as a function of upper-to-lower gap ratio (Ω)) is presented in Fig. 3.21. The dimensionless parameters of the applied voltage and the Casimir force are 4 and 2, respectively. This figure demonstrates that by increasing the gap ratio (Ω), the nanobridge deflection is increased as well due to the reduction of the effect of the upper plate electrical force.

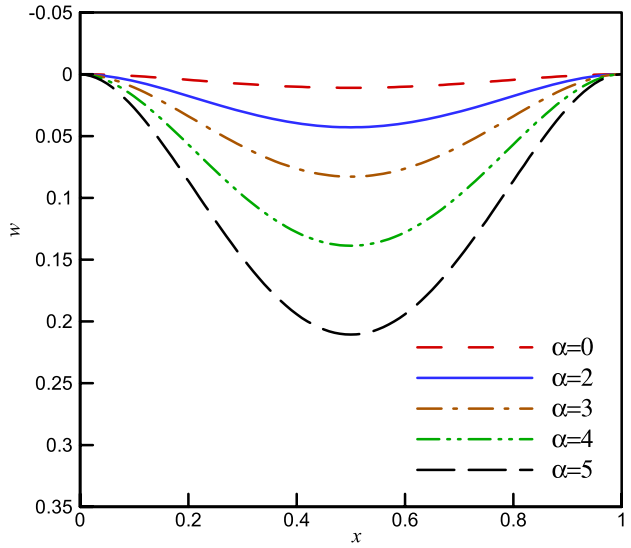

Figure 3.20 The nanobridge deflection for different values of the applied voltage.

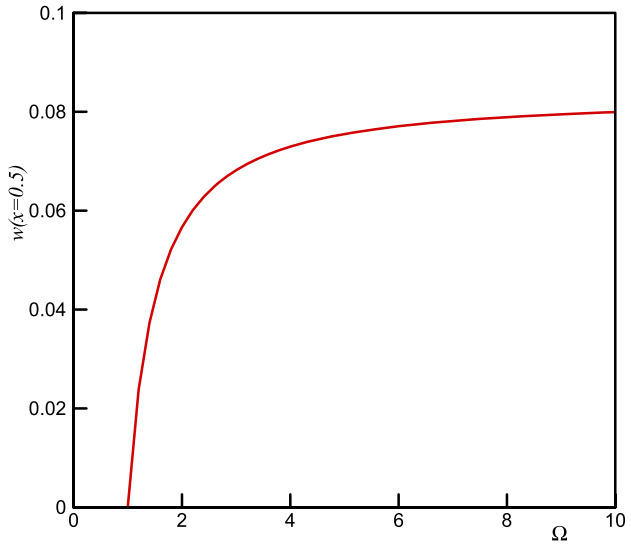

Figure 3.21 Effect of the upper-to-lower gap ratio on the nanobridge maximum deflection.

3.4.2 Parallel-plates microcapacitor

The beam model is an appropriate model to simulate the behavior of NEMS and MEMS with a relatively small width-to-length ratio. However, this model is not suitable for

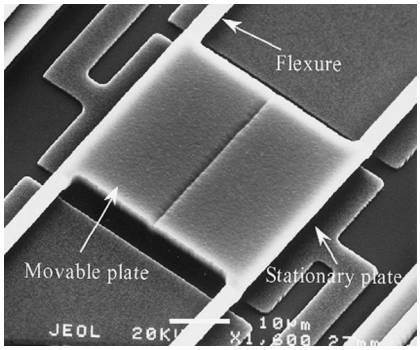

Figure 3.22 SEM image of a parallel-plates capacitor [60].

some NEMS and/or MEMS. For those systems, the plate model should be employed to investigate their behavior. Electrically actuated microplates are the essential component in microsize mirrors [55], pumps [56], microphones [57], and sensors [58].

Fig. 3.22 shows an SEM image of a parallel-plates capacitor with a rectangular movable plate. The model of a rectangular parallel-plates capacitor is demonstrated in Fig. 3.23. Based on Mindlin plate theory, the rectangular isotropic plate equation can be determined as [59]:

$$D\left(\frac{\partial^4 w}{\partial x^4}+2\frac{\partial^4 w}{\partial x^2\partial y^2}+\frac{\partial^4 w}{\partial y^4}\right)=F_{ext}(x,y), \tag{3.198}$$

$$D=\frac{Eh^3}{12(1-\upsilon^2)}. \tag{3.199}$$

By replacing the electrical force per unit area (instead of external force) in Eq. (3.198), the rectangular microcapacitor equation is derived as

$$D\left(\frac{\partial^4 w}{\partial x^4}+2\frac{\partial^4 w}{\partial x^2\partial y^2}+\frac{\partial^4 w}{\partial y^4}\right)=\frac{\varepsilon_0 V^2}{2(d-w)^2}, \tag{3.200}$$

which is subject to the following boundary conditions for the clamped microplate at all edges:

$$\begin{aligned}
&w(0,y)=w(a,y)=0, \quad 0\le y\le b,\\
&w(x,0)=w(y,b)=0, \quad 0\le x\le a,\\
&\frac{\partial w}{\partial x}(0,y)=\frac{\partial w}{\partial x}w(a,y)=0, \quad 0\le y\le b,\\
&\frac{\partial w}{\partial y}w(x,0)=\frac{\partial w}{\partial y}w(y,b)=0, \quad 0\le x\le a,
\end{aligned} \tag{3.201}$$

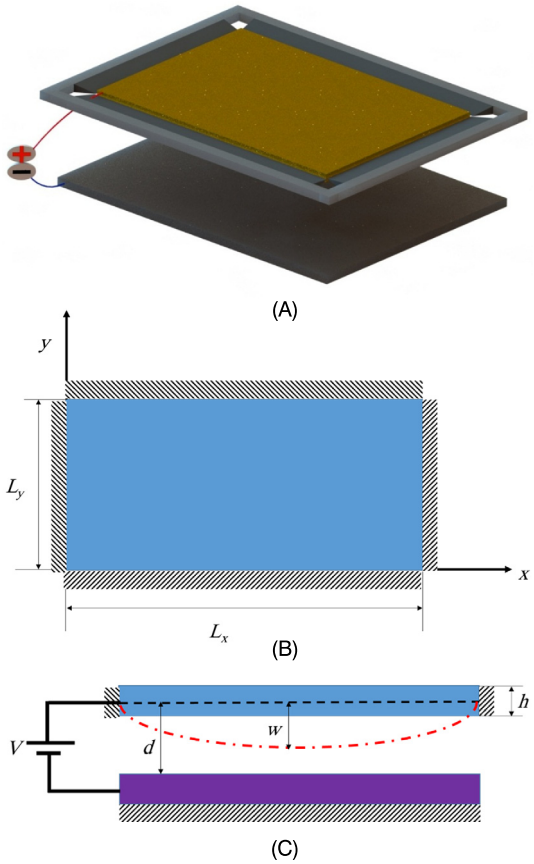

Figure 3.23 Schematic of a parallel-plates microcapacitor: (A) top view; (B) cross-sectional view.

$$D\left(\frac{\partial^4 w}{\partial x^4}+2\frac{\partial^4 w}{\partial x^2\partial y^2}+\frac{\partial^4 w}{\partial y^4}\right)=\frac{\varepsilon_0 V^2}{2(d-w)^2}. \tag{3.202}$$

To simulate the bending of a parallel-plates microcapacitor, a finite element technique can be employed. To this end, the four-node plate element is initially introduced, and the microcapacitor is modeled accordingly. A four-node plate element is shown in Fig. 3.24.

To extract the mode shape of the plate element, local coordinates (ξ, η) are considered, and an arbitrary component in the global coordinates (x, y) is transferred into a square element in local coordinates (see Fig. 3.24). The strain energy of the plate can be explained as [61]

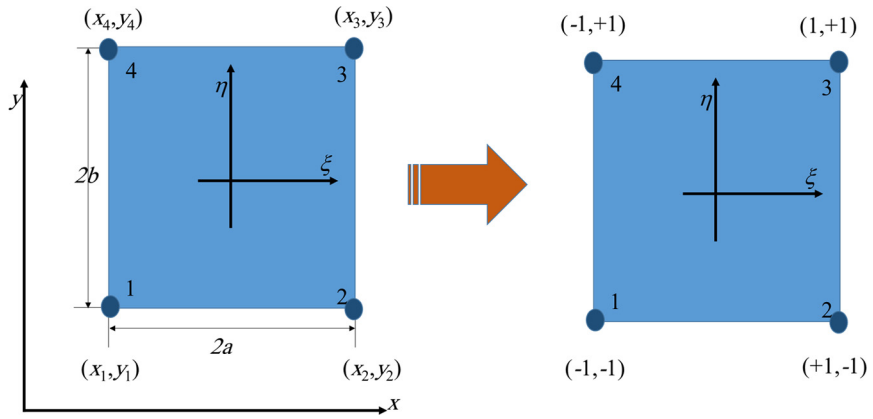

Figure 3.24 Four-node plate element.

$$\begin{aligned} U &= \frac{1}{2}\int_{\Omega} \boldsymbol{\sigma}_N^T \boldsymbol{\varepsilon}_N d\Omega + \frac{\kappa}{2}\int_{\Omega} \boldsymbol{\sigma}_S^T \boldsymbol{\varepsilon}_S d\Omega \\ &= \frac{1}{2}\int_A \frac{h^3}{12}\{\boldsymbol{\chi}\}^{\mathrm{T}}[\mathbf{D}^b]\{\boldsymbol{\chi}\}dA + \frac{1}{2}\int_A \kappa h\{\boldsymbol{\gamma}\}^{\mathrm{T}}\left[\mathbf{D}^s\right]\{\boldsymbol{\gamma}\}dA \end{aligned} \tag{3.203}$$

where

$$\{\boldsymbol{\chi}\} = \begin{bmatrix} -\partial\theta_y/\partial x \\ \partial\theta_x/\partial y \\ \partial\theta_x/\partial x - \partial\theta_y/\partial y \end{bmatrix}, \tag{3.204}$$

$$\{\boldsymbol{\gamma}\} = \begin{bmatrix} \theta_y + \partial w/\partial x \\ -\theta_x + \partial w/\partial y \end{bmatrix}, \tag{3.205}$$

$$\mathbf{D}^b = \frac{E}{1-\nu^2}\begin{bmatrix} 1 & \nu & 0 \\ \nu & 1 & 0 \\ 0 & 0 & \frac{1-\nu}{2} \end{bmatrix}, \tag{3.206}$$

$$\mathbf{D}^s = \frac{E}{1-\nu^2}\begin{bmatrix} G & 0 \\ 0 & G \end{bmatrix}. \tag{3.207}$$

The displacements are interpolated using shape functions as:

$$\begin{aligned} w &= \sum_{j=1}^{4} N_j w_j, \\ \theta_x &= \sum_{j=1}^{4} N_j \theta_{x_i}, \end{aligned} \tag{3.208}$$

$$\theta_\gamma = \sum_{j=1}^{4} N_j \theta_{\gamma_i}.$$

The shape functions are defined as

$$N_j = \frac{1}{4}\left(1+\xi_j\xi\right)\left(1+\eta_j\eta\right). \tag{3.209}$$

Using the above-mentioned shape function, displacements can be expressed based on the nodal displacement as

$$N_j = \frac{1}{4}\left(1+\xi_j\xi\right)\left(1+\eta_j\eta\right). \tag{3.210}$$

Using Eq. (3.210) in Eq. (3.203) yields

$$\begin{bmatrix} w \\ \theta_x \\ \theta y \end{bmatrix} = \begin{bmatrix} N_1 & 0 & 0 & \ldots & N_4 & 0 & 0 \\ 0 & N_1 & 0 & \ldots & 0 & N_4 & 0 \\ 0 & 0 & N_1 & \ldots & 0 & 0 & N_4 \end{bmatrix} \begin{bmatrix} w_1 \\ \theta_{x1} \\ \theta_{y1} \\ \ldots \\ w_4 \\ \theta_{x4} \\ \theta_{y4} \end{bmatrix} \tag{3.211}$$

where

$$U_e = \frac{1}{2}\{\mathbf{w}\}_e^{\mathrm{T}}[\mathbf{k}]_e\{\mathbf{w}\}_e. \tag{3.212}$$

The strain-displacement matrices for bending and shear contribution are in the form of

$$\left[\mathbf{B}^b\right] = \begin{bmatrix} \mathbf{B}_1^b & \mathbf{B}_2^b & \mathbf{B}_3^b & \mathbf{B}_4^b \end{bmatrix}, \tag{3.213}$$

$$\left[\mathbf{B}^s\right] = \begin{bmatrix} \mathbf{B}_1^s & \mathbf{B}_2^s & \mathbf{B}_3^s & \mathbf{B}_4^s \end{bmatrix} \tag{3.214}$$

where

$$\left[\mathbf{B}_i^b\right] = \begin{bmatrix} 0 & 0 & -\partial N_i/\partial x \\ 0 & \partial N_i/\partial y & 0 \\ 0 & \partial N_i/\partial x & -\partial N_i/\partial y \end{bmatrix}, \tag{3.215}$$

$$\left[\mathbf{B}^s\right] = \begin{bmatrix} \partial N_i/\partial x & 0 & N_i \\ \partial N_i/\partial y & -N_i & 0 \end{bmatrix}. \tag{3.216}$$

By replacing the shape functions in Eqs. (3.213) and (3.214), one obtains:

$$\left[\mathbf{B}_i^b\right]=\begin{bmatrix}0 & 0 & -\xi_j\left(1+\eta_j\eta\right)/4a\\ 0 & \left(1+\xi_j\xi\right)\eta_j/4b & 0\\ 0 & \xi_j\left(1+\eta_j\eta\right)/4a & -\left(1+\xi_j\xi\right)\eta_j/4b\end{bmatrix}, \tag{3.217}$$

$$\left[\mathbf{B}_i^s\right]=\begin{bmatrix}\xi_j\left(1+\eta_j\eta\right)/4a & 0 & \left(1+\xi_j\xi\right)\left(1+\eta_j\eta\right)/4\\ \left(1+\xi_j\xi\right)\eta_j/4b & -\left(1+\xi_j\xi\right)\left(1+\eta_j\eta\right)/4 & 0\end{bmatrix}. \tag{3.218}$$

By replacing the stiffness matrix and stress function in Eq. (3.212), the stiffness matrix due to bending is obtained as

$$\left[\mathbf{k}^b\right]=\frac{Eh^3}{48ab(1-\nu)^2}\begin{bmatrix}\mathbf{k}_{11}^b & \mathbf{k}_{12}^b & \mathbf{k}_{13}^b & \mathbf{k}_{14}^b\\ \mathbf{k}_{21}^b & \mathbf{k}_{22}^b & \mathbf{k}_{23}^b & \mathbf{k}_{24}^b\\ \mathbf{k}_{31}^b & \mathbf{k}_{32}^b & \mathbf{k}_{33}^b & \mathbf{k}_{34}^b\\ \mathbf{k}_{41}^b & \mathbf{k}_{42}^b & \mathbf{k}_{43}^b & \mathbf{k}_{44}^b\end{bmatrix} \tag{3.219}$$

where

$$\left[\mathbf{k}_{11}^b\right]=\begin{bmatrix}0 & 0 & 0\\ 0 & \frac{4}{3}\left\{\alpha^2+\frac{1}{2}(1-\nu)\right\}b^2 & -\frac{1}{2}(1+\nu)ab\\ 0 & -\frac{1}{2}(1+\nu)ab & \frac{4}{3}\left\{\beta^2+\frac{1}{2}(1-\nu)\right\}a^2\end{bmatrix}, \tag{3.220}$$

$$\left[\mathbf{k}_{12}^b\right]=\left[\mathbf{k}_{21}^b\right]=\begin{bmatrix}0 & 0 & 0\\ 0 & \frac{2}{3}\left\{\alpha^2-(1-\nu)\right\}b^2 & -\frac{1}{2}(3\nu-1)ab\\ 0 & \frac{1}{2}(3\nu-1)ab & \frac{1}{3}\left\{-4\beta^2+(1-\nu)\right\}a^2\end{bmatrix}, \tag{3.221}$$

$$\left[\mathbf{k}_{13}^b\right]=\left[\mathbf{k}_{31}^b\right]=\begin{bmatrix}0 & 0 & 0\\ 0 & \frac{2}{3}\left\{-\alpha^2-\frac{1}{2}(1-\nu)\right\}b^2 & \frac{1}{2}(1+\nu)ab\\ 0 & \frac{1}{2}(1+\nu)ab & \frac{2}{3}\left\{-\beta^2-\frac{1}{2}(1-\nu)\right\}a^2\end{bmatrix}, \tag{3.222}$$

$$\left[\mathbf{k}_{14}^b\right]=\left[\mathbf{k}_{41}^b\right]=\begin{bmatrix}0 & 0 & 0\\ 0 & \frac{1}{3}\left\{-4\alpha^2+(1-\nu)\right\}b^2 & \frac{1}{2}(3\nu-1)ab\\ 0 & -\frac{1}{2}(3\nu-1)ab & \frac{2}{3}\left\{\beta^2-(1-\nu)\right\}a^2\end{bmatrix}, \tag{3.223}$$

$$\left[\mathbf{k}_{22}^b\right]=\left[\mathbf{I}_3^T\right]\left[\mathbf{k}_{11}^b\right]\left[\mathbf{I}_3\right], \tag{3.224}$$

$$\left[\mathbf{k}_{23}^b\right]=\left[\mathbf{k}_{32}^b\right]=\left[\mathbf{I}_3^T\right]\left[\mathbf{k}_{14}^b\right]\left[\mathbf{I}_3\right], \tag{3.225}$$

$$\left[\mathbf{k}_{24}^b\right]=\left[\mathbf{k}_{42}^b\right]=\left[\mathbf{I}_3^T\right]\left[\mathbf{k}_{13}^b\right]\left[\mathbf{I}_3\right], \tag{3.226}$$

$$\left[\mathbf{k}_{33}^b\right]=\left[\mathbf{I}_1^T\right]\left[\mathbf{k}_{11}^b\right]\left[\mathbf{I}_1\right], \tag{3.227}$$

$$\left[\mathbf{k}_{34}^b\right]=\left[\mathbf{k}_{43}^b\right]=\left[\mathbf{I}_1^T\right]\left[\mathbf{k}_{12}^b\right]\left[\mathbf{I}_1\right], \tag{3.228}$$

$$\left[\mathbf{k}_{44}^{\mathrm{b}}\right]=\left[\mathbf{I}_2^{\mathrm{T}}\right]\left[\mathbf{k}_{11}^{\mathrm{b}}\right]\left[\mathbf{I}_2\right], \tag{3.229}$$

$$\mathbf{I}_1=\begin{bmatrix}-1&0&0\\0&1&0\\0&0&1\end{bmatrix},\quad \mathbf{I}_2=\begin{bmatrix}1&0&0\\0&-1&0\\0&0&1\end{bmatrix},\quad \mathbf{I}_3=\begin{bmatrix}1&0&0\\0&1&0\\0&0&-1\end{bmatrix}. \tag{3.230}$$

where $\alpha=\frac{a}{b}$ and $\beta=\frac{b}{a}$.Similarly, the stiffness matrix due to shear is defined as

$$\left[\mathbf{k}^{\mathrm{s}}\right]=\frac{Eh^3}{48ab\beta_s}\begin{bmatrix}\mathbf{k}_{11}^{\mathrm{s}}&\mathbf{k}_{12}^{\mathrm{s}}&\mathbf{k}_{13}^{\mathrm{s}}&\mathbf{k}_{14}^{\mathrm{s}}\\\mathbf{k}_{21}^{\mathrm{s}}&\mathbf{k}_{22}^{\mathrm{s}}&\mathbf{k}_{23}^{\mathrm{s}}&\mathbf{k}_{24}^{\mathrm{s}}\\\mathbf{k}_{31}^{\mathrm{s}}&\mathbf{k}_{32}^{\mathrm{s}}&\mathbf{k}_{33}^{\mathrm{s}}&\mathbf{k}_{34}^{\mathrm{s}}\\\mathbf{k}_{41}^{\mathrm{s}}&\mathbf{k}_{42}^{\mathrm{s}}&\mathbf{k}_{43}^{\mathrm{s}}&\mathbf{k}_{44}^{\mathrm{s}}\end{bmatrix} \tag{3.231}$$

where $\beta_{\mathrm{s}}=Eh^2/12\kappa Gb^2$ is a shear parameter, and

$$\left[\mathbf{k}_{11}^{\mathrm{s}}\right]=\begin{bmatrix}\left(1+\alpha^2\right)&\alpha^2b&-a\\\alpha^2b&\alpha^2b^2&0\\-a&0&a^2\end{bmatrix}, \tag{3.232}$$

$$\left[\mathbf{k}_{12}^{\mathrm{s}}\right]=\left[\mathbf{k}_{21}^{\mathrm{s}}\right]=\begin{bmatrix}\left(-1+\alpha^2\right)&\alpha^2b&a\\\alpha^2b&\alpha^2b^2&0\\-a&0&a^2\end{bmatrix}, \tag{3.233}$$

$$\left[\mathbf{k}_{13}^{\mathrm{s}}\right]=\left[\mathbf{k}_{31}^{\mathrm{s}}\right]=\begin{bmatrix}\left(-1-\alpha^2\right)&\alpha^2b&a\\\alpha^2b&\alpha^2b^2&0\\-a&0&a^2\end{bmatrix}, \tag{3.234}$$

$$\left[\mathbf{k}_{14}^{\mathrm{s}}\right]=\left[\mathbf{k}_{41}^{\mathrm{s}}\right]=\begin{bmatrix}\left(1-\alpha^2\right)&-\alpha^2b&-a\\\alpha^2b&\alpha^2b^2&0\\-a&0&a^2\end{bmatrix}, \tag{3.235}$$

$$\left[\mathbf{k}_{22}^{\mathrm{s}}\right]=\left[\mathbf{I}_3^{\mathrm{T}}\right]\left[\mathbf{k}_{11}^{\mathrm{s}}\right]\left[\mathbf{I}_3\right], \tag{3.236}$$

$$\left[\mathbf{k}_{23}^{\mathrm{s}}\right]=\left[\mathbf{k}_{32}^{\mathrm{s}}\right]=\left[\mathbf{I}_3^{\mathrm{T}}\right]\left[\mathbf{k}_{14}^{\mathrm{s}}\right]\left[\mathbf{I}_3\right], \tag{3.237}$$

$$\left[\mathbf{k}_{24}^{\mathrm{s}}\right]=\left[\mathbf{k}_{42}^{\mathrm{s}}\right]=\left[\mathbf{I}_3^{\mathrm{T}}\right]\left[\mathbf{k}_{13}^{\mathrm{s}}\right]\left[\mathbf{I}_3\right], \tag{3.238}$$

$$\left[\mathbf{k}_{33}^{\mathrm{s}}\right]=\left[\mathbf{I}_1^{\mathrm{T}}\right]\left[\mathbf{k}_{11}^{\mathrm{s}}\right]\left[\mathbf{I}_1\right], \tag{3.239}$$

$$\left[\mathbf{k}_{34}^{\mathrm{s}}\right]=\left[\mathbf{k}_{43}^{\mathrm{s}}\right]=\left[\mathbf{I}_1^{\mathrm{T}}\right]\left[\mathbf{k}_{12}^{\mathrm{s}}\right]\left[\mathbf{I}_1\right], \tag{3.240}$$

$$\left[\mathbf{k}_{44}^{\mathrm{s}}\right]=\left[\mathbf{I}_2^{\mathrm{T}}\right]\left[\mathbf{k}_{11}^{\mathrm{s}}\right]\left[\mathbf{I}_2\right]. \tag{3.241}$$

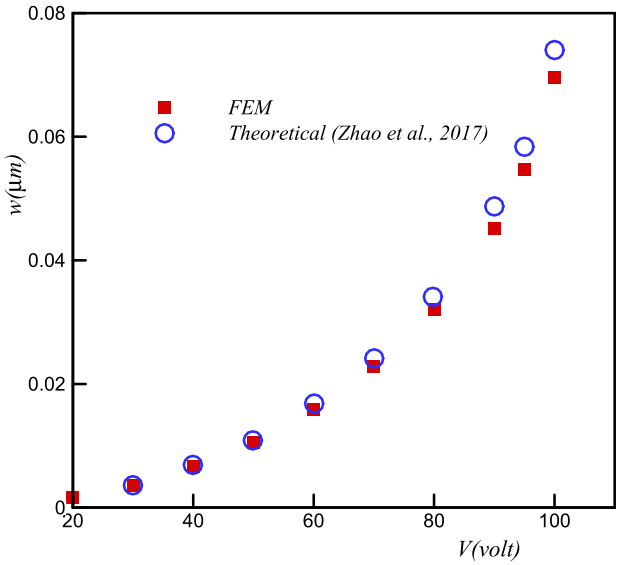

Figure 3.25 The maximum deflection of the microplate for various applied voltages: a comparison with theoretical investigation.

Table 3.1 The geometrical and mechanical properties of microcapacitors in μMKSV units.

Parameters	Value
Thickness (h)	1 μm
Length (L_x)	40 μm
Width (L_y)	20 μm
Poisson's ratio ν	0.28
Separation distance (d)	0.2 μm
Young's modulus (E)	1.30×10^5 MPa
Dielectric constant (ε_0)	8.854×10^{-6} pF/μm

The equivalent nodal force can be expressed as

$$\{\mathbf{f}_e\} = \int_A [\mathbf{N}]^T \begin{bmatrix} P \\ 0 \\ 0 \end{bmatrix} dA \tag{3.242}$$

where P is the external force per unit length in the Z-direction. For constant load, this yields

$$\{\mathbf{f}_e\} = Pab[\ 1 \quad 0 \quad 0 \quad 1 \quad 0 \quad 0 \quad 1 \quad 0 \quad 0 \quad 1 \quad 0 \quad 0\ ]^T. \tag{3.243}$$

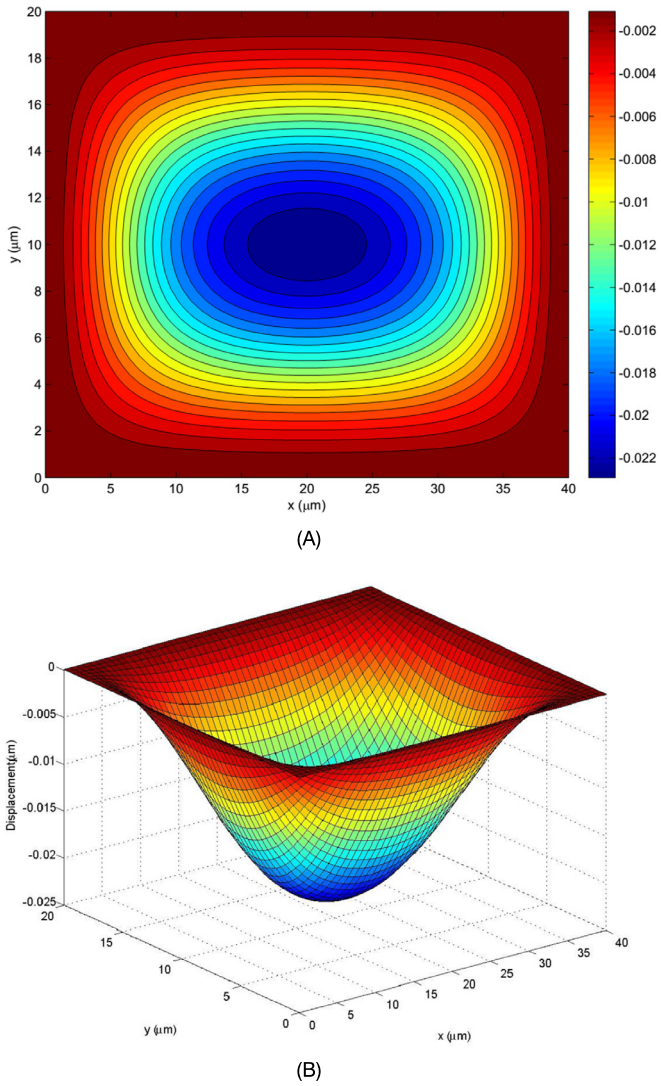

Figure 3.26 Capacitor deflection at $V = 70$ V: (A) 2D; (B) 3D.

Since the electrostatic force is nonlinear, conventional methods cannot be employed to obtain an FEM solution for microcapacitors. Hence, an iterative method is used. The electrical force at the nth step is determined from the plate deflection at the previous step as

$$p_n = \frac{1}{4}\sum_{j=1}^{4} \frac{\varepsilon_0 V^2}{2(d - w_j^{n-1})^2} \tag{3.244}$$

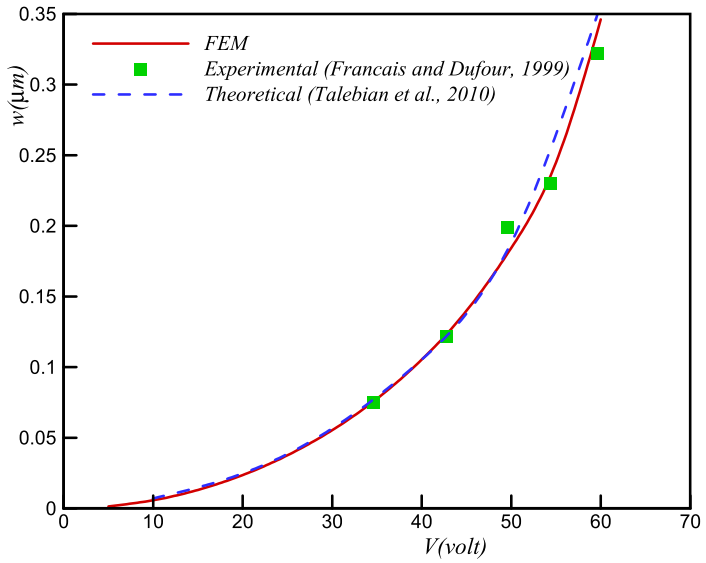

Figure 3.27 The maximum deflection of the microplate for various applied voltages: a comparison with theoretical [62] and experimental [63] data.

Table 3.2 Geometrical and mechanical properties of the microcapacitor in μMKSV units.

Parameters	Value
Thickness (h)	3 μm
Length (L_x)	250 μm
Width (L_y)	220 μm
Poisson's ratio ν	0.06
Separation distance (g)	1 μm
Young's modulus (E)	1.69×10^5 MPa
Dielectric constant (ε_0)	8.854×10^{-6} pF/μm

where w_j^{n-1} is the deflection of node j at step $n-1$. The initial guess considered here is $w^0(x, y) = 0$, and the iterative procedure continues until the relative error is less than selected tolerance, that is,

$$Error = \left| \frac{w^n(\frac{L_x}{2}, \frac{L_y}{2}) - w^{n-1}(\frac{L_x}{2}, \frac{L_y}{2})}{w^n(\frac{L_x}{2}, \frac{L_y}{2})} \right| \leq 10^{-6}. \tag{3.245}$$

In the simulation of NEMS and MEMS, very small numbers appear that can profoundly affect the accuracy of the numerical solution. To avoid this undesirable error, the di-

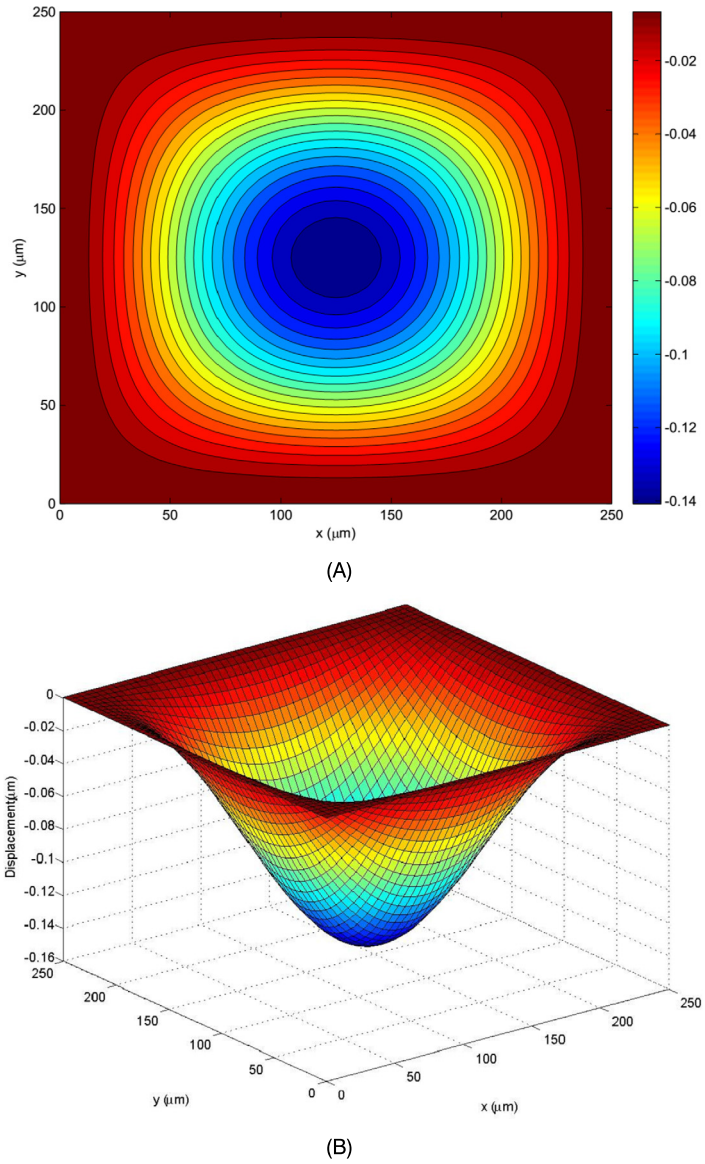

Figure 3.28 Capacitor deflection at $V = 45$ V: (A) 2D; (B) 3D.

mensionless parameter is employed. Another solution is using μMKSV (micrometer, kilogram, second, volt) unit system instead of MKSV (meter, kilogram, second, volt).

To verify the FEM solution, the maximum deflection of the microplate is investigated and compared with the analytical data obtained from [19] and displayed in

Fig. 3.25. The mechanical and geometrical properties of the microcapacitor are shown in Table 3.1 in μMKSV units. As demonstrated in Fig. 3.25, the presented FEM solution is in good agreement with the theoretical solution. In this case, the deflection of the microcapacitor (when the applied voltage is $V = 70$ V) is illustrated in Fig. 3.26.

Moreover, in Fig. 3.27, the maximum deflection of the microplate, with geometrical and mechanical properties presented in Table 3.2, is investigated and compared against theoretical [62] and experimental [63] data. As can be seen, the given FEM solution not only is in good agreement with the theoretical solution but also is very close to the experimental observations. For our case, the deflection of the microcapacitor when the applied voltage is $V = 45$ V is illustrated in Fig. 3.28.

3.5. Conclusion

In this chapter, three different numerical methods for solving the nonlinear differential equations governing the static behavior of micro- and nanoscale structures were introduced. After introducing the mathematical concepts of each method, the constitutive equations of the microstructure and nanostructure were extracted based on the continuum mechanics. Subsequently, the static behavior of nanostructures was investigated by numerical solutions.

In this and previous chapter, the static behavior of miniature structures was investigated. In the next chapter, some mathematical methods for investigating the dynamic performances of micro and nanostructures are presented.

References

[1] M. Keivani, A. Koochi, M. Abadyan, Coupled effects of surface energy and size dependency on the stability of nanotweezers using GDQ method, Microsystem Technologies 23 (5) (2017) 1295–1308.
[2] M. Keivani, A. Koochi, M. Abadyan, A new bilayer continuum model based on Gurtin-Murdoch and consistent couple-stress theories for stability analysis of beam-type nanotweezers, Journal of Mechanics 33 (2) (2017) 137–146.
[3] A. Koochi, H. Hosseini-Toudeshky, Coupled effect of surface energy and size effect on the static and dynamic pull-in instability of narrow nano-switches, International Journal of Applied Mechanics 7 (4) (2015) 1550064.
[4] M. Keivani, et al., Effect of surface layer on electromechanical stability of tweezers and cantilevers fabricated from conductive cylindrical nanowires, Surface Review and Letters 23 (2) (2016) 1550101.
[5] B. Wang, et al., Size-dependent pull-in instability of electrostatically actuated microbeam-based MEMS, Journal of Micromechanics and Microengineering 21 (2) (2011) 027001.
[6] M.Z. Nejad, A. Hadi, Non-local analysis of free vibration of bi-directional functionally graded Euler–Bernoulli nano-beams, International Journal of Engineering Science 105 (2016) 1–11.
[7] W.D. Yang, X. Wang, Nonlinear pull-in instability of carbon nanotubes reinforced nano-actuator with thermally corrected Casimir force and surface effect, International Journal of Mechanical Sciences 107 (2016) 34–42.

[8] R. Ansari, et al., Surface stress effect on the pull-in instability of hydrostatically and electrostatically actuated rectangular nanoplates with various edge supports, Journal of Engineering Materials and Technology 134 (4) (2012).
[9] M. Shojaeian, Y.T. Beni, H. Ataei, Electromechanical buckling of functionally graded electrostatic nanobridges using strain gradient theory, Acta Astronautica 118 (2016) 62–71.
[10] N. Fazli, et al., Influence of electrostatic force and the van der Waals attraction on the pull-in instability of the CNT-based probe–actuator, Canadian Journal of Physics 92 (9) (2013) 1047–1057.
[11] A. Farrokhabadi, A. Koochi, M. Abadyan, Modeling the instability of CNT tweezers using a continuum model, Microsystem Technologies 20 (2) (2014) 291–302.
[12] J.B. Ma, L. Jiang, S.F. Asokanthan, Influence of surface effects on the pull-in instability of NEMS electrostatic switches, Nanotechnology 21 (50) (2010) 505708.
[13] M. Karimi, M.H. Shokrani, A.R. Shahidi, Size-dependent free vibration analysis of rectangular nanoplates with the consideration of surface effects using finite difference method, Journal of Applied and Computational Mechanics 1 (3) (2015) 122–133.
[14] S. Gorthi, A. Mohanty, A. Chatterjee, Cantilever beam electrostatic MEMS actuators beyond pull-in, Journal of Micromechanics and Microengineering 16 (9) (2006) 1800–1810.
[15] F. Pan, et al., Squeeze film damping effect on the dynamic response of a MEMS torsion mirror, Journal of Micromechanics and Microengineering 8 (3) (1998) 200–208.
[16] W.C. Xie, H.P. Lee, S.P. Lim, Nonlinear dynamic analysis of MEMS switches by nonlinear modal analysis, Nonlinear Dynamics 31 (3) (2003) 243–256.
[17] D.-Y. Chiou, et al., Finite element modeling, characterization, and optimization design for the polymer-typed capacitive micro-arrayed ultrasonic transducer, Microsystem Technologies 14 (6) (2008) 787–797.
[18] B. Ahmad, R. Pratap, Elasto-electrostatic analysis of circular microplates used in capacitive micromachined ultrasonic transducers, IEEE Sensors Journal 10 (11) (2010) 1767–1773.
[19] L. Zhao, et al., Modeling of electrostatically actuated microplates, in: Micro Electro Mechanical Systems, Springer, 2017.
[20] C. Shu, B.E. Richards, Application of generalized differential quadrature to solve two-dimensional incompressible Navier–Stokes equations, International Journal for Numerical Methods in Fluids 15 (7) (1992) 791–798.
[21] A.M. Alneamy, et al., Electrostatic arch micro-tweezers, International Journal of Non-Linear Mechanics 118 (2020) 103298.
[22] A. Koochi, H. Hosseini-Toudeshky, M. Abadyan, Nonlinear beam formulation incorporating surface energy and size effect: application in nano-bridges, Applied Mathematics and Mechanics 37 (5) (2016) 583–600.
[23] A. Koochi, H. Hosseini-Toudeshky, M. Abadyan, A corrected model for static and dynamic electromechanical instability of narrow nanotweezers: incorporation of size effect, surface layer and finite dimensions, International Journal of Modern Physics B 32 (8) (2018) 1850089.
[24] A. Koochi, H. Hosseini-Toudeshky, M. Abadyan, A modified model for stability analysis of narrow-width NEMS tweezers: corrections due to surface layer, scale dependency, and force distributions, Scientia Iranica. Transaction B, Mechanical Engineering 24 (2) (2017) 673.
[25] M. Keivani, et al., A bilayer model for incorporating the simultaneous effects of surface energy and microstructure size dependency on the dynamic response and stability of electromechanical . . . , Surface Review and Letters 23 (5) (2016) 1650043.
[26] M. Keivani, et al., Modeling the coupled effects of surface layer and size effect on the static and dynamic instability of narrow nano-bridge structure, Journal of the Brazilian Society of Mechanical Sciences and Engineering 39 (2017) 1735–1744.
[27] A.R. Hadjesfandiari, G.F. Dargush, Couple stress theory for solids, International Journal of Solids and Structures 48 (18) (2011) 2496–2510.

[28] M.E. Gurtin, A. Ian Murdoch, A continuum theory of elastic material surfaces, Archive for Rational Mechanics and Analysis 57 (4) (1975) 291–323.
[29] K.F. Wang, B.L. Wang, Influence of surface energy on the non-linear pull-in instability of nano-switches, International Journal of Non-Linear Mechanics 59 (2014) 69–75.
[30] H.B. Palmer, The capacitance of a parallel-plate capacitor by the Schwartz–Christoffel transformation, Electrical Engineering 56 (3) (1937) 363–368.
[31] Y. Qian, et al., A dual-silicon-nanowires based U-shape nanoelectromechanical switch with low pull-in voltage, Applied Physics Letters 100 (11) (2012) 113102.
[32] E. Koukharenko, et al., Microelectromechanical systems vibration powered electromagnetic generator for wireless sensor applications, Microsystem Technologies 12 (10–11) (2006) 1071–1077.
[33] L. Latorre, et al., Characterization and modeling of a CMOS-compatible MEMS technology, Sensors and Actuators. A, Physical 74 (1–3) (1999) 143–147.
[34] D. Yan, A. Khajepour, R. Mansour, Design and modeling of a MEMS bidirectional vertical thermal actuator, Journal of Micromechanics and Microengineering 14 (7) (2004) 841.
[35] M. Keivani, et al., Dynamic instability analysis of U-shaped electromechanical nano-sensor operated in vdW regime, Journal of Vibroengineering 20 (1) (2018).
[36] M. Keivani, et al., Analysis of U-shaped NEMS in the presence of electrostatic, Casimir, and centrifugal forces using consistent couple stress theory, Iranian Journal of Science and Technology. Transaction A, Science 42 (2018) 1647–1658.
[37] R. Potekin, et al., Multi-frequency Atomic Force Microscopy based on enhanced internal resonance of an inner-paddled cantilever, Sensors and Actuators. A, Physical 273 (2018) 206–220.
[38] A.S. Rollier, et al., The stability and pull-in voltage of electrostatic parallel-plate actuators in liquid solutions, Journal of Micromechanics and Microengineering 16 (4) (2006) 794–801.
[39] O. Loh, A. Vaziri, H.D. Espinosa, The potential of MEMS for advancing experiments and modeling in cell mechanics, Experimental Mechanics 49 (1) (2009) 105–124.
[40] N.-C. Tsai, C.-Y. Sue, Review of MEMS-based drug delivery and dosing systems, Sensors and Actuators. A, Physical 134 (2) (2007) 555–564.
[41] J.G. Boyd, D. Kim, Nanoscale electrostatic actuators in liquid electrolytes, Journal of Colloid and Interface Science 301 (2) (2006) 542–548.
[42] G. Gramse, et al., Dynamic electrostatic force microscopy in liquid media, Applied Physics Letters 101 (21) (2012) 213108.
[43] G. Rezazadeh, et al., Dynamic characteristics and forced response of an electrostatically-actuated microbeam subjected to fluid loading, Microsystem Technologies 15 (9) (2009) 1355–1363.
[44] A. Kanani, et al., Modeling the size dependent pull-in instability of cantilever nano-switch immersed in ionic liquid electrolytes using strain gradient theory, Scientia Iranica. Transaction B, Mechanical Engineering 23 (3) (2016) 976.
[45] L.P. Teo, Casimir piston of real materials and its application to multilayer models, Physical Review A 81 (3) (2010) 032502.
[46] C.-J. Tong, et al., Optical micro-paddle beam deflection measurement for electrostatic mechanical testing of nano-scale thin film application to MEMS, Microsystem Technologies 16 (7) (2010) 1131–1137.
[47] H.M. Ouakad, The response of a micro-electro-mechanical system (MEMS) cantilever-paddle gas sensor to mechanical shock loads, Journal of Vibration and Control 21 (14) (2015) 2739–2754.
[48] X. Li, et al., Integrated MEMS/NEMS resonant cantilevers for ultrasensitive biological detection, Journal of Sensors (2009) 2009.
[49] Y.-H. Wang, C.-Y. Lee, C.-M. Chiang, A MEMS-based air flow sensor with a free-standing micro-cantilever structure, Sensors 7 (10) (2007) 2389–2401.
[50] X. Zhang, et al., Nanomechanical torsional resonators for frequency-shift infrared thermal sensing, Nano Letters 13 (4) (2013) 1528–1534.
[51] M. Aikele, et al., Resonant accelerometer with self-test, Sensors and Actuators. A, Physical 92 (1) (2001) 161–167.

[52] A. Shah-Mohammadi-Azar, et al., On the modeling of a capacitive angular speed measurement sensor, Measurement 46 (10) (2013) 3976–3981.
[53] H. Sedighi, et al., Non-linear dynamic instability of a double-sided nano-bridge considering centrifugal force and rarefied gas flow, International Journal of Non-Linear Mechanics 77 (2015) 96–106.
[54] M.I. Younis, MEMS linear and nonlinear statics and dynamics, in: R.T. Howe, A.J. Ricco (Eds.), Microsystems, Springer, New York, 2011.
[55] X. Zhang, et al., A study of the static characteristics of a torsional micromirror, Sensors and Actuators. A, Physical 90 (1–2) (2001) 73–81.
[56] R. Zengerle, A. Richter, H. Sandmaier, A micro membrane pump with electrostatic actuation, in: [1992] Proceedings IEEE Micro Electro Mechanical Systems, IEEE, 1992.
[57] P.-C. Hsu, C. Mastrangelo, K. Wise, A high sensitivity polysilicon diaphragm condenser microphone, in: Proceedings MEMS 98. IEEE. Eleventh Annual International Workshop on Micro Electro Mechanical Systems. An Investigation of Micro Structures, Sensors, Actuators, Machines and Systems (Cat. No. 98CH36176), IEEE, 1998.
[58] H.A. Tilmans, R. Legtenberg, Electrostatically driven vacuum-encapsulated polysilicon resonators: Part II. Theory and performance, Sensors and Actuators. A, Physical 45 (1) (1994) 67–84.
[59] J.N. Reddy, Theory and Analysis of Elastic Plates and Shells, CRC Press, 2006.
[60] K.B. Lee, Closed-form solutions of the parallel plate problem, Sensors and Actuators. A, Physical 133 (2) (2007) 518–525.
[61] M. Petyt, Introduction to Finite Element Vibration Analysis, Cambridge University Press, 2010.
[62] S. Talebian, et al., Effect of temperature on pull-in voltage and natural frequency of an electrostatically actuated microplate, Mechatronics 20 (6) (2010) 666–673.
[63] O. Francais, I. Dufour, Normalized abacus for the global behavior of diaphragms: pneumatic, electrostatic, piezoelectric or electromagnetic actuation, Journal of Modeling and Simulation of Microsystems 2 (1999) 149–160.

CHAPTER 4

Dynamic and time-dependent equations

4.1. Introduction

The behavior of nanoelectromechanical systems can be investigated from two different points of view. In the first approach, the static behavior of nanostructures is examined wherein the effect of time on the behavior of the system is ignored. However, the results of the static simulation are appropriate to assess the behavior of the electromechanical system when the DC voltage is applied slowly and, in turn, the effect of inertia on the performance of the system is negligible. In this case, the governing equations of the systems are time-independent.

On the contrary, when the variation rate of the applied DC voltage is significant or the actuation voltage is AC, the impact of inertia must be incorporated into the simulation. The performance of the structure in this situation including the impact of time on the governing equations is called the "dynamic behavior". Herein, the time-dependent dynamic behavior of a nanoelectromechanical system is investigated, and some mathematical methods are presented to solve the constitutive nonlinear time-dependent equation of systems. The rest of the chapter is organized as follows:

- "Galerkin method for dynamic problems,"
- "Rayleigh–Ritz method,"
- "Runge–Kutta method,"
- "Homotopy perturbation method for time-dependent differential equations,"
- "Energy balance method," and
- "Method of multiple scales."

4.2. Reduced-order approaches

The limitation of numerical and analytical solutions of time-dependent partial differential equations suggest that the concerned models (or governing equation of the system) need to be reduced to lower-order models capable of serving as the basis for additional analysis, which is known as the reduced-order methods. These methods have been widely employed previously by researchers to investigate the time-dependent behavior of the micro- and nanoelectromechanical systems. In the next subsections, two approaches based on the reduced-order method (i.e., the Galerkin method and the Rayleigh–Ritz method) for investigating the time-dependent behavior of nanostructures are proposed.

Nonlinear Differential Equations in Micro/nano Mechanics
https://doi.org/10.1016/B978-0-12-819235-1.00008-4
Copyright © 2020 Elsevier Ltd.
All rights reserved.

4.2.1 Galerkin method for dynamic problems

In Section 2.7, the Galerkin method was employed to investigate the static performance of a circular electromechanical microplate. For the time-dependent problems, the Galerkin method is attributed to a reduced-order approach for solving the nonlinear time-dependent partial differential equation. Since the Galerkin method is based on the weighted residual method, the weighted residual procedure for the dynamic problems is detailed in what follows.

The weighted residual method for the ordinary differential equation was presented in Section 2.7. This method can also be employed for the time-dependent partial differential equations. The following arbitrary partial differential equation is used to illustrate the concepts of the weighted residual method for the time-dependent partial differential equations:

$$D[y(x,t),x,t]=0, \quad c_1<x<c_2, \tag{4.1}$$

under arbitrary initial conditions and the following homogeneous boundary conditions:

$$y(c_1,t)=0, \quad y(c_2,t)=0. \tag{4.2}$$

The solution of Eq. (4.1) can be separated into the time-dependent part ($q_i(t)$) and time-independent part ($N_i(x)$). The weighted residual method seeks an approximated solution as

$$\tilde{y}(x,t)=\sum_{i=1}^{n} q_i(t)N_i(x) \tag{4.3}$$

where $\tilde{y}$ is an approximated solution for $y(x,t)$ and $q_i(t)$ represent unknown time-dependent functions, which can be determined by minimizing the errors. Also, $N_i(x)$ stand for trial functions, which must be *admissible*, similar to the time-independent problems. Then, the residual error is described as

$$R(x,t)=D\left[\tilde{y}(x,t),x,t\right]\neq 0. \tag{4.4}$$

Similar to the ordinary differential equation, the unknown function $q_i(t)$ can be evaluated by the following relation:

$$\int_a^b w_i(x,t)R(x,t)dx=0, \quad i=1,\ldots,n. \tag{4.5}$$

A system of n ordinary time-dependent differential equations is obtained by integrating Eq. (4.5), which can be solved for n values of $q_i(t)$. As mentioned in Section 2.7 for static problems, the weighted residual method results in a system of n algebraic equations.

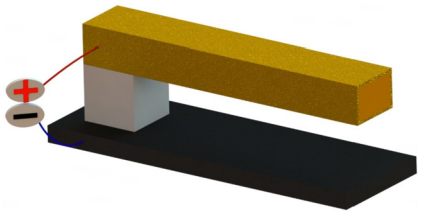

Figure 4.1 Schematic representation of a cantilever nanoactuator.

Similar to static problems, in the time-dependent problems, the weighting factors can be assessed through different methods such as least squares, subdomain collocation, point collocation, and Galerkin's method. In the Galerkin's method, the weighting functions are selected based on the trial solution as

$$w_i(x) = N_i(x), \quad i = 1, ..., n. \tag{4.6}$$

Hence, the unknown parameters are investigated as follows:

$$\int_a^b w_i(x)R(x)dx = \int_a^b N_i(x)R(x) = 0, \quad i = 1, ..., n. \tag{4.7}$$

This leads to n ordinary time-dependent differential equations.

4.2.1.1 Dynamic analysis of narrow nanoactuators

This section addresses the dynamic behavior of a narrow nanoactuator. As the surface energies can significantly change the dynamic performance of nanostructures, the modified couple stress theory involves the Gurtin–Murdoch surface elasticity to simulate the simultaneous impacts of size dependency and surface. As shown in Fig. 4.1, the nanoactuator is simulated by a nanobeam with length L. The moveable part of the nanoactuator has a uniform rectangular cross-section with width b and thickness h.

The surface energies are modeled assuming a zero-thickness surface layer. The strain energies of this layer can be investigated by [1,2]

$$U_s = \frac{1}{2}\int_0^L \oint_{\partial A} (\tau_{ij}\varepsilon_{ij} + \tau_{ni}u_{n,i})dsdx. \tag{4.8}$$

Also, the out-of-plane and in-plane components of the surface stress tensor are given by:

$$\tau_{ij} = \mu_0(u_{i,j} + u_{j,i}) + (\lambda_0 + \tau_0)u_{k,k}\delta_{ij} + \tau_0(\delta_{ij} - u_{j,i}), \tag{4.9}$$

$$\tau_{ni} = \tau_0(u_{n,i}) \tag{4.10}$$

where μ_0 and λ_0 indicate the surface elastic parameters and τ_0 denotes the surface residual stress. The stress tensor is described similar to the classical theory as

$$\varepsilon_{ij} = \frac{1}{2}(u_{i,j} + u_{j,i}). \tag{4.11}$$

The components of the displacement vector of an Euler–Bernoulli beam can be expressed as [3]

$$u_X = -Z\frac{\partial W(X,t)}{\partial X}, \quad u_Y = 0, \quad u_Z = W(X,t) \tag{4.12}$$

where W is the centerline deformation in the Z direction.

By substituting Eq. (4.12) into Eqs. (4.9) and (4.11), we get

$$\tau_{XX} = \tau_0 - ZE_0\frac{\partial^2 W(X,t)}{\partial X^2}, \quad \tau_{YY} = -(\tau_0 + \lambda_0)Z\frac{\partial^2 W(X,t)}{\partial X^2}, \quad \tau_{XY} = 0, \tag{4.13}$$

$$\tau_{nX} = \tau_0\frac{\partial u_n(X,Y,Z,t)}{\partial X}, \tag{4.14}$$

$$\varepsilon_{XX} = -Z\frac{\partial^2 W(X,t)}{\partial X^2}, \quad \varepsilon_{ZZ} = \varepsilon_{YY} = \varepsilon_{XY} = \varepsilon_{YZ} = \varepsilon_{ZX} = 0 \tag{4.15}$$

where $E_0 = \lambda_0 + 2\mu_0$ is the surface elastic modulus. By using Eqs. (4.13)–(4.15) and (4.10) in Eq. (4.9), the surface energy is obtained as

$$U_S = \frac{1}{2}\int_0^L \oint_{\partial A}\left\{\tau_0 n_Z^2\left(\frac{\partial W(X,t)}{\partial X}\right)^2 - \tau_0 Z\frac{\partial^2 W(X,t)}{\partial X^2} + E_0\left(-Z\frac{\partial^2 W(X,t)}{\partial X^2}\right)^2\right\} dsdX. \tag{4.16}$$

The strain energy density in the context of the modified couple stress theory is defined as [4]

$$U_B = \frac{1}{2}\int_0^L \int_A (\sigma_{ij}\varepsilon_{ij} + m_{ij}\chi_{ij})dAdx \tag{4.17}$$

where the stress tensor (σ_{ij}), deviator part of the couple stress tensor (m_{ij}), and symmetric curvature tensor (χ_{ij}) can be defined as:

$$\sigma_{ij} = \lambda\varepsilon_{mm}\varepsilon_{ij} + 2\mu\varepsilon_{ij}, \tag{4.18}$$

$$m_{ij} = 2l^2\mu\chi_{ij}, \tag{4.19}$$

$$\chi_{ij} = \frac{1}{2}\left((\nabla\theta)_{ij} + (\nabla\theta)_{ij}^T\right), \tag{4.20}$$

$$\theta_i = \frac{1}{2}(\nabla \times \vec{r})_i \tag{4.21}$$

where λ, l, μ, θ, and r are the Lame constants, material length scale parameter, shear modulus, rotation vector, and displacement vector, respectively.

The equilibrium relations of the surface layer based on the Gurtin and Murdoch elasticity [1] are defined as:

$$\begin{aligned} \tau^{+}_{mi,m} - \sigma^{+}_{i3} &= 0, \\ \tau^{-}_{mi,m} - \sigma^{-}_{i3} &= 0 \end{aligned} \tag{4.22}$$

where signs $-$ and $+$ represent the stresses on the lower and upper surface layer, respectively.

Also, σ_{zz} is zero in the classical beam theory. However, this assumption does not satisfy the surface conditions of the surface elasticity model. To overcome this defect, the linear distribution of σ_{zz} through the beam thickness, which satisfies the equilibrium requirement on the lower and upper surfaces can be considered as follows [5]:

$$\sigma_{ZZ} = \frac{1}{2}(\sigma^{+}_{ZZ} + \sigma^{-}_{ZZ}) + \frac{Z}{h}(\sigma^{+}_{ZZ} - \sigma^{-}_{ZZ}). \tag{4.23}$$

By using Eq. (4.22) in Eq. (4.23), we get

$$\sigma_{ZZ} = \frac{1}{2}\left(\tau_0\left(\frac{\partial^2 u^{+}_{Z}}{\partial X^2} - \frac{\partial^2 u^{-}_{Z}}{\partial X^2}\right)\right) + \frac{Z}{h}\left(\tau_0\left(\frac{\partial^2 u^{+}_{Z}}{\partial X^2} + \frac{\partial^2 u^{-}_{Z}}{\partial X^2}\right)\right). \tag{4.24}$$

Considering small deflection and substituting Eq. (4.12) into Eqs. (4.18)–(4.21) and (4.24), we obtain

$$\chi_{XY} = -\frac{1}{2}\frac{\partial^2 W(X)}{\partial X^2}, \quad \chi_{XX} = \chi_{YY} = \chi_{ZZ} = \chi_{YZ} = \chi_{ZX} = 0, \tag{4.25}$$

$$m_{XY} = -\mu l^2 \frac{\partial^2 W(X)}{\partial X^2}, \quad m_{XX} = m_{YY} = m_{ZZ} = m_{YZ} = m_{ZX} = 0, \tag{4.26}$$

$$\begin{aligned} &\sigma_{XX} = -ZE\frac{\partial^2 W(X,t)}{\partial X^2} + \nu\sigma_{ZZ}, \quad \sigma_{ZZ} = \frac{2Z\tau_0}{h}\frac{\partial^2 W(X,t)}{\partial X^2}, \\ &\sigma_{YY} = \sigma_{XY} = \sigma_{YZ} = \sigma_{ZX} = 0 \end{aligned} \tag{4.27}$$

where ν and E are the Poisson's ratio and Young's modulus, respectively.

Substituting Eq. (4.25) into Eq. (4.27), the bulk strain energy (U_B) is determined as

$$U_B = \frac{1}{2}\int_0^L \int_A \left\{ -Z\frac{\partial^2 W}{\partial X^2}\left(-ZE\frac{\partial^2 W}{\partial X^2} + \frac{2Z\tau_0\nu}{h}\frac{\partial^2 W}{\partial X^2}\right) + \mu l^2 \left(\frac{\partial^2 W}{\partial X^2}\right)^2 \right\} dA dX. \tag{4.28}$$

The external work is done by distributed electrical force (f_{elec}), squeezed film damping force (f_{sd}), and Casimir force (f_{Cas}) as given below:

$$W_{ext} = \int_0^L \int_0^W \left[f_{elec} + f_{Cas} + f_{sd}\right] dW dX. \tag{4.29}$$

Table 4.1 Comparison of the capacitance values using different models [11].

Geometry		Numerical [9]	Deviation (%)		
h/b	*h/g*	C_g/ε_0	Eq. (4.31)	Linear fringing field	Parallel plates
0.5	0.5	3.61	<0.1	−34.5	−72.3
0.5	1	5.12	0.4	−25.7	−61.0
0.5	2.5	8.97	0.4	−17.7	−44.3
0.5	5	14.71	0.6	−12.9	−32.1
1	0.5	2.96	0.6	−51.9	−83.1
1	1	3.96	0.7	−40.3	−74.8
1	2.5	6.29	0.4	−29.3	−60.2
1	5	9.52	0.5	−22.4	−47.5

The electrical force can be calculated by differentiating the capacitor potential relative to the gap (g),

$$f_{elec} = -\frac{1}{2} V^2 \frac{dC_g}{dg}. \tag{4.30}$$

The electrical field is not uniform for a narrow microbeam, and the edge effect should be incorporated. For the narrow-width charged beams, several corrections have been proposed for incorporating the fridging field such as Palmer's formula [6], Mejis–Fokkema formula [7], Nishiyama and Nakamura model [8], Batra correction [9], and Hu and Wei model [10]. Some of the common fridging field correction models are summarized in Table 1.1.

Using the Batra's correction, the capacitance of the capacitor created by a narrow beam over an infinite plate can be evaluated by the following relation [9]:

$$C_g = \varepsilon_0 \left[\frac{b}{g} - 0.36 + 0.85 \left(\frac{b}{g} \right)^{0.24} + 2.5 \left(\frac{h}{g} \right)^{0.24} \right]. \tag{4.31}$$

By using Eq. (4.31) in Eq. (4.30), the electrostatic force per unit length of the beam is defined as

$$f_{elec} = \frac{\varepsilon_0 b V^2}{2(g-W)^2} \left[1 + 0.2 \left(\frac{g-W}{b} \right)^{0.76} + 0.6 \frac{h}{b} \left(\frac{g-W}{h} \right)^{0.76} \right]. \tag{4.32}$$

Table 4.1 shows the capacitance of a beam parallel to an infinite plate for different geometrical parameters. The data are computed by Batra's correction (i.e., Eq. (4.31)), parallel plate assumption (i.e., Eq. (1.1)), and Palmer's model (i.e., Eq. (2.10)). According to Table 4.1, for a narrow beam, the capacitance values investigated by the parallel plate assumption and Palmer's model have significant differences with those of a fully

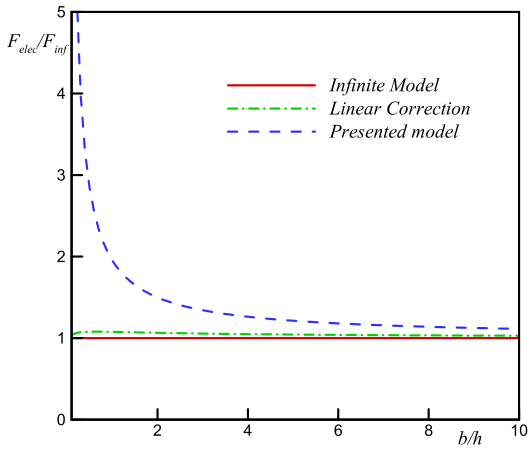

Figure 4.2 Effect of finite dimension correction on the electrical force.

numerical solution. However, the difference in capacitance values between the Batra's model and the numerical solution is less than 1%.

Fig. 4.2 illustrates the electrical force obtained by the three different models (e.g., Batra's model, the parallel plate model, and Palmer's model) at different width-to-thickness ratios. To simplify the comparison between the models, the electrical forces are normalized by dividing by those obtained by the parallel plate model. Fig. 4.2 demonstrates that although the results of the narrow beam model converge to the classic models for wide beams (larger width-to-thickness ratios), there are significant differences between the results of the proposed model and classical electrical force computed by the narrow beam and parallel plate models at smaller width-to-thickness ratios. Furthermore, Fig. 4.2 reveals that the classical models are independent of the width-to-thickness ratio.

The Casimir force between two infinite parallel plates has been demonstrated in previous sections; however, it needs to be modified for narrow microbeams and nanobeams. The corrected Casimir force regarding the effects of finite dimensions and edges can be expressed as [11]

$$f_{Cas} = f_{Cas\parallel} + \gamma_{1si}\frac{\hbar c}{g^3} \tag{4.33}$$

where $\gamma_{1si} = 0.00523$ is the universal coefficient [30] and $f_{Cas\parallel}$ is the Casimir force between two infinite plates, which was described in Eq. (2.65). Now, by replacing relation (2.65) in Eq. (4.33), the Casimir force per unit length of the narrow beam is obtained as follows:

$$f_{Cas} = \frac{\pi^2\hbar cb}{240(g-W)^4} + 0.00523\frac{\hbar c}{(g-W)^3}. \tag{4.34}$$

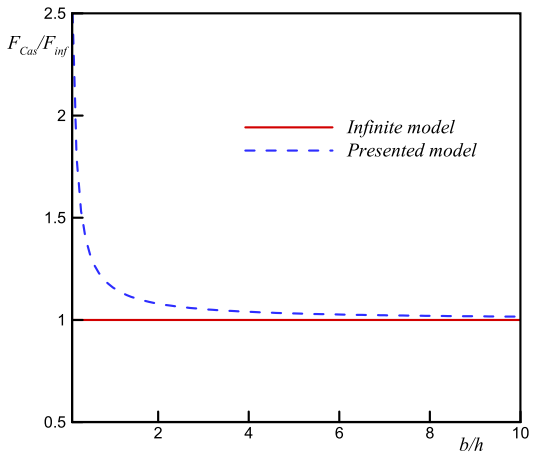

Figure 4.3 Effect of finite dimension correction on the Casimir force.

The effect of finite dimension modification on the Casimir force is illustrated in Fig. 4.3. In this figure, the Casimir force is normalized by dividing by the parallel plate Casimir force. Fig. 4.3 demonstrates that although the modified Casimir force converges to the parallel plate model for large width-to-thickness ratios, the finite dimension corrections significantly alter the Casimir force for narrow beams.

As mentioned in Chapter 1, the squeezed film damping is the most common and dominant energy loss mechanism in NEMS/MEMS. The damping force due to squeezed film on a plate is presented in Eq. (1.17). By replacing g with $g - W$ in Eq. (1.17), the damping force induced by the squeeze film acting on the nanoactuator is achieved as follows:

$$F_{sd} = \int_{-b/2}^{b/2} P(Y,t)dY = -\frac{\kappa_{eff} b^3}{(g - W(X,t))^3} \frac{\partial W(X,t)}{\partial t} \tag{4.35}$$

where κ_{eff} is the effective viscosity coefficient which can be modified by using the Veijola et al. relation [12],

$$\kappa_{eff} = \frac{\kappa}{1 + 9.638 K_n^{1.159}}, \tag{4.36}$$

where κ stands for the viscosity coefficient at 1 atm, and K_n denotes the Knudsen number.

In the dynamic behavior simulation, the kinetic energy should also incorporate Hamilton's principle. The kinetic energy is defined as

$$T = \frac{1}{2} \int_0^L \int_A \rho \left(\frac{\partial W(X,t)}{\partial t} \right)^2 dA dX. \tag{4.37}$$

To extract the constitutive equation of the system, Hamilton's principle is applied:

$$\int_{t_1}^{t_2} (\delta T - \delta U_B - \delta U_S + \delta W_{ext})\, dt = 0. \tag{4.38}$$

Substituting Eqs. (4.16), (4.28), (4.29), and (4.37) into Eq. (4.38):

$$\begin{aligned}
&\int_{t_1}^{t_2}\int_0^L \left[\begin{array}{l} \left(EI + \mu A l^2 + E_0 I_0 - \dfrac{2\tau_0 \upsilon I}{h}\right)\dfrac{\partial^4 W}{\partial X^4} \\ -\tau_0 S_0 \dfrac{\partial^2 W}{\partial X^2} \rho A \dfrac{\partial^2 W}{\partial t^2} - F_{ext}(X,t) \end{array}\right] \delta W dX dt \\
&+ \int_{t_1}^{t_2} \left[\tau_0 S \frac{\partial W}{\partial X}\delta W - \left(EI + \mu A l^2 + E_0 I_0 - \frac{2\tau_0 \upsilon I}{h}\right)\frac{\partial^3 W}{\partial X^3}\delta W\right]_0^L dt \\
&+ \int_{t_1}^{t_2} \left[\left(EI + \mu A l^2 + E_0 I_0 - \frac{2\tau_0 \upsilon I}{h}\right)\frac{\partial^2 W}{\partial X^2}\delta\left(\frac{\partial W}{\partial X}\right)\right]_0^L dt + \int_0^L \left[\rho A \frac{\partial W}{\partial t}\delta W\right]_{t_1}^{t_2} dX = 0.
\end{aligned} \tag{4.39}$$

By setting each term of the above variational equation equal to zero and substituting the relation of external forces (squeezed film damping, electrical and Casimir forces), the nonlinear constitutive equation of the system is obtained as

$$\begin{aligned}
&\rho A \frac{\partial^2 W}{\partial t^2} + \frac{\kappa_{eff} b^3}{(g-W)^3}\frac{\partial W}{\partial t} + \left(EI + \mu A l^2 + E_0 I_0 - \frac{2\tau_0 \upsilon I}{h}\right)\frac{\partial^4 W}{\partial X^4} - \tau_0 S_0 \frac{\partial^2 W}{\partial X^2} \\
&= \frac{\varepsilon_0}{2}\frac{bV^2}{(g-W)^2}\left[1 + 0.2\left(\frac{g-W}{b}\right)^{0.76} + 0.6\frac{h}{b}\left(\frac{g-W}{h}\right)^{0.76}\right] \\
&+ \frac{\pi^2 \hbar c b}{240(g-W)^4} + 0.00523\frac{\hbar c}{(g-W)^3}
\end{aligned} \tag{4.40}$$

and the boundary conditions are:

$$\begin{aligned}
&\tau_0 S_0 \frac{\partial W}{\partial X} - \left(EI + \mu A l^2 + E_0 I_0 - \frac{2\tau_0 \upsilon I}{h}\right)\frac{\partial^3 W}{\partial X^3}\bigg|_{X=0,L} = 0 \quad \text{or} \quad \delta W|_{X=0,L} = 0, \\
&\left(EI + \mu A l^2 + E_0 I_0 - \frac{2\tau_0 \upsilon I}{h}\right)\frac{\partial^2 W}{\partial X^2}\bigg|_{X=0,L} = 0 \quad \text{or} \quad \delta\left(\frac{\partial W}{\partial X}\right)\bigg|_{X=0,L} = 0.
\end{aligned} \tag{4.41}$$

For a rectangular section, we have

$$\begin{aligned}
I_0 &= \int_S z^2 ds = \frac{1}{2}bh^2 + \frac{1}{6}h^3, \\
S_0 &= \int_S n_z^2 ds = 2b.
\end{aligned} \tag{4.42}$$

Now, letting $x = X/L$ and $w = W/g$, the dimensionless governing equation of the nanoactuator with rectangular cross-section energy is summarized as:

$$\frac{\partial^2 w}{\partial \tau^2} + \frac{\hat{c}}{\gamma^3(1-w)^3}\frac{\partial w}{\partial \tau} + \left(1 + \frac{6}{1+\upsilon}\left(\frac{l}{h}\right)^2 + e_0\right)\frac{\partial^4 w}{\partial x^4} - t_0\frac{\partial^2 w}{\partial x^2}$$
$$= \frac{\alpha^2}{(1-w)^2}\left[1 + (0.2 + 0.6\eta^{0.24})\gamma^{0.76}(1-w)^{0.76}\right] \tag{4.43}$$
$$+ \frac{\beta_{Cas}}{(1-w)^4}(1 + 0.127\gamma(1-w)),$$

$$w(0,\tau) = \frac{\partial w}{\partial x}(0,\tau) = 0, \tag{4.44}$$

$$\left(1 + \frac{6}{1+\upsilon}\left(\frac{l}{h}\right)^2 + e_0\right)\frac{\partial^2 w}{\partial x^2}(1,\tau) = 0,$$
$$t_0\frac{\partial w}{\partial x}(1,\tau) - \left(1 + \frac{6}{1+\upsilon}\left(\frac{l}{h}\right)^2 + e_0\right)\frac{\partial^3 w}{\partial x^3}(1,\tau) = 0 \tag{4.45}$$

where the dimensionless parameters are defined as:

$$\alpha^2 = \frac{\varepsilon_0\varepsilon_r b V^2 L^4}{2g^3 EI}, \tag{4.46}$$

$$\beta_{Cas} = \frac{\pi^2 \hbar c b L^4}{240 g^5 EI}, \tag{4.47}$$

$$\tau = \sqrt{\frac{EI}{\rho b h L^4}}t, \tag{4.48}$$

$$e_0 = \frac{E_0 I_0 h - \tau_0 \upsilon I}{EIh}, \tag{4.49}$$

$$t_0 = \frac{2b\tau_0 L^2}{EI}, \tag{4.50}$$

$$\gamma = \frac{g}{b}, \tag{4.51}$$

$$\eta = \frac{h}{b}, \tag{4.52}$$

$$\hat{c} = \kappa_{eff} L^2 \sqrt{\frac{1}{\rho b h EI}}. \tag{4.53}$$

In the above equation, τ is the dimensionless time, α is the dimensionless parameter of the applied voltage, β_{cas} indicates the dimensionless parameter of the Casimir force, and $\hat{c}$ is the dimensionless parameter pertinent to the effective viscosity of the gas trapped underneath the nanoactuator. Also, γ and η are the geometrical parameters indicating

the gap-to-width ratio and the thickness-to-width ratio, respectively. Moreover, t_0 and e_0 are the dimensionless surface parameters: while e_0 is related to both surface elasticity and surface residual stress, t_0 is only affected by the surface residual stress.

Eq. (4.43) is discretized into a finite degree of freedom (DOF) system to assess the dynamic performance of the nanoactuator by using the Galerkin method. This discretization yields a system of ordinary time-dependent differential equations that can be solved by an arbitrary numerical or semianalytical process. In the reduced-order method, the displacement is assumed as a sum of time-dependent and position-dependent parts,

$$w(x,\tau) = \sum_{i=1}^{n} q_i(\tau)\,\phi_i(x), \tag{4.54}$$

where index i indicates the number of included modes in the Galerkin solution. The undamped mode shapes of the nanobeam satisfy all of the boundary conditions and can be used as the basis functions in the Galerkin procedure. The simultaneous effects of size dependency and surface energies are taken into account to investigate the free vibrations of nanobeam and determine its mode shapes. The dimensionless constitutive equation of undamped free vibration of a nanobeam is described by incorporating the surface effect and size dependency:

$$\frac{\partial^2 w}{\partial \tau^2} + \left(1 + \frac{6}{1+\upsilon}\left(\frac{l}{h}\right)^2 + e_0\right)\frac{\partial^4 w}{\partial x^4} - t_0\frac{\partial^2 w}{\partial x^2} = 0. \tag{4.55}$$

The solution of the above equation can be assumed as

$$w(x) = \phi(x)\sin(\omega\tau). \tag{4.56}$$

By using Eq. (4.56) in Eq. (4.55), one gets

$$-\phi^2 + \left(1 + \frac{6}{1+\upsilon}\left(\frac{l}{h}\right)^2 + e_0\right)\frac{d^4\phi}{dx^4} - t_0\frac{d^2\phi}{dx^2} = 0. \tag{4.57}$$

The solution of Eq. (4.57) is expressed as

$$\phi(x) = C_1\sin(\xi_i x) + C_2\cos(\xi_i x) + C_3\sinh(\lambda_i x) + C_4\cosh(\lambda_i x) \tag{4.58}$$

where

$$\lambda_i^2 - \xi_i^2 = \frac{1 + \frac{6}{1+\upsilon}(\frac{l}{h})^2 + e_0}{t_0}. \tag{4.59}$$

By imposing the boundary conditions, the nontrivial solution can be examined from the following relation:

$$\begin{vmatrix} 0 & 1 & 0 & 1 \\ \xi_i & 0 & \lambda_i & 0 \\ -\xi_i^2 \sin(\lambda_i) & -\xi_i^2 \cos(\lambda_i) & \lambda_i^2 \sinh(\lambda_i) & \lambda_i^2 \cosh(\lambda_i) \\ t_0\xi_i \cos(\xi_i) - D\xi_i^3 \cos(\xi_i) & -t_0\xi_i sin(\xi_i) + D\xi_i^3 sin(\xi_i) & t_0\lambda_i \cosh(\lambda_i) - D\lambda_i^3 \cosh(\lambda_i) & t_0\lambda_i sinh(\lambda_i) - D\lambda_i^3 sinh(\lambda_i) \end{vmatrix} = 0 \tag{4.60}$$

where

$$D = 1 + \frac{6}{1+\upsilon}\left(\frac{l}{h}\right)^2 + e_0. \tag{4.61}$$

After some mathematical elaboration, the mode shapes of the cantilever beam are specified by considering both size dependency and surface energies as follows:

$$\begin{aligned} \phi_i(x) = &-\frac{\xi_i^2 \cos(\xi_i) + \lambda_i^2 \cosh(\lambda_i)}{\xi_i^2 sin(\xi_i) + \lambda_i^2 sinh(\lambda_i)}\left(\sin(\xi_i x) - \frac{\xi_i}{\lambda_i}\sinh(\lambda_i x)\right) \\ &+ \cos(\xi_i x) - \cosh(\lambda_i x) \end{aligned} \tag{4.62}$$

where ξ_i and λ_i can be described by:

$$\xi_i = \frac{\sqrt{2D(-t_0 + \sqrt{4\omega_i^4 D + t_0^2}}}{2D}, \tag{4.63}$$

$$\lambda_i = \frac{\sqrt{2D(t_0 + \sqrt{4\omega_i^4 D + t_0^2}}}{2D} \tag{4.64}$$

in the above relations, ω_i is determined by solving Eq. (4.60); and the obtained results are plotted in Fig. 4.4. As can be seen, the first natural frequency of the beam is increased by increasing the size or surface parameter.

As mentioned in the static case, which was solved by the Galerkin procedure, the nonlinear term can be expanded by using a Taylor's series around $w = 0$. Another approach is multiplying both sides of the differential equation (4.43) by $(1 - w)^4$. The first approach is used in the static problem solved by the Galerkin method (i.e., in Section 2.7). However, in this section, the second approach is employed.

The following system of ordinary differential equations is achieved by multiplying both sides of Eq. (4.43) by $(1 - w)^4$ then multiplying the result by $\varphi_i(x)$, integrating it

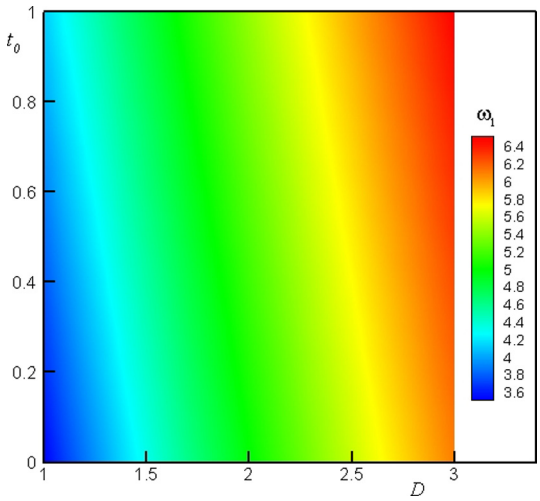

Figure 4.4 The first natural frequency on nanobeam by considering both size and surface effect.

from $x = 0$ to 1, and using the mode shapes orthogonality:

$$\begin{aligned}
&\left(1-\sum_{j=1}^{N} q_j\phi_j\right)^4 \int_0^1 \phi_i\phi_i dx\ddot{q}_i + \frac{\hat{c}(1-\sum_{j=1}^{N} q_j\phi_j)}{\gamma^3}\int_0^1 \phi_i\phi_i dx\dot{q}_i \\
&+\left(1+\frac{6}{(1+\upsilon)}\left(\frac{l}{h}\right)^2+e_0\right)\left(1-\sum_{j=1}^{N} q_j\phi_j\right)^4 \int_0^1 \left(\phi_i\sum_{j=1}^{N} q_j\frac{d^4\phi_j}{dx^4}\right)dx \\
&-t_0\left(1-\sum_{j=1}^{N} q_j\phi_j\right)^4 \int_0^1 \left(\phi_i\sum_{j=1}^{N} q_j\frac{d^2\phi_j}{dx^2}\right)dx \\
&-\int_0^1 \phi_i\alpha^2\left(1-\sum_{j=1}^{N} q_j\phi_j\right)^2\left[1+(0.2+0.6\eta^{0.24})\gamma^{0.76}\left(1-\sum_{j=1}^{N} q_j\phi_j\right)^{0.76}\right]dx \\
&-\int_0^1 \phi_i\beta_{Cas}\left(1+0.127\gamma\left(1-\sum_{j=1}^{N} q_j\phi_j\right)\right)dx = 0 \quad \text{for } i=1,2,..,N
\end{aligned} \tag{4.65}$$

where N is the number of the available terms in the Galerkin solution.

The time-dependent tip deflection of the nanoactuator and its phase plane are plotted in Fig. 4.5A–B, respectively. In this figure, the dimensionless external voltage increases from zero to the pull-in value. Fig. 4.5 demonstrates an upward trend for the maximum tip deflection of the nanoactuator when increasing the applied voltage.

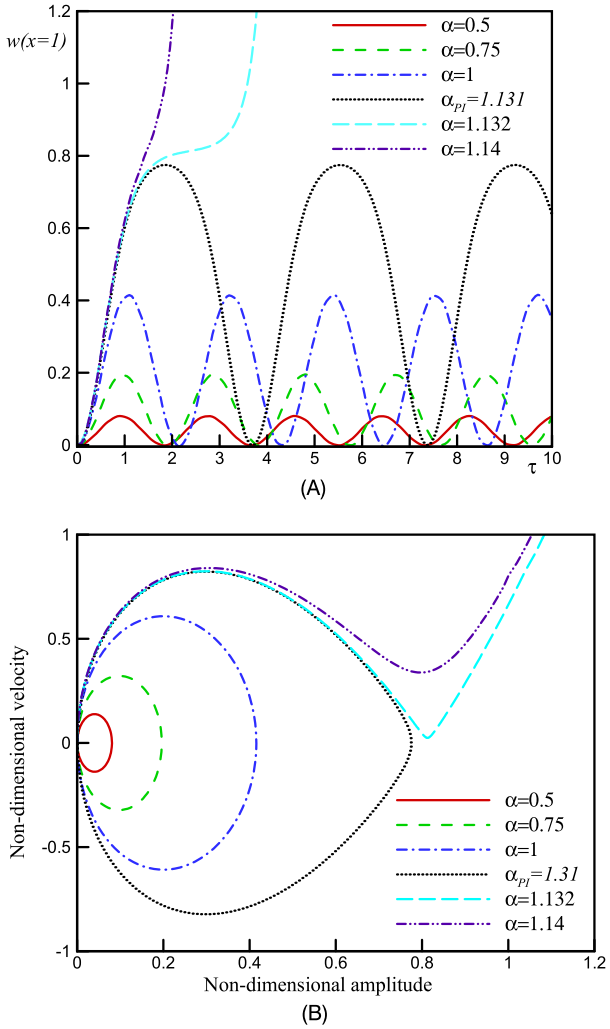

Figure 4.5 Dynamic behavior of nanoactuator for different values of dimensionless voltage parameter from zero to pull-in value: (A) time history, (B) phase plane.

Once the applied voltage exceeds the pull-in voltage, the nanoactuator tip deflection dramatically rises, and the pull-in instability emerges. The phase-plane diagram of the nanoactuator reveals that it has two fixed points, namely stable center point and unstable saddle-node. For the external voltage lower than the pull-in value, the homoclinic trajectory starts from the unstable branch saddle-node and returns at the stable center point. However, for the applied voltage larger than the pull-in value, the nanoactuator suddenly falls onto the substrate.

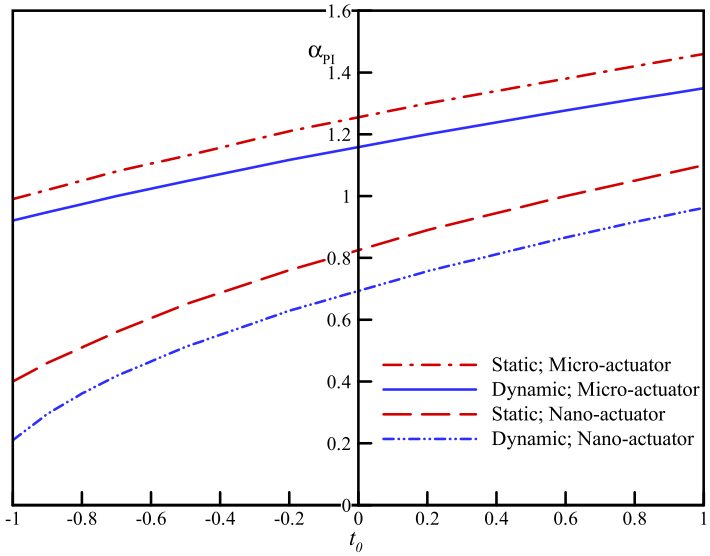

Figure 4.6 Impact of surface residual stress on the pull-in voltage.

Fig. 4.6 shows the impacts of surface residual stress on the pull-in voltage of micro- and nanoactuators, wherein both static and dynamic pull-in voltages are investigated. It should be noted that the effect of the Casimir force is neglected in the microactuator. Furthermore, the interaction between the pull-in voltage curve and the horizontal axis at $t_0 = 0$ is attributed to ignoring surface energies. A comparison between the pull-in voltages of micro- and nanoactuator for the values obtained by neglecting surface energies reveals that surface stresses induce softening or hardening outcomes depending on the material surface properties. For instance, when the surface stress is positive, surface energies increase the pull-in voltage. However, for the material with negative surface stress, the pull-in voltage decreases the surface effect.

Fig. 4.7 shows the pull-in voltage for different values of surface stiffness parameter (e_0). Similar to surface residual stress, the surface elasticity might pose hardening or softening effects depending on the material surface properties. The surface elasticity and surface residual stress might be positive or negative based on the material properties and the arrangements of surface atoms. For example, both surface elasticity and surface residual stress are positive ($E_0 = 8.45$ N/m and $\tau_0 = 0.0208$ N/m) for 110 planes of silicon (Si (110)) [13], while the surface elasticity is negative and surface residual stress are positive ($E_0 = -10.036$ N/m and $\tau_0 = 0.605$ N/m) for 100 planes of silicon (Si (100)) [14]. Figs. 4.6 and 4.7 reveal that Casimir forces decrease the pull-in voltage. Due to inertia forces, the dynamic pull-in voltages of both micro- and nanoactuator are smaller than the static pull-in value.

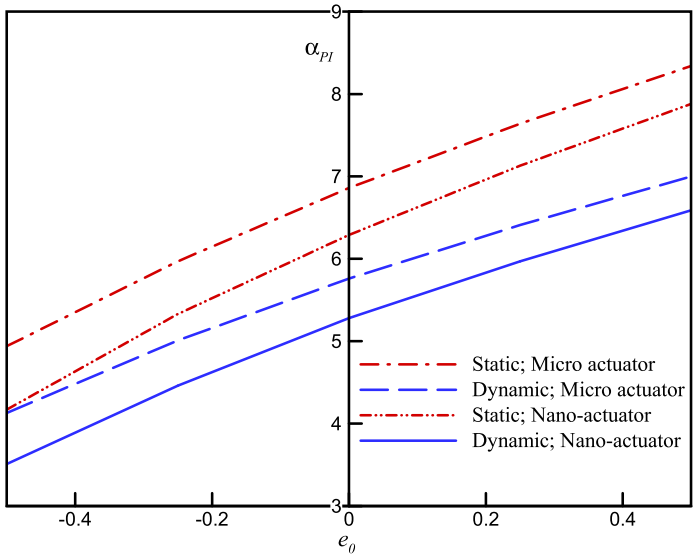

Figure 4.7 Impact of surface stiffness on the pull-in voltage.

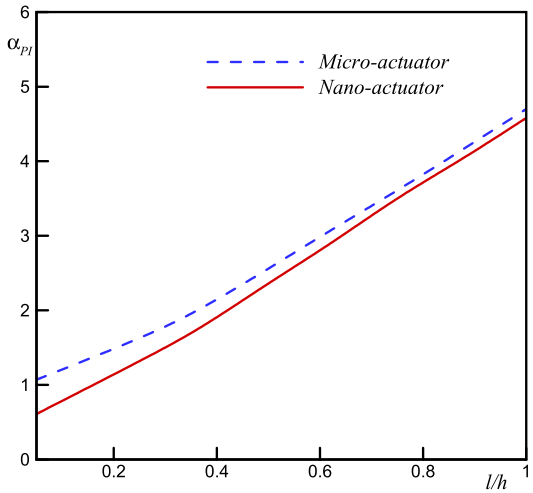

Figure 4.8 Impact of scale dependency and Casimir forces on the dynamic pull-in voltage.

Fig. 4.8 shows the impact of material size-to-thickness ratio (l/h) on the dynamic pull-in voltage of micro- and nanoactuator. As can be observed, the dynamic pull-in voltage is enlarged by increasing the material length scale parameter, decreasing the actuator thickness, or both. Moreover, Casimir forces abruptly reduce the dynamic pull-in

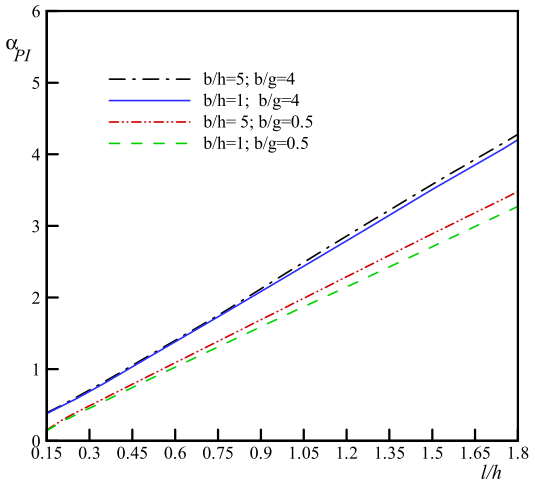

Figure 4.9 Influence of size parameter on the dynamic pull-in voltage.

voltage for smaller values of the material size-to-thickness ratios, while the impact of Casimir force for larger sizes is insignificant in comparison with the size effect.

The dynamic pull-in voltage of two nanoactuators with different cross-sections (i.e., $b = 4g$ and $b = 0.5g$) are plotted in Fig. 4.9 to examine the effects of both geometrical parameters and size dependency. This figure demonstrates that, regardless of the cross-section, the size has a hardening effect and increases the pull-in voltage of the nanoactuator.

The squeezed film damping is affected by both the geometrical parameters and the fluid viscosity. Hence, the time-dependent tip deflection and phase plane of a nanoactuator are assessed for two different cross-sections. As seen in Figs. 4.10 and 4.11, for the wide beam ($b/g = 4$), the damping characteristics approach the critical state and, in turn, the system returns to the stable focus point swifter than in the case of the underdamping conditions. On the contrary, for the narrow beam ($b/g = 0.5$), the system is in the underdamped situation. Therefore, the nanoactuator oscillates at the fundamental damped frequency with decreasing amplitude and converges to its equilibrium position in the end.

4.2.1.2 Dynamic analysis of narrow nanoactuators with AC actuation

The dynamic behavior of the nanoactuator under AC voltage differs from that under purely DC electrical potential. While the DC voltage can create either static deflection of time-dependent vibration, the AC voltage creates oscillatory motion [15]. AC stimulation is usually used for primary-resonance excitation of NEMS and MEMS for various applications such as RF filters [16] and sensors [17]. In the primary-resonance

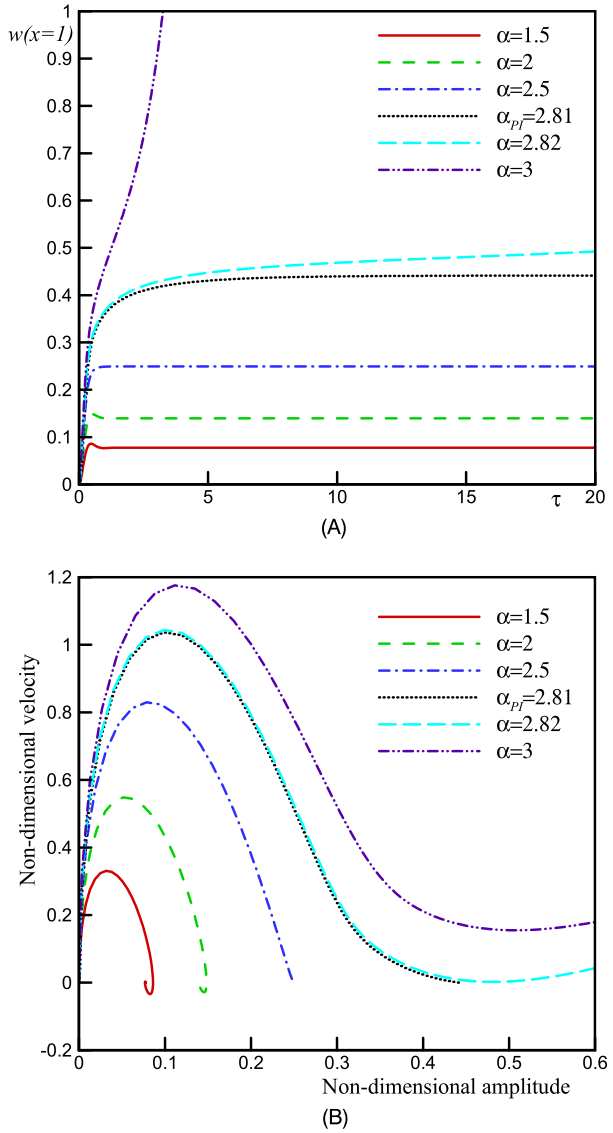

Figure 4.10 Influence of squeeze film damping parameter on the dynamic behavior of a wide nanoactuator ($b = 4g$): (A) time history, (B) phase plane, Casimir force.

excitation, the frequency of the AC voltage is near to the natural frequency of the system [18]. In this section, the dynamic behavior of the nanoactuator under the combined *AC–DC* load is described. When the nanoactuator is simultaneously stimulated by AC and DC loads, the electrical force of Eq. (4.32) is modified as

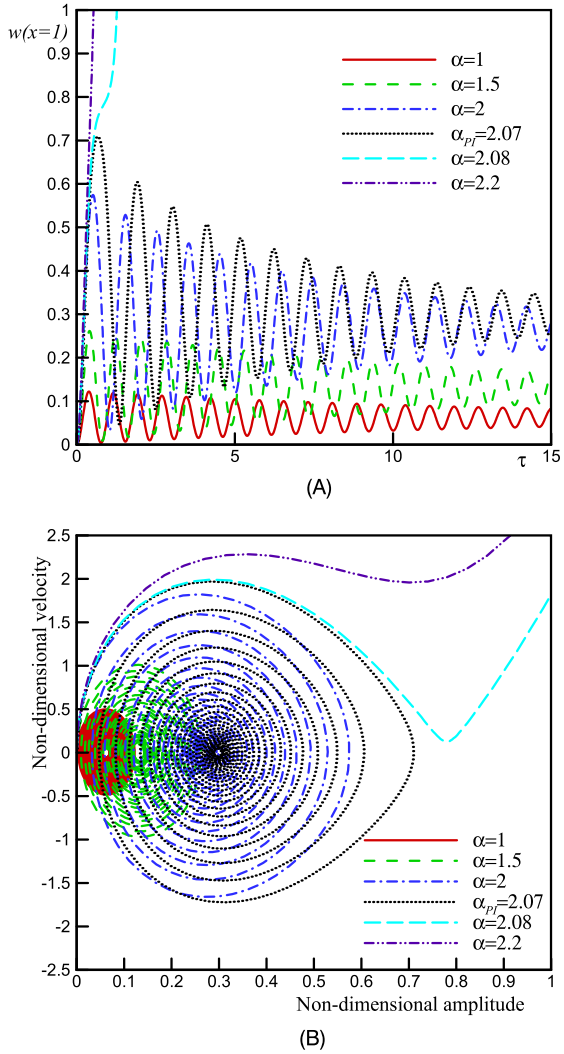

Figure 4.11 Influence of squeeze film damping parameter on the dynamic behavior of a wide nanoactuator ($b = 4g$): (A) time history, (B) phase plane, Casimir force.

$$f_{elec} = \frac{\varepsilon_0 \varepsilon_r}{2} \frac{b(V_{DC} + V_{AC}\cos(\omega_{AC} t))^2}{(g-W)^2} \left[1 + 0.2\left(\frac{g-W}{b}\right)^{0.76} + 0.6\frac{h}{b}\left(\frac{g-W}{h}\right)^{0.76} \right]. \tag{4.66}$$

By replacing the former electrical force with the old one in Eq. (4.40), the governing equation of nanoactuator under both AC and DC loads is written as

$$\rho A\frac{\partial^2 W}{\partial t^2}+\frac{\kappa_{\mathit{eff}}b^3}{(g-W)^3}\frac{\partial W}{\partial t}+\left(EI+\mu Al^2+E_0I_0-\frac{2\tau_0\upsilon I}{h}\right)\frac{\partial^4 W}{\partial X^4}-\tau_0S_0\frac{\partial^2 W}{\partial X^2}$$
$$=\frac{\varepsilon_0\varepsilon_r}{2}\frac{b(V_{DC}+V_{AC}\cos(\omega_{AC}t))^2}{(g-W)^2}\left[1+0.2\left(\frac{g-W}{b}\right)^{0.76}+0.6\frac{h}{b}\left(\frac{g-W}{h}\right)^{0.76}\right] \quad (4.67)$$
$$+\frac{\pi^2\hbar cb}{240(g-W)^4}+0.00523\frac{\hbar c}{(g-W)^3}$$

and the boundary conditions are:

$$\tau_0S_0\frac{\partial W}{\partial X}-\left(EI+\mu Al^2+E_0I_0-\frac{2\tau_0\upsilon I}{h}\right)\frac{\partial^3 W}{\partial X^3}\bigg|_{X=0,L}=0 \quad \text{or} \quad \delta W|_{X=0,L}=0,$$
$$\left(EI+\mu Al^2+E_0I_0-\frac{2\tau_0\upsilon I}{h}\right)\frac{\partial^2 W}{\partial X^2}\bigg|_{X=0,L}=0 \quad \text{or} \quad \delta\left(\frac{\partial W}{\partial X}\right)\bigg|_{X=0,L}=0. \quad (4.68)$$

For a rectangular section, I_0 and S_0 are mentioned in Eq. (4.42).

Now, using $x=X/L$ and $w=W/g$, the dimensionless governing equation of the nanoactuator with rectangular cross-section energy is written as:

$$\frac{\partial^2 w}{\partial\tau^2}+\frac{\hat{c}}{\gamma^3(1-w)^3}\frac{\partial w}{\partial\tau}+\left(1+\frac{6}{1+\upsilon}\left(\frac{l}{h}\right)^2+e_0\right)\frac{\partial^4 w}{\partial x^4}-t_0\frac{\partial^2 w}{\partial x^2}$$
$$=\frac{(\alpha_{DC}+\alpha_{AC}\cos(\Omega_{Ac}\tau))^2}{(1-w)^2}\left[1+(0.2+0.6\eta^{0.24})\gamma^{0.76}(1-w)^{0.76}\right] \quad (4.69)$$
$$+\frac{\beta_{Cas}}{(1-w)^4}(1+0.127\gamma(1-w)),$$
$$w(0,\tau)=\frac{\partial w}{\partial x}(0,\tau)=0, \quad (4.70)$$
$$\left(1+\frac{6}{1+\upsilon}\left(\frac{l}{h}\right)^2+e_0\right)\frac{\partial^2 w}{\partial x^2}(1,\tau)=0,$$
$$t_0\frac{\partial w}{\partial x}(1,\tau)-\left(1+\frac{6}{1+\upsilon}\left(\frac{l}{h}\right)^2+e_0\right)\frac{\partial^3 w}{\partial x^3}(1,\tau)=0. \quad (4.71)$$

The dimensionless parameters of the above equation are defined in Eqs. (4.47)–(4.53). The different parameters are given as:

$$\alpha_{DC}=V_{DC}\sqrt{\frac{\varepsilon_0\varepsilon_r bL^4}{2g^3EI}}, \quad (4.72)$$

$$\alpha_{AC}=V_{AC}\sqrt{\frac{\varepsilon_0\varepsilon_r bL^4}{2g^3EI}}, \quad (4.73)$$

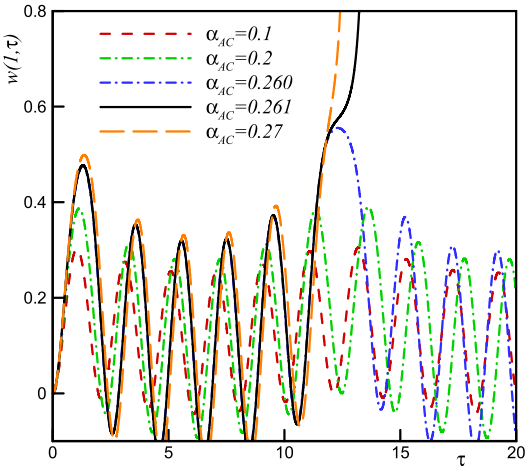

Figure 4.12 Time-dependent dynamic behavior of nanoactuator under both AC and DC load.

$$\Omega_{AC} = \omega_{AC}\sqrt{\frac{\rho bhL^4}{EI}}. \tag{4.74}$$

In the above equations, α_{DC} and α_{AC} are the DC and AC voltage dimensionless parameters, respectively. Also, Ω_{AC} is related to the AC voltage frequency-to-beam's natural frequency ratio.

The vibrations of a cantilever electromechanical nanoactuator are illustrated in Fig. 4.12. Furthermore, in this figure, rather than the AC voltage, the influence of size dependency and the surface effect are considered. It demonstrates that, in contrast to DC voltage, when the nanoactuator is under AC voltage, the vibration amplitude evolves over time. Similar to DC actuation, the system becomes unstable by increasing the AC potential.

The phase diagram of a nanoactuator under the AC load is shown in Fig. 4.13. As can be seen, the system doesn't have oscillation behavior, and the instability occurs by increasing the applied AC voltage.

The frequency response of the nanoactuator under AC voltage is demonstrated in Fig. 4.14. As can be observed, for $\alpha_{AC} = 0.2$ and $\alpha_{AC} = 0.3$, the system is stable for the frequency ratio between 2 and 5. An unstable range in observed by increasing the dimensionless parameter of the AC voltage to 0.4 (i.e., $\alpha_{AC} = 0.4$). The maximum deflection of nanoactuator for different AC voltage is presented in Fig. 4.15. This figure demonstrated that similar to the DC voltage by increasing the AC voltage, the maximum deflection of the nanoactuator enhances up to the pull-in point.

4.2.2 Rayleigh–Ritz method

The Rayleigh–Ritz technique is a variational method that can be coupled with the reduced-order method to solve the nonlinear time-dependent partial differential equa-

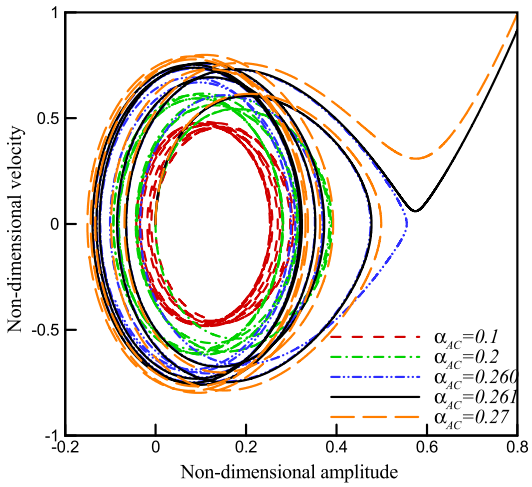

Figure 4.13 Phase diagram of nanoactuator under both AC and DC load.

tions. In this method, similar to the Galerkin technique, the solution is approximated in terms of the trial functions. The solution is obtained by minimizing the residual errors in the Galerkin method. In contrast, it is determined in the Rayleigh–Ritz method by minimizing the variational form of the constitutive equations. The most central difference between the Rayleigh–Ritz and Galerkin methods is in the trial function selection. In the Galerkin method, the trial solutions must be continuous all across the domain of interest and precisely satisfy the specified boundary conditions. However, in the Rayleigh–Ritz method, although the trial solution must be continuous over the domain of interest, it needs to meet the essential or geometrical boundary conditions.

4.2.2.1 Dynamic analysis of nanowire-based sensor in the accelerating field

The mechanical performance of nanosensors can be profoundly affected by external accelerating fields (centrifugal acceleration, constant acceleration, or both). A typical nanowire-fabricated sensor is manufactured from a deformable nanowire hanged over a fixed solid plate. This type of sensor has been extensively applied in modern measurement devices working in an accelerating field [19] such as automotive sensors [20], centrifugal separators [21], fault detection of roller bearing [22], CNC high-speed spindle errors detector [23], balancing power plant rotating equipment [24], and turbomachinery angular speed detectors [25].

A typical nanowire fabricated sensor is presented in Fig. 4.16. The length, radius, and initial gap of a nanosensor are denoted by L, R, and g, respectively. The nanowire can be assumed as a cantilever Euler beam whose displacement vector is explained in Eq. (2.9).

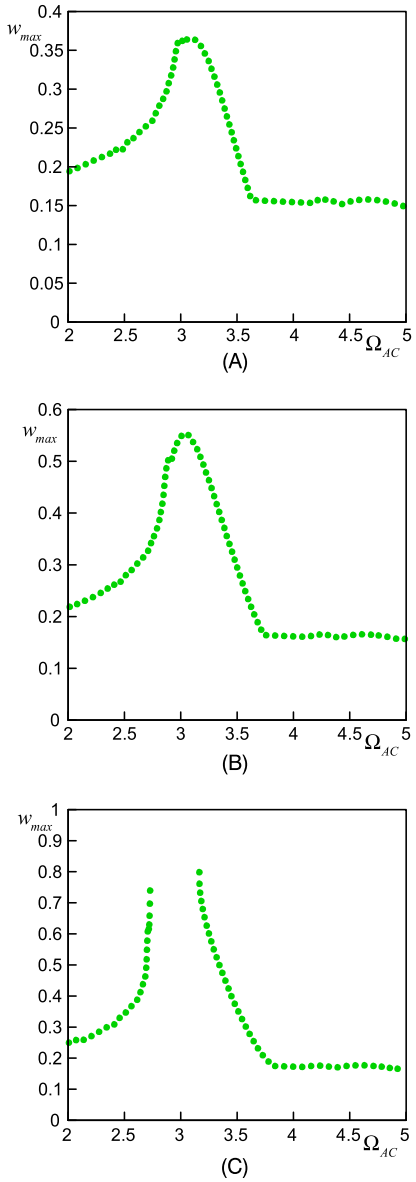

Figure 4.14 Frequency–response curve of a nanoactuator under both AC and DC load: (A) $\alpha_{AC} = 0.2$, (B) $\alpha_{AC} = 0.3$, and (C) $\alpha_{AC} = 0.4$.

Herein, the strain gradient elasticity is employed together with the Gurtin–Murdoch surface elasticity to derive the scale-dependent constitutive equation of the nanosensor by considering the coupling effect of size dependency and surface. Strain gradient elasticity is a comprehensive size-dependent theory which incorporates the size dependency

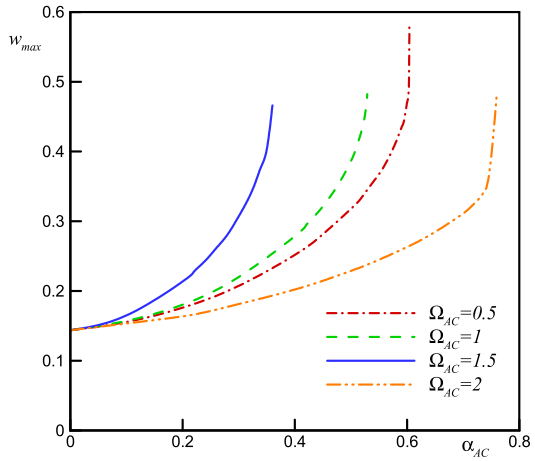

Figure 4.15 Maximum deflection of a nanoactuator for different values of AC voltage frequency.

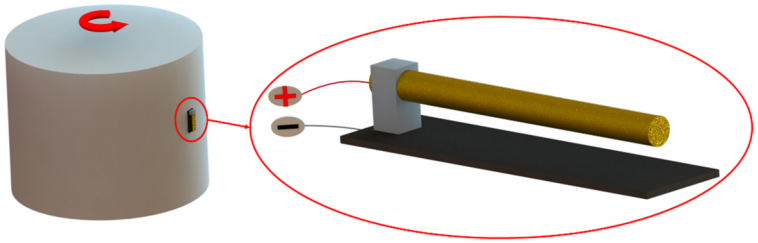

Figure 4.16 Nanosensor under in the centrifugal field.

in the simulation [26–29]. The total strain energy of the system is defined as the sum of the bulk body energy (U_B) and the surface layer energy (U_S):

$$U = U_B + U_S \tag{4.75}$$

where the bulk strain energy and surface layer energy are described in the context of the strain gradient elasticity and the Gurtin–Murdoch surface elasticity, respectively. Based on these theories, the total strain energy of the nanosensor is achieved as [29]

$$U = \frac{1}{2}\int_0^L \oint_{\partial A} \tau_{ij}\varepsilon_{ij} ds dX + \frac{1}{2}\int_{\vartheta} \left(\sigma_{ij}\varepsilon_{ij} + p_i\gamma_i + \tau^{(1)}_{ijk}\eta^{(1)}_{ijk} + m^s_{ij}\chi^s_{ij}\right) d\vartheta. \tag{4.76}$$

The parameters of Eq. (4.76) can be expressed as follows [1,30]:

$$\varepsilon_{ij} = \frac{1}{2}\left(u_{i,j} + u_{j,i}\right), \tag{4.77}$$

$$\gamma_i = \varepsilon_{mm,i}, \tag{4.78}$$

$$\eta_{ijk}^{(1)} = \frac{1}{3}\left(\varepsilon_{jk,i} + \varepsilon_{ij,k} + \varepsilon_{ki,j}\right) - \frac{1}{15}\left[\delta_{ki}\left(\varepsilon_{mm,j} + 2\varepsilon_{mj,m}\right) + \delta_{jk}\left(\varepsilon_{mm,i} + 2\varepsilon_{mi,m}\right)\right] - \frac{1}{15}\delta_{ij}\left(\varepsilon_{mm,k} + 2\varepsilon_{mk,m}\right), \tag{4.79}$$

$$\chi_{ij}^{s} = \frac{1}{2}e_{jkl}u_{l,ki}, \tag{4.80}$$

$$\sigma_{ij} = 2\mu\left(\varepsilon_{ij} + \frac{\nu}{1-2\nu}\varepsilon_{mm}\delta_{ij}\right), \tag{4.81}$$

$$p_i = 2\mu l_0^2 \gamma_i, \tag{4.82}$$

$$\tau_{ijk}^{(1)} = 2\mu l_1^2 \eta_{ijk}^{(1)}, \tag{4.83}$$

$$m_{ij}^{s} = 2\mu l_2^2 \chi_{ij}^{s}, \tag{4.84}$$

$$\tau_{XX} = \tau_0 + E_0\left(-Z\frac{\partial^2 w}{\partial X^2}\right), \tag{4.85}$$

$$\tau_{nX} = \tau_0 \frac{\partial u_n}{\partial X} \tag{4.86}$$

where μ, ν, E_0, and τ_0 are the shear modulus, Poisson's ratio, surface modulus, and surface residual stress, respectively. Furthermore, l_2, l_1, and l_0 are additional material parameters added for simulating the microstructure dependency, which can be evaluated experimentally [31,32] or using molecular dynamics [33]. Zhang and Zhao used the shifts of resonant frequencies to determine the length scale parameter [34]. The experimental observation by Al-Rub and Voyiadjis demonstrated that the length scale for metals ranges between 0.2 and 20 μm [31]. Wang et al. experimentally measured the material length scale of Cu and Ni equal to 4 and 5 μm, respectively [32].

By substituting Eq. (2.9) into Eqs. (4.77)–(4.84), the nonzero components are obtained as:

$$\varepsilon_{11} = -z\frac{\partial^2 W}{\partial X^2}, \tag{4.87}$$

$$\gamma_1 = -Z\frac{\partial^3 W}{\partial X^3}, \quad \gamma_3 = -\frac{\partial^2 W}{\partial X^2}, \tag{4.88}$$

$$\begin{aligned}
&\eta_{111}^{(1)} = -\frac{2}{5}Z\frac{\partial^3 W}{\partial X^3},\\
&\eta_{113}^{(1)} = \eta_{131}^{(1)} = \eta_{311}^{(1)} = -\frac{4}{15}\frac{\partial^2 W}{\partial X^2},\\
&\eta_{122}^{(1)} = \eta_{212}^{(1)} = \eta_{221}^{(1)} = \eta_{133}^{(1)} = \eta_{313}^{(1)} = \eta_{331}^{(1)} = \frac{1}{5}Z\frac{\partial^3 W}{\partial X^3},\\
&\eta_{223}^{(1)} = \eta_{232}^{(1)} = \eta_{322}^{(1)} = \frac{1}{15}\frac{\partial^2 W}{\partial X^2},\\
&\eta_{333}^{(1)} = \frac{1}{5}\frac{\partial^2 W}{\partial X^2},
\end{aligned} \tag{4.89}$$

$$\chi_{12}^{s} = \chi_{21}^{s} = -\frac{\partial^2 W}{\partial X^2}, \tag{4.90}$$

$$\sigma_{11} = -EZ\frac{\partial^2 W}{\partial X^2}, \tag{4.91}$$

$$\begin{aligned} p_1 &= -2\mu l_0^2 Z\frac{\partial^3 W}{\partial X^3}, \\ p_3 &= -2\mu l_0^2\frac{\partial^2 W}{\partial X^2}, \end{aligned} \tag{4.92}$$

$$\begin{aligned} \tau_{111}^{(1)} &= -\frac{4}{5}\mu l_1^2 Z\frac{\partial^3 W}{\partial X^3}, \\ \tau_{113}^{(1)} &= \tau_{131}^{(1)} = \tau_{311}^{(1)} = -\frac{8}{15}\mu l_1^2\frac{\partial^2 W}{\partial X^2}, \\ \tau_{122}^{(1)} &= \tau_{212}^{(1)} = \tau_{221}^{(1)} = \tau_{133}^{(1)} = \tau_{313}^{(1)} = \tau_{331}^{(1)} = \frac{2}{5}\mu l_1^2 Z\frac{\partial^3 W}{\partial X^3}, \\ \tau_{223}^{(1)} &= \tau_{232}^{(1)} = \tau_{322}^{(1)} = \frac{2}{15}\mu l_1^2\frac{\partial^2 W}{\partial X^2}, \\ \tau_{333}^{(1)} &= \frac{2}{5}\mu l_1^2\frac{\partial^2 W}{\partial X^2}, \end{aligned} \tag{4.93}$$

$$m_{12}^{s} = m_{21}^{s} = -\mu l_2^2\frac{\partial^2 W}{\partial X^2}. \tag{4.94}$$

The total strain energy of the nanosensor can be defined by substituting Eqs. (4.84)–(4.94) into Eq. (4.76):

$$\begin{aligned} U = {} & \frac{1}{2}\int_0^L \int_A \left\{ EZ^2\left(\frac{\partial^2 W}{\partial X^2}\right)^2 + 2\mu l_0^2 Z^2\left(\frac{\partial^3 W}{\partial X^3}\right)^2 + 2\mu l_0^2 Z^2\left(\frac{\partial^2 W}{\partial X^2}\right)^2 \right. \\ & + 2\mu l_2^2 Z^2\left(\frac{\partial^2 W}{\partial X^2}\right)^2 + \frac{4}{25}\mu l_1^2 Z^2\left(\frac{\partial^3 W}{\partial X^3}\right)^2 + \frac{48}{225}\mu l_1^2\left(\frac{\partial^2 W}{\partial X^2}\right)^2 + \frac{6}{25}\mu l_1^2 Z^2\left(\frac{\partial^3 W}{\partial X^3}\right)^2 \\ & \left. + \frac{1}{75}\mu l_1^2\left(\frac{\partial^2 W}{\partial X^2}\right)^2 + \frac{1}{25}\mu l_1^2\left(\frac{\partial^2 W}{\partial X^2}\right)^2 \right\} dA dX \\ & + \frac{1}{2}\int_0^L \oint_{\partial A}\left(-\left(\tau_0 + E_0\frac{\partial u_X}{\partial X}\right)Z\frac{\partial^2 W}{\partial X^2} + \tau_0 n_Z^2\left(\frac{\partial W}{\partial X}\right)^2\right) ds dX \\ = {} & \frac{1}{2}\int_0^L \left[\left(EI + 2\mu A l_0^2 + \frac{8}{15}\mu A l_1^2 + \mu A l_2^2\right)\left(\frac{\partial^2 W}{\partial X^2}\right)^2 \right. \\ & \left. + A\left(2\mu l_0^2 + \frac{4}{5}\mu l_1^2\right)\left(\frac{\partial^3 W}{\partial X^3}\right)^2\right] dX \\ & + \frac{1}{2}\int_0^L \oint_{\partial A}\left(-\left(\tau_0 + E_0\frac{\partial u_X}{\partial X}\right)Z\frac{\partial^2 W}{\partial X^2} + \tau_0 n_Z^2\left(\frac{\partial W}{\partial X}\right)^2\right) ds dX \end{aligned} \tag{4.95}$$

where I is the second area moment, and A is the cross-section area.

The work of external forces can be calculated by using the following equation:

$$W_{ext} = \int_0^L \int_0^W F_{ext}(X, t) dW dX. \tag{4.96}$$

Here, F_{ext} is the sum of all external forces exerted on the sensor, as given below:

$$F_{ext} = F_{elec} + F_a + \begin{cases} F_{vdW} & \text{vdW regime,} \\ F_{Cas} & \text{Casimir regime} \end{cases} \tag{4.97}$$

where F_{elec} is the electrical force, F_{vdW} denotes the force due to van der Waals attraction, F_{Cas} is the Casimir force, and F_a represents the force induced by the accelerating field.

The external electrical potential results in a lateral force on the nanowire, which can be calculated by differentiating the electrical stored energy in the capacitor created by nanowire and fixed plane [35]:

$$F_{elec} = \frac{\pi \varepsilon_0 V^2}{(g - W) \ln^2(2\frac{g-W}{R})} \tag{4.98}$$

where ε_0 is the permittivity of vacuum, and V stands for the applied voltage.

When the separation between the moveable wire and ground is smaller than the retardation length, the van der Waals force, which is affected by the material properties, should be taken into account. However, for long separation (i.e., the separation longer than the retardation length), the Casimir force is dominant and not affected by the material properties [36]. For the small separation, the van der Waals force of a wire parallel to a plate can be described as [37]

$$F_{vdW} = \frac{\bar{A} R^2}{(g - W)^4} \tag{4.99}$$

where $\bar{A}$ is the Hamaker constant. Also, the Casimir force is defined as [38]

$$F_{Cas} = \frac{\hbar c}{(g - W)^3} \frac{1}{8\pi \ln(\frac{g-W}{R})} + \frac{\hbar c}{(g - W)^3} \frac{1}{16\pi \ln^2(\frac{g-W}{R})}. \tag{4.100}$$

The acceleration force per unit length (F_a) is the sum of the centrifugal force and the force caused by the constant accelerating field:

$$F_a = \rho A a \pm \rho A (r + g + w)\omega^2 \tag{4.101}$$

where r is the rotating machine radius, ω denotes the angular velocity of the rotary machine, and a is the constant acceleration. For the case of $g \ll r$, Eq. (4.101) is reduced

to

$$F_a = \pi\rho R^2(a \pm r\omega^2). \tag{4.102}$$

It is worth noting that the sign of centrifugal force depends on the installed sensor position. In other words, the centrifugal force is positive once the substrate of the sensor is fixed on the inner side of the machine, while it is negative when the substrate of the sensor is mounted on the outer side of the machine.

The nanosensors are frequently affected by the pressure of the gas squeezed between the nanowire and the fixed plate. The work performed by the gas flow damping can be described by

$$W_d = \int_0^L \int_0^W c_f \frac{\partial W(X,t)}{\partial t} dW dx \tag{4.103}$$

where c_f denotes the damping coefficients. The effect of the squeezed film between two parallel plates can be estimated through the conventional or modified Reynolds equations [39]. However, in this study, the gas flow damping coefficient was calculated by evaluating the drag force of the flow around a deflected cylinder. The deflection of nanosensor yields an airflow over the nanowire whose behavior changes by increasing the Stokes number (St), and, thus, the damping coefficient is determined for low and high Stoke numbers as follows [40]:

$$c_f = \begin{cases} 4\pi\mu_f \left(\dfrac{St}{2}\right)^{\frac{1}{2}} & \text{for high Stokes numbers,} \\ \dfrac{4\pi\mu_f}{\log(4/St^*) - 0.0572 + 1.8K_n} & \text{for low Stokes numbers} \end{cases} \tag{4.104}$$

where μ_f is the viscosity, $St^* = \frac{R}{\upsilon}\frac{\partial w}{\partial t}$, υ is the momentum diffusivity, and K_n is the Knudsen number. The nanowire kinetic energy can be defined as

$$T = \frac{1}{2}\int_0^L \int_A \rho \left[\left(\frac{\partial W(X,t)}{\partial t}\right)^2\right] dA dX. \tag{4.105}$$

The total energy can be evaluated by using Eqs. (4.95), (4.96), (4.103), and (4.105), as given below:

$$\Pi = \frac{1}{2}\int_0^L \int_A \rho \left(\frac{\partial W}{\partial t}\right)^2 dA dX - \int_0^L (c_s + c_f)\frac{\partial W}{\partial t} W dX$$
$$- \frac{1}{2}\int_0^L \oint_{\partial A} \left(-\left(\tau_0 + E_0 Z\frac{\partial^2 W}{\partial X^2}\right) Z\frac{\partial^2 W}{\partial X^2} + \tau_0 n_Z^2 \left(\frac{\partial W}{\partial X}\right)^2\right) ds dX$$

$$-\frac{1}{2}\int_0^L \left[\begin{array}{l}\left(EI+2\mu Al_0^2+\frac{8}{15}\mu Al_1^2+\mu Al_2^2+E_0I_0\right)\left(\frac{\partial^2 W}{\partial X^2}\right)^2 \\ +I\left(2\mu l_0^2+\frac{4}{5}\mu l_1^2\right)\left(\frac{\partial^3 W}{\partial X^3}\right)^2\end{array}\right]dX$$
$$+\int_0^L\int_0^W F_{ext}(X,t)dWdX. \tag{4.106}$$

The dimensionless total energy is obtained using Eqs. (4.98), (4.99), (4.100), and (4.102) and assuming $w=W/g$ and $x=X/L$:

$$\bar{\Pi}=\frac{1}{2}\int_0^1\left(\frac{\partial w}{\partial \tau}\right)^2dx-\int_0^1\int_0^w \hat{c}_f\frac{\partial w}{\partial \tau}dwdx-\frac{1}{2}\int_0^1 t_0\left(\frac{\partial w}{\partial x}\right)^2dx$$
$$-\frac{1}{2}\int_0^1\left[\begin{array}{l}\left(1+e_0+\frac{2}{15(1+\upsilon)}\left(30\left(\frac{l_0}{R}\right)^2+8\left(\frac{l_1}{R}\right)^2+15\left(\frac{l_2}{R}\right)^2\right)\right)\left(\frac{\partial^2 w}{\partial x^2}\right)^2 \\ +\frac{1}{15(1+\upsilon)(L/R)^2}\left(5\left(\frac{l_0}{R}\right)^2+2\left(\frac{l_1}{R}\right)^2\right)\left(\frac{\partial^3 w}{\partial x^3}\right)^2\end{array}\right]dx$$
$$+\int_0^1\int_0^w\left(\delta-\Theta\omega^2+\frac{\alpha}{(1-w)\ln^2(2k(1-w))}+\left\{\begin{array}{l}\frac{\beta_{vdW}}{(1-w)^4} \\ \frac{\beta_{Cas}\left[1+\frac{1}{2\ln(k(1-w))}\right]}{(1-w)^3\ln(k(1-w))}\end{array}\right.\right)dwdx \tag{4.107}$$

where

$$k=\frac{g}{R}, \tag{4.108}$$
$$\tau=\sqrt{\frac{E}{\rho}}\frac{R^2t}{2L^2}, \tag{4.109}$$
$$\alpha=\frac{4\varepsilon_0V^2L^4}{ER^4g^2}, \tag{4.110}$$
$$\beta_{Cas}=\frac{\hbar cL^4}{4\pi^2g^4R^4E}, \tag{4.111}$$
$$\beta_{vdW}=\frac{4\bar{A}L^4}{g^5\pi R^2E}, \tag{4.112}$$
$$\hat{c}_f=\frac{2c_sL^2}{\pi R^3\sqrt{\rho E}}, \tag{4.113}$$
$$t_0=\frac{20\tau_0L^2}{R^3E}, \tag{4.114}$$

$$e_0 = \frac{4E_0}{ER}, \tag{4.115}$$

$$\Theta = \frac{4\rho r L^4}{ER^2 g}, \tag{4.116}$$

$$\delta = \frac{4\rho L^4}{ER^2 ga}. \tag{4.117}$$

In the above equation, τ is the dimensionless time, α is the dimensionless parameter of the applied voltage, β_{cas} indicates the dimensionless parameter of the Casimir force, β_{vdW} indicates the dimensionless parameter of the van der Waals force, and $\hat{c}_f$ is the dimensionless parameter pertinent to the airflow gas damping ratio. Also, k is the geometrical parameter indicating the gap-to-width ratio and the thickness-to-width ratio, respectively. Moreover, t_0 and e_0 are dimensionless surface parameters related to surface elasticity and surface residual stress, respectively. Moreover, Θ and δ are the centrifugal, and constant acceleration field parameters, respectively.

To implement the Rayleigh–Ritz method, the nanowire deflection is separated into time-dependent and time-independent parts:

$$w(x) = \sum_{i=1}^{N} q_i(t)\phi_i(x). \tag{4.118}$$

It is burdensome to specify the exact mode shapes of a nanobeam based on both strain gradient theory and surface elasticity. Nevertheless, satisfying the essential boundary condition is sufficient for the time-independent terms in the Rayleigh–Ritz method. Therefore, the mode shapes of the classical fixed–free beam which satisfies all essential boundary conditions can be used for this purpose:

$$\phi_i(x) = \cosh(\omega_i x) - \cos(\omega_i x) - \frac{\cosh(\omega_i) - \cos(\omega_i)}{\sinh(\omega_i) - \sin(\omega_i)}(\sinh(\omega_i x) - \sin(\omega_i x)). \tag{4.119}$$

To find the solution, the total energy is minimized:

$$\frac{\partial \Pi}{\partial q_i} = 0, \quad i = 0, 1, ..., N. \tag{4.120}$$

Thus, Eq. (4.120) leads to the following system of ordinary differential equations:

$$\ddot{q}_i + \hat{c}\dot{q}_i + \left[1 + e_0 + \frac{2}{15(1+\upsilon)}\left(30\left(\frac{l_0}{R}\right)^2 + 8\left(\frac{l_1}{R}\right)^2 + 15\left(\frac{l_2}{R}\right)\right)\right]\omega_i^4 q_i$$
$$- \frac{1}{15(1+\upsilon)(L/h)^2}\left[5\left(\frac{l_0}{R}\right)^2 + 2\left(\frac{l_1}{R}\right)^2\right]\int_0^1 \phi_i \frac{\partial^6}{\partial x^6}\left(\sum_{j=1}^{N} q_j\phi_j\right)$$

$$
\begin{aligned}
&-\int_0^1 \phi_i \left\{ t_0 \sum_{j=1}^{N} q_j \frac{d^2\phi_j}{dx^2} \right\} dx - \int_0^1 \bar{F}_{ext}\phi_i dx \\
&+ \frac{1}{15(1+\upsilon)\left(L/h\right)^2}\left(5\left(\frac{l_0}{R}\right)^2 + 2\left(\frac{l_1}{R}\right)^2\right)\frac{\partial^3}{\partial X^3}\left(\sum_{j=1}^{N} q_j\phi_j\right)\frac{d^2\phi_i}{dX^2}\bigg|_{x=1} \\
&-\frac{1}{15(1+\upsilon)\left(L/h\right)^2}\left(5\left(\frac{l_0}{R}\right)^2 + 2\left(\frac{l_1}{R}\right)^2\right)\frac{\partial^3}{\partial X^3}\left(\sum_{j=1}^{N} q_j\phi_j\right)\frac{d^2\phi_i}{dX^2}\bigg|_{x=0} = 0
\end{aligned} \tag{4.121}
$$

where

$$
\begin{aligned}
\bar{F}_{ext} = \delta \pm \Theta\omega^2 &\frac{\eta^2}{(1-\sum_{j=1}^{N} q_j\phi_j)\ln^2(2k(1-\sum_{j=1}^{N} q_j\phi_j))} \\
&+ \begin{cases} \dfrac{\gamma_{vdW}}{(1-\sum_{j=1}^{N} q_j\phi_j)^4} & \text{vdW}, \\ \dfrac{\gamma_{Cas}\left[1+\frac{1}{2\ln(k(1-\sum_{j=1}^{N} q_j\phi_j))}\right]}{(1-\sum_{j=1}^{N} q_j\phi_j)^3\ln(k(1-\sum_{j=1}^{N} q_j\phi_j))} & \text{Casimir}. \end{cases}
\end{aligned} \tag{4.122}
$$

The system of differential equations can be solved numerically to determine the instability parameters.

The dynamic behavior of nanostructures can be assessed using the phase diagram. Hence, the time-dependent deflections and phase diagrams of a nanosensor were plotted to show different phenomena. Fig. 4.17 illustrates the dimensionless deflection of the nanosensor at its free end ($w(x=1)$) as a function of dimensionless time (τ). The deflection is plotted for different external voltages up to the pull-in value. According to the figure, the maximum displacement of the nanosensor is escalated by increasing the voltage. As the external potential reaches the pull-in voltage, the nanosensor tip displacement increases rapidly. The phase plane of nanosensor, when neglecting the gas flow damping, is drawn in Fig. 4.18. From the figure, one sees that the nanosensor has an unstable saddle-node and a stable center point.

Fig. 4.19 shows the effects of the gas flow damping on the dimensionless deflection of a nanosensor at its free end ($w(x=1)$) as a function of dimensionless time. The deflection is exhibited for different external voltages up to the pull-in value. As can be seen in this figure, identical to the undamped sensor, the maximum displacement of the nanosensor increases by increasing the voltage when considering the squeezed film damping. Moreover, the nanosensor tip displacement improves swiftly once the external potential approaches the pull-in value. Fig. 4.20 illustrates the effect of the squeezed film damping on the phase plane of the nanosensor. As can be observed in the figure, the stable center node converts to a stable focus node when the squeezed film damping

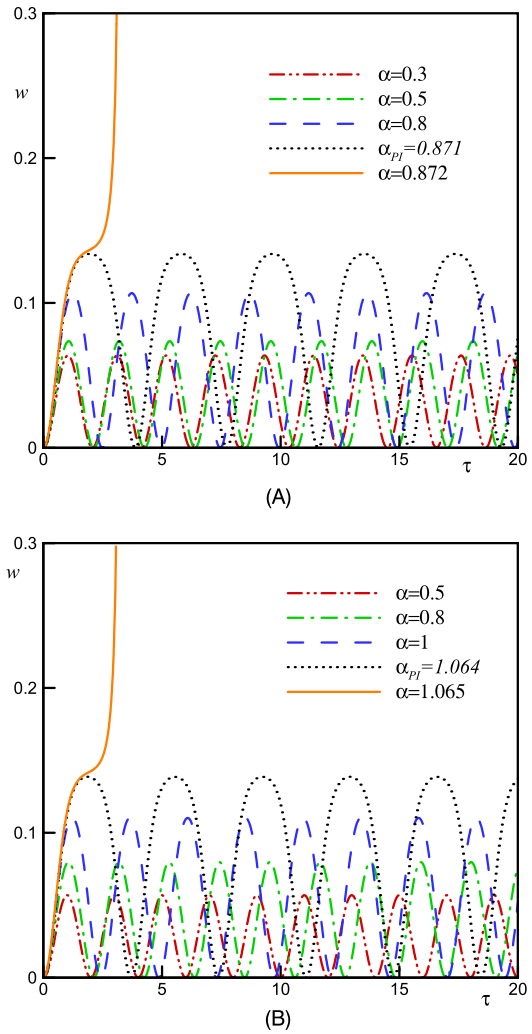

Figure 4.17 Time-dependent deflection of nanosensor (neglecting squeezed film damping): (A) van der Waals regime; (B) Casimir regime.

is taken into account, with the presence of an unstable saddle-node as another fixed point. When the applied voltage is less than the pull-in value, the path converges to the stable focus node due to the squeezed film damping. In contrast, when the external potential is higher than the pull-in voltage, the paths separate and, in turn, the instability is induced.

The impact of a microstructure on the instability voltage of the nanosensor is shown in Fig. 4.21. To this end, all length scale parameters are considered to be equal (i.e.,

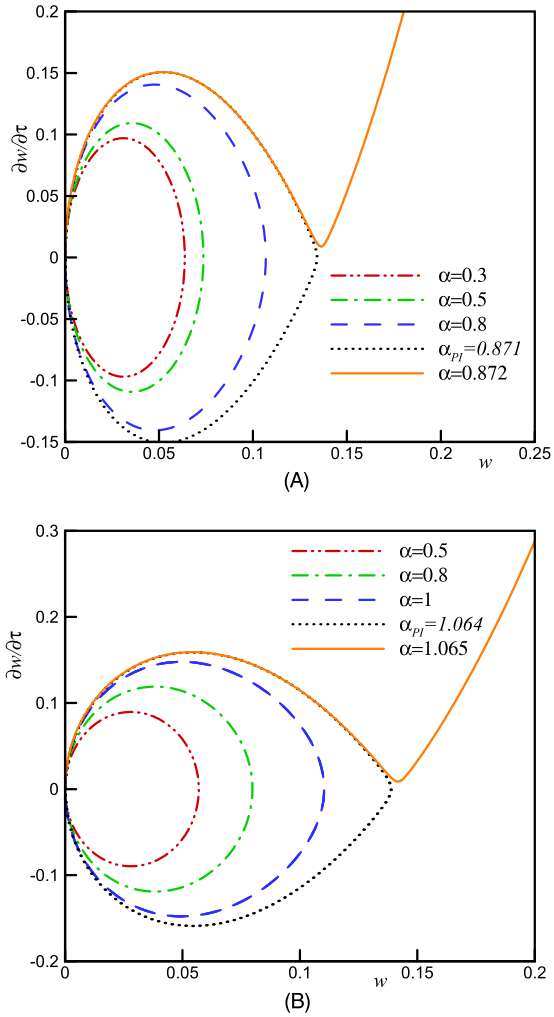

Figure 4.18 Phase plane of the nanosensor by neglecting the squeezed film damping: (A) van der Waals regime; (B) Casimir regime.

$l_0 = l_1 = l_2 = l$), and the dimensionless instability voltage is determined for different l/R values. Fig. 4.21 illustrates that the instability voltage increases by increasing the length scale parameter.

When the nanosensor is attached to a rotating device, the angular velocity of the shaft can dramatically change the dynamic behavior of the sensor. Figs. 4.22 and 4.23 show the time-dependent deflection and phase plane of the nanosensor for different values of angular velocities when the external voltage is equal to the pull-in value. It is worth noting that the results of Figs. 4.22 and 4.23 are related to the sensors embedded inside

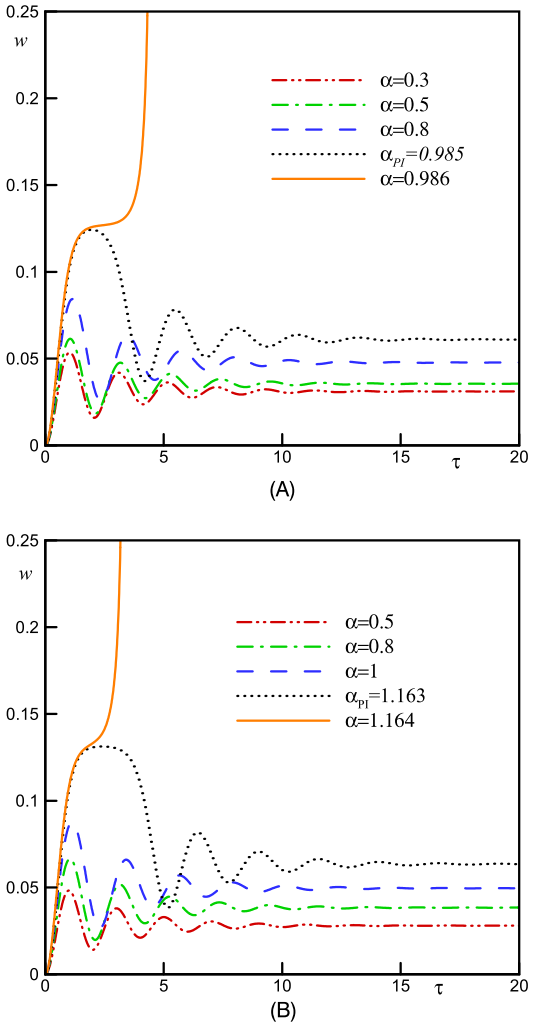

Figure 4.19 Effect of gas flow damping on the time-dependent deflection of a nanosensor: (A) van der Waals regime; (B) Casimir regime.

and fixed outside the rotary device, respectively. Figs. 4.22A–B demonstrate the time history and the phase diagram of nanosensor at pull-in voltage, respectively. Fig. 4.23A illustrates that the tip deflection of the nanosensor increases rapidly at the pull-in voltage. Moreover, according to Fig. 4.23B, the stable center point of a nanoswitch becomes an unstable saddle point at the pull-in voltage. In addition to tip deflection, this figure reveals that the tip velocity increases rapidly at the pull-in point. Fig. 4.23 demonstrates that when the nanosensor is fixed inside the rotary device, an increase in the angular velocity elevates the pull-in deflection of the nanosensor and reduces its pull-in volt-

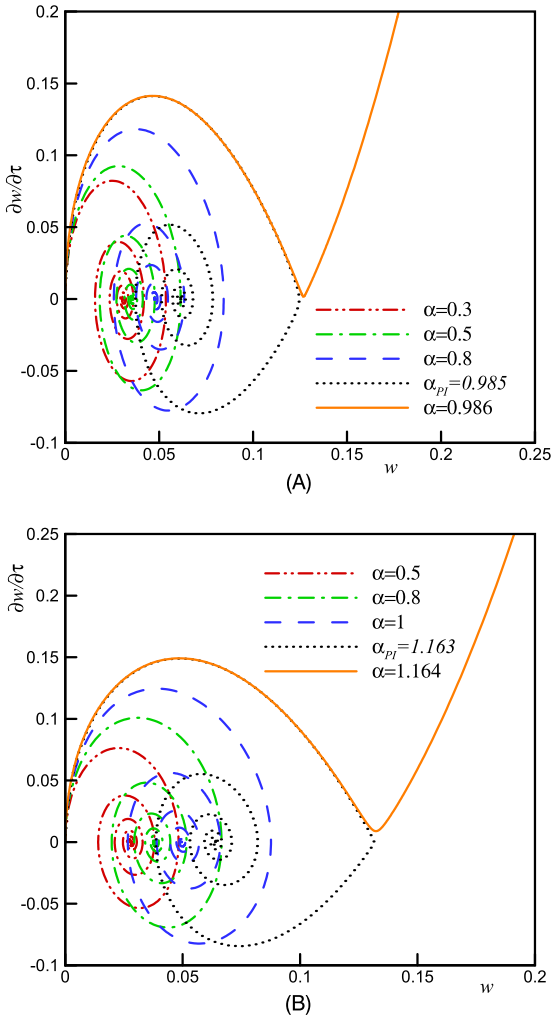

Figure 4.20 Impact of gas flow damping on the phase plane of a nanosensor: (A) van der Waals regime; (B) Casimir regime.

age. In contrast, when the nanosensor is fixed outside the rotary device, the pull-in time of the nanosensor is lengthened by increasing the angular velocity and the pull-in phenomenon occurs at higher values of the applied potential.

4.3. Runge–Kutta method

Runge Kutta methods are a family of explicit and implicit iterative methods developed by German mathematicians Carl Runge and Wilhelm Kutta based on Taylor's expan-

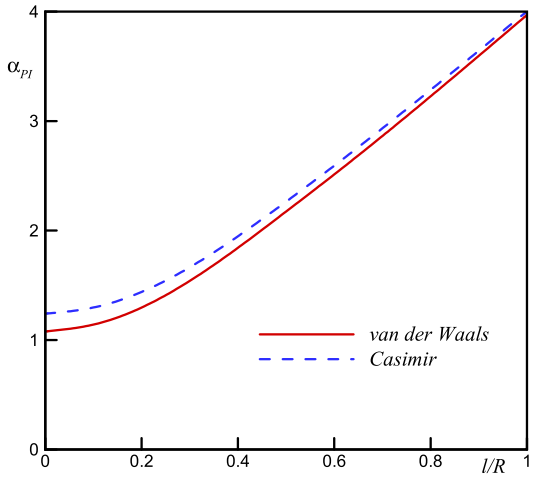

Figure 4.21 Impacts of microstructure on the nanosensor instability voltage.

sion, which can be used to find an approximate solution for an ordinary differential equation. To explain the basics of the Runge–Kutta method, consider the following first-order initial value problem:

$$\dot{y} = f(y, t); \quad y(t_0) = y_0. \tag{4.123}$$

The solution aims to approximate the unknown function $y(t)$. In general, the rth order Runge–Kutta method is defined as follows:

$$y_{n+1} = y_n + h\sum_{i=1}^{s} b_i k_i + O(h^{s+1}) \tag{4.124}$$

where

$$k_i = f\left(t_n + hc_i, y_n + h\sum_{j=1}^{r} a_{ij}k_j\right). \tag{4.125}$$

The coefficients are typically presented in a Butcher tableau as follows:

$$\begin{array}{c|cccc} c_1 & a_{11} & a_{12} & \cdots & a_{1r} \\ c_2 & a_{21} & a_{22} & \cdots & a_{2r} \\ \vdots & \vdots & \vdots & \ddots & \vdots \\ c_r & a_{1r} & a_{2r} & \cdots & a_{rr} \\ \hline & b_1 & b_2 & \cdots & b_r \end{array} \tag{4.126}$$

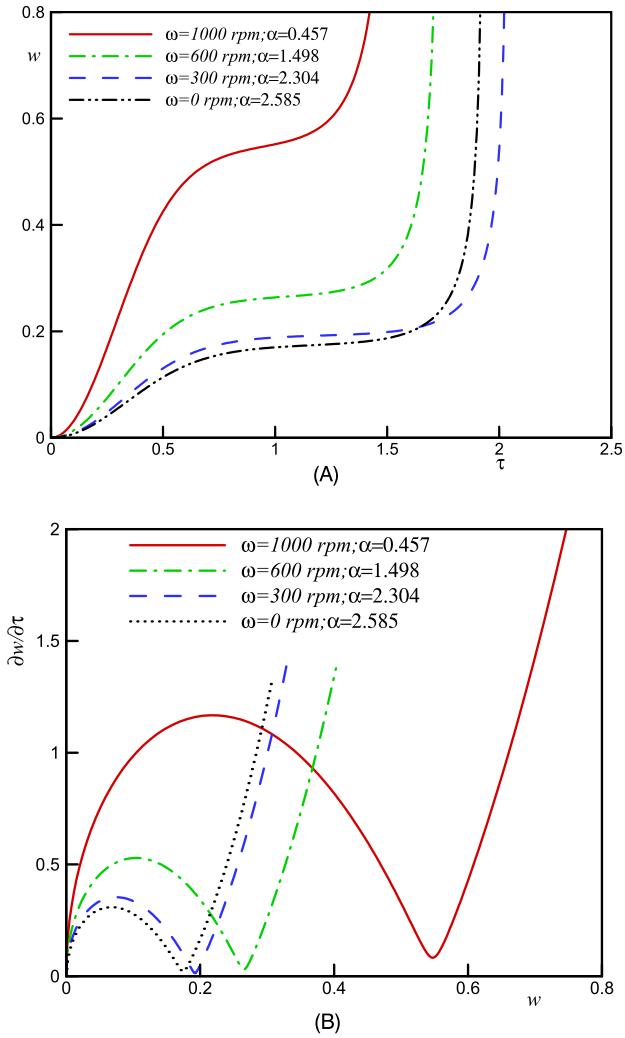

Figure 4.22 Impact of the angular velocities on the dynamic behavior of the sensor at pull-in voltage: (A) time history; (B) phase diagram (nanosensor mounted inside the rotary).

The Runge–Kutta method is consistent if

$$\sum_{j=1}^{i-1} a_{ij} = c_i \quad \text{for } i = 2, \ldots, r. \tag{4.127}$$

The most well-known Runge–Kutta method is the fourth-order version whose coefficients are defined as:

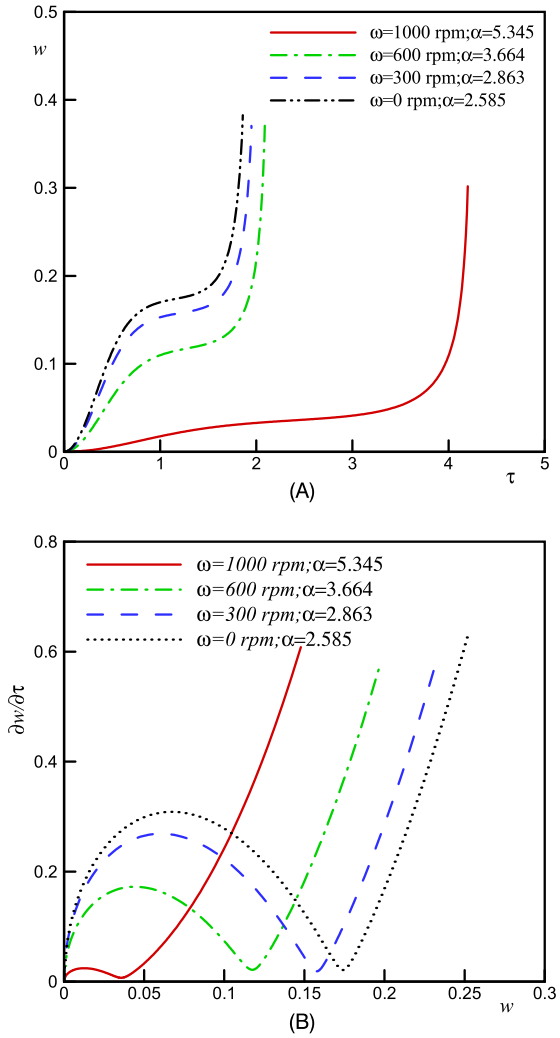

Figure 4.23 Impact of the angular velocities on the dynamic behavior of the sensor at pull-in voltage: (A) time history; (B) phase diagram (nanosensor mounted outside the rotary).

$$\begin{array}{c|cccc} 0 & & & & \\ 1/2 & 1/2 & & & \\ 1/2 & 0 & 1/2 & & \\ 1 & 0 & 0 & 1 & \\ \hline & \frac{1}{6} & \frac{2}{3} & \frac{2}{3} & \frac{1}{6} \end{array} \tag{4.128}$$

whereby the solution of Eq. (4.123) can be obtained by using the fourth-order Runge–Kutta method, as given below:

$$\begin{aligned} y_{n+1} &= y_n + \frac{1}{6}(k_1 + 2k_2 + 2k_3 + k_4), \\ t_{n+1} &= t_n + h \end{aligned} \tag{4.129}$$

where

$$\begin{aligned} k_1 &= hf(t_n, y_n), \\ k_2 &= hf\left(t_n + \frac{h}{2}, y_n + \frac{k_1}{2}\right), \\ k_3 &= hf\left(t_n + \frac{h}{2}, y_n + \frac{k_2}{2}\right), \\ k_3 &= hf(t_n + h, y_n + k_3) \end{aligned} \tag{4.130}$$

and where h is the time step; if it is reduced, the accuracy of the solution is enhanced.

In the following subsections, the dynamic performances of two rotational NEMS are addressed. It should be noted that the constitutive equations of these rotational NEMS are developed by combining the lumped parameter model and the micromechanic continuum technique.

4.3.1 Dynamic behavior of rotational nanomirror

Among the most common electromechanical systems are torsional actuators, which have been used widely in the nanoelectromechanical systems (NEMS) and microoptoelectromechanical systems (MOEMS), such as variable attenuators, tuneable torsional capacitors, torsional radio frequency switches, and digital light processing chips [31–34]. Previously researchers have studied the static and dynamic performance of the rotational NEMS and NEMS [41–47].

A torsional nanomirror is constructed from a conductive electrode (mirror) suspended over a fixed conductive electrode (substrate) using torsional nanobeams. The mirror can rotate and be used for transporting signals by rotating these torsional beams. Herein, the dynamic behavior of a rotational nanomirror is investigated by using the fourth-order Runge–Kutta method.

Fig. 4.24 shows an SEM image of a rotational micromirror with plates on both sides of the rotational arms. Schematic modeling representations of a torsional nanomirror with one side plate and associated side views are depicted in Fig. 4.25.

The constitutive equation of a torsional nanomirror can be extracted by minimizing the total energy of the system. The torsional elastic energy is stored in the nanobeam by rotating the mirror due to the torsional torque. Hence, the elastic energy of the system,

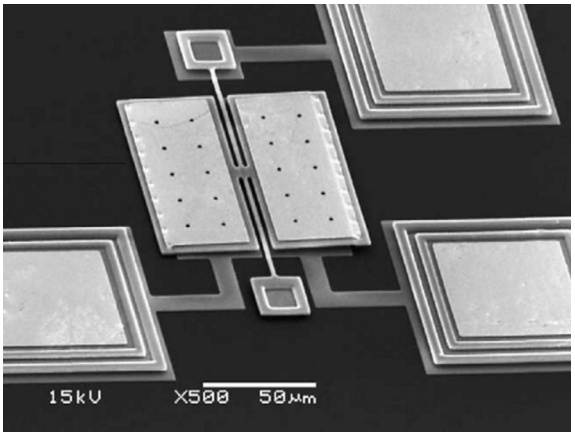

Figure 4.24 SEM image of a micromirror [48].

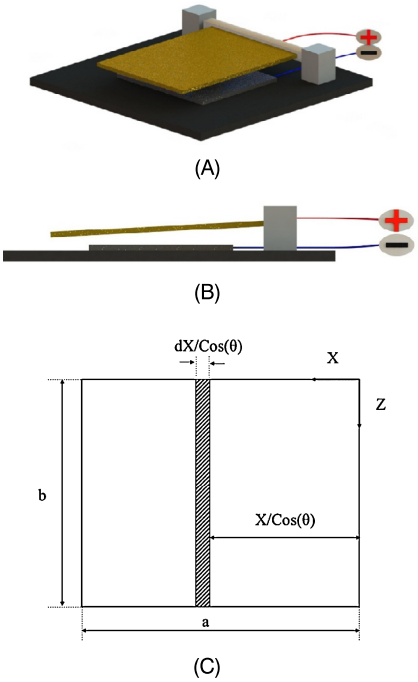

Figure 4.25 (A) Schematics reorientation, (B) side view, and (C) top view of a nanomirror.

which is the sum of the strain energy stored in the torsional beams, is given as follows:

$$U_{elas} = \frac{1}{2}K\theta^2 + \frac{1}{2}K\theta^2 = K\theta^2 \tag{4.131}$$

where K is the torsional stiffness of the nanobeam, and θ is the rotation angle of the mirror. The variation of strain energy is obtained as

$$\delta U_{das} = \delta\left(K\theta^2\right) = 2K\theta\delta\theta. \tag{4.132}$$

The work done by the Casimir force can be obtained by integrating the work done by the infinitesimal Casimir force on an infinitesimal element on the mirror:

$$W_{Cas} = \int_0^{\gamma}\int_A dF_{Cas}d\gamma \tag{4.133}$$

where $\gamma = \sin(\theta)$. By replacing g with $D-\gamma$ in Eq. (1.7), the Casimir force on an infinitesimal element is obtained as

$$dF_{Cas} = \frac{\pi^2\hbar cb}{240(D-x\sin(\theta))^4}dx. \tag{4.134}$$

Rewriting Eq. (4.133) yields

$$\delta W_{Cas} = \int_0^{a} dF_{Cas}(x\cos(\theta))\delta\theta. \tag{4.135}$$

Using Eq. (4.134) in Eq. (4.135) and integrating over the mirror area yields

$$\delta W_{Cas} = \frac{\pi^2\hbar cb\cos(\theta)}{240\sin^2(\theta)}\left[\frac{-D+3a\sin(\theta)}{6(D-a\sin(\theta))^3} + \frac{1}{6D^2}\right]\delta\theta. \tag{4.136}$$

The work done by electrical force can be determined by applying the capacitor model. Based on this technique, the stored electrical capacitive energy ($W_{Coulomb}$) in a parallel plate capacitor (C) is given by

$$W_{Coulomb} = \frac{1}{2}CV^2. \tag{4.137}$$

For an infinitesimal element, the area is bdx, and the gap is $D-\gamma$. Hence, by using Eq. (1.1), the capacitance of an infinitesimal element is obtained as:

$$dC = \frac{\varepsilon bdX}{D-X\sin(\theta)}. \tag{4.138}$$

The work done by the electric force varies as follows:

$$\delta W_{Coulomb} = \frac{V^2}{2}\int_{a_1}^{a_2}\delta(dC). \tag{4.139}$$

By substituting Eq. (4.138) into Eq. (4.139), the variational work done by the Coulomb force can be specified by

$$\delta W_{Coulomb} = \frac{\varepsilon V^2 b}{2\sin^2(\theta)}\left[\frac{2D}{2D - a_2\sin(\theta)} - \frac{2D}{2D - a_1\sin(\theta)} + \ln\left(\frac{2D - a_2\sin(\theta)}{2D - a_1\sin(\theta)}\right)\right]\delta\theta. \tag{4.140}$$

The kinetic energy of the rotating part of the mirror is

$$T = \frac{1}{2} I_v \dot{\theta}^2 \tag{4.141}$$

where I_v is the main plate's moment of inertia. Also, the variational kinetic energy is

$$\delta T = I_v \dot{\theta}\delta\dot{\theta}. \tag{4.142}$$

The damping virtual work depends on the velocity, and the damping coefficient (c_d) is defined as

$$W_d = \int_0^{\theta} -c_d \frac{\partial\theta}{\partial t} d\theta. \tag{4.143}$$

The variation of the above relation is

$$\delta W_d = -c_d \dot{\theta}\delta\theta. \tag{4.144}$$

Hamilton's principle is applied to derive the constitutive equation of a rotational nanomirror:

$$\delta(U - V) = \delta T + \delta U_{elas} - \delta W_d - \delta W_{Coulomb} - \delta W_{Cas} = 0. \tag{4.145}$$

Using Eq. (4.145) in conjunction with Eqs. (4.132), (4.136), (4.140), (4.142), and (4.144), the constitutive equation of a rotational nanomirror is extracted as

$$\begin{aligned} &I_v\ddot{\theta} + c_d\dot{\theta} + \frac{2\mu J\theta}{L} - \frac{\pi^2\hbar c b}{240\sin^2(\theta)}\left[\frac{-D + 3a\sin(\theta)}{6(D - a\sin(\theta))^3} + \frac{1}{6D^2}\right] \\ &- \frac{\varepsilon V^2 b}{2\sin^2(\theta)}\left[\frac{D}{D - a_2\sin(\theta)} - \frac{D}{D - a_1\sin(\theta)} + \ln\left[\frac{D - a_2\sin(\theta)}{D - a_1\sin(\theta)}\right]\right] = 0 \end{aligned} \tag{4.146}$$

where

$$J = \begin{cases} \dfrac{\pi t^4}{2} & \text{for circular cross-section,} \\ \dfrac{tw^3}{3}\left[1 - \dfrac{192w}{\pi^5 t}\displaystyle\sum_{n=1}^{\infty}\frac{1}{(2n-1)^5}\tanh\left[\frac{(2n-1)\pi t}{2w}\right]\right. & \text{for rectangular cross-section.} \end{cases} \tag{4.147}$$

We will use the following dimensionless parameters:

$$\tau = \sqrt{\frac{\mu J}{L I_v}} t, \tag{4.148}$$

$$\eta = \frac{\pi^2 \hbar c b a^3 L}{480 D^5 \mu J}, \tag{4.149}$$

$$\lambda = V \sqrt{\frac{\varepsilon a^3 b L}{4 D^3 \mu J}}, \tag{4.150}$$

$$\alpha = \frac{a_1}{a}, \tag{4.151}$$

$$\beta = \frac{a_2}{a}, \tag{4.152}$$

$$\Theta = \frac{\theta a}{D}, \tag{4.153}$$

$$C = c_d \sqrt{\frac{L}{\mu J I_v}}$$

where τ is the dimensionless time, η is the dimensionless parameter of the Casimir force, λ is the electrical force dimensionless parameter, Θ is rotating angle-to-the maximum rotating angle ratio, and C is pertinent to the damping ratio. Also, α and β are two geometrical parameters indicating the position of the electrode in the substrate.

The dimensionless governing equation of motion is obtained as

$$\ddot{\Theta} + C\dot{\Theta} + \Theta - \frac{\lambda^2}{\Theta^2}\left(\frac{1}{1-\beta\Theta} - \frac{1}{1-\alpha\Theta} + \ln\left(\frac{1-\beta\Theta}{1-\alpha\Theta}\right)\right) - \frac{\eta}{\Theta^2}\left[\frac{1}{6}\left(\frac{3\Theta-1}{(1-\Theta)^3}+1\right)\right] = 0. \tag{4.154}$$

To investigate the dynamic stability of the system, Eq. (4.154) is represented in terms of state-space variables as follows:

$$\begin{bmatrix} q_1 \\ q_2 \end{bmatrix} = \begin{bmatrix} \Theta \\ \dot{\Theta} \end{bmatrix}. \tag{4.155}$$

By considering the state-space formulation, the stability of fixed points can be investigated by plotting the phase portraits. By using Eq. (4.155), Eq. (4.154) reduces to the

following system of first-order differential equations:

$$\begin{bmatrix} \dot{q}_1 \\ \dot{q}_2 \end{bmatrix} = \begin{bmatrix} F_1(q_1, q_2) \\ F_2(q_1, q_2) \end{bmatrix} = \begin{bmatrix} q_2 \\ -Cq_2 - q_1 + \frac{\lambda^2}{q_1^2}\left(\frac{1}{1-\beta q_1} - \frac{1}{1-\alpha q_1} + \ln\left(\frac{1-\beta q_1}{1-\alpha q_1}\right)\right) + \frac{\eta}{q_1^2}\left[\frac{1}{6}\left(\frac{3q_1-1}{(1-q_1)^3}+1\right)\right] \end{bmatrix}. \tag{4.156}$$

The equilibrium points are determined for any applied voltage by setting the right-hand side of Eq. (4.156) equal to zero. Also, the eigenvalues of the Jacobian matrix can be used to check the stability of equilibrium points [49]. The Jacobian matrix is defined as:

$$Jacobian = \begin{bmatrix} \frac{\partial F_1(q_1,q_2)}{\partial q_1} & \frac{\partial F_1(q_1,q_2)}{\partial q_2} \\ \frac{\partial F_2(q_1,q_2)}{\partial q_1} & \frac{\partial F_2(q_1,q_2)}{\partial q_2} \end{bmatrix} = \begin{bmatrix} 0 & 1 \\ \frac{\partial F_2(q_1,q_2)}{\partial q_1} & -C \end{bmatrix}. \tag{4.157}$$

The eigenvalues of the Jacobian are investigated by using the following relation:

$$\det\left(\begin{bmatrix} 0 & 1 \\ \frac{\partial F_2(q_1,q_2)}{\partial q_1} & -C \end{bmatrix} - \lambda \begin{bmatrix} 1 & 0 \\ 0 & 1 \end{bmatrix}\right) = 0, \tag{4.158}$$

which leads to the following quadratic equation:

$$\lambda^2 + C\lambda - \frac{\partial F_2(q_1, q_2)}{\partial q_1} = 0. \tag{4.159}$$

The solution of the above equation is simplified to

$$\lambda_{1,2} = \frac{1}{2}\left(-C \pm \sqrt{C^2 + 4\frac{\partial F_2(q_1, q_2)}{\partial q_1}}\right). \tag{4.160}$$

In the absence of any damping effects, when both λ_1 and λ_2 have merely an imaginary part, the equilibrium point is a center point. However, by increasing the voltage, one of the eigenvalues becomes real and positive, and the other becomes real and negative, i.e., the fixed point becomes an unstable saddle point beyond the pull-in. When a damping force exists, if the eigenvalues are non-real and of the form of $a \mp bi$ ($a \neq 0$), then there are an unstable spiral point for $a > 0$ and a stable spiral point for $a < 0$.

The fourth-order Runge–Kutta is applied to solve Eq. (4.156). The time-dependent rotation angle of the nanomirror and its phase plane are plotted in Figs. 4.26 and 4.27, respectively. Fig. 4.26 demonstrates an upward trend for the nanomirror rotation angle by enlarging the applied voltage. The phase-plane diagram of the nanomirror (Fig. 4.27)

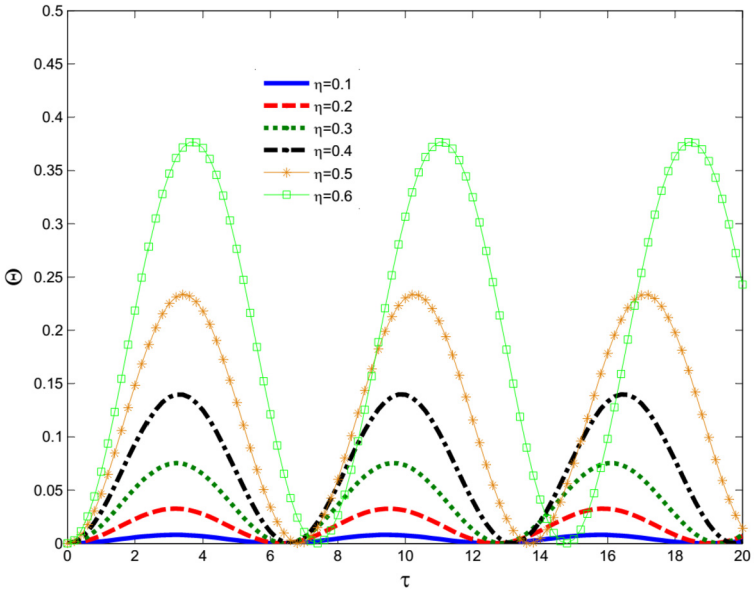

Figure 4.26 Time-dependent rotation angle of nanomirror for different applied voltage by neglecting the damping effect.

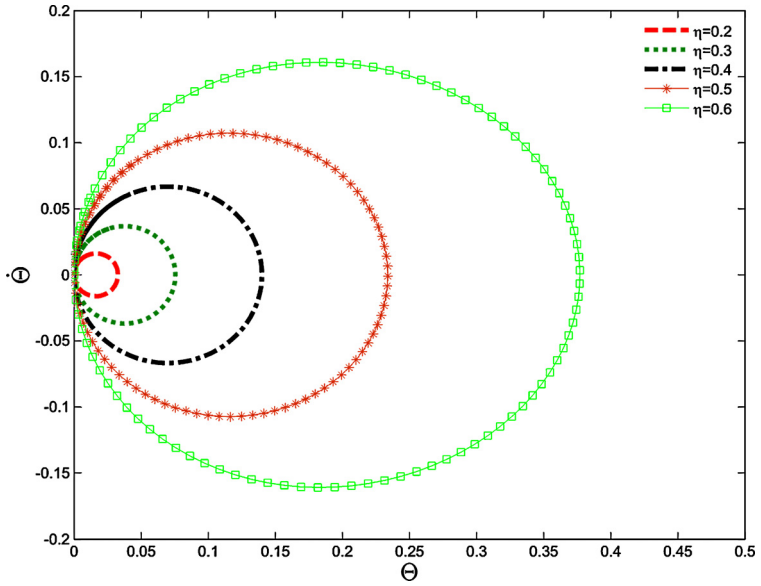

Figure 4.27 Phase portrait of a nanomirror by neglecting the damping effect.

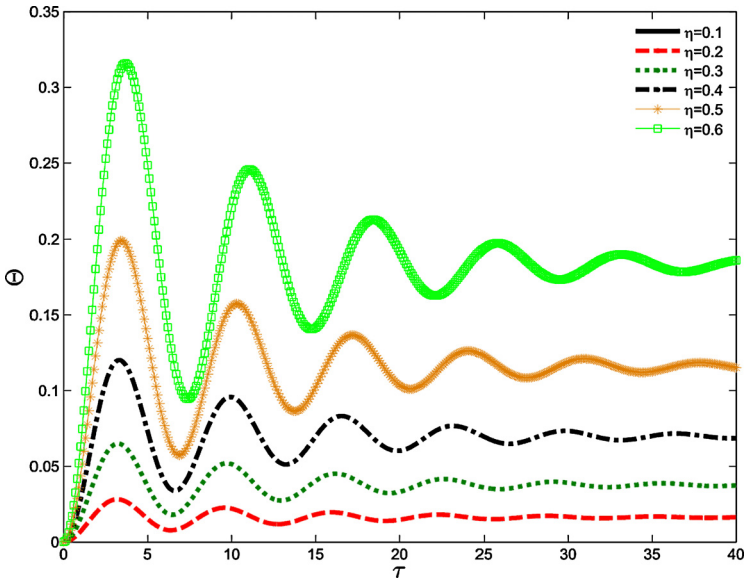

Figure 4.28 Time-dependent rotation angle of a nanomirror for different applied voltage by considering the damping effect.

shows that the nanoactuator includes two fixed points, including the stable center point and the unstable saddle-node. The homoclinic trajectory initiates from the unstable branch saddle-node and returns to the stable center point.

The impact of the damping on the dimensionless rational angle of the nanomirror is demonstrated in Fig. 4.28 as a function of dimensionless time. As can be seen, identical to the mirror without damping, the rotation angle of the nanomirror is elevated by increasing the voltage in the presence of the damping effect. Fig. 4.29 illustrates the effect of damping on the phase plane of the nanomirror, revealing that the stable center node converts to a stable focus point when the damping is taken into account. Furthermore, another fixed point here is an unstable saddle-node.

4.3.2 Torsion/bending dynamic analysis of a circular nanoscanner

Rotational micro- and nanoscanners are developed as essential elements in the fabrication of optical switches, light modulators, and so forth. A typical nanoscanner is presented in Fig. 4.30. The nanoscanner is constructed from a moveable circular plate attached to two nanoscale beams. By imposing a DC voltage differential between the scanner and fixed ground, the moveable plane deflects and rotates simultaneously.

For long arms, the simultaneous torsion and bending affect the performance of the torsional electromechanical nanostructures [50,51]. To extract the governing equation of a nanoscanner, the Lagrangian equation is employed. To extract the Lagrangian,

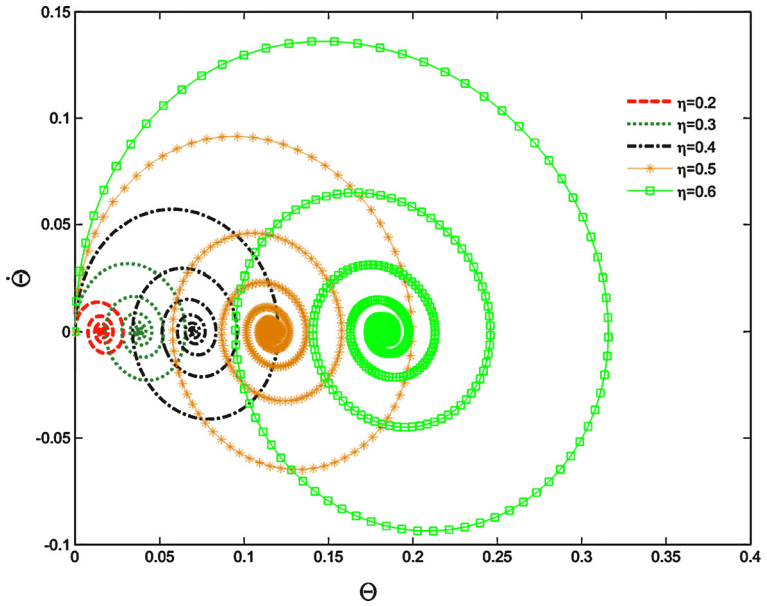

Figure 4.29 Phase portrait of a nanomirror by considering the damping effect.

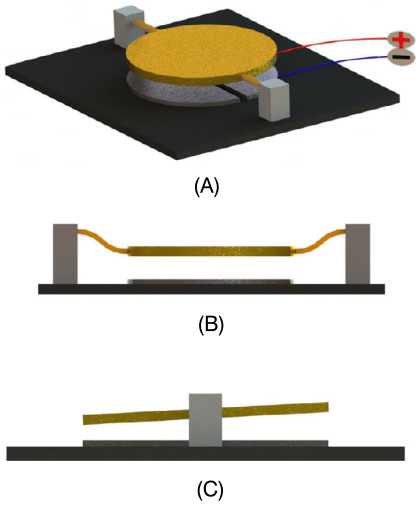

Figure 4.30 Schematic diagram of rotational nanoscanner: (A) 3D view, (B) front view, and (C) side view.

the kinetic energy of the system, the potential energy, and the virtual work done by the damping, electrical force, and quantum vacuum fluctuations are computed subsequently. Firstly, the kinetic energy should be evaluated.

The kinetic energy of the nanoscanner is due to both rotation and deflection of the scanner. As seen in Fig. 4.30, θ denotes the rerating angle of the nanoscanner and δ shows the scanner deflection. Also

$$T = \frac{1}{2} I_v \dot{\theta}^2 + \frac{1}{2} m \dot{\delta}^2 \tag{4.161}$$

where I_v is the scanner moment of inertia, m is the mirror mass, and overdot indicates a derivative with respect to time. For a thin circle, the moment of inertia has the following relation with the circle mass and radius:

$$I_v = \frac{1}{4} m R^2. \tag{4.162}$$

The elastic strain energy stored in the nanobeams (V_{elas}) is due to the torsion and bending of the beam. As the nanoscanner is hanged over the ground by two nanobeams, the total elastic strain energy is the sum of strain energy stored in each beam:

$$V_{elas} = 2\left(\frac{1}{2} K_\theta \theta^2 + \frac{1}{2} K_\delta \delta^2\right) \tag{4.163}$$

where K_θ and K_δ are the equivalent effective torsional and lateral spring constants, respectively. They are defined as follows:

$$K_\theta = \frac{2GJ}{L}, \tag{4.164}$$

$$K_\delta = \frac{24EI}{L^3} \tag{4.165}$$

where L is the length of the beam, E is the Young's modulus, and G is the shear modulus. Moreover, J is the nanobeam cross-section polar moment of inertia and I is the cross-section moment of inertia. For a rectangular and circular cross-section, the polar moment of inertia and I are given by the following equations:

$$I = \begin{cases} \dfrac{wt^3}{12} & \text{rectangular,} \\ \dfrac{\pi t^4}{4} & \text{circular,} \end{cases} \tag{4.166}$$

$$J = \begin{cases} \dfrac{tw^3}{3}\left[1 - \dfrac{192w}{\pi^5 t}\displaystyle\sum_{n=1}^{\infty} \frac{1}{(2n-1)^5} \tanh\left[\frac{(2n-1)\pi t}{2w}\right]\right] & \text{rectangular,} \\ \dfrac{\pi t^4}{2} & \text{circular.} \end{cases} \tag{4.167}$$

For a rectangular cross-section, w is the nanobeam width and t is the nanobeam thickness. Also, for a circular cross-section t is the radius.

As the final term of Lagrangian, the virtual work done by the electrical and Casimir forces is computed as

$$\tilde{\delta} W_{ext} = F_{ext}\tilde{\delta}\delta + M_{ext}\tilde{\delta}\theta \tag{4.168}$$

where $\tilde{\delta} W_{ext}$ is the virtual work done by an external load, F is the total external forces act on the scanner (i.e., lateral damping, electrical force, and Casimir force), and M is the total external moment act on the nanoscanner (i.e., torsional damping, electrical moment and Casimir moment). Also $\tilde{\delta}\delta$ and $\tilde{\delta}\theta$ are the virtual deflection and virtual rotation of a nanoscanner, respectively.

It has been shown that for a minimal rotation angle, linear viscous damping can be used for simulating the squeezed film damping in both lateral and torsional directions [52]:

$$F_d = -C_\delta \dot{\delta}, \tag{4.169}$$

$$M_d = -C_\theta \dot{\theta} \tag{4.170}$$

where F_d indicates the lateral damping force, and M_d indicated the torsional damping moment. Also, C_δ and C_θ are the lateral and torsional damping coefficients, respectively.

For investigating the total external force on the nanoscanner, the force on an infinitesimal element is determined. Then by integrating over the nanoscanner area, the total force is obtained. Similarly, the total moment acting on the nanoscanner can be computed.

The electrical force on this element can be achieved by using the parallel plates capacitor model. As mentioned in Section 4.1, the electrical force between two parallel plates is

$$f_{elec} = \frac{\varepsilon A V^2}{2g^2} \tag{4.171}$$

where A is the plate area and g is the plates' separation gap. The integrating element is shown in Fig. 4.31. The area of this differential element is given by

$$dA = r dr d\varphi. \tag{4.172}$$

If the nanoscanner rotates and deflects, the distance between a differential element and fixed ground is reduced from g to $g - \delta - r\sin(\theta)\sin(\varphi)$.

By replacing the reduced gap in Eq. (4.171), the electrical force of a differential element is obtained as

$$dF_{elec} = \frac{\varepsilon_0 V^2}{2\left(D - \delta - r\sin(\theta)\sin(\varphi)\right)^2} r dr d\varphi. \tag{4.173}$$

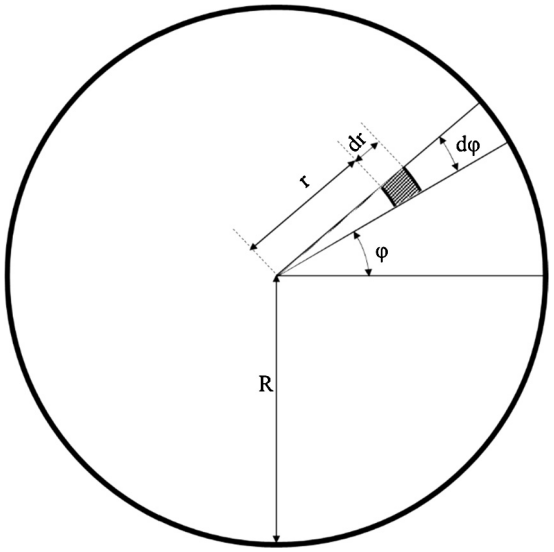

Figure 4.31 Differential element on the circular nanoscanner surface.

The electrical force only applies to the half of the main-plane. Therefore, the electrical force is obtained as

$$F_{elec} = \int_0^{\pi} \int_0^{R} dF_{elec} = \frac{\varepsilon V^2}{\sin^2(\theta)} \left[-\frac{\pi(D-\delta) + 2R\sin(\theta)}{(D-\delta)} + 2(D-\delta)\frac{\pi - \arctan(\frac{\sqrt{(D-\delta)^2 - R^2\sin^2(\theta)}}{R\sin(\theta)})}{\sqrt{(D-\delta)^2 - R^2\sin^2(\theta)}} \right]. \tag{4.174}$$

The Casimir force acts on both sides of the nanoscanner. For the sake of generality, we can assume that the electrical force applies to the left side of the nanoscanner. Hence, the distance between a differential element in the left side which rotates toward the fixed ground is given by the following relation:

$$g_L = g - \delta - r\sin(\theta)\sin(\varphi). \tag{4.175}$$

In contrast, the right side of the nanoscanner gets away from the main-plate. Therefore, the distance between the right side of nanoscanner and the fixed ground is given by

$$g_R = g - \delta + r\sin(\theta)\sin(\varphi). \tag{4.176}$$

By substituting Eqs. (4.172) and (4.175) into Eq. (1.7), the Casimir force on an infinitesimal element on the left side of the nanoscanner is obtained as:

$$dF_{Cas}^{L} = \frac{\pi^2 \hbar c}{240\left(g - \delta - r\sin(\theta)\sin(\varphi)\right)^4} r dr d\varphi. \tag{4.177}$$

Similarly, by substituting Eqs. (4.172) and (4.176) into Eq. (1.7), the Casimir force on an infinitesimal element on the left side of the nanoscanner is obtained as

$$dF_{Cas}^{R} = \frac{\pi^2 \hbar c}{240\left(g - \delta + r\sin(\theta)\sin(\varphi)\right)^4} r dr d\varphi. \tag{4.178}$$

By integrating over the main-plate, the Casimir force is obtained as

$$F_{Cas} = \int_0^{\pi}\int_0^{R} dF_{Cas}^{R} + \int_{\pi}^{2\pi}\int_0^{R} dF_{Cas}^{L} = \frac{\pi^3 \hbar c R^2}{240\left((g-\delta)^2 - R^2\sin^2(\theta)\right)^{\frac{5}{2}}}. \tag{4.179}$$

The moment acting on the main-plate can be achieved by integrating the moment acting on a differential element. By using the electrical force on an infinitesimal element (Eq. (4.173)), the electrical moment on an infinitesimal element is obtained as

$$dM_{elec} = \frac{\varepsilon_0 V^2}{2\left(g - \delta - r\sin(\theta)\sin(\varphi)\right)^2} r^2 \cos(\theta)\sin(\varphi)\, dr d\varphi. \tag{4.180}$$

By integrating over the scanner, the electrical moment is computed as

$$\begin{aligned} M_{elec} &= \int_0^{\pi}\int_0^{R} dM_{elec} \\ &= \frac{\varepsilon V^2 \cos(\theta)}{2\sin^3(\theta)}\left[\left(\pi + 2\arctan\left(\frac{R\sin(\theta)}{\sqrt{(D-\delta)^2 - \sin^2(\theta)R^2}}\right)\right)\frac{2(D-\delta)^2 - \sin^2(\theta)R^2}{\sqrt{(D-\delta)^2 - \sin^2(\theta)R^2}}\right. \\ &\quad \left. - 4R\sin(\theta) - 2\pi(D-\delta)\right]. \end{aligned} \tag{4.181}$$

By using the Casimir force on an infinitesimal element (Eq. (4.173)), the Casimir moment on an infinitesimal element in the left and right sides of main-plate is obtained as:

$$dM_{Cas}^{L} = \frac{\pi^2 \hbar c \sin(\theta)\, Cos(\varphi)}{240\left(g - \delta - r\sin(\theta)\sin(\varphi)\right)^4} r^2 dr d\varphi, \tag{4.182}$$

$$dM_{Cas}^{R} = \frac{\pi^2 \hbar c \sin(\theta)\, Cos(\varphi)}{240\left(g - \delta + r\sin(\theta)\sin(\varphi)\right)^4} r^2 dr d\varphi. \tag{4.183}$$

By integrating over the main-plate area, the Casimir moment is obtained as

$$M_{Cas} = \int_0^{\pi} \int_0^{R} dM_{Cas}^{L} - \int_{\pi}^{2\pi} \int_0^{R} dM_{Cas}^{R} = \frac{\pi^3 \hbar c R^4 \sin(\theta)\cos(\theta)}{240\left((g-\delta)^2 - R^2\sin^2(\theta)\right)^{\frac{5}{2}}}. \tag{4.184}$$

The Lagrangian (L) is given as

$$L = T - V_{elas}. \tag{4.185}$$

By substituting Eqs. (4.161) and (4.163) into Eq. (4.185), the Lagrangian is obtained as

$$L = \frac{1}{2} I_v \dot{\theta}^2 + \frac{1}{2} m\dot{\delta}^2 - K_\theta \theta^2 - K_\delta \delta^2). \tag{4.186}$$

The famous Lagrange's equations are given as

$$\frac{d}{dt}\left(\frac{\partial L}{\partial \dot{q}_i}\right) - \frac{\partial L}{\partial q_i} = Q_i \tag{4.187}$$

where Q_i is the ith generalized force and q_i is the ith generalized coordinate. For the nanoscanner, the generalized coordinates are rotating (θ) and bending (δ) angles. The virtual work relation (i.e., Eq. (4.168)) indicates that the generalized force is:

$$\begin{aligned} Q_1 &= F_{ext}, \\ Q_2 &= M_{ext}. \end{aligned} \tag{4.188}$$

By substituting Eqs. (4.186) and (4.188) into Eq. (4.187), the constitutive equation of a nanoscanner is obtained as:

$$m\ddot{\delta} + 2K_\delta \delta = F_{ext}, \tag{4.189}$$

$$I_v \ddot{\theta} + 2K_\theta \dot{\theta} = M_{ext}. \tag{4.190}$$

By substituting Eqs. (4.170), (4.174), and (4.179) into Eq. (4.189) and using Eqs. (4.170), (4.181), and (4.183) in Eq. (4.190), the governing equation of a nanoscanner is obtained as:

$$\begin{aligned} m\ddot{\delta} + C_\delta \dot{\delta} + 2K_\delta \delta = {} & \frac{\pi^3 \hbar c R^2}{240\left((g-\delta)^2 - R^2\sin^2(\theta)\right)^{\frac{5}{2}}} \\ & + \frac{\varepsilon_0 V^2}{\sin^2(\theta)}\left[-\frac{\pi(g-\delta) + 2R\sin(\theta)}{(g-\delta)} + 2(g-\delta)\frac{\pi - \arctan\left(\frac{\sqrt{(g-\delta)^2 - R^2\sin^2(\theta)}}{R\sin(\theta)}\right)}{\sqrt{(g-\delta)^2 - R^2\sin^2(\theta)}}\right], \end{aligned} \tag{4.191}$$

$$I_v\ddot{\theta} + C_\theta\dot{\theta} + 2K_\theta\theta = \frac{\pi^3\hbar c R^4 \sin(\theta)\cos(\theta)}{240\left((g-\delta)^2 - R^2\sin^2(\theta)\right)^{\frac{5}{2}}} + \frac{\varepsilon V^2\cos(\theta)}{2\sin^3(\theta)}\left[\begin{array}{l}(\pi + 2\arctan(\frac{R\sin(\theta)}{\sqrt{(g-\delta)^2 - \sin^2(\theta)R^2}}))\frac{2(g-\delta)^2 - \sin^2(\theta)R^2}{\sqrt{(g-\delta)^2 - \sin^2(\theta)R^2}} \\ -4R\sin(\theta) - 2\pi(g-\delta)\end{array}\right]. \tag{4.192}$$

In the case of a small rotation, one can assume that $\sin(\theta) \cong \theta$, $\cos(\theta) \cong 1$. Also, by considering $\theta_{\max} = \frac{g}{R}$, $\Delta = \frac{\delta}{g}$, and $\Theta = \frac{\theta}{\theta_{\max}}$, the dimensionless system of differential equations governing the dynamic behavior of a nanoscanner is given as:

$$\ddot{\Delta} + c_\Delta\dot{\Delta} + 2k_\Delta\Delta = \frac{\beta_{Cas}}{2\left((1-\Delta)^2 - \Theta^2\right)^{\frac{5}{2}}} + \frac{\alpha^2[-\frac{\pi(1-\Delta)+2\Theta}{(1-\Delta)} + 2(1-\Delta)\frac{\pi - \arctan(\frac{\sqrt{(1-\Delta)^2-\Theta^2}}{\Theta})}{\sqrt{(1-\Delta)^2-\Theta^2}}]}{4\Theta^2}, \tag{4.193}$$

$$\ddot{\Theta} + c_\Theta\dot{\Theta} + 2\Theta = \frac{\beta_{Cas}\Theta}{\left((1-\Delta)^2 - \Theta^2\right)^{\frac{5}{2}}} + \frac{\alpha^2[(\pi + 2\arctan(\frac{\Theta}{\sqrt{(1-\Delta)^2-\Theta^2}}))\frac{2(1-\Delta)^2-\Theta^2}{\sqrt{(1-\Delta)^2-\Theta^2}} - 4\Theta - 2\pi(1-\Delta)]}{\Theta^3} \tag{4.194}$$

where the overdot indicates a derivative with respect to t. Also, the dimensionless parameters are given as:

$$\Omega = \sqrt{\frac{K_\theta}{I_v}}, \tag{4.195}$$

$$\tau = \Omega t, \tag{4.196}$$

$$c_\Theta = \frac{C_\theta}{I_v\Omega}, \tag{4.197}$$

$$c_\Delta = \frac{C_\delta}{m\Omega}, \tag{4.198}$$

$$k_\Delta = \frac{K_\delta}{m\Omega^2}, \tag{4.199}$$

$$\beta_{Cas} = \frac{\pi^3\hbar c R^4}{240K_\theta g^5}, \tag{4.200}$$

$$\alpha^2 = \frac{\varepsilon V^2 R^4}{2K_\theta g^3}. \tag{4.201}$$

In the above equations, τ is the dimensionless time, k_Δ is pertinent to the lateral stiffness, α is the dimensionless electrical potential parameter, and β_{Cas} is the Casimir force dimensionless parameter. Also, c_θ and c_δ are related to transverse and rotational damping coefficient, respectively.

It worth noting that by using Eqs. (4.164) and (4.165), one can simplify Eq. (4.199) as follows:

$$k_\Delta = 12(1+\nu)\left(\frac{R}{L}\right)^2. \tag{4.202}$$

To solve the system of differential equations by using the Runge–Kutta method, Eqs. (4.193) and (4.194) are represented in terms of state-space variables as follows:

$$\begin{bmatrix} q_1 \\ q_2 \\ q_3 \\ q_4 \end{bmatrix} = \begin{bmatrix} \Delta \\ \dot{\Delta} \\ \Theta \\ \dot{\Theta} \end{bmatrix}. \tag{4.203}$$

By considering the state-space formulation, the system of second-order differential equation reduces to the following system of first-order differential equations:

$$\begin{bmatrix} \dot{q}_1 \\ \dot{q}_2 \\ \dot{q}_3 \\ \dot{q}_4 \end{bmatrix} = \begin{bmatrix} F_1(q_1, q_2, q_3, q_4) \\ F_2(q_1, q_2, q_3, q_4) \\ F_3(q_1, q_2, q_3, q_4) \\ F_4(q_1, q_2, q_3, q_4) \end{bmatrix}$$

$$\begin{bmatrix} q_3 \\ -c_\Delta q_3 - 2k_\Delta q_1 + \frac{\beta_{Cas}}{2((1-q_1)^2-q_2^2)^{\frac{5}{2}}} + \frac{\alpha^2[-\frac{\pi(1-q_1)+2q_2}{(1-q_1)} + 2(1-q_1)\frac{\pi-\arctan(\frac{\sqrt{(1-q_1)^2-q_2^2}}{q_2})}{\sqrt{(1-q_1)^2-q_2^2}}]}{4q_2^2} \\ q_4 \\ -c_\Theta q_4 - 2q_2 + \frac{\beta_{Cas} q_2}{((1-q_1)^2-q_2^2)^{\frac{5}{2}}} + \frac{\alpha^2[(\pi+2\arctan(\frac{q_2}{\sqrt{(1-q_1)^2-q_2^2}}))\frac{2(1-q_1)^2-q_2^2}{\sqrt{(1-q_1)^2-q_2^2}} - 4q_2 - 2\pi(1-q_1)]}{q_2^3} \end{bmatrix}. \tag{4.204}$$

The above system of first-order differential equations can be solved by using Eqs. (4.129) and (4.130).

The time-dependent dimensionless rotating angle and lateral deflection of a nanoscanner are plotted in Figs. 4.32 and 4.33, respectively. In these figures, the dimensionless parameters of torsional and lateral damping are equally assumed to be 0.1. Also, the dimensionless parameter of the Casimir force is 0.1 (i.e., $\beta_{Cas} = 0.1$) and the

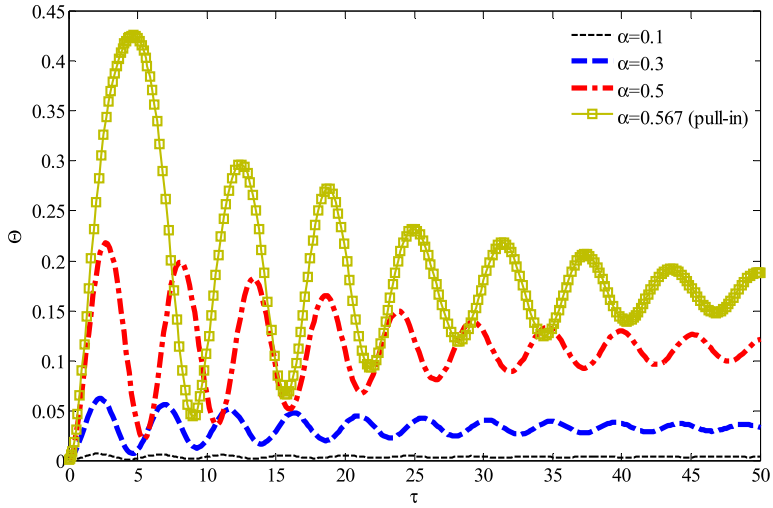

Figure 4.32 The time-dependent rotation angle of a nanoscanner for different applied voltage.

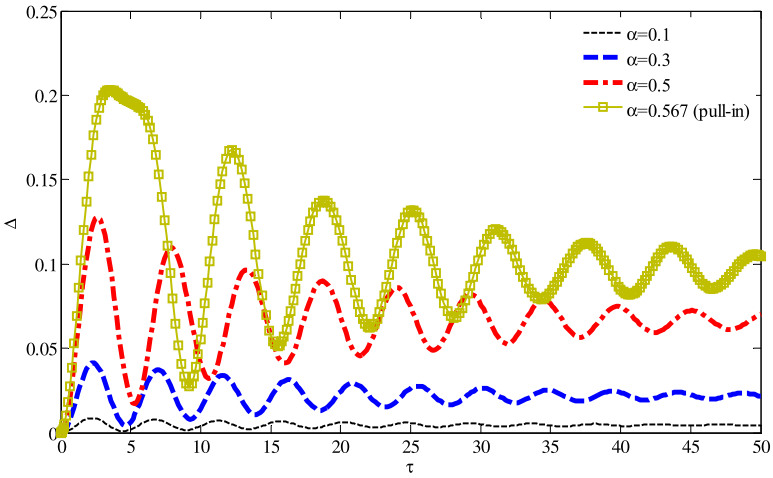

Figure 4.33 Time-dependent deflection of a nanoscanner for different applied voltage.

dimensionless parameter of lateral spring constant is 1 (i.e., $k_\Delta = 1$). Figs. 4.32 and 4.33 demonstrate an upward trend for both rotating angle and lateral deflection when increasing the applied voltage. For the nanoscanner with considered parameters, for the applied voltage less than the pull-in value, the dimensionless parameter of the rotating angle is very close to the dimensionless parameter of lateral deflection. However, at the pull-in point, the pull-in angle is considerably more significant than the pull-in deflection. The phase-plane diagrams of the nanoscanner for rotation and lateral deflection

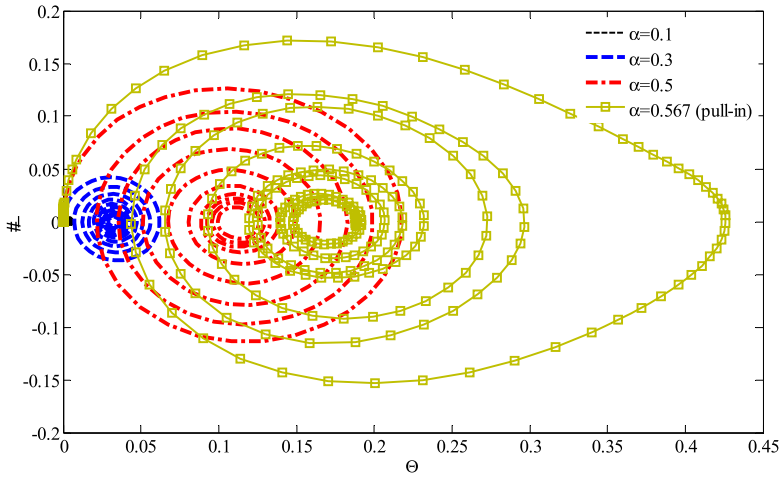

Figure 4.34 Rotation phase portrait of a nanoscanner.

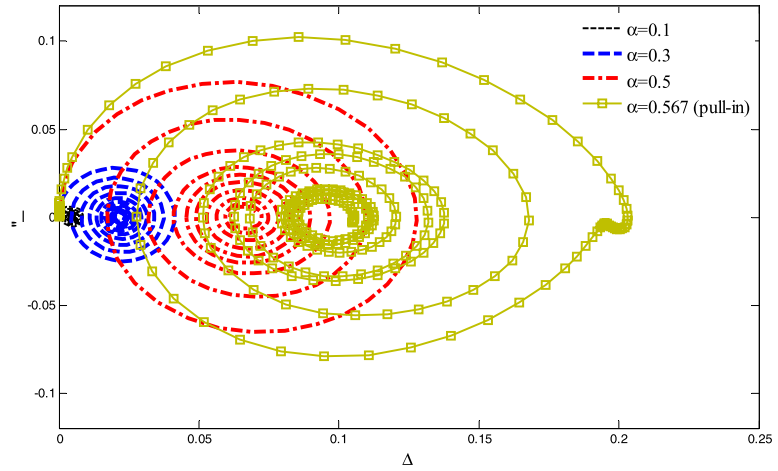

Figure 4.35 Lateral deflection phase portrait of a nanoscanner.

are plotted in Figs. 4.34 and 4.35, respectively. These figures demonstrate that for both rotation and deflection the paths converge to the stable focus node due to the damping effect.

4.4. Homotopy perturbation method for time-dependent differential equations

The concepts of the homotopy perturbation method were explained in Section 2.2. In Section 2.2.1, the static behavior of a cantilever nanoactuator in the van der Waals regime was investigated by using the homotopy perturbation method. The homotopy perturbation method can also be applied to investigate the dynamic behavior of the micro- and nanostructures [53,54]. To investigate the dynamic behavior of micro- and nanostructures by the homotopy perturbation method, firstly a reduced-order method such as Galerkin method should be employed to transform the partial differential equation into a time-dependent initial value ordinary differential equation. The homotopy perturbation method for the time-dependent differential equation is very similar to that explained in Section 2.2. Therefore, the minor difference between the application of the homotopy perturbation method to a time-dependent differential equation with that of the static behavior is explained as an example. In the following section, the dynamic behavior of a nonlocal electrostatic nanobridge is examined by employing the homotopy perturbation method.

4.4.1 Dynamic behavior of a nonlocal nanobridge with the surface effect

A clamped–clamped nanobeam hanged over a substrate is known as an electromechanical nanobridge. This ultrasmall structure is one of the crucial components in MEMS/NEMS that is highly potential for developing micro- and nanoresonators [55], micro- and nanoswitches [56], micro- and nanomemories [57], and micro- and nanosensors [58].

As mentioned in Section 4.1, some experimental observations demonstrate that by reducing the dimensions of the metal-manufactured structures the material size dependency can substantially affect the material properties [30,59,60]. This phenomenon cannot be simulated using conventional continuum theory. To overcome this deficiency in conventional elasticity for simulation of the scale dependency, higher-order continuum theories were developed to consider the size-dependency in miniature structures. In the previous section, some size-dependent continuum theories, including modified couple stress theory, couple stress theory, consistent couple stress theory, strain gradient elasticity, and surface elasticity, were employed to investigate the performance of micro/nanostructures. Herein the size-dependent performance of an electromechanical nanobridge is investigated in the context of the nonlocal elasticity. The nonlocal theory has been widely applied for simulating the static and dynamic behavior of micro- and nanostructures [54,61–69].

An SEM image of a microbridge and doubly-clamped microresonator are presented in Figs. 4.36 and 4.37, respectively. Fig. 4.38 illustrates a modeling simulation of a typical electromechanical nanobridge. The nanobridge is constructed from a doubly-clamped

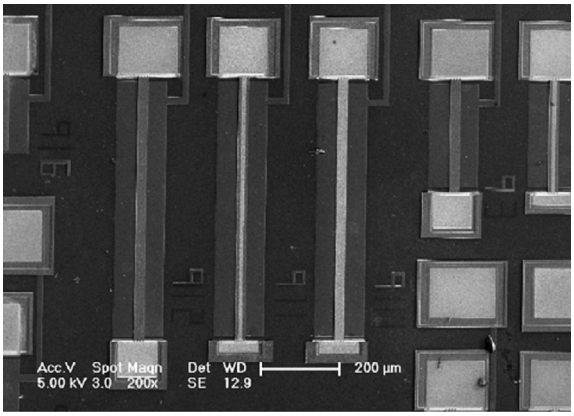

Figure 4.36 SEM image of a nanobridge [70].

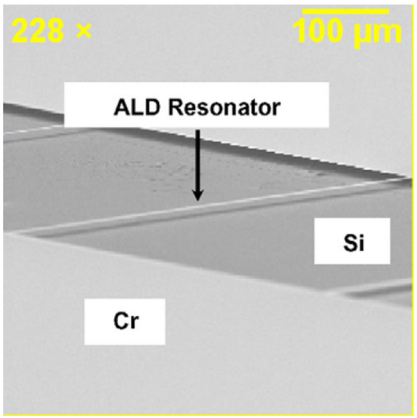

Figure 4.37 SEM image of doubly-clamped nanoresonator [71].

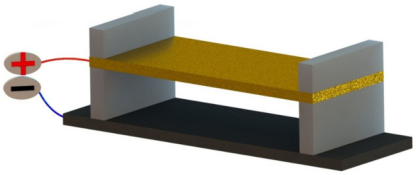

Figure 4.38 A typical electromechanical nanobridge.

nanobeam over a fixed ground. Applying a voltage difference between the nanobeam and substrate results in the bending of the moveable part of nanobridge (clamped–clamped beam) toward the fixed ground because of the electrical and the van der Waals forces.

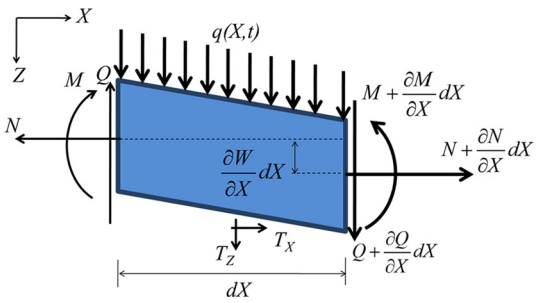

Figure 4.39 Free-body diagram of an element of the nanobeam.

A free-body diagram of an incremental element of a nanobeam with length dx is presented in Fig. 4.39. In this figure, $q(x, t)$ is the distributed transverse load, M is the bending moment, Q is the shear force, and N is the axial force. The interaction between the bulk material and surface layer results in the contact tractions on the interface between the surface layer and bulk material.

The following equilibrium equations can be achieved by using Newton's second law [14]:

$$\frac{\partial Q}{\partial X}+\int_S T_Z ds+q(X,t)-\rho A\frac{\partial^2 W}{\partial t^2}=0, \tag{4.205}$$

$$\frac{\partial M}{\partial X}-\int_S T_X Z ds-N\frac{\partial w}{\partial X}+Q=0. \tag{4.206}$$

Substituting the shear force (Q) from Eq. (4.206) into Eq. (4.205) results in

$$\rho A\frac{\partial^2 W}{\partial t^2}+\frac{\partial^2 M}{\partial X^2}-\frac{\partial}{\partial X}\int_s T_x z ds-\int_s T_Z ds-\frac{\partial}{\partial X}\left(N\frac{\partial W}{\partial X}\right)-q(X,t)=0. \tag{4.207}$$

The contact tractions on the surface element are attained from the following equilibrium equations [2]:

$$\frac{\partial \tau_{ix}}{\partial X}-T_i=\rho_0\frac{\partial^2 u_i^s}{\partial t^2} \tag{4.208}$$

where u_i^s indicates the surface deflection in i direction ($i=X, Z$), and ρ_0 is the surface layer mass density. Replacing Eq. (4.208) in Eq. (4.207) yields

$$\begin{aligned}&\rho A\frac{\partial^2 w}{\partial t^2}+\frac{\partial^2 M}{\partial X^2}-\frac{\partial}{\partial X}\int_s\frac{\partial \tau_{XX}}{\partial X}Z ds-\int_s\frac{\partial \tau_{ZX}}{\partial X}ds-\frac{\partial}{\partial X}\left(N\frac{\partial W}{\partial X}\right)\\&+\int_s\rho_0\frac{\partial^2 u_Z^s}{\partial t^2}ds-q(X,t)=0.\end{aligned} \tag{4.209}$$

The nonlocal bending moment and shear stress can be defined by the following relation from the local parameters [72]:

$$\left(1-\mu_b\nabla^2\right)M^{nl}=M^{l}, \tag{4.210}$$

$$\left(1-\mu_s\nabla^2\right)\tau_{XX}^{nl}=\tau_{XX}^{l}, \tag{4.211}$$

$$\left(1-\mu_s\nabla^2\right)\tau_{ZX}^{nl}=\tau_{ZX}^{l} \tag{4.212}$$

where μ_b is the bulk nonlocal parameter and μ_s is the nonlocal surface parameter. For the sake of simplicity, the nonlocal parameters can assume equally (i.e., $\mu_b=\mu_s=e_0^2a^2$). By substituting Eqs. (4.210)–(4.212) into Eq. (4.262), the following relation is achieved:

$$\begin{aligned}&\frac{\partial^2 M}{\partial X^2}-\frac{\partial}{\partial X}\int_s\frac{\partial\tau_{XX}}{\partial X}Zds-\int_s\frac{\partial\tau_{ZX}}{\partial X}ds\\&+\left(1-e_0^2a^2\frac{\partial}{\partial X^2}\right)\left[\rho A\frac{\partial^2 w}{\partial t^2}-\frac{\partial}{\partial X}\left(N\frac{\partial W}{\partial X}\right)+\int_s\rho_0\frac{\partial^2 u_Z^s}{\partial t^2}ds-q(X,t)\right]=0.\end{aligned} \tag{4.213}$$

For a local beam, the surface shear stress, bending moment, and axial force are given by:

$$N=\frac{EA}{2L}\int_0^l\left(\frac{\partial W}{\partial X}\right)^2dX+N_0, \tag{4.214}$$

$$M=EI\frac{\partial^2 W}{\partial W^2}-\frac{2\nu I}{h}\left(\tau_0\frac{\partial^2 W}{\partial x^2}-\rho_0\frac{\partial^2 W}{\partial t^2}\right), \tag{4.215}$$

$$\tau_{XX}=\tau_0+E_0\left(\frac{\partial W}{\partial X}-Z\frac{\partial^2 W}{\partial X^2}\right), \tag{4.216}$$

$$\tau_{ZX}=\tau_0\frac{\partial W}{\partial X} \tag{4.217}$$

where N_0 indicates the initial axial force, τ_0 indicates the surface residual stress, and E_0 is the surface elasticity. By substituting Eqs. (4.214)–(4.217) in Eq. (4.213), the governing equation of the nonlocal nanobridge incorporating the surface energies is achieved as:

$$\begin{aligned}&\left(EI+E_0I_0-\frac{2\nu I\tau_0}{h}\right)\frac{\partial^4 W}{\partial X^4}+\frac{2\nu I\rho_0}{h}\frac{\partial^4 W}{\partial X^2\partial t^2}-\tau_0S_0\frac{\partial^2 W}{\partial X^2}\\&=\left(1-e_0^2a^2\frac{\partial^2}{\partial X^2}\right)\left[q(X,t)+\left(N_0+\frac{EA}{2l}\int_0^l\left(\frac{\partial W}{\partial X}\right)^2dX\right)\frac{\partial^2 W}{\partial X^2}-(\rho A+\rho_0S_0)\frac{\partial^2 W}{\partial t^2}\right].\end{aligned} \tag{4.218}$$

For a clamped–clamped nanobeam, the boundary conditions at both ends are geometrical. Therefore, the boundary conditions for a nonlocal clamped–clamped nanobeam are similar to those of the local clamped–clamped nanobeam. The clamped support

prevents the deflection and rotation of the nanobeam. So, the boundary conditions are given as:

$$\begin{aligned} &W(0,t) = W(L,t) = 0, \\ &\frac{\partial}{\partial X} W(0,t) = \frac{\partial}{\partial X} W(L,t) = 0. \end{aligned} \tag{4.219}$$

For an electromechanical nanobridge operated in the van der Waals regime, the transverse load is the sum of electrical force (Eq. (2.13)) and van der Waals (Eq. (2.14)) force. By replacing $q(x,t)$ with the sum of Eqs. (2.13) and (2.14), the governing equation of a nonlocal electromechanical nanobridge is rewritten as

$$\begin{aligned} &\left(EI + E_0 I_0 - \frac{2\nu I \tau_0}{h}\right) \frac{\partial^4 W}{\partial X^4} + \frac{2\nu I \rho_0}{h} \frac{\partial^4 W}{\partial X^2 \partial t^2} - \tau_0 S_0 \frac{\partial^2 W}{\partial X^2} \\ &= \left(1 - e_0^2 a^2 \frac{\partial^2}{\partial X^2}\right) \left[\left(N_0 + \frac{EA}{2l} \int_0^l \left(\frac{\partial W}{\partial X}\right)^2 dX\right) \frac{\partial^2 W}{\partial X^2} - (\rho A + \rho_0 S_0) \frac{\partial^2 W}{\partial t^2}\right] \\ &\left(1 - e_0^2 a^2 \frac{\partial^2}{\partial X^2}\right) \left[\frac{\varepsilon b V^2}{2(g-W)^2} \left[1 + 0.65 \left(\frac{g-W}{b}\right)\right] + \frac{\bar{A} b}{6\pi (g-W)^3}\right]. \end{aligned} \tag{4.220}$$

To simplify the analysis, the following dimensionless parameters are defined:

$$w = \frac{W}{g}, \tag{4.221}$$

$$x = \frac{X}{L}, \tag{4.222}$$

$$\beta_{vdW} = \frac{AbL^4}{6\pi g^4 EI}, \tag{4.223}$$

$$\alpha = \frac{\varepsilon_0 b V^2 L^4}{2g^3 EI}, \tag{4.224}$$

$$\gamma = 0.65 \frac{g}{b}, \tag{4.225}$$

$$\eta = 6 \frac{g^2}{h^2}, \tag{4.226}$$

$$\tau = \sqrt{\frac{EI}{\rho b h L^4}}\, t, \tag{4.227}$$

$$f_0 = \frac{N_0 L^2}{EI}, \tag{4.228}$$

$$\zeta_0 = \frac{E_0 I_0}{EI}, \tag{4.229}$$

$$t_1 = \frac{2\nu \tau_0}{Eh}, \tag{4.230}$$

$$t_2 = \frac{\tau_0 S_0 L^2}{EI}, \tag{4.231}$$

$$\delta = \frac{e_0 a}{L}, \tag{4.232}$$

$$\rho_1 = \frac{\nu \rho_0 h}{6\rho L^2}, \tag{4.233}$$

$$\rho_2 = \frac{\rho_0 S_0}{\rho A}. \tag{4.234}$$

Using the above equation, the dimensionless governing equation of an electromechanical nanobridge is obtained as

$$\begin{aligned}
&(1+\zeta_0-t_1)\frac{\partial^4 w}{\partial x^4}+\rho_1\frac{\partial^4 w}{\partial x^2\partial\tau^2}-t_2\frac{\partial^2 w}{\partial x^2}\\
&=\left(1-\delta^2\frac{\partial^2}{\partial x^2}\right)\left[\frac{\alpha}{(1-w)^2}\left(1+0.65\gamma(1-w)\right)+\frac{\beta_{vdW}}{(1-w)^3}\right]\\
&\left(1-\delta^2\frac{\partial^2}{\partial x^2}\right)\left[\left(f_0+\eta\int_0^1\left(\frac{\partial w}{\partial x}\right)^2 dx\right)\frac{\partial^2 w}{\partial x^2}-(1+\rho_2)\frac{\partial^2 w}{\partial \tau^2}\right].
\end{aligned} \tag{4.235}$$

To find the homotopy perturbation solution, the nonlinear partial differential equation (4.213) should be reduced to a partial differential equation. To this end, Galerkin's method can be employed. As mentioned in Section 4.2.1, in the Galerkin method, the solution is assumed as

$$w(x,\tau)=\sum_{i=1}^{n} q_i(\tau)\,\phi_i(x). \tag{4.236}$$

As the boundary conditions of a nonlocal doubly-clamped beam are similar to those of the local doubly-clamped beam, the classical mode shapes of the clamped–clamped beam can be used in the Galerkin procedures:

$$\phi_i(x)=\cosh(\lambda_i x)-\cos(\lambda_i x)-\frac{\cosh(\lambda_i)-\cos(\lambda_i)}{\sinh(\lambda_i)-\sin(\lambda_i)}\left(\sinh(\lambda_i x)-\sin(\lambda_i x)\right). \tag{4.237}$$

In the Galerkin procedure, the nonlinear terms of the electrical and the van der Waals forces are rewritten as a series of w using the Taylor expansion. By using the first mode shape of the clamped–clamped beam ($\lambda_1 = 4.73004074$), substituting Eq. (4.236) into Eq. (4.235), multiplying both sides of the obtained equation by $\phi_1(x)$, and integrating the result from 0 to 1, one obtains

$$\frac{d^2 q}{d\tau^2}+b_4(q(\tau))^4+b_3(q(\tau))^3+b_2(q(\tau))^2+b_1 q(\tau)+b_0=0 \tag{4.238}$$

where

$$b_0 = -\frac{(\beta(1+0.65\gamma)+\alpha)\,A_1}{\rho_1 B_1 + (1+\rho_2)\left(1-\delta^2 B_1\right)}, \tag{4.239}$$

$$b_1 = \frac{(1+\zeta_0-t_1)\,\lambda_1^4 - t_1 B_1 - (\beta(2+0.65\gamma)+3\alpha)\left(A_2-\delta^2 B_1\right) - f_0\left(B_1-\delta^2\lambda_1^4\right)}{\rho_1 B_1 + (1+\rho_2)\left(1-\delta^2 B_1\right)}, \tag{4.240}$$

$$b_2 = -\frac{(\beta(3+0.65\gamma)+6\alpha)\left(A_3-\delta^2 B_2\right)}{\rho_1 B_1 + (1+\rho_2)\left(1-\delta^2 B_1\right)}, \tag{4.241}$$

$$b_3 = \frac{-(\beta(4+0.65\gamma)+10\alpha)\left(A_4-\delta^2 B_3\right) - \eta\left(B_1 D_1 - \delta^2\lambda_1^4 D_1\right)}{\rho_1 B_1 + (1+\rho_2)\left(1-\delta^2 B_1\right)}, \tag{4.242}$$

$$b_4 = \frac{-(\beta(5+0.65\gamma)+15\alpha)\left(A_5-\delta^2 B_4\right)}{\rho_1 B_1 + (1+\rho_2)\left(1-\delta^2 B_1\right)}. \tag{4.243}$$

In the above equations,

$$A_n = \int_0^1 \phi_1^n dx, \quad n = 1, 2, 3, 4, 5, \tag{4.244}$$

$$B_n = \int_0^1 \phi_1 \left(\phi_1^n\right)'' dx, \quad n = 1, 2, 3, 4, \tag{4.245}$$

$$D_1 = \int_0^1 (\phi_1')^2 dx. \tag{4.246}$$

Similar to what was mentioned for the application of a homotopy perturbation for the static analysis of NEMS, to solve the nonlinear differential equation (4.238), a homotopy perturbation can be constructed as follows:

$$H(q,p) = (1-p)\left[\ddot{q} + b_1 q\right] + p\left[\ddot{q} + b_1 q + b_2 q^2 + b_3 q^3 + b_4 q^4 + b_0\right] = 0. \tag{4.247}$$

According to the homotopy perturbation method, the approximate solution if q is defined as the following power series in p:

$$q = q_0 + q_1 p + q_2 p^2 + q_3 p^3 + \cdots. \tag{4.248}$$

The embedding parameter is also employed to find the fundamental frequency as

$$b_1 = \omega^2 - p\omega_1 - p^2\omega_2 - \cdots. \tag{4.249}$$

An approximate solution for the fundamental frequency can be achieved by setting $q = 1$:

$$\omega^2 = b_1 + \omega_1 + \omega_2 + \ldots. \tag{4.250}$$

Using Eqs. (4.249) and (4.250) in (4.248) yields:

$$p^0 : \ddot{q}_0(\tau) + \omega^2 q_0(\tau) = 0, \tag{4.251}$$

$$p^1 : \ddot{q}_1(\tau) + \omega^2 q_1(\tau) = \omega_1 q_0(\tau) - b_2 \left(q_0(\tau)\right)^2 - b_3 \left(q_0(\tau)\right)^3 - b_4 \left(q_0(\tau)\right)^4 - b_0, \tag{4.252}$$

$$\begin{aligned} p^2 : \ddot{q}_2(\tau) + \omega^2 q_2(\tau) &= \omega_1 q_1(\tau) + \omega_2 q_0(\tau) \\ &- \left[2b_2 q_0(\tau) + 3b_3 \left(q_0(\tau)\right)^2 + 4b_4 \left(q_0(\tau)\right)^3\right] q_1(\tau) \\ &- \left[b_2 q_0(\tau)^2 + b_3 \left(q_0(\tau)\right)^3 + b_4 \left(q_0(\tau)\right)^4\right]. \end{aligned} \tag{4.253}$$

The initial conditions for the above equation are:

$$\begin{aligned} q_i &= \begin{cases} A, & i = 1, \\ 0, & \text{otherwise}, \end{cases} \\ \dot{q}_i &= 0. \end{aligned} \tag{4.254}$$

The solution of Eq. (4.251) with the initial condition of (4.254) is $q_0 = A\cos(\omega\tau)$. Substituting this solution into Eq. (4.252) yields

$$\begin{aligned} \ddot{q}_1(\tau) + \omega^2 q_1(\tau) &= \left(\omega_1 A - \frac{3}{4} b_3 A^3\right) \cos(\omega\tau) + \left(-\frac{1}{2} b_4 A^4 - \frac{1}{2} b_2 A^2\right) \cos(2\omega\tau) \\ &- \frac{1}{2} b_2 A^2 - \frac{3}{8} b_4 A^4 - \frac{1}{4} b_3 A^3 \cos(3\omega\tau) - b_0 - \frac{1}{8} b_4 A^4 \cos(4\omega\tau). \end{aligned} \tag{4.255}$$

Because the solution q_0 is in the form of $q_0 = A\cos(\omega\tau)$, the solution of Eq. (4.252) should not contain the $\cos(\omega\tau)$ term. This means that

$$\omega_1 A - \frac{3}{4} b_3 A^3 = 0 \Rightarrow \omega_1 = \frac{3}{4} b_3 A^2. \tag{4.256}$$

By using the above relation, the solution of Eq. (4.255) is achieved as:

$$\begin{aligned} q_1(\tau) = &\frac{\cos(\omega\tau)\left(48 b_4 A^4 + 160 b_2 A^2 - 15 b_3 A^3 + 480 b_0\right)}{480\omega^2} \\ &+ \frac{\cos(2\omega\tau)\left(80 b_4 A^4 + 80 b_2 A^2\right)}{480\omega^2} + \frac{b_3 A^3 \cos(3\omega\tau)}{32\omega^2} \\ &+ \frac{b_4 A^4 \cos(4\omega\tau)}{120\omega^2} + \frac{-480 b_0 - 180 b_4 A^4 - 240 b_2 A^2}{480\omega^2}. \end{aligned} \tag{4.257}$$

Considering two terms in Eq. (4.250) yields

$$\omega_2 = \omega^2 - b_1 - \omega_1. \tag{4.258}$$

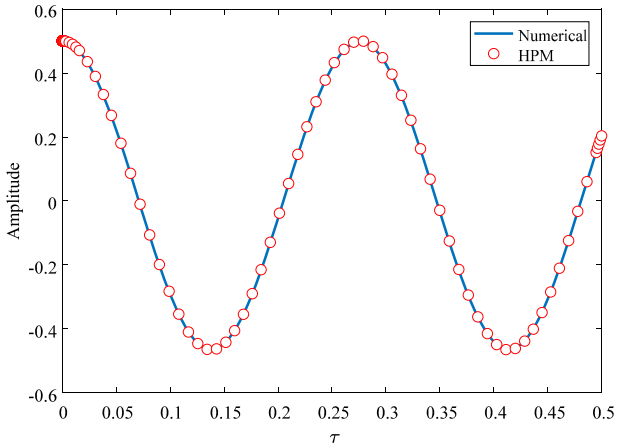

Figure 4.40 Comparison between the homotopy perturbation solution and the numerical solution.

Substituting Eq. (4.258) into Eq. (4.253) and eliminating the secular terms gives

$$\omega = \left[\frac{b_1}{2} + \frac{3}{8}b_3A^2 + \left(\frac{b_1^2}{4} + \frac{3b_1b_3A^2}{8} + \frac{15b_3^2A^4}{8} - \frac{7b_2b_4A^4}{4} + \frac{b_2b_3A^3}{2} + \frac{3b_0b_3A}{2} - \frac{5b_2^2A^2}{6} + \frac{3b_3b_4A^5}{10} - 3b_4b_0A^2 - \frac{63b_4^2A^6}{80} - 2b_2b_0\right)^{1/2}\right]^{1/2}. \tag{4.259}$$

To investigate the accuracy of the proposed homotopy perturbation solution, the time-dependent variation of the normalized amplitude (q) is plotted in Fig. 4.40. As seen, while only two terms are considered in the homotopy perturbation procedure, the results are in perfect agreement with the numerical solution.

The impact of the van der Waals parameter (β_{vdw}) on the frequency of the nanobridge is shown in Fig. 4.41. As seen, by increasing the van der Waals parameter, the frequency of the system reduces. This trend can be seen until the critical value of the van der Waals parameter, when the frequency disappears and the pull-in occurs. Fig. 4.41 demonstrates that the critical values of the van der Waals force decrease by increasing the applied voltage parameter (α).

Fig. 4.42 illustrates the impact of the surface residual stress parameter (ζ_0) on the nanobridge frequency. The surface residual stress might be positive or negative depending on the material properties. Fig. 4.42 demonstrates that an increase in the surface residual stress parameter results in an enhancement in the frequency of the nanobridge. This can affect the pull-in instability. For example, when the applied voltage parameter is 30 (i.e., $\alpha = 30$), the nanobridge with $\zeta < 0.054$ is unstable. However, the nanobridge is stable for $\zeta > 0.054$. The influence of the nonlocal parameter on the frequency of the

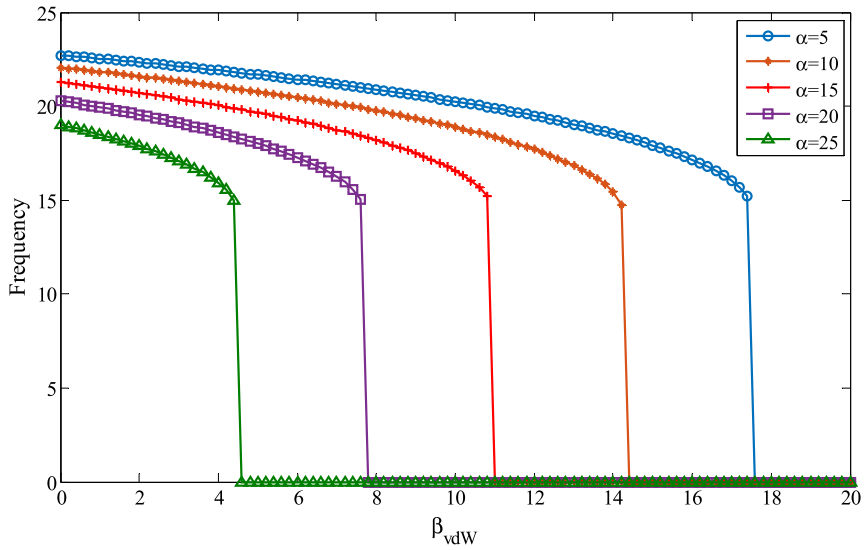

Figure 4.41 Effect of van der Waals force on the nanobridge frequency.

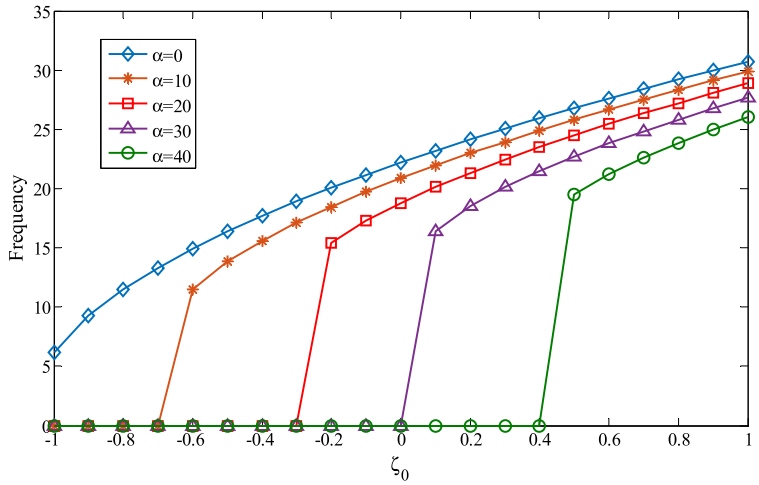

Figure 4.42 Effect of surface residual stress parameter (ζ_0) on the nanobridge frequency.

system is presented in Fig. 4.43. This figure demonstrates that the nonlocal parameter reduces the frequency. This trend is similar to the results of [54].

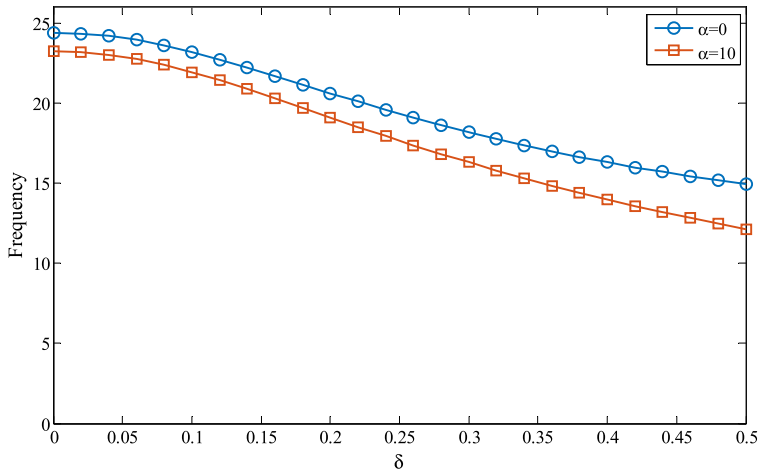

Figure 4.43 Effect of the nonlocal parameter on the nanobridge frequency.

4.5. Energy balance method

In the energy balance method, the time-dependent governing equation of the system is defined in the variational form. Incorporating the Hamiltonian with the collocation method, the frequency of the system can be obtained [73].

The idea of the energy balance method comes from the fact that for an oscillating system with the frequency of ω, when $\omega t = 0$, the whole energy of the system is in the form of kinetic energy, and when $\omega t = \frac{\pi}{2}$, the whole energy of the system is in the form of potential energy. Hence, when $\omega t = \frac{\pi}{4}$, a balance between the kinetic and potential energy of the system can be assumed. The energy balance method utilizes the advantage of this point to collocate a solution at $\omega t = \frac{\pi}{4}$. While the idea of the energy balance method is straightforward, the results are valid for investigating the vibration of some highly nonlinear systems. Interestingly, even the lowest-order approximations are of high accuracy [73–77].

To illustrate the basic idea of the energy balance method, consider the following initial value problem:

$$\frac{\partial^2 w(t)}{\partial t^2} + f(w(t)) = 0 \tag{4.260}$$

with the following initial conditions:

$$\begin{aligned} w(0) &= w_0, \\ \frac{\partial w(0)}{\partial t} &= 0 \end{aligned} \tag{4.261}$$

where f is a general nonlinear function of w. Using the variational principle, Eq. (4.260) can be rewritten as:

$$J(w) = \int_o^t \left(-\frac{1}{2}\dot{w}^2 + F(w) \right) dt, \tag{4.262}$$

$$F(w) = \int f(w) dw. \tag{4.263}$$

Eq. (4.262) shows the Hamiltonian. Hence, the above relation can be rewritten as:

$$H = \frac{1}{2}\dot{w}^2 + F(w) = F(w_0), \tag{4.264}$$

or

$$R(t) = \frac{1}{2}\dot{w}^2 + F(w) - F(A) = 0. \tag{4.265}$$

The amplitude and frequency are essential physical parameters in the oscillating system. Therefore, a trial solution with the amplitude of A and frequency of ω is assumed as

$$u(t) = A\cos(\omega t). \tag{4.266}$$

Substituting the approximated solution (Eq. (4.266)) into Eq. (4.265) results in

$$R(t) = \frac{1}{2}\omega^2 A^2 \sin^2(\omega t) + F(A\cos(\omega t)) - F(A) = 0. \tag{4.267}$$

It should be noted that for the exact solution $w(t)$, Eq. (4.265) becomes zero for all values of t. However, since Eq. (4.266) is only an approximation to the exact solution, R cannot be made zero everywhere. Evaluating Eq. (4.267) at $\omega t = \frac{\pi}{4}$ gives

$$\omega = \sqrt{\frac{2(F(A) - F(A\cos\omega t))}{A^2 \sin^2 \omega t}}. \tag{4.268}$$

4.5.1 Nonlinear oscillation of a nanoresonator

Resonators, or resonant sensors, denote the set of sensors that use a structure vibrating at resonance [78–80]. Micro- and nanoresonators are among the essential components for different applications such as sensors [81,82], accelerometers [83], and communication and signal processing devices [84].

The static instability of a double-side nanobridge was investigated in Section 2.5.1 in the context of the couple stress theory. A nanoresonator has the same structure and geometry as the double-sided nanobridge studied in Section 2.5.1, the sole difference is the gap distance which is equal for both the upper and lower plates. Fig. 4.44 illustrates

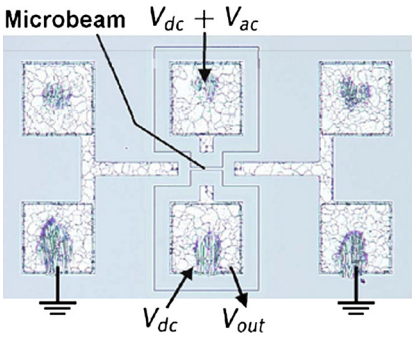

Figure 4.44 Microscope image of a clamped–clamped microresonator [85].

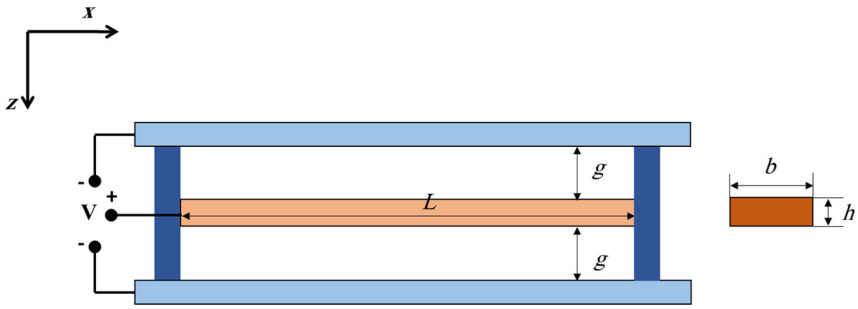

Figure 4.45 Two-dimensional view of a typical nanoresonator.

a microscope image of a microresonator. The two-dimensional modeling view of a double-clamped resonator is presented in Fig. 4.45.

As mentioned in Section 2.5.1, the strain energy of a doubly-clamped beam based on the couple stress theory is given by

$$U = \frac{1}{2}\int_0^L \left[(EI + 4A\eta)\left(\frac{\partial^2 W}{\partial X^2}\right)^2 + EA\left(\frac{\partial U}{\partial X} + \frac{1}{2}\left(\frac{\partial W}{\partial X}\right)^2\right)^2 \right] dX. \tag{4.269}$$

The work done by the external force (f_{ext}) is given by

$$W_{ext} = \int_0^L f_{ext} W(X)\, dX. \tag{4.270}$$

The initial gap of the nanoresonator is assumed to be in the Casimir regime, therefore the external force acting on the nanoresonator is the sum of electrical force (f_{elec}) and Casimir force (f_{Cas}).

By considering $\Omega = 1$ in Eq. (2.220), the total electrical force per unit length that is effective on the moving electrode is obtained as

$$f_{elec} = \frac{\varepsilon_0 b V^2}{2(g-W)^2}\left(1 + 0.65\frac{g-W}{b}\right) - \frac{\varepsilon_0 b V^2}{2(g+W)^2}\left(1 + 0.65\frac{g+W}{b}\right). \tag{4.271}$$

Similarly, using Eq. (2.221), the Casimir force per unit length is obtained as

$$f_{Cas} = \frac{\pi^2 \hbar c b}{240\left(g-W\right)^4} - \frac{\pi^2 \hbar c b}{240\left(g+W\right)^4}. \tag{4.272}$$

The kinetic energy is similar to that mentioned in Eq. (4.337), namely

$$T = \frac{1}{2}\int_0^L \left[\rho A\left(\frac{\partial U}{\partial t}\right)^2 + \rho A(W)^2 + \rho I(\frac{\partial^2 W}{\partial t \partial x})^2\right] dX. \tag{4.273}$$

Nanoresonators are usually manufactured with high-quality factors to reduce energy loss. Therefore, the damping effect can be neglected.

Hamilton's principle can be employed to extract the governing equation of the system:

$$\int_{t_1}^{t_2} (\delta T - \delta U + \delta W_{ext})\, dt = 0. \tag{4.274}$$

By using Eqs. (4.269), (4.270), and (4.273) in the above relation, one obtains

$$\begin{aligned}
&-\int_{t_1}^{t_2}\int_0^L \left[\frac{\partial}{\partial X}\left(EA\left(\frac{\partial U}{\partial X} + \frac{1}{2}(\frac{\partial W}{\partial X})^2\right)\right) - \rho A\frac{\partial^2 U}{\partial t^2}\right]\delta U dx dt \\
&+\int_{t_1}^{t_2}\left[EA\left(\frac{\partial U}{\partial X} + \frac{1}{2}\left(\frac{\partial W}{\partial X}\right)^2\right)\delta U\right]_0^L dt \\
&+\int_{t_1}^{t_2}\int_0^L \left[\begin{array}{l}\rho A\dfrac{\partial^2 W}{\partial t^2} - \rho I\dfrac{\partial^4 W}{\partial t^2 \partial X^2} + (EI + 4\mu A l^2)\dfrac{\partial^4 W}{\partial X^4} - F_{ext}(X,t) \\ \quad - EA\dfrac{\partial}{\partial X}\left(\left(\dfrac{\partial U}{\partial X} + \dfrac{1}{2}\left(\dfrac{\partial W}{\partial X}\right)^2\right)\dfrac{\partial W}{\partial X}\right)\end{array}\right]\delta W dx dt \\
&+\int_{t_1}^{t_2}\left[\left(-(EI + 4\mu A l^2)\frac{\partial^3 W}{\partial X^3} + EA\left(\frac{\partial U}{\partial X} + \frac{1}{2}\left(\frac{\partial W}{\partial X}\right)^2\right)\frac{\partial W}{\partial X}\right)\delta W\right]_0^L dt \\
&+\int_{t_1}^{t_2}\left[\left((EI + 4\mu A l^2)\frac{\partial^2 W}{\partial X^2} + \rho I\frac{\partial^3 W}{\partial t^2 \partial X}\right)\delta\left(\frac{\partial W}{\partial X}\right)\right]_0^L dt
\end{aligned}$$

$$-\int_0^L \left[\rho A \frac{\partial W}{\partial t}\delta W\right]_{t_1}^{t_2} dX - \int_0^L \left[\rho A \frac{\partial U}{\partial t}\delta U\right]_{t_1}^{t_2} dX$$
$$-\int_0^L \left[\rho I \frac{\partial^2 W}{\partial t \partial X}\delta\left(\frac{\partial W}{\partial X}\right)\right]_{t_1}^{t_2} dX = 0. \tag{4.275}$$

The above variational equation results in the following differential equations:

$$\frac{\partial}{\partial X}\left(EA\left(\frac{\partial U}{\partial X} + \frac{1}{2}\left(\frac{\partial W}{\partial X}\right)^2\right)\right) = \rho A \frac{\partial^2 U}{\partial t^2}, \tag{4.276}$$

$$\rho A \frac{\partial^2 W}{\partial t^2} - \rho I \frac{\partial^4 W}{\partial t^2 \partial X^2} + (EI + 4\mu A l^2)\frac{\partial^4 W}{\partial X^4} - \frac{\partial}{\partial X}\left(EA\left(\frac{\partial U}{\partial X} + \frac{1}{2}\left(\frac{\partial W}{\partial X}\right)^2\right)\frac{\partial W}{\partial X}\right) = F_{ext}(X, t). \tag{4.277}$$

Moreover, Eq. (4.123) results in the following boundary conditions:

$$EA\frac{\partial}{\partial X}\left(\frac{\partial U}{\partial X} + \frac{1}{2}\left(\frac{\partial W}{\partial X}\right)^2\right)\Bigg|_{X=0,L} = 0 \quad \text{or} \quad \delta U|_{X=0,L} = 0, \tag{4.278}$$

$$\left.-\left(EI + \mu A\left(2l_0^2 + \frac{8}{15}l_1^2 + l_2^2\right)\right)\frac{\partial^3 W}{\partial X^3} + EA\left(\frac{\partial U}{\partial X} + \frac{1}{2}\left(\frac{\partial W}{\partial X}\right)^2\right)\right)\frac{\partial W}{\partial X} + \mu I\left(2l_0^2 + \frac{4}{5}l_1^2\right)\frac{\partial^5 W}{\partial X^5}\Bigg|_{X=0,L} = 0 \quad \text{or} \quad \delta W|_{X=0,L} = 0, \tag{4.279}$$

$$-(EI + 4\mu A l^2)\frac{\partial^3 W}{\partial X^3} + EA\frac{\partial}{\partial X}\left(\frac{\partial U}{\partial X} + \frac{1}{2}\left(\frac{\partial W}{\partial X}\right)^2\right)\frac{\partial W}{\partial X}\Bigg|_{X=0,L} = 0 \quad \text{or} \quad \delta W|_{X=0,L} = 0, \tag{4.280}$$

$$\left(EI + 4\mu A l^2\right)\frac{\partial^2 W}{\partial X^2}\Bigg|_{X=0,L} = 0 \quad \text{or} \quad \delta\left(\frac{\partial W}{\partial X}\right)\Bigg|_{X=0,L} = 0. \tag{4.281}$$

By neglecting the effect of rotating inertia and using Eq. (2.231), the constitutive equation of a nanoresonator reduces from a system of two partial differential equations to the following partial differential equation:

$$\rho A \frac{\partial^2 W}{\partial t^2} + \left(EI + 4\mu A l^2\right)\frac{\partial^4 W}{\partial X^4} - \left[\frac{EA}{2L}\int_0^L \left(\frac{\partial W}{\partial X}\right)^2 dX\right]\frac{\partial^2 W}{\partial X^2} = f_{elec} + f_{Cas} \tag{4.282}$$

with the following boundary condition for a clamped–clamped nanobeam:

$$W(0) = \frac{\partial W(0)}{\partial X} = W(L) = \frac{\partial W(L)}{\partial X} = 0. \tag{4.283}$$

Finally, by considering $w = W/x$ and $x = X/L$, the dimensionless governing equation and the boundary conditions of the double-sided nanobridge are determined as:

$$\frac{\partial^2 w}{\partial \tau^2} + (1+\delta)\frac{\partial^4 w}{\partial x^4} - \eta\left(\int_0^1 \left(\frac{\partial w}{\partial x}\right)^2 dx\right)\frac{\partial^2 w}{\partial x^2} = \frac{\beta_{Cas}}{(1-w)^4} - \frac{\beta_{Cas}}{(1+w)^4} + \frac{\alpha}{(1-w)^2} - \frac{\alpha}{(1+w)^2} + \frac{\gamma\alpha}{1-w} - \frac{\gamma\alpha}{1+w}, \tag{4.284}$$

$$w(0) = w(1) = \frac{\partial w}{\partial x}(0) = \frac{\partial w}{\partial x}(1) = 0 \tag{4.285}$$

where

$$\beta_{Cas} = \frac{\pi^2 hcbL^4}{240EIg^5}, \tag{4.286}$$

$$\alpha = \frac{\varepsilon_0 bV^2 L^4}{2g^3 EI}, \tag{4.287}$$

$$\gamma = 0.65\frac{g}{b}, \tag{4.288}$$

$$\delta = \frac{48\mu l^2}{Eh^2}, \tag{4.289}$$

$$\eta = 6\frac{g^2}{h^2}, \tag{4.290}$$

$$\tau = \sqrt{\frac{EI}{\rho bhL^4}}t. \tag{4.291}$$

By employing the Galerkin procedure, the partial differential equation (4.284) reduces to an ordinary differential equation. By using only one mode in the Galerkin procedure, the resonator deflection can be expressed as

$$w = q_1(\tau)\phi_1(x) \tag{4.292}$$

where is the first mode of a clamped–clamped beam is

$$\phi_1(x) = \cosh(\lambda_1 x) - \cos(\lambda_1 x) - \frac{\cosh(\lambda_1) - \cos(\lambda_1)}{\sinh(\lambda_1) - \sin(\lambda_1)}(\sinh(\lambda_1 x) - \sin(\lambda_1 x)). \tag{4.293}$$

By multiplying both sides of Eq. (4.284) by $(1-w^2)^4$, one obtains

$$\begin{aligned}(1-w^2)^4\frac{\partial^2 w}{\partial \tau^2} + (1+\delta)(1-w^2)^4\frac{\partial^4 w}{\partial x^4} - \eta(1-w^2)^4\left(\int_0^1 \left(\frac{\partial w}{\partial x}\right)^2 dx\right)\frac{\partial^2 w}{\partial x^2} \\ = \beta_{Cas}(1+w)^4 - \beta_{Cas}(1-w)^4 + \alpha(1+w)^4(1-w)^2 - \alpha(1+w)^2(1-w)^4 \\ + \alpha\gamma(1+w)^4(1-w)^3 - \alpha\gamma(1+w)^3(1-w)^4.\end{aligned} \tag{4.294}$$

Substituting Eq. (4.292) in Eq. (4.294), multiplying by $\phi_1(x)$, and integrating the resulting relation from 0 to 1 yields

$$\begin{aligned}&\left(a_2 - 4a_4q_1^2 + 6a_6q_1^4 - 4a_8q_1^6 + a_{10}q_1^8\right)\ddot{q}\\&+ E_1q_1 + E_2q_1^3 + E_3q_1^5 + E_4q_1^7 + E_5q_1^9 + E_6q_1^{11} = 0\end{aligned} \tag{4.295}$$

where

$$a_0 = \int_0^1 \phi_1'^2 dx, \tag{4.296}$$

$$a_i = \int_0^1 \phi_1^i dx, \quad i = 1, 2, .., 10, \tag{4.297}$$

$$b_i = \int_0^1 \phi_1^{2i-1}\phi_1^{(IV)} dx, \quad i = 1, 2, .., 5, \tag{4.298}$$

$$c_i = \int_0^1 \phi_1^{2i-1}\phi_1'' dx, \quad i = 1, 2, .., 5, \tag{4.299}$$

$$E_1 = (1+\delta)b_1 - 2(4\beta_{Cas} + 2\alpha + \alpha\gamma)a_2, \tag{4.300}$$

$$E_2 = -4(1+\delta)b_2 - \eta c_1 a_0 - 2(4\beta_{Cas} - 4\alpha - 3\alpha\gamma)a_4, \tag{4.301}$$

$$E_3 = 6(1+\delta)b_3 + 4\eta c_2 a_0 - 2(2\alpha + 3\alpha\gamma)a_6, \tag{4.302}$$

$$E_4 = -4(1+\delta)b_4 - 6\eta c_3 a_0 + 2\alpha\gamma a_8, \tag{4.303}$$

$$E_5 = (1+\delta)b_5 + 4\eta c_4 a_0, \tag{4.304}$$

$$E_6 = -\eta c_5 a_0. \tag{4.305}$$

The initial conditions for Eq. (4.295) are considered as zero velocity and displacement magnitude A:

$$\begin{aligned}q(0) &= A,\\ \dot{q}(0) &= 0.\end{aligned} \tag{4.306}$$

Following the energy balance method, the variational principle of Eq. (4.295) is defined as

$$J(q_1) = \int_o^t \left(-\frac{1}{2}\dot{q}_1^2\left(a_2 - 4a_4q_1^2 + 6a_6q_1^4 - 4a_8q_1^6 + a_{10}q_1^8\right) + F(q)\right)dt \tag{4.307}$$

where

$$F(q_1) = \int (E_1q_1 + E_2q_1^3 + E_3q_1^5 + E_4q_1^7 + E_5q_1^9 + E_6q_1^{11})dq_1. \tag{4.308}$$

The Hamiltonian form can be rewritten as

$$H = \frac{1}{2}\dot{q}_1^2\left(a_2 - 4a_4q_1^2 + 6a_6q_1^4 - 4a_8q_1^6 + a_{10}q_1^8\right) + F(q_1) = F(A), \tag{4.309}$$

or

$$\begin{aligned} H &= \frac{1}{2}\dot{q}_1^2\left(a_2 - 4a_4q_1^2 + 6a_6q_1^4 - 4a_8q_1^6 + a_{10}q_1^8\right) \\ &+ \frac{1}{2}E_1q_1^2 + \frac{1}{4}E_2q_1^4 + \frac{1}{6}E_3q_1^6 + \frac{1}{8}E_4q_1^8 + \frac{1}{10}E_5q_1^{10} + \frac{1}{12}E_6q_1^{12} \\ &= \frac{1}{2}E_1A^2 + \frac{1}{4}E_2A^4 + \frac{1}{6}E_3A^6 + \frac{1}{8}E_4A^8 + \frac{1}{10}E_5A^{10} + \frac{1}{12}E_6A^{12}. \end{aligned} \tag{4.310}$$

A trial solution with amplitude A and frequency ω is assumed as

$$q_1(\tau) = A\cos(\omega\tau). \tag{4.311}$$

Substituting the approximate solution into Eq. (4.310) results in

$$\begin{aligned} &\frac{1}{2}(-A\omega\sin(\omega\tau))^2\Big\{a_2 - 4a_4A^2\cos^2(\omega\tau) + 6a_6A^4\cos^4(\omega\tau) \\ &- 4a_8A^6\cos^6(\omega\tau) + a_{10}A^8\cos^8(\omega\tau)\Big\} + \frac{1}{2}E_1A^2(\cos^2(\omega\tau) - 1) \\ &+ \frac{1}{4}E_2A^4(\cos^4(\omega\tau) - 1) + \frac{1}{6}E_3A^6(\cos^6(\omega\tau) - 1) + \frac{1}{8}E_4A^8(\cos^8(\omega\tau) - 1) \\ &+ \frac{1}{10}E_5A^{10}(\cos^{10}(\omega\tau) - 1) + \frac{1}{12}E_6A^{12}(\cos^{12}(\omega\tau) - 1) = 0. \end{aligned} \tag{4.312}$$

Evaluating Eq. (4.267) at $\omega t = \frac{\pi}{4}$ gives

$$\omega = \sqrt{\frac{16E_1 + 12E_2A^2 + \frac{28}{3}E_3A^4 + \frac{15}{2}E_4A^6 + \frac{31}{5}E_5A^8 + \frac{63}{12}E_6A^{10}}{16a_2 - 32a_4A^2 + 24a_6A^4 - 8a_8A^6 + a_{10}A^8}}. \tag{4.313}$$

Substituting Eq. (4.313) into Eq. (4.311), one obtains

$$q_1(\tau) = A\cos\left(\tau\sqrt{\frac{16E_1 + 12E_2A^2 + \frac{28}{3}E_3A^4 + \frac{15}{2}E_4A^6 + \frac{31}{5}E_5A^8 + \frac{63}{12}E_6A^{10}}{16a_2 - 32a_4A^2 + 24a_6A^4 - 8a_8A^6 + a_{10}A^8}}\right). \tag{4.314}$$

Moreover, the nanoresonator deflection is given by

$$\begin{aligned} w(x,\tau) &= A\left[\cosh(\lambda_1x) - \cos(\lambda_1x) - \frac{\cosh(\lambda_1) - \cos(\lambda_1)}{\sinh(\lambda_1) - \sin(\lambda_1)}(\sinh(\lambda_1x) - \sin(\lambda_1x))\right] \\ &.\cos\left(\tau\sqrt{\frac{16E_1 + 12E_2A^2 + \frac{28}{3}E_3A^4 + \frac{15}{2}E_4A^6 + \frac{31}{5}E_5A^8 + \frac{63}{12}E_6A^{10}}{16a_2 - 32a_4A^2 + 24a_6A^4 - 8a_8A^6 + a_{10}A^8}}\right). \end{aligned} \tag{4.315}$$

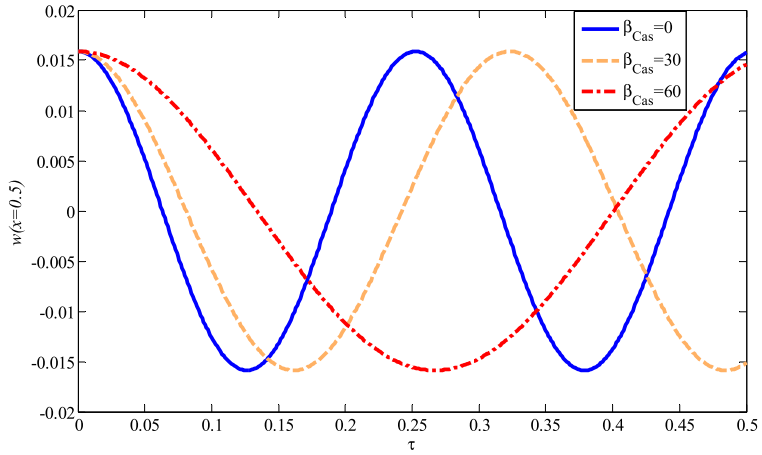

Figure 4.46 Time-dependent deflection of the center point ($w(x = 0.5)$) for different values of the Casimir force parameter.

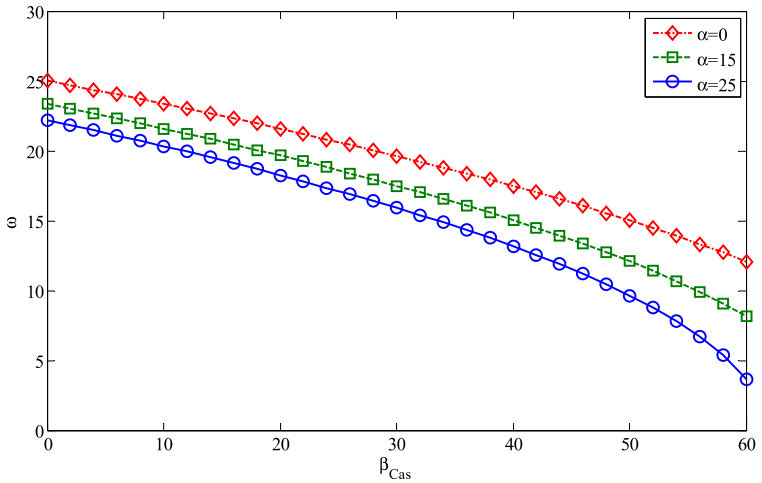

Figure 4.47 Effect of Casimir force parameter on the frequency of a nanoresonator.

Fig. 4.46 demonstrates the time-dependent deflection of the center point ($w(x = 0.5)$) for different values of the Casimir force parameter. This figure demonstrates that the frequencies of the nanoresonator reduce by increasing the Casimir force. This phenomenon has been illustrated more clearly in Fig. 4.47. In this figure, the frequency of the nanoresonator is plotted as a function of the nondimensional Casimir force parameter. The impact of the applied voltage is also investigated in Fig. 4.47. As seen, by increasing the applied voltage, the frequency of the nanoresonator decreases.

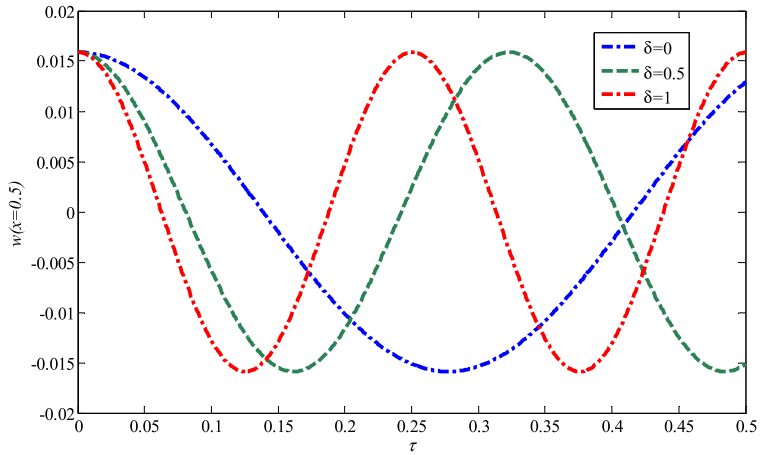

Figure 4.48 Time-dependent deflection of the center point ($w(x = 0.5)$) for different values of the size dependency parameter.

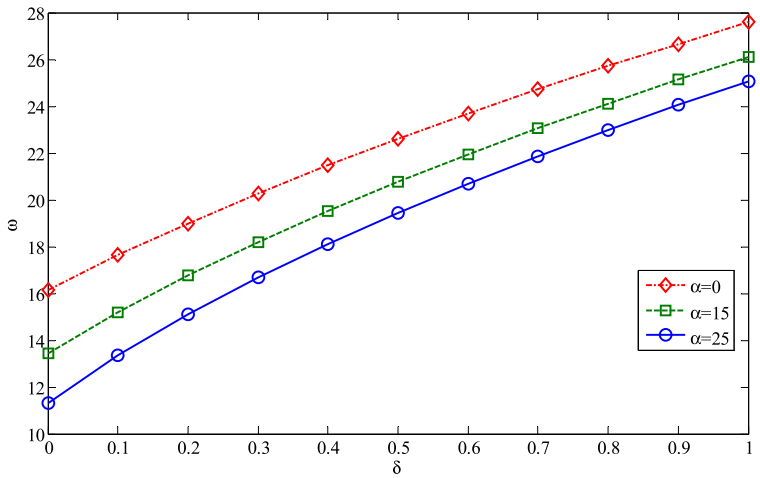

Figure 4.49 Effect of the size dependency parameter on the frequency of a nanoresonator.

Fig. 4.48 demonstrates the time-dependent deflection of the center point ($w(x = 0.5)$) for different values of size dependency parameter (δ). This figure demonstrates that an increase in the size parameter enhances the frequency of the nanoresonator. This phenomenon has been illustrated more clearly in Fig. 4.49. In this figure, the frequency of the nanoresonator is plotted as a function of the dimensionless size parameter. The impact of the applied voltage is also investigated in Fig. 4.47. This figure demonstrates that the size dependency tends to increase the nanoresonator frequency since the

stiffness of the nanoresonator increases as the effect of size dependency energy becomes highlighted.

4.6. Method of multiple scales

In the multiple scales technique, the solution is considered to be a function of multiple independent scales or variables instead of a single variable [86]. This method has been widely applied previously by researchers to predict the nonlinear oscillation of micro/nanoscale structures [87–93].

To illustrate the method of multiple scales, consider the following second-order time-dependent differential equation:

$$\ddot{u} + f(u) = 0 \tag{4.316}$$

where f is a general function. By expanding the function f, Eq. (4.316) is rewritten as

$$\ddot{u} + \sum_{n=1}^{N} \alpha_n u^n = 0 \tag{4.317}$$

where

$$\alpha_n = \frac{1}{n!} f^n(u_0) \tag{4.318}$$

with f^n being the nth order derivative of f with respect to the argument.

Firstly, a new scaled time parameter is introduced as [86]

$$T_n = \varepsilon^n t. \tag{4.319}$$

Therefore, the derivatives with respect to time can be explained as the derivatives with respect to the scaled time parameter (T_n) as follows:

$$\frac{d}{dt} = \frac{dT_0}{dt}\frac{\partial}{\partial T_0} + \frac{dT_1}{dt}\frac{\partial}{\partial T_1} + \cdots = D_0 + \varepsilon D_1 + \cdots, \tag{4.320}$$

$$\frac{d}{dt} = D_0^2 + 2\varepsilon D_0 D_1 + \varepsilon^2 (D_1^2 + 2D_0 D_2) + \cdots. \tag{4.321}$$

The solution of Eq. (4.317) can be defined as

$$u(t, \varepsilon) = \varepsilon u_1(T_0, T_1, T_2, \ldots) + \varepsilon^2 u_2(T_0, T_1, T_2, \ldots) + \varepsilon^3 u_3(T_0, T_1, T_2, \ldots) + \ldots. \tag{4.322}$$

It should be noted that the number of needed scaled time parameters depends on the order of the expansion. By substituting Eqs. (4.320)–(4.322) in Eq. (4.317) and equating the coefficients of like powers of ε to zero, a system of differential equations is

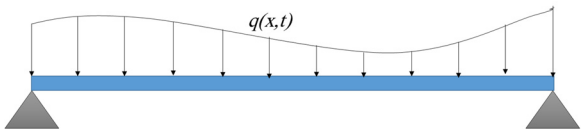

Figure 4.50 Doubly-supported micro/nanobeam.

obtained. The final solution can be achieved from the obtained system of differential equations. Subsequently, the method of multiple scales is employed to investigate the size-dependent free-vibration of a microbeam based on the strain gradient theory.

4.6.1 Free-vibration of a microbeam based on the strain gradient elasticity

In Section 4.2.2.1, the strain gradient elasticity was incorporated with the Gurtin–Murdoch elasticity to investigate the dynamic behavior of a nanowire-based sensor. In his section, the free-vibration of a doubly-supported nanobeam is examined based on the strain gradient theory.

Fig. 4.50 shows a schematic view of a doubly-supported micro/nanobeam with an arbitrary external force. The governing equation of the micro/nanobeam can be extracted by using Hamilton's principle. To this end, the strain energy of the system, the kinetic energy, and the work done by the external forces should be determined. The displacement field of an Euler–Bernoulli beam by considering both longitudinal and lateral deflection can be expressed as [3]:

$$\begin{aligned} u_X(X,Y,Z,t) &= U(X,t) - Z\frac{\partial W(X,t)}{\partial X}, \\ u_Y(X,Y,Z,t) &= 0, \\ u_Z(X,Y,Z,t) &= W(X,t). \end{aligned} \tag{4.323}$$

The strain energy based on the strain gradient theory can be explained as

$$U_{SGT} = \frac{1}{2}\int_{\vartheta}\left(\sigma_{ij}\varepsilon_{ij} + p_i\gamma_i + \tau^{(1)}_{ijk}\eta^{(1)}_{ijk} + m^s_{ij}\chi^s_{ij}\right)d\vartheta. \tag{4.324}$$

Eqs. (4.77)–(4.87) identify the parameters of the above equation. By using Eq. (4.323) in Eqs. (4.77)–(4.87), the components of Eq. (4.324) are obtained as:

$$\begin{aligned} &\varepsilon_{XX} = \frac{\partial U(X,t)}{\partial X} + \frac{1}{2}\left(\frac{\partial W(X,t)}{\partial X}\right)^2 - Z\frac{\partial^2 W(X,t)}{\partial X^2}, \\ &\varepsilon_{YY} = \varepsilon_{ZZ} = \varepsilon_{XY} = \varepsilon_{YZ} = \varepsilon_{ZX} = 0, \end{aligned} \tag{4.325}$$

$$\sigma_{XX} = E\left[\frac{\partial U(X,t)}{\partial X} + \frac{1}{2}\left(\frac{\partial W(X,t)}{\partial X}\right)^2 - Z\frac{\partial^2 W(X,t)}{\partial X^2}\right], \tag{4.326}$$

$$\sigma_{ZZ} = \sigma_{YY} = \sigma_{XY} = \sigma_{YZ} = \sigma_{ZX} = 0,$$

$$\gamma_X = \frac{\partial^2 U(X,t)}{\partial X^2} - Z\frac{\partial^3 W(X,t)}{\partial X^3} + \frac{\partial W(X,t)}{\partial X}\frac{\partial^2 W(X,t)}{\partial X^2}, \tag{4.327}$$

$$\gamma_Z = -\frac{\partial^2 W(X,t)}{\partial X^2}, \quad \gamma_Y = 0,$$

$$p_X = 2\mu l_0^2\left(\frac{\partial^2 U(X,t)}{\partial X^2} - Z\frac{\partial^3 W(X,t)}{\partial X^3} + \frac{\partial W(X,t)}{\partial X}\frac{\partial^2 W(X,t)}{\partial X^2}\right), \tag{4.328}$$

$$p_Z = -2\mu l_0^2\frac{\partial^2 W(X,t)}{\partial X^2}, \quad p_Y = 0,$$

$$\eta^{(1)}_{XXX} = \frac{2}{5}\left(\frac{\partial^2 U(X,t)}{\partial X^2} - Z\frac{\partial^3 W(X,t)}{\partial X^3} + \frac{\partial W(X,t)}{\partial X}\frac{\partial^2 W(X,t)}{\partial X^2}\right),$$

$$\eta^{(1)}_{XXZ} = \eta^{(1)}_{ZXX} = \eta^{(1)}_{XZX} = -\frac{4}{15}\frac{\partial^2 W(X,t)}{\partial X^2},$$

$$\eta^{(1)}_{XYY} = \eta^{(1)}_{XZZ} = \eta^{(1)}_{YXY} = \frac{1}{5}\left(-\frac{\partial^2 U(X,t)}{\partial X^2} + Z\frac{\partial^3 W(X,t)}{\partial X^3} - \frac{\partial W(X,t)}{\partial X}\frac{\partial^2 W(X,t)}{\partial X^2}\right),$$

$$\eta^{(1)}_{YYX} = \eta^{(1)}_{ZXZ} = \eta^{(1)}_{ZX} = \frac{1}{5}\left(-\frac{\partial^2 U(X,t)}{\partial X^2} + Z\frac{\partial^3 W(X,t)}{\partial X^3} - \frac{\partial W(X,t)}{\partial X}\frac{\partial^2 W(X,t)}{\partial X^2}\right),$$

$$\eta^{(1)}_{YYZ} = \eta^{(1)}_{YZY} = \eta^{(1)}_{ZYY} = \frac{1}{15}\frac{\partial^2 W(X,t)}{\partial X^2}, \quad \eta^{(1)}_{ZZZ} = \frac{1}{5}\frac{\partial^2 W(X,t)}{\partial X^2},$$

$$\eta^{(1)}_{XXY} = \eta^{(1)}_{XYX} = \eta^{(1)}_{XYZ} = \eta^{(1)}_{XZY} = \eta^{(1)}_{YXX} = \eta^{(1)}_{YXZ} = 0,$$

$$\eta^{(1)}_{YYY} = \eta^{(1)}_{YZX} = \eta^{(1)}_{YZZ} = \eta^{(1)}_{ZXY} = \eta^{(1)}_{ZYX} = \eta^{(1)}_{ZYZ} = \eta^{(1)}_{ZZY} = 0, \tag{4.329}$$

$$\tau^{(1)}_{XXX} = \frac{4}{5}\mu l_1^2\left(\frac{\partial^2 U(X,t)}{\partial X^2} - Z\frac{\partial^3 W(X,t)}{\partial X^3} + \frac{\partial W(X,t)}{\partial X}\frac{\partial^2 W(X,t)}{\partial X^2}\right),$$

$$\tau^{(1)}_{XXZ} = \tau^{(1)}_{ZXX} = \tau^{(1)}_{XZX} = -\frac{8}{15}\mu l_1^2\frac{\partial^2 W(X,t)}{\partial X^2},$$

$$\tau^{(1)}_{XYY} = \tau^{(1)}_{XZZ} = \tau^{(1)}_{YXY} = \frac{2}{5}\mu l_1^2\left(-\frac{\partial^2 U(X,t)}{\partial X^2} + Z\frac{\partial^3 W(X,t)}{\partial X^3} - \frac{\partial W(X,t)}{\partial X}\frac{\partial^2 W(X,t)}{\partial X^2}\right),$$

$$\tau^{(1)}_{YYX} = \tau^{(1)}_{ZXZ} = \tau^{(1)}_{ZZX} = \frac{2}{5}\mu l_1^2\left(-\frac{\partial^2 U(X,t)}{\partial X^2} + Z\frac{\partial^3 W(X,t)}{\partial X^3} - \frac{\partial W(X,t)}{\partial X}\frac{\partial^2 W(X,t)}{\partial X^2}\right),$$

$$\tau^{(1)}_{YYZ} = \tau^{(1)}_{YZY} = \tau^{(1)}_{ZYY} = \frac{2}{15}\mu l_1^2\frac{\partial^2 W(X,t)}{\partial X^2}, \quad \tau^{(1)}_{ZZZ} = \frac{2}{5}\mu l_1^2\frac{\partial^2 W(X,t)}{\partial X^2},$$

$$\tau^{(1)}_{XXY} = \tau^{(1)}_{XYX} = \tau^{(1)}_{XYZ} = \tau^{(1)}_{XZY} = \tau^{(1)}_{YXX} = \tau^{(1)}_{YXZ} = 0,$$

$$\tau^{(1)}_{YYY} = \tau^{(1)}_{YZX} = \tau^{(1)}_{YZZ} = \tau^{(1)}_{ZXY} = \tau^{(1)}_{ZYX} = \tau^{(1)}_{ZYZ} = \tau^{(1)}_{ZZY} = 0, \tag{4.330}$$

$$\mu_{XY} = -4\varsigma \frac{\partial^2 W(X,t)}{\partial X^2}, \quad \mu_{YX} = -4\varsigma' \frac{\partial^2 W(X,t)}{\partial X^2}, \tag{4.331}$$
$$\mu_{XX} = \mu_{YY} = \mu_{ZZ} = \mu_{YZ} = \mu_{ZY} = \mu_{ZX} = \mu_{XZ} = 0,$$

$$m^s_{XY} = m^s_{YX} = -\mu l_2^2 \frac{\partial^2 W(X,t)}{\partial X^2}, \tag{4.332}$$
$$m^s_{XX} = m^s_{YY} = m^s_{ZZ} = m^s_{YZ} = m^s_{ZY} = m^s_{ZX} = m^s_{XZ} = 0,$$

$$\chi^s_{XY} = \chi^s_{YX} = -\frac{1}{2} \frac{\partial^2 W(X,t)}{\partial X^2}, \tag{4.333}$$
$$\chi^s_{XX} = \chi^s_{YY} = \chi^s_{ZZ} = \chi^s_{YZ} = \chi^s_{ZY} = \chi^s_{ZX} = \chi^s_{XZ} = 0.$$

By substituting Eqs. (4.325)–(4.333) into Eq. (4.324), the strain energy of the system in the context of the strain gradient elasticity is given by:

$$U_{SGT} = \frac{1}{2} \int_0^L \int_A \left\{ \begin{array}{l} E\left[\frac{\partial U}{\partial X} + \frac{1}{2}\left(\frac{\partial W}{\partial X}\right)^2 - Z\frac{\partial^2 W}{\partial X^2}\right]^2 \\ + 2\mu l_0^2 \left(\frac{\partial^2 U}{\partial X^2} - Z\frac{\partial^3 W}{\partial X^3} + \frac{\partial W}{\partial X}\frac{\partial^2 W}{\partial X^2}\right)^2 \\ + \mu l_2^2 \left(\frac{\partial^2 W}{\partial X^2}\right)^2 + \frac{32}{75}\mu l_1^2 \left(\frac{\partial^2 W}{\partial X^2}\right)^2 \\ + \frac{2}{75}\mu l_1^2 \left(\frac{\partial^2 W}{\partial X^2}\right)^2 + 2\mu l_0^2 \left(\frac{\partial^2 W}{\partial X^2}\right)^2 + \frac{2}{25}\mu l_1^2 \left(\frac{\partial^2 W}{\partial X^2}\right)^2 \\ + \frac{8}{25}\mu l_1^2 \left(\frac{\partial^2 U}{\partial X^2} - Z\frac{\partial^3 W}{\partial X^3} + \frac{\partial W}{\partial X}\frac{\partial^2 W}{\partial X^2}\right)^2 \\ + \frac{12}{25}\mu l_1^2 \left(-\frac{\partial^2 U}{\partial X^2} + Z\frac{\partial^3 W}{\partial X^3} - \frac{\partial W}{\partial X}\frac{\partial^2 W}{\partial X^2}\right)^2 \end{array} \right\} dA dX. \tag{4.334}$$

By integrating over the cross-section area, we have

$$U_{SGT} = \frac{1}{2} \int_0^L \left\{ \begin{array}{l} \left(EI + 2\mu A l_0^2 + \frac{8}{15}\mu A l_1^2 + \mu A l_2^2\right)\left(\frac{\partial^2 W}{\partial X^2}\right)^2 \\ + I\left(2\mu l_0^2 + \frac{4}{5}\mu l_1^2\right)\left(\frac{\partial^3 W}{\partial X^3}\right)^2 \\ EA\left(\frac{\partial u}{\partial X} + \frac{1}{2}\left(\frac{\partial W}{\partial X}\right)^2\right)^2 \\ + \mu A\left(2l_0^2 + \frac{4}{5}l_1^2\right)\left(\frac{\partial^2 u}{\partial X^2} + \frac{\partial W}{\partial X}\frac{\partial^2 W}{\partial X^2}\right)^2 \end{array} \right\} dX. \tag{4.335}$$

The beam kinetic energy can be defined as

$$T = \frac{1}{2}\int_o^L \int_A \rho \left[\left(\frac{\partial W}{\partial t} \right)^2 + \left(\frac{\partial U}{\partial t} - Z\frac{\partial^2 W}{\partial t \partial X} \right)^2 \right] dA dX \tag{4.336}$$

where ρ is the beam density. By integrating over the cross-section area, we have

$$T = \frac{1}{2}\int_0^L \left[\rho A \left(\frac{\partial U}{\partial t} \right)^2 + \rho A (W)^2 + \rho I \left(\frac{\partial^2 W}{\partial t \partial x} \right)^2 \right] dX. \tag{4.337}$$

Finally, the work of the external forces can be calculated using the following equation:

$$W_{ext} = \int_0^L \int_0^W q(X,t) dW dX. \tag{4.338}$$

Hamilton's principle can be employed to extract the governing equation of the system:

$$\int_{t_1}^{t_2} (\delta T - \delta U_{SGT} + \delta W_{ext})\, dt = 0. \tag{4.339}$$

By using Eqs. (4.335), (4.337), and (4.338) in the above relation, one obtains

$$\begin{aligned}
&-\int_{t_1}^{t_2}\int_0^L \left[\begin{array}{l} \frac{\partial}{\partial X}\left[EA\left(\frac{\partial U}{\partial X} + \frac{1}{2}\left(\frac{\partial W}{\partial X} \right)^2 \right) \right. \\ \left. -\mu A\left(2l_0^2 + \frac{4}{5}l_1^2 \right) \frac{\partial^2}{\partial X^2}\left(\frac{\partial U}{\partial X} + \frac{1}{2}\left(\frac{\partial W}{\partial X} \right)^2 \right) \right] - \rho A \frac{\partial^2 U}{\partial t^2} \end{array} \right] \delta U dx dt \\
&+\int_{t_1}^{t_2}\int_0^L \left[\begin{array}{l} \rho A\frac{\partial^2 W}{\partial t^2} - \rho I \frac{\partial^4 W}{\partial t^2 \partial X^2} + \left(EI + \mu A\left(2l_0^2 + \frac{8}{15}l_1^2 + l_2^2 \right) \right) \frac{\partial^4 W}{\partial X^4} \\ -\mu I\left(2l_0^2 + \frac{4}{5}l_1^2 \right) \frac{\partial^6 W}{\partial X^6} - q(X,t) - \frac{\partial}{\partial X}\left\{ \left[EA\left(\frac{\partial U}{\partial X} + \frac{1}{2}\left(\frac{\partial W}{\partial X} \right)^2 \right) \right. \right. \\ \left. \left. -\mu A\left(2l_0^2 + \frac{4}{5}l_1^2 \right) \frac{\partial^2}{\partial X^2}\left(\frac{\partial U}{\partial X} + \frac{1}{2}\left(\frac{\partial W}{\partial X} \right)^2 \right) \right] \frac{\partial W}{\partial X} \right\} \end{array} \right] \delta W dx dt \\
&+\int_{t_1}^{t_2} \left[EA\left(\frac{\partial U}{\partial X} + \frac{1}{2}\left(\frac{\partial W}{\partial X} \right)^2 \right) \delta U \right]_0^L dt + \int_{t_1}^{t_2} \left[\left(\mu I\left(2l_0^2 + \frac{4}{5}l_1^2 \right) \frac{\partial^3 W}{\partial X^3} \right) \delta\left(\frac{\partial^2 W}{\partial X^2} \right) \right]_0^L dt \\
&+\int_{t_1}^{t_2} \left[\left(\begin{array}{l} -\left(EI + \mu A\left(2l_0^2 + \frac{8}{15}l_1^2 + l_2^2 \right) \right) \frac{\partial^3 W}{\partial X^3} \\ +EA\left(\frac{\partial U}{\partial X} + \frac{1}{2}\left(\frac{\partial W}{\partial X} \right)^2 \right) \frac{\partial W}{\partial X} + \mu I\left(2l_0^2 + \frac{4}{5}l_1^2 \right) \frac{\partial^5 W}{\partial X^5} \end{array} \right) \delta W \right]_0^L dt
\end{aligned}$$

$$+\int_{t_1}^{t_2}\left[\left(\begin{array}{l}\left(EI+\mu A\left(2l_0^2+\dfrac{8}{15}l_1^2+l_2^2\right)\dfrac{\partial^2 W}{\partial X^2}\right.\\ \left.+\rho I\dfrac{\partial^3 W}{\partial t^2\partial X}-\mu I\left(2l_0^2+\dfrac{4}{5}l_1^2\right)\dfrac{\partial^4 W}{\partial X^4}\right)\end{array}\right)\delta\left(\frac{\partial W}{\partial X}\right)\right]_0^L dt$$
$$-\int_0^L\left[\rho A\frac{\partial W}{\partial t}\delta W\right]_{t_1}^{t_2}dX-\int_0^L\left[\rho A\frac{\partial U}{\partial t}\delta U\right]_{t_1}^{t_2}dX-\int_0^L\left[\rho I\frac{\partial^2 W}{\partial t\partial X}\delta\left(\frac{\partial W}{\partial X}\right)\right]_{t_1}^{t_2}dX=0. \tag{4.340}$$

The above variational equation results in the following differential equations:

$$\begin{aligned}&\frac{\partial}{\partial X}\left(EA\left(\frac{\partial U}{\partial X}+\frac{1}{2}\left(\frac{\partial W}{\partial X}\right)^2\right)\right.\\&\left.-\mu A\left(2l_0^2+\frac{4}{5}l_1^2\right)\frac{\partial^2}{\partial X^2}\left(\frac{\partial U}{\partial X}+\frac{1}{2}\left(\frac{\partial W}{\partial X}\right)^2\right)\right)=\rho A\frac{\partial^2 U}{\partial t^2},\end{aligned} \tag{4.341}$$

$$\begin{aligned}&-\frac{\partial}{\partial X}\left\{\left[EA\left(\frac{\partial U}{\partial X}+\frac{1}{2}\left(\frac{\partial W}{\partial X}\right)^2\right)-\mu A\left(2l_0^2+\frac{4}{5}l_1^2\right)\frac{\partial^2}{\partial X^2}\left(\frac{\partial U}{\partial X}+\frac{1}{2}\left(\frac{\partial W}{\partial X}\right)^2\right)\right]\frac{\partial W}{\partial X}\right\}\\&+\rho A\frac{\partial^2 W}{\partial t^2}-\rho I\frac{\partial^4 W}{\partial t^2\partial X^2}+\left(EI+\mu A\left(2l_0^2+\frac{8}{15}l_1^2+l_2^2\right)\frac{\partial^4 W}{\partial X^4}\right.\\&\left.-\mu I\left(2l_0^2+\frac{4}{5}l_1^2\right)\frac{\partial^6 W}{\partial X^6}=q(X,t).\right.\end{aligned} \tag{4.342}$$

Moreover, Eq. (4.123) results in the following boundary conditions:

$$\left.\begin{aligned}&EA\left(\frac{\partial U}{\partial X}+\frac{1}{2}\left(\frac{\partial W}{\partial X}\right)^2\right)\\&-\mu A\left(2l_0^2+\frac{4}{5}l_1^2\right)\frac{\partial^2}{\partial X^2}\left(\frac{\partial U}{\partial X}+\frac{1}{2}\left(\frac{\partial W}{\partial X}\right)^2\right)\end{aligned}\right|_{X=0,L}=0\quad\text{or}\quad\delta U|_{X=0,L}=0, \tag{4.343}$$

$$\left.\begin{aligned}&-\left(EI+\mu A\left(2l_0^2+\frac{8}{15}l_1^2+l_2^2\right)\right)\frac{\partial^3 W}{\partial X^3}\\&+EA\left(\frac{\partial U}{\partial X}+\frac{1}{2}\left(\frac{\partial W}{\partial X}\right)^2\right)\frac{\partial W}{\partial X}+\mu I\left(2l_0^2+\frac{4}{5}l_1^2\right)\frac{\partial^5 W}{\partial X^5}\end{aligned}\right|_{X=0,L}=0\quad\text{or}\quad\delta W|_{X=0,L}=0, \tag{4.344}$$

$$\left.\begin{aligned}&\left(EI+\mu A\left(2l_0^2+\frac{8}{15}l_1^2+l_2^2\right)\right)\frac{\partial^2 W}{\partial X^2}\\&+\rho I\frac{\partial^3 W}{\partial t^2\partial X}-\mu I\left(2l_0^2+\frac{4}{5}l_1^2\right)\frac{\partial^4 W}{\partial X^4}\end{aligned}\right|_{X=0,L}=0\quad\text{or}\quad\delta\left(\frac{\partial W}{\partial X}\right)\Big|_{X=0,L}=0, \tag{4.345}$$

$$\mu I\left(2l_0^2+\frac{4}{5}l_1^2\right)\frac{\partial^3 W}{\partial X^3}\bigg|_{X=0,L}=0 \quad \text{or} \quad \delta\left(\frac{\partial^2 W}{\partial X^2}\right)\bigg|_{X=0,L}=0. \tag{4.346}$$

For a simply-supported beam, the boundary conditions are given by:

$$U(0)=U(L)=0, \tag{4.347}$$

$$W(0)=W(L)=0, \tag{4.348}$$

$$\begin{aligned}&\left(EI+\mu A\left(2l_0^2+\frac{8}{15}l_1^2+l_2^2\right)\right)\frac{\partial^2 W(0)}{\partial X^2}-\mu I\left(2l_0^2+\frac{4}{5}l_1^2\right)\frac{\partial^4 W(0)}{\partial X^4}=0\\&\left(EI+\mu A\left(2l_0^2+\frac{8}{15}l_1^2+l_2^2\right)\right)\frac{\partial^2 W(L)}{\partial X^2}-\mu I\left(2l_0^2+\frac{4}{5}l_1^2\right)\frac{\partial^4 W(L)}{\partial X^4}=0,\end{aligned} \tag{4.349}$$

$$\frac{\partial^2 W}{\partial X^2}(0)=\frac{\partial^2 W}{\partial X^2}(L)=0. \tag{4.350}$$

The longitudinal kinetic energy is small in comparison to the lateral kinetic energy. Hence, by neglecting the longitudinal kinetic energy, Eq. (4.351) can be rewritten as

$$\frac{\partial}{\partial X}\left(EA\left(\frac{\partial U}{\partial X}+\frac{1}{2}\left(\frac{\partial W}{\partial X}\right)^2\right)-\mu A\left(2l_0^2+\frac{4}{5}l_1^2\right)\frac{\partial^2}{\partial X^2}\left(\frac{\partial U}{\partial X}+\frac{1}{2}\left(\frac{\partial W}{\partial X}\right)^2\right)\right)=0. \tag{4.351}$$

The above equation implies that

$$EA\left(\frac{\partial U}{\partial X}+\frac{1}{2}\left(\frac{\partial W}{\partial X}\right)^2\right)-\mu A\left(2l_0^2+\frac{4}{5}l_1^2\right)\frac{\partial^2}{\partial X^2}\left(\frac{\partial U}{\partial X}+\frac{1}{2}\left(\frac{\partial W}{\partial X}\right)^2\right)=C, \tag{4.352}$$

in which C is a constant. By integrating the above equation and employing the boundary conditions of a simply-supported beam, one obtains [89]

$$C=\frac{EA}{2L}\int_0^L\left(\frac{\partial W}{\partial X}\right)^2 dX. \tag{4.353}$$

By substituting Eq. (4.353) into Eq. (4.342), the constitutive equation of a micro/nanobeam reduces from a system of two partial differential equations to the following partial differential equation:

$$\rho A\frac{\partial^2 W}{\partial t^2}+\psi_1\frac{\partial^4 W}{\partial X^4}-\psi_2\frac{\partial^6 W}{\partial X^6}-\left(\frac{EA}{2L}\int_0^L\left(\frac{\partial W}{\partial X}\right)^2 dX\right)\frac{\partial^2 W}{\partial X^2}=q(X,t) \tag{4.354}$$

where

$$\begin{aligned}\psi_1 &= \left(EI + \mu A\left(2l_0^2 + \frac{8}{15}l_1^2 + l_2^2\right),\right.\\ \psi_2 &= \mu I\left(2l_0^2 + \frac{4}{5}l_1^2\right).\end{aligned} \tag{4.355}$$

It should be noted that in the above simplification the effect of rotating inertia ($\rho I \frac{\partial^4 W}{\partial t^2 \partial X^2}$) has been neglected.

For free-vibration analysis of a micro/nanobeam is it assumed that the external load is absent (i.e., $q(x, t) = 0$). The dimensionless parameter of lateral deflection is defined by dividing the deflection (W) by the beam thickness (h). Also, the dimensionless parameter of the location along the beam length is defined by dividing the longitudinal position (X) by the beam length (L). Therefore, by multiplying both sides of Eq. (4.354) by $\frac{L^4}{D_1 h}$, the dimensionless nonlinear governing equation for free-vibration of a micro/nanobeam in the context of strain gradient theory is simplified as

$$\frac{\partial^2 w}{\partial \tau^2} + \frac{\partial^4 w}{\partial x^4} - \xi^2 \frac{\partial^6 w}{\partial x^6} - \left(\eta \int_0^1 \left(\frac{\partial w}{\partial x}\right)^2 dx\right)\frac{\partial^2 w}{\partial x^2} = 0 \tag{4.356}$$

where

$$x = \frac{X}{L}, \tag{4.357}$$

$$w = \frac{W}{h}, \tag{4.358}$$

$$\eta = \frac{EAh^2}{2\psi_1}, \tag{4.359}$$

$$\tau = \sqrt{\frac{\rho A L^2}{\psi_1}}\, t, \tag{4.360}$$

$$\xi^2 = \frac{\psi_2}{\psi_1 L^2}. \tag{4.361}$$

In the reduced-order method, the displacement is divided into the time-dependent and position-dependent parts:

$$w(x, \tau) = q(\tau)\,\phi(x) \tag{4.362}$$

where is the mode shape of a doubly supported beam [91] is

$$\phi(x) = \sin(n\pi x). \tag{4.363}$$

By using Eqs. (4.362) and (4.363) in Eq. (4.356), one obtains

$$\ddot{q}(\tau) + \omega_0^2 \left(q(\tau) + \lambda q^3(\tau)\right) = 0 \tag{4.364}$$

where

$$\omega_0^2 = (n\pi)^4 + \xi^2 (n\pi)^6, \tag{4.365}$$

$$\lambda = \frac{\eta (n\pi)^4}{2\omega_0^2}. \tag{4.366}$$

Eq. (4.364) is the standard Duffing equation. To investigate the natural frequency of the micro/nanobeam in the context of the strain gradient theory, the multiple scales method can be employed. To this end, a new scaled time parameter is introduced as

$$T_n = \varepsilon^n \tau. \tag{4.367}$$

The first and second derivatives with respect to the dimensionless parameter of time (i.e., τ) can be represented as the derivatives with respect to the scaled time parameter (T_n) as follows:

$$\frac{d}{dt} = \frac{dT_0}{dt}\frac{\partial}{\partial T_0} + \frac{dT_1}{dt}\frac{\partial}{\partial T_1} + \cdots = D_0 + \varepsilon D_1 + \cdots, \tag{4.368}$$

$$\frac{d}{dt} = D_0^2 + 2\varepsilon D_0 D_1 + \varepsilon^2 (D_1^2 + 2D_0 D_2) + \cdots \tag{4.369}$$

where

$$D_k = \frac{\partial}{\partial T_k}. \tag{4.370}$$

The solution of Eq. (4.346) can be defined as

$$q(t, \varepsilon) = \varepsilon q_1(T_0, T_1, T_2, ...) + \varepsilon^2 q_2(T_0, T_1, T_2, ...) + \varepsilon^3 q_3(T_0, T_1, T_2, ...) .... \tag{4.371}$$

It should be noted that the number of needed scaled time parameters depends on the order of expansion. By substituting Eqs. (4.368)–(4.371) into Eq. (4.364) and equating the coefficients of like powers of ε to zero, one obtains:

$$\text{order } \varepsilon: \quad \left(D_0^2 + \omega_0^2\right) q_1 = 0, \tag{4.372}$$

$$\text{order } \varepsilon^2: \quad 2D_0 D_1 q_1 + \left(D_0^2 + \omega_0^2\right) q_2 = 0, \tag{4.373}$$

$$\text{order } \varepsilon^3: \quad (D_1^2 + 2D_0 D_2) q_1 + 2D_0 D_1 q_2 + \left(D_0^2 + \omega_0^2\right) q_3 + \lambda \omega_0^2 q_1^3 = 0. \tag{4.374}$$

The solution of Eq. (4.372) is given by

$$q_1 = A(T_1, T_2) \exp(i\omega_0 T_0) + \bar{A} \exp(-i\omega_0 T_0) \tag{4.375}$$

where $i^2 = -1$. Also, A is an unknown complex function and $\bar{A}$ is the complex conjugate of A. Using Eq. (4.375) in Eq. (4.373) yields

$$D_0^2 q_2 + \omega_0^2 q_2 = -2i\omega_0 D_1 A \exp(i\omega_0 T_0) + cc \tag{4.376}$$

where cc denotes the "complex conjugate." Excluding the secular terms in Eq. (4.376) results in

$$D_1 A = 0. \tag{4.377}$$

Therefore the solution of (4.376) is zero:

$$q_2 = 0. \tag{4.378}$$

By using Eqs. (4.375) and (4.378), Eq. (4.374) is rewritten as

$$\left(D_0^2 + \omega_0^2\right) q_3 = -\left[2i\omega_0 D_2 A + 3\lambda\omega_0^2 A^2 \bar{A}\right] \exp(i\omega_0 T_0) - \lambda\omega_0^2 A^3 \exp(3i\omega_0 T_0) + cc. \tag{4.379}$$

Excluding the secular terms in Eq. (4.379) results in

$$2i\omega_0 D_2 A + 3\lambda\omega_0^2 A^2 \bar{A} = 0. \tag{4.380}$$

Parameter A can be expressed in polar form as

$$A = \frac{1}{2} a \exp(i\beta) \tag{4.381}$$

were a and β are real functions of T_2. Replacing Eq. (4.381) in Eq. (4.380) and separating the imaginary and real parts of result, one obtains:

$$wa' = 0, \tag{4.382}$$

$$\omega_0 a\beta' - \frac{3}{8}\lambda\omega_0^2 a^3 = 0 \tag{4.383}$$

where primes denote the derivatives with respect to T_2. Eq. (4.382) implies that a is a constant. Therefore, the solution of Eq. (4.383) is given by

$$\beta = \frac{3}{8}\lambda\omega_0 a^2 T_2 + \beta_0. \tag{4.384}$$

Therefore, Eq. (4.382) can be rewritten as

$$A = \frac{1}{2} a \exp\left(\frac{3}{8}\lambda\omega_0 a^2 \varepsilon^2 ti + \beta_0 i\right). \tag{4.385}$$

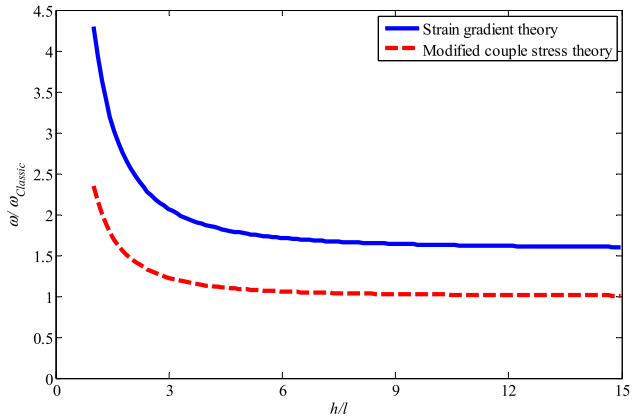

Figure 4.51 The frequency of a doubly supported microbeam.

Finally, by using Eqs. (4.376), (4.378), and (4.385), the solution of Eqs. (4.364) is obtained as

$$q = \varepsilon a \cos(\omega t + \beta_0) + O(\varepsilon^3) \tag{4.386}$$

where the frequency of the doubly-supported micro/nanobeam is given by

$$\omega = \omega_0 \left[1 + \frac{3}{8}\lambda \varepsilon^2 a^2\right] + O(\varepsilon^3). \tag{4.387}$$

The initial conditions of the doubly-supported mico/nanobeam can be expressed as:

$$\begin{aligned} q(0) &= w\left(x = \frac{1}{2}\right) = w_{\max}, \\ \dot{q}(0) &= 0. \end{aligned} \tag{4.388}$$

Applying the initial conditions results in:

$$\begin{aligned} \beta_0 &= 0, \\ \varepsilon a &= w_{\max}. \end{aligned} \tag{4.389}$$

It should be noted that, by setting $l_0 = 0$, $l_1 = 0$, and $l_2 = l$, the frequency of the micro/nanobeam in the context of the modified couple stress theory is obtained. Also, by neglecting all length scale parameters, the classical frequencies can be achieved. The frequencies of the micro/nanobeam as a function of length scale parameter-to-the beam thickness ratio is plotted in Fig. 4.51. In this figure, all length scale parameters are equally assumed to be l. Fig. 4.51 demonstrates that by reducing the length scale parameter, the

frequency of the beam increases. In other words, the size dependency tends to increase the beam frequencies since the stiffness of the micro/nanobeam increases as the effect of size dependency becomes highlighted. While for higher values of h/l (i.e., thick beam) the frequencies based on the modified couple stress theory converge to the classical frequencies, the strain gradient theory implies frequencies higher than the classical value for substantial values of h/l.

4.7. Conclusion

The time-dependent performance of MEMS and MEMS is crucial when the variation rate of the applied DC voltage is significant, or the actuation voltage is AC. In this chapter, six mathematical methods for solving the partial time-dependent nonlinear differential equations of micro- and nanostructures were explained. The proposed methods were employed for investigating the dynamic performance of several micro- and nanoscale structures. Similar to static analysis, the application procedure of the mathematical methods was explained through examples. Moreover, we describe the nanostructure simulation procedure, incorporating the micro- and nanoscale phenomena techniques, as well as the impact of the physical phenomena on the behavior of the ultrasmall structures.

References

[1] M.E. Gurtin, A. Ian Murdoch, A continuum theory of elastic material surfaces, Archive for Rational Mechanics and Analysis 57 (4) (1975) 291–323.
[2] M.E. Gurtin, A.I. Murdoch, Surface stress in solids, International Journal of Solids and Structures 14 (6) (1978) 431–440.
[3] C.L. Dym, I.H. Shames, Solid Mechanics: A Variational Approach, augmented edition, Springer, New York, USA, 2013.
[4] F. Yang, et al., Couple stress based strain gradient theory for elasticity, International Journal of Solids and Structures 39 (10) (2002) 2731–2743.
[5] P. Lu, et al., Thin plate theory including surface effects, International Journal of Solids and Structures 43 (16) (2006) 4631–4647.
[6] H.B. Palmer, The capacitance of a parallel-plate capacitor by the Schwartz–Christoffel transformation, Electrical Engineering 56 (3) (1937) 363–368.
[7] N. Van Der Meijs, J. Fokkema, VLSI circuit reconstruction from mask topology, Integration 2 (2) (1984) 85–119.
[8] H. Nishiyama, M. Nakamura, Capacitance of a strip capacitor, IEEE Transactions on Components, Hybrids, and Manufacturing Technology 13 (2) (1990) 417–423.
[9] R.C. Batra, M. Porfiri, D. Spinello, Electromechanical model of electrically actuated narrow microbeams, Journal of Microelectromechanical Systems 15 (5) (2006) 1175–1189.
[10] Y.-C. Hu, C.-S. Wei, An analytical model considering the fringing fields for calculating the pull-in voltage of micro curled cantilever beams, Journal of Micromechanics and Microengineering 17 (1) (2006) 61.
[11] H. Gies, K. Klingmüller, Casimir edge effects, Physical Review Letters 97 (22) (2006) 220405.

[12] T. Veijola, et al., Equivalent-circuit model of the squeezed gas film in a silicon accelerometer, Sensors and Actuators. A, Physical 48 (3) (1995) 239–248.
[13] H. Sadeghian, et al., Characterizing size-dependent effective elastic modulus of silicon nanocantilevers using electrostatic pull-in instability, Applied Physics Letters 94 (22) (2009) 221903.
[14] Y. Fu, J. Zhang, Size-dependent pull-in phenomena in electrically actuated nanobeams incorporating surface energies, Applied Mathematical Modelling 35 (2) (2011) 941–951.
[15] A. Bhushan, M. Inamdar, D. Pawaskar, Investigation of the internal stress effects on static and dynamic characteristics of an electrostatically actuated beam for MEMS and NEMS application, Microsystem Technologies 17 (12) (2011) 1779–1789.
[16] L. Lin, R.T. Howe, A.P. Pisano, Microelectromechanical filters for signal processing, Journal of Microelectromechanical Systems 7 (3) (1998) 286–294.
[17] M.I. Younis, A. Nayfeh, A study of the nonlinear response of a resonant microbeam to an electric actuation, Nonlinear Dynamics 31 (1) (2003) 91–117.
[18] A.H. Nayfeh, M.I. Younis, Dynamics of MEMS resonators under superharmonic and subharmonic excitations, Journal of Micromechanics and Microengineering 15 (10) (2005) 1840.
[19] S.J. Fiedziuszko, Applications of MEMS in communication satellites, in: 13th International Conference on Microwaves, Radar and Wireless Communications. MIKON-2000. Conference Proceedings (IEEE Cat. No. 00EX428), IEEE, 2000.
[20] W.J. Fleming, Overview of automotive sensors, IEEE Sensors Journal 1 (4) (2001) 296–308.
[21] C.-T. Huang, et al., Design and simulation of a microfluidic blood-plasma separation chip using microchannel structures, Separation Science and Technology 45 (1) (2009) 42–49.
[22] L. Renaudin, et al., Natural roller bearing fault detection by angular measurement of true instantaneous angular speed, Mechanical Systems and Signal Processing 24 (7) (2010) 1998–2011.
[23] H. Azimloo, et al., Bifurcation analysis of an electro-statically actuated micro-beam in the presence of centrifugal forces, International Journal of Non-Linear Mechanics 67 (2014) 7–15.
[24] M.S. Lebold, et al., Using torsional vibration analysis as a synergistic method for crack detection in rotating equipment, in: 2004 IEEE Aerospace Conference Proceedings (IEEE Cat. No. 04TH8720), IEEE, 2004.
[25] M. Bodson, J. Chiasson, R.T. Novotnak, Nonlinear speed observer for high-performance induction motor control, IEEE Transactions on Industrial Electronics 42 (4) (1995) 337–343.
[26] H. Sedighi, A. Koochi, M. Abadyan, Modeling the size dependent static and dynamic pull-in instability of cantilever nanoactuator based on strain gradient theory, International Journal of Applied Mechanics 6 (5) (2014) 1450055.
[27] I. Karimipour, et al., Electromechanical instability of nanobridge in ionic liquid electrolyte media: influence of electrical double layer, dispersion forces and size effect, Indian Journal of Physics 90 (5) (2016) 563–575.
[28] M. Keivani, et al., Using strain gradient elasticity in conjunction with Gurtin–Murdoch theory for modeling the coupled effects of surface and size phenomena on the instability of narrow nano-switch, Proceedings of the Institution of Mechanical Engineers. Part C, Journal of Mechanical Engineering Science 231 (17) (2017) 3277–3288.
[29] A. Yekrangi, et al., Scale-dependent dynamic behavior of nanowire-based sensor in accelerating field, Journal of Applied and Computational Mechanics 5 (2) (2019) 486–497.
[30] D.C.C. Lam, et al., Experiments and theory in strain gradient elasticity, Journal of the Mechanics and Physics of Solids 51 (8) (2003) 1477–1508.
[31] R.K.A. Al-Rub, G. Voyiadjis, Determination of the material intrinsic length scale of gradient plasticity theory, International Journal of Multiscale Computational Engineering 2 (3) (2004).
[32] W. Wang, et al., A study of microbend test by strain gradient plasticity, International Journal of Plasticity 19 (3) (2003) 365–382.

[33] R. Maranganti, P. Sharma, A novel atomistic approach to determine strain-gradient elasticity constants: tabulation and comparison for various metals, semiconductors, silica, polymers and the (ir) relevance for nanotechnologies, Journal of the Mechanics and Physics of Solids 55 (9) (2007) 1823–1852.
[34] Y. Zhang, Y.-P. Zhao, Measuring the nonlocal effects of a micro/nanobeam by the shifts of resonant frequencies, International Journal of Solids and Structures 102 (2016) 259–266.
[35] M. Keivani, et al., On the dynamic instability of nanowire-fabricated electromechanical actuators in the Casimir regime: coupled effects of surface energy and size dependency, Physica. E, Low-Dimensional Systems and Nanostructures 76 (2016) 60–69.
[36] Y.P. Zhao, L.S. Wang, T.X. Yu, Mechanics of adhesion in MEMS — a review, Journal of Adhesion Science and Technology 18 (4) (2003) 519–546.
[37] M. Keivani, et al., Static and dynamic instability of nanowire-fabricated nanoelectromechanical systems: effects of flow damping, van der Waals force, surface energy and microstructure, Canadian Journal of Physics 94 (6) (2016) 594–603.
[38] M. Keivani, A. Koochi, M. Abadyan, A new model for stability analysis of electromechanical nano-actuator based on Gurtin–Murdoch and consistent couple-stress theories, Journal of Vibroengineering 18 (3) (2016).
[39] C. Feng, Y.-P. Zhao, D. Liu, Squeeze-film effects in MEMS devices with perforated plates for small amplitude vibration, Microsystem Technologies 13 (7) (2007) 625.
[40] C.L. Berli, A. Cardona, On the calculation of viscous damping of microbeam resonators in air, Journal of Sound and Vibration 327 (1–2) (2009) 249–253.
[41] Y. Beni, M. Abadyan, A. Koochi, Effect of the Casimir attraction on the torsion/bending coupled instability of electrostatic nano-actuators, Physica Scripta 84 (6) (2011) 65801.
[42] H. Moeenfard, A. Darvishian, M.T. Ahmaidan, Static behavior of nano/micromirrors under the effect of Casimir force, an analytical approach, Journal of Mechanical Science and Technology 26 (2) (2012) 537–543.
[43] A. Darvishian, et al., A coupled two degree of freedom pull-in model for micromirrors under capillary force, Acta Mechanica 223 (2) (2012) 387–394.
[44] J.P. Zhao, et al., A study of dynamic characteristics and simulation of MEMS torsional micromirrors, Sensors and Actuators. A, Physical 120 (1) (2005) 199–210.
[45] H. Sedighi, et al., A modified model for circular scanner-type nano-mirrors with size-dependency, squeeze film damping and Casimir effects by considering finite conductivity, Microsystem Technologies 23 (4) (2017) 875–888.
[46] H. Sedighi, et al., Size-dependent dynamic behavior and instability analysis of nano-scale rotational varactor in the presence of Casimir attraction, International Journal of Applied Mechanics 8 (2) (2016) 1650018.
[47] M. Keivani, et al., Modeling the effect of microstructure on the coupled torsion/bending instability of rotational nano-mirror in Casimir regime, Microsystem Technologies 23 (7) (2017) 2931–2942.
[48] J.M. Huang, et al., An approach to the coupling effect between torsion and bending for electrostatic torsional micromirrors, Sensors and Actuators. A, Physical 115 (1) (2004) 159–167.
[49] H. Mohammad-Sedighi, et al., Microstructure-dependent dynamic behavior of torsional nano-varactor, Measurement 111 (2017) 114–121.
[50] M. Keivani, et al., A 2-DOF model for incorporating the effect of microstructure on the coupled torsion/bending instability of nano-mirror in Casimir regime, Optik 130 (2017) 1272–1284.
[51] M. Keivani, et al., A 2-DOF microstructure-dependent model for the coupled torsion/bending instability of rotational nanoscanner, Applied Physics. A 122 (10) (2016) 927.
[52] H. Moeenfard, M.T. Ahmadian, The influence of vertical deflection of the supports in modeling squeeze film damping in torsional micromirrors, Microelectronics Journal 43 (8) (2012) 530–536.
[53] H. Moeenfard, M. Mojahedi, M.T. Ahmadian, A homotopy perturbation analysis of nonlinear free vibration of Timoshenko microbeams, Journal of Mechanical Science and Technology 25 (3) (2011) 557.

[54] H.M. Sedighi, The influence of small scale on the pull-in behavior of nonlocal nanobridges considering surface effect, Casimir and van der Waals attractions, International Journal of Applied Mechanics 6 (03) (2014) 1450030.
[55] J. Muñoz-Gamarra, et al., Integration of NEMS resonators in a 65 nm CMOS technology, Microelectronic Engineering 110 (2013) 246–249.
[56] M. Dragoman, et al., Microwave switches based on graphene, Journal of Applied Physics 105 (5) (2009) 054309.
[57] A. Uranga, et al., Exploitation of non-linearities in CMOS-NEMS electrostatic resonators for mechanical memories, Sensors and Actuators. A, Physical 197 (2013) 88–95.
[58] C. Hierold, et al., Nano electromechanical sensors based on carbon nanotubes, Sensors and Actuators. A, Physical 136 (1) (2007) 51–61.
[59] N.A. Fleck, et al., Strain gradient plasticity: theory and experiment, Acta Metallurgica Et Materialia 42 (2) (1994) 475–487.
[60] A.W. McFarland, J.S. Colton, Role of material microstructure in plate stiffness with relevance to microcantilever sensors, Journal of Micromechanics and Microengineering 15 (5) (2005) 1060–1067.
[61] T. Murmu, M. McCarthy, S. Adhikari, Vibration response of double-walled carbon nanotubes subjected to an externally applied longitudinal magnetic field: a nonlocal elasticity approach, Journal of Sound and Vibration 331 (23) (2012) 5069–5086.
[62] K. Kiani, Characterization of free vibration of elastically supported double-walled carbon nanotubes subjected to a longitudinally varying magnetic field, Acta Mechanica 224 (12) (2013) 3139–3151.
[63] M. Mirramezani, H.R. Mirdamadi, M. Ghayour, Nonlocal vibrations of shell-type CNT conveying simultaneous internal and external flows by considering slip condition, Computer Methods in Applied Mechanics and Engineering 272 (2014) 100–120.
[64] E.M. Miandoab, A. Yousefi-Koma, H.N. Pishkenari, Nonlocal and strain gradient based model for electrostatically actuated silicon nano-beams, Microsystem Technologies 21 (2) (2015) 457–464.
[65] F. Najar, et al., Nonlinear nonlocal analysis of electrostatic nanoactuators, Composite Structures 120 (2015) 117–128.
[66] A.G. Arani, et al., Nonlinear vibration of coupled nano-and microstructures conveying fluid based on Timoshenko beam model under two-dimensional magnetic field, Acta Mechanica 226 (8) (2015) 2729–2760.
[67] H.M. Sedighi, M. Keivani, M. Abadyan, Modified continuum model for stability analysis of asymmetric FGM double-sided NEMS: corrections due to finite conductivity, surface energy and nonlocal effect, Composites. Part B, Engineering 83 (2015) 117–133.
[68] M. Rahmanian, et al., Free vibrations analysis of carbon nanotubes resting on Winkler foundations based on nonlocal models, Physica. B, Condensed Matter 484 (2016) 83–94.
[69] S. Bornassi, H. Haddadpour, Nonlocal vibration and pull-in instability analysis of electrostatic carbon-nanotube based NEMS devices, Sensors and Actuators. A, Physical 266 (2017) 185–196.
[70] M. Nie, Q.-A. Huang, W. Li, Pull-in characterization of doubly-clamped composite beams, Sensors and Actuators. A, Physical 151 (2) (2009) 118–126.
[71] Y.-J. Chang, et al., Micromachined resonators of high Q-factor based on atomic layer deposited alumina, Sensors and Actuators. A, Physical 154 (2) (2009) 229–237.
[72] F. Mahmoud, et al., Static analysis of nanobeams including surface effects by nonlocal finite element, Journal of Mechanical Science and Technology 26 (11) (2012) 3555–3563.
[73] I. Mehdipour, D. Ganji, M. Mozaffari, Application of the energy balance method to nonlinear vibrating equations, Current Applied Physics 10 (1) (2010) 104–112.
[74] S. Ganji, D. Ganji, S. Karimpour, He's energy balance and He's variational methods for nonlinear oscillations in engineering, International Journal of Modern Physics B 23 (03) (2009) 461–471.
[75] N. Jamshidi, D. Ganji, Application of energy balance method and variational iteration method to an oscillation of a mass attached to a stretched elastic wire, Current Applied Physics 10 (2) (2010) 484–486.

[76] Y. Fu, J. Zhang, L. Wan, Application of the energy balance method to a nonlinear oscillator arising in the microelectromechanical system (MEMS), Current Applied Physics 11 (3) (2011) 482–485.
[77] M. Ghalambaz, M. Ghalambaz, M. Edalatifar, Buckling analysis of cantilever nanoactuators immersed in an electrolyte: a close form solution using Duan-Rach modified Adomian decomposition method, Journal of Applied and Computational Mechanics 1 (4) (2015) 207–219.
[78] R. Langdon, Resonator sensors-a review, Journal of Physics. E, Scientific Instruments 18 (2) (1985) 103.
[79] M. Elwenspoek, R. Wiegerink, Mechanical Microsensors, Springer Science & Business Media, 2012.
[80] G. Stemme, Resonant silicon sensors, Journal of Micromechanics and Microengineering 1 (2) (1991) 113.
[81] A. Hajjam, S. Pourkamali, Fabrication and characterization of MEMS-based resonant organic gas sensors, IEEE Sensors Journal 12 (6) (2011) 1958–1964.
[82] H.A. Tilmans, M. Elwenspoek, J.H. Fluitman, Micro resonant force gauges, Sensors and Actuators. A, Physical 30 (1–2) (1992) 35–53.
[83] A. Tocchio, A. Caspani, G. Langfelder, Mechanical and electronic amplitude-limiting techniques in a MEMS resonant accelerometer, IEEE Sensors Journal 12 (6) (2011) 1719–1725.
[84] R. Mestrom, et al., Modelling the dynamics of a MEMS resonator: simulations and experiments, Sensors and Actuators. A, Physical 142 (1) (2008) 306–315.
[85] R. Mestrom, et al., Experimental validation of hardening and softening resonances in a clamped-clamped beam MEMS resonator, Procedia Chemistry 1 (1) (2009) 812–815.
[86] A.H. Nayfeh, D.T. Mook, Nonlinear Oscillations, John Wiley & Sons, 2008.
[87] M. NikkhahBahrami, A. Ataei, A large deflection model for the dynamic pull-in analysis of electrostatically actuated nanobeams in presence of intermolecular surface forces [*J*], in: Advanced Research in Physics and Engineering, 2010.
[88] W. Xia, L. Wang, L. Yin, Nonlinear non-classical microscale beams: static bending, postbuckling and free vibration, International Journal of Engineering Science 48 (12) (2010) 2044–2053.
[89] M.H. Kahrobaiyan, et al., A nonlinear strain gradient beam formulation, International Journal of Engineering Science 49 (11) (2011) 1256–1267.
[90] S. Ramezani, A micro scale geometrically non-linear Timoshenko beam model based on strain gradient elasticity theory, International Journal of Non-Linear Mechanics 47 (8) (2012) 863–873.
[91] J. Zhao, et al., Nonlinear microbeam model based on strain gradient theory, Applied Mathematical Modelling 36 (6) (2012) 2674–2686.
[92] E.M. Miandoab, et al., Chaos prediction in MEMS–NEMS resonators, International Journal of Engineering Science 82 (2014) 74–83.
[93] M. Rahaeifard, M.T. Ahmadian, K. Firoozbakhsh, Size-dependent dynamic behavior of microcantilevers under suddenly applied DC voltage, Proceedings of the Institution of Mechanical Engineers. Part C, Journal of Mechanical Engineering Science 228 (5) (2014) 896–906.

Index

A

Accelerating force, 133, 135, 136
Accelerometer microsensor, 2
Actuation
  method, 1, 5, 6
  voltage, 118, 161, 248
Actuator
  bending, 68
  deflection, 62, 68
Admissible trial functions, 96
Adomian decomposition, 43, 49
  conventional, 31, 43
  method, 31, 43, 50, 60–63
Adomian polynomials, 43, 44, 47, 55, 56, 58
Algebraic equations, 92, 93, 96, 97, 108, 116, 125, 128, 135
Arms
  nanotweezers, 116
  radius, 87
  rotational, 199
  tweezers, 87
Atomic force microscopy (AFM), 2, 3, 19, 126
Attracting electrical force, 44
Axisymmetric
  bending, 96
  microplate, 99
  microplate deflection, 98

B

Beam
  cantilever, 2, 19, 22, 32, 118, 172
  deflection, 41, 45, 63, 144
  density, 241
  element, 138
  element deflection, 139
  geometry, 51
  length, 14, 82, 244
  linear stiffness coefficients, 19
  parallel, 166
  theory, 140
  thickness, 14, 127, 165, 244
  width, 15, 41
Bending, 41, 97, 147, 150, 206, 208, 212, 218
  moment, 45, 94, 140, 219, 220
  rigidity, 11, 95
  stiffness, 11
Biosensors, 126

C

Cantilever
  beam, 2, 19, 22, 32, 118, 172
  electromechanical nanoactuator, 181
  Euler beam, 182
  MEMS resonators, 32
  microactuators stiffness, 19
  microbeams, 32
  nanoactuator, 32, 217
  nanoswitch, 44, 46, 47
  nanowires, 118, 119
  NEMS/MEMS, 129, 133
Capacitance, 5, 6, 34, 72, 86, 95, 166, 201
  model, 86, 95
  parallel plate capacitors, 34
  per unit length, 34, 72
  values, 166, 167
Capacitor, 5, 34, 72, 86, 166, 187
  model, 201
  parallel plate, 33, 120, 201
  potential, 166
Casimir
  attraction, 144
  force, 10, 11, 44, 46, 47, 49, 80, 81, 83, 113, 114, 116, 117, 126–128, 133, 135, 165, 167–170, 175, 176, 187
    dimensionless parameter, 115, 142, 214
  interaction, 46
  moment, 209, 211, 212
  parameters, 49
  regime, 113, 138
Centerline
  bending, 41
  deflection, 94
Circular
  micromembrane, 93
  microplate, 94, 97, 99
  nanoscanner, 206

Clamped
beams, 14, 19
microplate, 146
Constitutive equation, 12, 23, 25, 35, 52, 100, 111, 122, 123, 127, 156, 169, 182, 199, 202, 212, 231
dimensionless, 171
for axisymmetric bending, 95
nonlinear, 169
Continuum mechanics, 12, 18, 23, 26, 156
nanoscale, 23
Couple stress, 11, 53, 78, 79, 109, 111, 217, 228, 229
tensor, 12, 52, 71, 79, 109, 164

D

Damping, 14, 18, 22, 188, 191, 206, 207
characteristics, 177
coefficient, 14, 15, 17, 22, 188, 202
effect, 22, 204, 206, 216, 230
force, 16, 168, 204
ratio, 14, 18, 22, 190, 203
torsional, 209
virtual work, 202
DC electrical potential, 177
DC voltage, 8, 85, 99, 161, 177, 181, 206, 248
Deflected
nanoactuator, 34
nanoswitch, 46, 72
nanowire, 72, 73
Deflection
beam, 41, 45, 63, 144
dimensionless, 67, 142, 144, 191
nanobeam, 44
nanobridge, 83, 144
nanoresonator, 234
nanosensor, 188
nanowire, 190
profile, 97, 98
static, 19, 42, 177
surface, 219
virtual, 35, 209
Degree of freedom (DOF), 171
Detachment length, 68, 69, 117
Differential equation, 19, 23, 31, 32, 36, 43, 55, 63, 64, 90, 93, 121, 126, 138, 142, 191, 213, 214, 231, 237
nonlinear, 26, 31, 43, 66, 96, 107, 123, 156, 223
time-dependent, 162, 163, 171, 217, 237
Differential transformation method, 77
Dimensionless
boundary conditions, 58
Casimir force, 116
constitutive equation, 171
deflection, 67, 142, 144, 191
electrical potential, 214
equation, 36, 47, 54, 63, 74, 89, 127, 142
governing equation, 36, 58, 82, 88, 114, 122, 134, 170, 180, 203, 222, 232
instability voltage, 193
nonlinear governing equation, 244
parameter, 36, 41, 47, 54, 58, 62, 66, 74, 76, 83, 88, 89, 114, 115, 117, 123, 127, 128, 134, 135, 170, 180, 181, 190, 203, 214
size parameter, 236
surface parameters, 171, 190
time, 170, 190, 191, 203, 206, 214
Dispersion forces, 10, 116
Displacement vector, 71, 79, 112, 164, 165, 182

E

Electrical
attracting force, 44
attraction, 141
effect, 73
energy, 5, 34, 95, 113
field, 5, 33, 42, 46, 166
force, 5, 6, 8, 33, 34, 36, 43, 46, 47, 49, 72, 113, 119, 121, 124, 126, 141, 142, 165–167, 178, 179, 187, 201, 207, 209
dimensionless parameter, 128, 203
moment, 209, 211
potential, 6, 33, 34
signal, 6
virtual work, 35
Electrically actuated microplates, 146
Electrode deflections, 87
Electromechanical
microplate, 162
nanobridge, 217, 221, 222
Electrostatic
force, 6, 8, 87, 93, 144, 153
nanotweezers, 85
Energy balance method, 227
Energy loss, 13–17, 168, 230
Epoxy beams, 11
Euler beam, 140
cantilever, 182

F

Finite difference method (FDM), 124, 125
Finite element method (FEM), 136
  solution, 97–99, 139, 142, 144, 153, 155, 156
Free end, 19, 36, 41, 68, 118, 119, 129–131, 191
  nanobeam, 119
  nanowire, 118, 124, 131
Fringing field, 6, 34, 36, 42, 43, 47, 49, 113
  effect, 6, 34, 42

G

Galerkin
  method, 90, 93, 96, 98, 99, 161–163, 171, 172, 182, 217, 222
  procedure, 96, 97, 99, 171, 172, 222, 232
  solution, 96, 97, 99, 171, 173
  technique, 182
Generalized Differential Quadrature (GDQ), 108, 109, 115, 123
Governing equation, 46, 75, 82, 94–96, 114, 118, 131–133, 161, 206, 212, 220, 221, 230, 238, 241
  dimensionless, 36, 58, 82, 88, 114, 122, 134, 170, 180, 203, 222, 232
  nanoactuator, 35, 179
  nonlinear, 100
Graphene substrate, 65
Green's function, 63, 64

H

Homotopy perturbation, 41, 223, 225
Homotopy perturbation method, 31, 217, 223
Homotopy perturbation solution, 41, 222, 225

I

Instability voltage, 49, 58, 83, 124, 136, 192
  dimensionless, 193

L

Length scale parameter, 52, 80, 111, 165, 176, 185, 193, 247
Lumped parameter model, 8, 18, 21–23, 199

M

Maximum deflection, 62, 97–99, 144, 155, 156
Micro nanoresonators, 8
Micro nanostructures stiffness, 19
Microactuator, 19, 175
Microbeam, 238
  plastic work hardening, 11
Microbridge, 217
Microcapacitor, 147, 156
  parallel plate, 8
Microelectromechanical systems (MEMS), 1, 3–6, 13, 15–19, 22, 31, 50, 64, 77, 93, 99, 100, 107, 118, 125, 129, 145, 154, 168, 177, 217, 248
Microgears, 126
Micromechanic continuum technique, 199
Micromembrane, 93, 95, 96
  circular, 93
Micromirrors, 8
Microoptoelectromechanical systems (MOEMS), 199
Microplate, 93–95, 97–99, 155, 156
  circular, 94, 97, 99
Microresonator, 2, 229
Microscale, 17
Microstructure, 1, 156, 192
Microswitch, 2, 75–77
Microtweezers, 2, 90, 109
Microvalves, 126
Midplane deflection, 94
Mindlin couple stress theory, 12
Miniature structures, 1, 11, 12, 52, 217
Modified Adomian decomposition method, 50, 58, 62, 63
Monotonic iteration method, 70
Movable
  component deflection, 8
  nanowire, 71
Multiple scales technique, 237

N

Nanoactuator, 32–36, 41–47, 125, 126, 163, 168, 170, 171, 173, 175–177, 180, 181
  cantilever, 32, 217
  deflected, 34
  dimensionless governing equation, 58
  governing equation, 179
  tip deflection, 174
Nanobeam, 2, 19, 32, 44, 52, 68, 130–133, 163, 167, 171, 190, 199, 201, 208, 218, 219
  constructing material, 34
  deflection, 44
  free end, 119
  thickness, 208

tip, 133
width, 42, 208
Nanobridge, 83, 138, 141, 144, 217, 218, 225
constitutive equations, 81
deflection, 83, 144
element, 80
frequency, 225
Nanoelectromechanical systems (NEMS), 1, 3–6, 13, 15–19, 22, 31, 44, 50, 58, 64, 70, 77, 93, 99, 100, 107, 125, 129, 145, 154, 161, 168, 177, 199, 217, 223
rotational, 199
Nanomirror, 204, 206
rotation angle, 204
rotational, 199, 202
torsional, 199
Nanoplates, 93
Nanoresonator, 2, 22, 217, 228–230, 235, 236
deflection, 234
frequency, 236
Nanoscale, 1, 17, 23, 26, 34, 51, 116
beams, 206
continuum, 26
continuum mechanics, 23
continuum models, 23
effects, 26
phenomena, 1, 18, 23, 26, 31, 248
sphere, 13
structures, 32, 156
Nanoscanner, 206, 208–212
area, 209
circular, 206
Nanosensor, 182–184, 186, 188, 191–195, 217
deflection, 188
tip displacement, 191
Nanostructures, 1, 4, 14, 17–19, 23, 31, 58, 77, 78, 100, 107, 109, 126, 156, 161, 163, 191, 217, 248
static behavior, 100, 156, 161
stiffness, 19
Nanoswitch, 2, 44–46, 49, 70, 75–77, 126, 194, 217
cantilever, 44, 46, 47
deflected, 46, 72
in Casimir regime, 44
Nanotweezers, 2, 85, 88, 90, 109, 112–114, 116, 126
arms, 114
dimensionless governing equation, 114
freestanding, 85, 90, 116
operated, 85
Nanowire, 70, 72–76, 109, 118, 119, 121, 123, 182, 187, 188
deflected, 72, 73
deflection, 190
diameter, 72
fabricated sensor, 182
fabricated switch, 73
free end, 118, 124, 131
manufactured nanoswitch, 70
manufactured nanotweezers, 85
movable, 71
radius ratio, 74
Natural frequency, 22, 172, 178, 181, 245
NEMS/MEMS
cantilever, 129, 133
nonlinear differential equations, 107
sensors, 6
Nodal deflection, 129, 139
Nonlinear
constitutive equation, 169
differential equation, 26, 66, 96, 107, 123, 156, 223
governing equation, 100
Nonlocal nanobridge, 217, 220
Nonuniform electric field, 6, 34, 113
Numerical solution, 31, 41, 49, 61, 63, 107, 129, 136, 154, 156, 167, 225

P

Paddle area, 124, 136
Parallel
beams, 5, 166
conducting plates, 11
flat plates, 10
plates, 5, 10, 33, 34, 46, 113, 114, 120, 141, 166–168, 188, 209
capacitor, 33, 95, 120, 201, 209
Casimir force, 168
microcapacitor, 8
Partial differential equations, 124, 161, 162, 182, 217, 222
Pertinent voltage, 8
Piezoresistive silicon nanowires, 93
Plates, 5, 8, 10, 34, 93, 199, 228
parallel, 5, 10, 33, 34, 46, 113, 114, 120, 141, 166–168, 188, 209
Polypropylene microcantilevers stiffness, 11

R

Radio frequency (RF), 2
Rayleigh–Ritz method, 181
Retardation length, 11, 187
Rotation
  angle, 201, 204, 206, 209
  tensor, 111
  tensor gradient, 111
  vector, 52, 71, 165
  virtual, 209
Rotational
  arms, 199
  damping coefficient, 214
  micromirror, 199
  nanomirror, 199, 202
  NEMS, 199
  springs, 52
Runge–Kutta method, 195

S

Scanner deflection, 208
Scanning electron microscope (SEM) image, 2, 32, 64, 85, 93, 109, 129, 146, 199, 217
Silicon nanowire, 70
Slide film damping, 16
Squeezed film, 15, 16, 168, 188
  damping, 15, 16, 168, 169, 177, 191, 192, 209
  damping force, 165
  for parallel plates, 16
Stable center point, 174, 191, 194, 206
Static
  behavior, 44, 156, 217
  deflection, 19, 42, 177
  problems, 162, 163
Stiffness
  bending, 11
  constant, 22
  nanostructures, 19
  parameter, 175
  torsional, 201
Stress tensor, 12, 25, 26, 35, 52, 109–111, 119, 131, 163, 164
Substrate, 2, 17, 44, 45, 49, 68, 72, 141, 174, 188, 199, 203, 217, 218
Surface
  deflection, 219
  elasticity, 13, 111, 115, 165, 171, 175, 190, 217, 220
  energies, 13, 109, 111, 163, 171, 172, 175, 220

T

Thermoplastic damping, 13
Torsional
  beams, 199, 200
  damping, 209
  damping coefficients, 209
  damping moment, 209
  nanobeams, 199
  nanomirror, 199
  stiffness, 201
Trial
  functions, 90, 92, 97, 162, 182
  solution, 92, 93, 96, 163, 182, 228, 234
Tuneable torsional capacitors, 199

U

Ultrasmall structures, 13, 15, 22, 32, 70, 78, 248

V

Van der Waals force, 10, 62
Variation iteration method, 84
Virtual
  deflection, 35, 209
  rotation, 209
  work, 35, 207, 209, 212
Viscous damping, 209

W

Weighting coefficients, 107, 108, 116
Wire bending, 75